Downloaded from orbit.dtu.dk on: May 02, 2024

DTU Library

Electrochemical TEM experiments on solid oxide cells

Ma, Zhongtao

Publication date:
2023

Document Version
Publisher's PDF, also known as Version of record

Link back to DTU Orbit

Citation (APA):
Ma, Z. (2023). *Electrochemical TEM experiments on solid oxide cells*. Technical University of Denmark.

General rights
Copyright and moral rights for the publications made accessible in the public portal are retained by the authors and/or other copyright owners and it is a condition of accessing publications that users recognise and abide by the legal requirements associated with these rights.

- Users may download and print one copy of any publication from the public portal for the purpose of private study or research.
- You may not further distribute the material or use it for any profit-making activity or commercial gain
- You may freely distribute the URL identifying the publication in the public portal

If you believe that this document breaches copyright please contact us providing details, and we will remove access to the work immediately and investigate your claim.

DTU

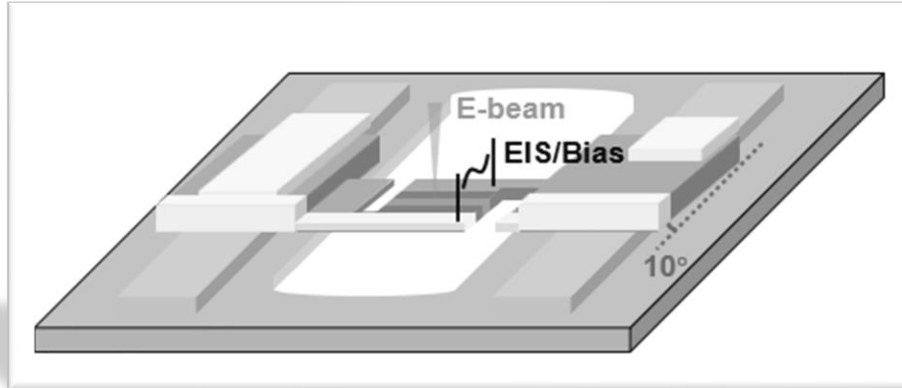

Electrochemical TEM experiments on solid oxide cells

Ph.D. Thesis

By Zhongtao Ma

June 1st, 2023

Section for Imaging and Structural Analysis

Department of Energy Conversion and Storage

Technical University of Denmark

Contents

Preface v

List of publications vi

Abstract 1

Chapter 1: Introduction 2

1.1 Motivation 2

1.2 Goal of project 3

1.3 Thesis overview 3

References 4

Chapter 2: Theory and Methods 6

2.1 Electron Microscopy 6

2.1.1 TEM 7

2.1.2 The configuration of TEM 7

2.1.3 Difference between TEM mode and STEM mode 9

2.1.4 Detectors 10

2.1.5 Contrast 11

2.1.6 In situ environmental TEM (ETEM) 14

2.1.7 SEM 16

2.1.8 Electron energy loss spectroscopy (EELS) 17

2.1.9 Energy dispersive spectroscopy (EDS) 19

2.2 The solid oxide cell (SOC) 21

2.2.1 Working principles of SOEC and SOFC 21

2.2.2 Thermodynamics of SOC 22

2.3 Electrochemical impedance spectroscopy (EIS) 23

2.4 Focused ion-beam scanning electron microscopy (FIB-SEM) 25

2.5 Pulsed laser deposition (PLD) 26

References 27

Chapter 3: Literature review 33

3.1 TEM heating experiments in reactive gasses 33

3.2 In situ biasing experiments in gases 35

3.2.1 Interpretation of EIS response signal 36

References 37

Chapter 4: Experimental requirements for high temperature solid state electrochemical TEM experiments 41
Abstract 41
1 Introduction 42
2 Materials and Methods 43
2.1 Materials and cell preparation 43
2.2 TEM sample preparation 44
2.3 Electrochemical TEM 45
3 Results and discussion 46
3.1 TEM sample preparation routine 46
3.2 Background Resistance and Capacitance 48
3.3 Sample fracture 52
3.4 Influence of electron beam 52
3.5 EIS-TEM measurements of single materials 53
3.6 Cell design 59
3.7 Cell geometries 61
3.8 EIS-TEM results from a cell 62
4 Conclusion 64
Acknowledgement 64
References 65
Supporting information 70
Chapter 5: Electrochemical Impedance Spectroscopy integrated with Environmental Transmission Electron Microscopy 73
Abstract 73
1 Introduction 74
2 Results and Discussion 76
2.1 Structure of the CGO sample 76
2.2 Morphology and Oxidation state 77
2.3 EIS electrical circuit model 78
2.4 EIS data analysis 80
2.5 The effect of porous Pt 85
2.6 Reproducibility of test results 86
3 Conclusion 87

4 Experimental Methods 88
4.1 Sintered pellet preparation 88
4.2 TEM sample preparation 88
4.3 EIS-TEM experiments 89
4.4 Error analysis 90
Acknowledgements 90
References 91
Supporting Information 95
Chapter 6: High Temperature Electrochemical ETEM study on solid oxide cells 107
Abstract 107
1 Introduction 107
2 Experimental 109
2.1 PLD deposition and characterization 109
2.2 symmetric cell fabrication 110
2.3 electrochemical TEM experiments 111
3 Results and Discussion 114
3.1 Application 1: EIS test of Pt-CGO-YSZ-CGO-STN 114
3.2 Application 2: High temperature biasing of Pt-LSC-YSZ-LSC-STN 118
4 Conclusion 127
References 128
Chapter 7: Conclusion 132
Chapter 8: Outlook 134
Appendix 1: *Small Methods - 2023 - Ma - Electrochemical Impedance Spectroscopy Integrated with Environmental Transmission Electron* 136
Appendix 2: *Manuscript of "Ion-beam deposited platinum as electrical contacting material in operando electron microscopy experiments at elevated temperatures"* 147
Appendix 3: *Licenses of 1) using the manuscript of Chapter 5 and 2) Figure 2 in Chapter 2* .. 165

Preface

This thesis is submitted in candidacy of the Ph.D. degree from the Technical University of Denmark (DTU). The PhD project is part of the "*High-temperature Electrochemical Impedance Spectroscopy Transmission electron microscopy on energy materials* (HEIST)" project. Financial support was from the European Research Council (ERC) under the European Union's Horizon 2020 research and innovation programme. The work was carried out for a three year period time, from June 2020 to May 2023, under supervision of Professor Søren Bredmose Simonsen from Imaging and Structural Analysis (ISA) at DTU Energy, Professor Christodoulos Chatzichristodoulou from Low Temperature Electrochemistry at DTU Energy, Professor Kristian Speranza Mølhave from Nanocharacterization at National Centre for Nano Fabrication and Characterization (DTU Nanolab). The sample preparation of this project is conducted in ISA section, DTU Energy and sample characterization is completed in DTU Nanolab.

I would like to express my most sincere gratitude to my supervisors, Søren Bredmose Simonsen, Christodoulos Chatzichristodoulou and Kristian Speranza Mølhave for their invaluable guidance, support, and encouragement with kindness and patience throughout my research.

At ISA section, I would like to thank our section leader Luise Theil Kuhn and all of my colleagues. Everyone has a harmonious relationship with each other, which creates a pleasant working environment for my research. Thanks to my supervisors, Søren Bredmose Simonsen, who gave me the training of TEM both in Risø and in Lyngby and taught me everything about it. Christodoulos Chatzichristodoulou for the EIS measurement and data analysis. Thanks to Karl Tor Sune Thydén for the training of crossbeam and SEM, which are extremely important in my project. Thanks to Salvatore De Angelis for the training of SEMs. Thanks to my fellow PhD student in HEIST group Waynah Lou Dacayan for the great cooperation and help. Thanks to all my friends Mette, Luke, Domenico, Estrid, Cedrik, Xinyu, Adi, Suraj, Kristofer, Michael, Anastasia, and Mariana for their helpful discussions and activities.

At DTU energy. Thanks to Ebtisam Abdellahi, who gives the best sample polishing. Thanks to Francesco Chiabrera and Elena Marzia Sala who give PLD sample preparation. Thanks to all my Chinese friends here Qingjie, Yifan, Baichen, Zhipeng, Kai, Shu, Yichen, Kun, Hua, Yun, Jianan and Xuan.

At DTU Nanolab. Thanks to Jens Kling for the help and training of operating ETEM, STEM, EDS and EELS. Thanks to Shima Kadkhodazadeh for the EELS data analysis. Thanks to Elisabetta Maria Fiordaliso for the help of Helios FIB-SEM. Thanks to Frederik Ryberg Madsen for the help of Hydra FIB-SEM.

At the University of Rome Tor Vergata where I did my external stay, I would like to thank Simone Sanna and Antonello Tebano for their host. Thanks to Simone for the help of YSZ film deposition and X-ray diffraction. Thanks to Antonello for the teaching of the principle of X-ray rocking curve and θ-2θ scan. Thanks to Daniele Di Castro for the teaching of equipment operation.

I was always accompanied by my family and friends in China while growing up and during this 3 years study, for which I am very grateful.

Zhongtao Ma

Kgs. Lyngby, May 2023

List of publications

List of included publications included in this thesis:

Journal paper:

1) Ma, Z., Dacayan, W.L., Chatzichristodoulou, C., Mølhave, K.S., Chiabrera, F.M., Zhang, W., and Simonsen, S.B. (2023). Electrochemical Impedance Spectroscopy Integrated with Environmental Transmission Electron Microscopy. Small Methods *n/a*, 2201713.
2) Ma, Z., Chatzichristodoulou, C., Dacayan, W.L., Mølhave, K.S., Chiabrera, F.M., and Simonsen, S.B. (2023). Experimental requirements for high temperature solid state electrochemical TEM experiments. *In preparation*.
3) Ma, Z., Chatzichristodoulou, C., Mølhave, K.S., Chiabrera, F.M., Dacayan, W.L., and Simonsen, S.B. (2023). High Temperature Electrochemical ETEM study on solid oxide cells. *In preparation*.

List of publications not included in this thesis:

Journal paper:

1) Yao, Y., Ma, Z., Dou, Y., Lim, S.Y., Zou, J., Stamate, E., Jensen, J.O., and Zhang, W. (2022). Random Occupation of Multimetal Sites in Transition Metal-Organic Frameworks for Boosting the Oxygen Evolution Reaction. Chemistry – A European Journal *28*, e202104288.
2) Sala, E.M., Mazzanti, N., Chiabrera, F.M., Sanna, S., Mogensen, M.B., Hendriksen, P.V., Ma, Z., Simonsen, S.B., and Chatzichristodoulou, C. (2023). Unravelling the role of dopants in the electrocatalytic activity of ceria towards CO2 reduction in solid oxide electrolysis cells. Physical Chemistry Chemical Physics *25*, 3457-3471.
3) Sanna, S. and Krymskaya, O. and Ma, Z. and De Angelis, S. and Di Castro, D. and Felici, R. and Coati, A. and Balestrino, G. and Simonsen, S. B. and Tebano, A., Ionic Transport in Samarium Doped Ceria Free-Standing Single Crystal Membrane. Available at SSRN: https://ssrn.com/abstract=4407528 or http://dx.doi.org/10.2139/ssrn.4407528
4) Simonsen, S.B., Ma, Z., Mariegaard, E., De Angelis, Dacayan, W.L., Mølhave, K.S., Chatzichristodoulou, C., Ion-beam deposited platinum as electrical contacting material in operando electron microscopy experiments at elevated temperatures. *In submission.*

Conference paper:

1) Simonsen, S.B., Dacayan, W.L., Ma, Z., Chatzichristodoulou, C., Zhang, W., and Mølhave, K.S. (2021). Development of high-temperature electrochemical TEM and its application on solid oxide electrolysis cells. Microsc microanal 27, 3138-3139.
2) Dacayan, W.L., Chatzichristodoulou, C., Ma, Z., Zhang, W., Mølhave, K.S., and Simonsen, S.B. (2021). Combining EIS with in Situ TEM in Characterizing Solid Oxide Cell Components. ECS Meeting Abstracts *MA2021-02*, 1899.

Abstract

In response to climate change and its potential negative impacts, there is a growing trend of using sustainable energy to replace fossil fuels. Developing related fuel production and storage technologies is becoming increasingly important. Solid oxide electrolysis/fuel cell (SOEC/SOFC) has become a research hotspot due to its high energy conversion efficiency, relatively lower cost, low noise, and scalability. However, its degradation mechanisms at high working temperatures are still unclear. In order to enable larger-scale commercial applications, further optimization is required in terms of cost and operational stability. The performance of SOC-related components, such as electrodes and electrolytes, needs to be improved, and their degradation mechanisms need to be further studied. Advanced characterization methods, especially in situ techniques, are necessary to introduce.

Electrochemical impedance spectroscopy is a powerful technique in electrochemistry, and one of its advantages is allowing operando characterization on a running system without causing damage to the research object. It works by applying an oscillating voltage/current (the frequency usually ranges from 0.01 to 1000000 Hz) and collecting response current/voltage. By fitting the data with an equivalent electric circuit model (ECM) of the electrochemical system, one can get the contributions of different processes in the reaction.

Environmental TEM can inlet different gases into the column and, with a DENS solutions lighting holder, heating and biasing can be also applied to the sample. This unique combination allows us to mimic the practical environments of running a solid oxide electrolysis/fuel cell/materials. In addition, by combining simultaneous EIS or biasing signal, one can investigate the structural/elemental evolutions and their effect on the electrochemical performance on a running system inside the ETEM.

In this PhD project, I focus on the application of electrochemical ETEM to investigate the properties of solid oxide materials/structures used for SOFC/SOEC, which can potentially also be applied to batteries and thermoelectric devices. Firstly, I identify the key considerations for conducting solid-state electrochemical TEM experiments, including sample preparation, electrochemical measurement, failure factors, and optimization methods. I developed an entire sample preparation process using FIB-SEM and provided examples of typical EIS spectra for pure electronic, pure ionic, and mixed ionic and electronic conductors, as well as cell structures. Next, I demonstrate the feasibility of combining EIS with environmental TEM to investigate the electrochemical properties of a micro CGO sample in reactive gases at elevated temperatures, the derived transport and surface reaction data are consistent with those from literatures. Finally, I conducted the high temperature EIS-TEM measurement on a nano CGO-YSZ-CGO model cell and applied a high temperature biasing measurement on an nano LSC-YSZ-LSC cell in different atmospheres and at high temperatures. The results from EIS-TEM and biasing-TEM are consistent with we expected with two arcs contributed by transport and surface properties respectively. For high temperature biasing-TEM experiments, the (S)TEM structure analysis, the STEM-EDS, and STEM-EELS results revealed the decomposition of LSC layers under the cathodic biasing. Those results demonstrated the feasibility of apply high temperature EIS-TEM or biasing-TEM experiments on the cell structures in the ETEM.

Generally speaking, this work demonstrates the feasibility of performing high temperature electrochemical measurements on solid oxide samples inside the ETEM, which can serve as an important methods for future studies on energy materials or cell studies.

Chapter 1: Introduction

1.1 Motivation

Fossil fuels have been a primary energy source of humankind for more than hundreds of years. The great amount of usage not only results in global warming, but also significant pollution, leading to issues such as climate change, public health risks, and depletion of natural resources. Therefore, it is urgent to adopt sustainable energy sources such as wind, solar, or biomass energy. However, those energy sources have the drawback of fluctuating production, for instance, solar energy is unavailable at night, and wind turbines require wind. In order to match supply with demand, further development of energy conversion and storage techniques are necessary, which should be able to scale up and highly efficient. The solid oxide electrolysis cells (SOEC) and solid oxide fuel cells (SOFC) are very promising candidates. SOECs can produce chemical fuels by electrolysis of H_2O, CO_2 or CO_2+H_2O, and SOFC can generate electricity and heat by electrochemical reactions with air/oxygen and fuels such as H_2 or hydrocarbons [1,2]. SOECs/SOFCs have very high energy conversion efficiency [3], and H_2 and syngas are very good energy carriers for energy storge. However, the current cost of solid oxide cell (SOC) system is still high. The median system cost in 2020 was around \$2,450/kW_{net} [4]. And the relatively high degradation rate of 1% per 1000 hours calls for improvements of the SOC systems with more rational design. Some of the problems in SOC needed to be tackled are Sr element segregating on the perovskite LSCF or LSC cathode materials during ORR process [5,6], Ni coarsening in the anode material Ni-YSZ [7], and poisoning caused by Cr [8], S [9], Cl [10]. In order to solve existing problems and improve the SOC performance and to lower its price, it is necessary to develop new characterization methods to know the root causes. Especially, it is critical to determine the relationship between the electrochemical activity under working conditions and the structure/composition of components for the energy devices and coupling them [11].

Transmission electron microscopy (TEM) has demonstrated its potential in analyzing crystal structures and observing micro-sized samples, thanks to its very high resolution, which can be below 0.05 nm [12]. Since SOFC/SOEC operate at high temperatures and in reactive gas environments, the performance of related materials needs to be characterized under those conditions. The environmental TEM (ETEM) equipped the gas supply system can provide gas environments in the sample chamber, and special TEM holders and matched microelectromechanical systems (MEMS) chips can provide stimulus like heating and biasing. In

those conditions, the reactions can happen on the sample while doing the TEM characterization, enabling the in-situ ETEM characterization [13]. Meanwhile, electron energy loss spectroscopy (EELS), energy dispersive X-ray spectroscopy (EDS), scanning TEM (STEM), and SAED can reveal important information like the element distribution or migration or their valence state change [14].

Electrochemical impedance spectroscopy (EIS) is a powerful and widely used technique in electrochemistry with the advantage of allowing non-destructive operando characterization of an active system [15]. With those experimental conditions described above, it is feasible to perform electrochemical ETEM on SOC using *in situ* TEM and *in situ* EIS/biasing experiments. Through this method, researchers can directly observe real-time reactions occurring at the atomic scale under practical conditions. The evolution of chemical, structural, and morphological changes, as well as simultaneous electrochemical responses, can be recorded without damaging the sample [11].

1.2 Goal of project

The main objective of this project is to develop a characterization method for high temperature *in situ* electrochemical ETEM measurements where EIS/biasing and TEM are combined (EIS-TEM or biasing TEM). We try to simulate the practical working environment of a SOC by using special TEM sample holder and matched MEMS chip to provide high-temperature and electrical signals, and run the electrochemical experiment in gas atmosphere inside the ETEM. This method combines EIS and biasing measurements, and techniques related to ETEM/TEM to acquire electrochemical response and structural and elemental information such as new phase formation, element diffusion, and valence change of the target.

1.3 Thesis overview

In Chapter 2, we present the theory and methods related to this thesis. In Chapter 3, we review the literature on in situ heating/biasing experiments of SOC and related EIS interpretation. In Chapter 4, we discuss general considerations for the method of high-temperature solid-state electrochemical TEM experiments, including sample preparation, electrochemical measurement, failure factors, and recommended optimization methods for both pure materials and cell structures. In Chapter 5, we demonstrate the concept of combining EIS with environmental TEM (ETEM) by testing a specially designed micro-CGO sample. In Chapter 6, we demonstrate the feasibility of conducting high-temperature EIS-TEM or biasing-TEM experiments on model SOEC/SOFC cells.

Finally, in Chapter 7, we summarize the results and conclusions derived from the experiments and provide an outlook in Chapter 8 for future method development and experimental design.

References

1 Addo, P. K., Molero-Sanchez, B., Chen, M., Paulson, S. & Birss, V. CO/CO2 Study of High Performance La0.3Sr0.7Fe0.7Cr0.3O3–δ Reversible SOFC Electrodes. *Fuel Cells* 15, 689-696, doi:https://doi.org/10.1002/fuce.201400196 (2015).

2 Gómez, S. Y. & Hotza, D. Current developments in reversible solid oxide fuel cells. *Renewable and Sustainable Energy Reviews* 61, 155-174, doi:https://doi.org/10.1016/j.rser.2016.03.005 (2016).

3 Schiller, G., Henne, R., Mohr, P. & Peinecke, V. High performance electrodes for an advanced intermittently operated 10-kW alkaline water electrolyzer. *International Journal of Hydrogen Energy* 23, 761-765, doi:https://doi.org/10.1016/S0360-3199(97)00122-5 (1998).

4 Whiston, M. M. *et al.* Meeting U.S. Solid Oxide Fuel Cell Targets. *Joule* 3, 2060-2065, doi:https://doi.org/10.1016/j.joule.2019.07.018 (2019).

5 Koo, B. *et al.* Sr Segregation in Perovskite Oxides: Why It Happens and How It Exists. *Joule* 2, 1476-1499, doi:https://doi.org/10.1016/j.joule.2018.07.016 (2018).

6 Rupp, G. M., Opitz, A. K., Nenning, A., Limbeck, A. & Fleig, J. Real-time impedance monitoring of oxygen reduction during surface modification of thin film cathodes. *Nature Materials* 16, 640-645, doi:10.1038/nmat4879 (2017).

7 Jiao, Z., Takagi, N., Shikazono, N. & Kasagi, N. Study on local morphological changes of nickel in solid oxide fuel cell anode using porous Ni pellet electrode. *Journal of Power Sources* 196, 1019-1029, doi:https://doi.org/10.1016/j.jpowsour.2010.08.047 (2011).

8 Yokokawa, H. *et al.* Achievements of NEDO Durability Projects on SOFC Stacks in the Light of Physicochemical Mechanisms. *Fuel Cells* 19, 311-339, doi:https://doi.org/10.1002/fuce.201800187 (2019).

9 Xiong, Y. *et al.* Sulfur Poisoning of SOFC Cathodes. *Journal of The Electrochemical Society* 156, B588, doi:10.1149/1.3090169 (2009).

10 Haga, K., Shiratori, Y., Ito, K. & Sasaki, K. Chlorine Poisoning of SOFC Ni-Cermet Anodes. *Journal of The Electrochemical Society* 155, B1233, doi:10.1149/1.2980521 (2008).

11 Hwang, S., Chen, X., Zhou, G. & Su, D. In Situ Transmission Electron Microscopy on Energy-Related Catalysis. *Advanced Energy Materials* 10, 1902105, doi:https://doi.org/10.1002/aenm.201902105 (2020).

12 Kisielowski, C. *et al.* Detection of Single Atoms and Buried Defects in Three Dimensions by Aberration-Corrected Electron Microscope with 0.5-Å Information Limit. *Microsc. microanal.* 14, 469-477, doi:10.1017/S1431927608080902 (2008).

13 Molina-Luna, L. *et al.* Enabling nanoscale flexoelectricity at extreme temperature by tuning cation diffusion. *Nature Communications* 9, 4445, doi:10.1038/s41467-018-06959-8 (2018).

14 Serra-Maia, R. *et al.* Nanoscale Chemical and Structural Analysis during In Situ Scanning/Transmission Electron Microscopy in Liquids. *ACS Nano* 15, 10228-10240, doi:10.1021/acsnano.1c02340 (2021).

15 Balazs, G. B. & Glass, R. S. ac impedance studies of rare earth oxide doped ceria. *Solid State Ionics* 76, 155-162, doi:https://doi.org/10.1016/0167-2738(94)00242-K (1995).

Chapter 2: Theory and Methods

This chapter is to provide readers basic theory and introduction to experimental methods utilized in this thesis. The goal of this project is to build an in-situ platform for high-temperature solid-state electrochemical experiments inside the TEM. Therefore, I will begin by introducing the principles and configuration of electron microscopy including the environmental TEM. Subsequently, I will introduce how to conduct TEM experiments in an in-situ manner. Moving on, I will provide an overview of the principles of EIS and explain the related data analysis. Additionally, I will offer readers a brief introduction to SOC. Finally, I will introduce the equipment utilized for model cell sample preparation, namely the PLD system for film growing and the FIB system for lift-out and sample structure fabrication.

2.1 Electron Microscopy

When a beam of high-energy electrons interacts with a material, it generates various signals. Above the sample, signals such as backscattered electrons, secondary electrons, cathodoluminescence, and characteristic x-rays are produced, while below the sample, transmitted and diffracted electrons can be detected (Figure 1) [1,2]. These signals provide valuable information about the sample's composition, structure, and properties and can be used to create images, maps, and spectra for further analysis [3].

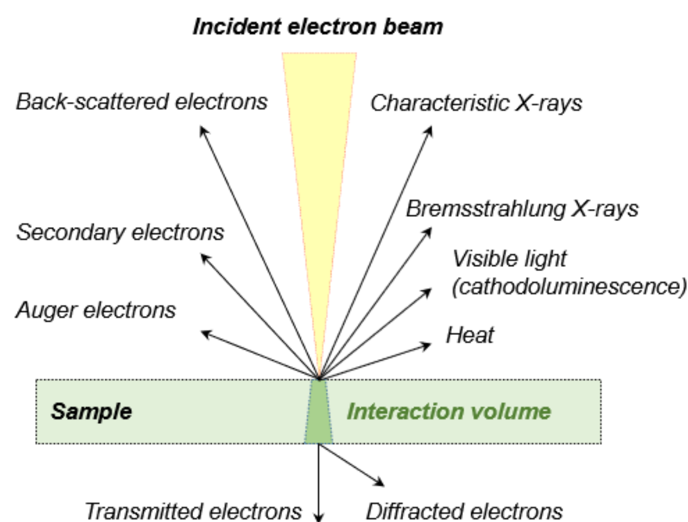

Figure 1: Signals generated by electron interaction with the sample.

Different signals carry different information about the target sample. For example, (scanning) transmission electron microscopy (TEM/STEM) collect transmitted electrons and diffracted electrons. Scanning electron microscopy (SEM), on the other hand, collects backscattered electrons, secondary electrons, and Auger electrons [4]. In contrast, Energy dispersive spectroscopy (EDS) collects characteristic x-rays and bremsstrahlung x-rays that are produced [5]. By those signals from electron microscopes, researchers can obtain valuable information about the sample's properties, enabling them to better understand the material and its behavior.

2.1.1 TEM

Transmission electron microscopy (TEM) visualize the structure of materials and biological specimens at high resolution, with its first version built by Ernst Ruska and Max Knoll [6].

According to Rayleigh's earlier work [7], in optical microscopy, the relation between the point resolution *r*, the light wavelength λ, and limit angle β of aperture can be described by the equation:

$$r = \frac{0.61\lambda}{sin\ \beta} \qquad (2.1)$$

Which means the smaller the wavelength of the wave is, the higher resolution the microscopy can reach. There are several common waves like electromagnetic waves such as visible light and x-ray, and electron wave. Visible light has wavelengths between 400 to 700 nm [8]. X-rays have shorter wavelengths, typically ranging from 0.01 to 10 nm [9]. While the electrons shortest wavelength. According to de Broglie's studies [10], the wavelength λ can be expressed by:

$$\lambda = \frac{h}{p} \qquad (2.2)$$

Where the *h* is Planck constant, *p* is momentum of the electron. The accelerating voltage can affect the speed and therefore the momentum of the electrons. For example, considering the relativistic effect, for a 300 kV electron gun, the wavelength is around 2 pm [11]. So, the electron microscope has the potential of making microscopy with much higher resolution compared with visible light and x-ray.

2.1.2 The configuration of TEM

The main parts of TEM include these: the electron gun, the condenser system, the sample, objective lens system, the projector system, and detectors [12]. Most of my TEM work is conducted by a FEI Titan ETEM. Figure 2 presents the configuration of the ETEM in DTU Nanolab.

2.1.2.1 Gun system

The gun in a TEM is the source of the electron beam that is focused and accelerated towards the sample. Common types of electron sources used in TEMs include tungsten filament, lanthanum hexaboride (LaB_6), and field emission guns (FEGs) [14]. Among them, FEGs are preferred due to their ability to generate a highly coherent and intense electron beam with a small size, enabling high-resolution imaging. The FEGS need a high vacuum environment during operation, so an extra IGP closed to the gun is added to keep the pressure around 1E-10 mbar [15].

2.1.2.2 Condenser systems

The condenser system is responsible for shaping and focusing the electron beam before it reaches the sample. It also includes apertures, which control the size and shape of the electron beam, and a set of deflector/alignment coils such as stigmators to move and correct for any beam displacement or distortion. The condenser system works as we adjust the intensity, spot size and beam shift on the user interface [16].

The system typically consists of two or more condenser lenses work together. In TEM mode, the C1 and C2 work together to make the electrons to illuminate the specimen with parallel beam. While in the STEM mode, all condenser lenses are used, and upper-objective pole piece (C3) work together to focus the beam to the smallest possible spot onto the sample.

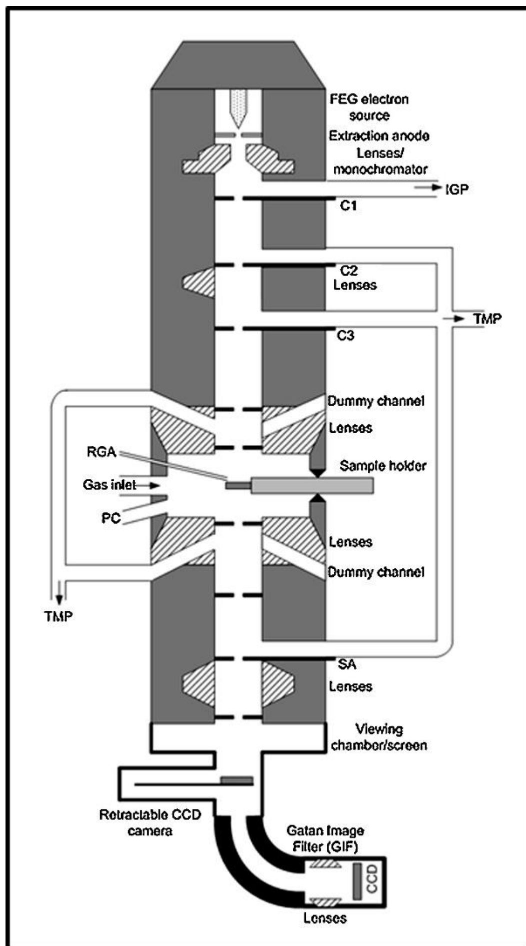

Figure 2: Schematic diagram of the ETEM and pump system in ETEM column, with key components such as FEG: field emission gun; IGP: ion getter pump; TMP: turbo molecular pump; RGA: residual gas analyzer; PC: plasma cleaner; C1 to C3: condenser apertures; SA: selected area aperture. [13] (the usage of this figure has got the permission from authors and the publisher, license shown in Appendix 3)

2.1.2.3 Sample

In order to allow the electrons to go through the TEM sample, it is necessary to make the sample electron transparent, normally below 100 nm. The sample is installed on the sample stage of the TEM holder. While the TEM holder is inserted, the sample stage and goniometer work together to allow for the positioning, rotation, and tilting of the sample during imaging and analysis. These functions enable the acquisition of images and diffraction patterns from different regions and angles of the sample and are compatible with various sample types and sizes [17].

2.1.2.4 objective lens, intermediate lens, and projector lens

The lens of TEM, which is the electromagnetic coil, can concentrates electrons by electromagnetic force due to negative charge of electrons. The majority of TEMs are equipped with twin-lens objective lens with one pole piece above and one below the sample. The one above the sample is to provide additional beam control, while the other is situated below the sample to amplify the image by approximately 50 times [18]. In TEM mode, the latter works, and is responsible for focusing the electron beam transmitted through the sample. In STEM mode the one above the sample works to focus the beam to smallest spot together with condenser lenses.

The intermediate lens is positioned between the objective lens and the projector lenses. The intermediate lens can switch to project either the back focal plane or the image plane of objective lens to form images or diffraction patterns of the sample to switch between imaging and diffraction with minimal distortion [19]. There are many projector lenses, and their purpose is simply to magnify. The image plane of intermediate lens is put on the object plane of the first projector lens to achieve larger magnification.

The selected area electron diffraction (SAED) aperture can be put in the image plane of objective lens, and can be used to select a small area of the specimen, from which the diffraction pattern of corresponding region can be obtained. The SAED aperture can be adjusted in size to control the size of the selected area. The objective aperture, on the other hand, is in the back focal plane of the objective lens. It is used to control the convergence angle of the electron beam. By adjusting the size of the objective aperture, the electrons with highest scatter angle can be removed, and this aperture can be used to control the contrast of bright-field images (BF-TEM) [20].

2.1.3 Difference between TEM mode and STEM mode

As Figure 3a shows, when we use TEM mode to characterize, a parallel electron beam is controlled to shine the sample. After interaction with the sample, the electrons scattered will be focused by objective lens, forming the diffraction pattern and images at back focal plane and image plane respectively. Both the transmitted electrons and the scattered electrons can be collected for imaging.

Unlike the TEM, as Figure 3b shows, a STEM illuminates a small region and scans across the sample by with a convergent smallest spot. Scan coils the is used for moving the beam by charging

in the coils, scanning the sample with the constant incidence angle [21]. After interactions with the sample, the electrons are scattered into different angles.

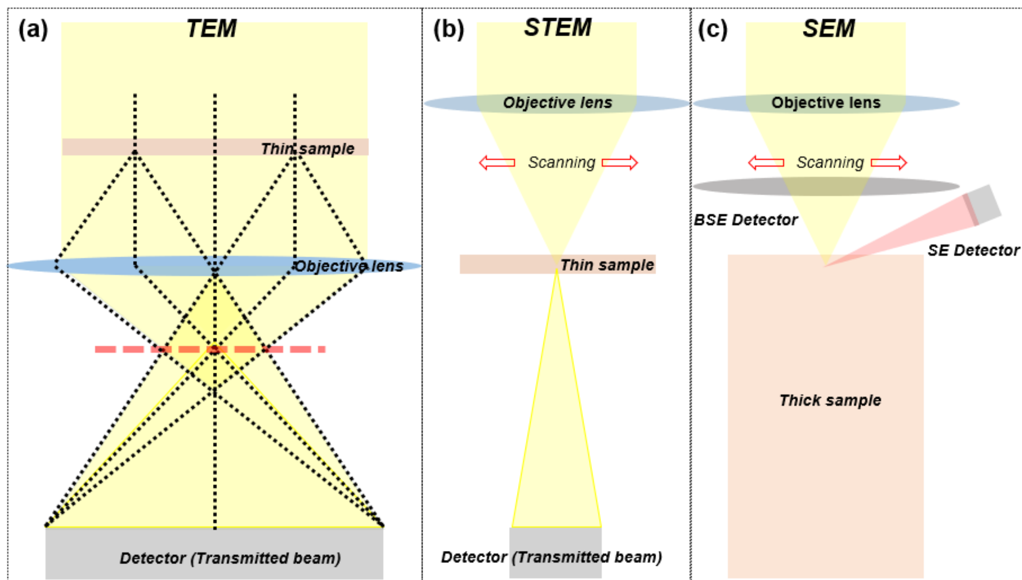

Figure 3: Electron path diagrams for different instruments of TEM, STEM and SEM respectively.

2.1.4 Detectors

For TEM mode electrons are usually projected on either a fluorescent screen or a CCD camera. The fluorescent screen is typically made of a thin layer of Zn-sulfide, which emits visible light when struck by electrons, on which the operator can do the microscope alignment and preliminary observations. In front of the CCD is a phosphor scintillator that converts the electron signal to visible light. The CCD camera has array detectors to record those light signals.

For STEM mode, if the scatter angle of electrons is over 50 mrad off axis, they can be collected by High Angle Annular Dark Field (HAADF) detector, while for the angles of 10 - 50 mrad and smaller than 10 mrad (unscattered), the Angular Dark Field (ADF) and Bright Field (BF) detectors can be applied respectively to collect those signals and image the sample respectively. The HAADF and ADF detector with a ring structure allows the electrons to go through the center, in this case the Electron energy loss spectroscopy (EELS) can be applied to collect those electrons unscattered and slightly scattered with small energy loss after interaction with the sample, which can be called STEM-EELS [22].

2.1.5 Contrast

2.1.5.1 Mass thickness contrast

Both TEM and STEM will use Mass-thickness contrast for imaging. Mass-thickness contrast in electron microscopy is a result of incoherent elastic scattering (Rutherford scattering) of electrons in the sample. This scattering is strongly correlated with the atomic number Z and the thickness t of the specimen [3].

In STEM mode it is possible to achieve high-resolution mass-thickness contrast, so-called Z contrast, by using the HAADF detector. The higher thickness and atomic number of materials result in a brighter contrast in HAADF images due to more electrons scattered at a large angle, and inelastic scattering can be negligible here (Z-contrast). For basic dark field imaging, annular dark field (ADF) detector can be used, and for basic bright field imaging, BF detector can be used, which gives an opposite contrast to HAADF images. HAADF detector can record images at the atomic level by Z-contrast, which is especially useful when combined with electron energy-loss spectroscopy (STEM-EELS) [23].

2.1.5.2 Diffraction contrast

For crystalline samples, some scattered electrons that are diffracted by a precise group of hkl planes in Bragg's condition. This results in intensity change in the images and is known as diffraction contrast. In the bright-field image, areas in Bragg's condition appear dark due to a loss of image intensity. Conversely, in the dark-field image, the corresponding areas appear bright due to an increase in image intensity.

There will be diffraction contrast in most TEM images. In mass-thickness contrast imaging, they can be effectively removed by using an objective aperture to block the diffracted electrons in the back focal plane [23].

2.1.5.3 Phase contrast

After the electron wave interaction with materials, both the phase and the amplitude of the electron beam is altered during the elastic scattering. Detectors are only able to directly measure the amplitude. However, the phase shift will also affect the imaging by wave interference patterns that can be measured via the intensity in the image plane. As a result, the HRTEM can record the phase changes from very small features down to the atomic scale [24].

The phase shift is known as the *Contrast Transfer Function (CTF)*, which can be described by the following equation:

$$K(q) = sin\,[2\pi(-\frac{\Delta f \lambda q^2}{2} + C_s \lambda^3 q^4/4)] \quad (2.5)$$

Where the Δf is defocus of the objective lens (using the convention that underfocus is positive and overfocus is negative), C_s is the spherical aberration of the objective lens [24], q is the spatial frequency (units of m^{-1}) and λ is electron wave. We can find the CTF is the function of C_s and Δf, and it can directly affect the electron wave in the back focal plane. If we apply FFT of the image of a thin amorphous layer, we will be able to find the effect of CTF by adjusting the focus.

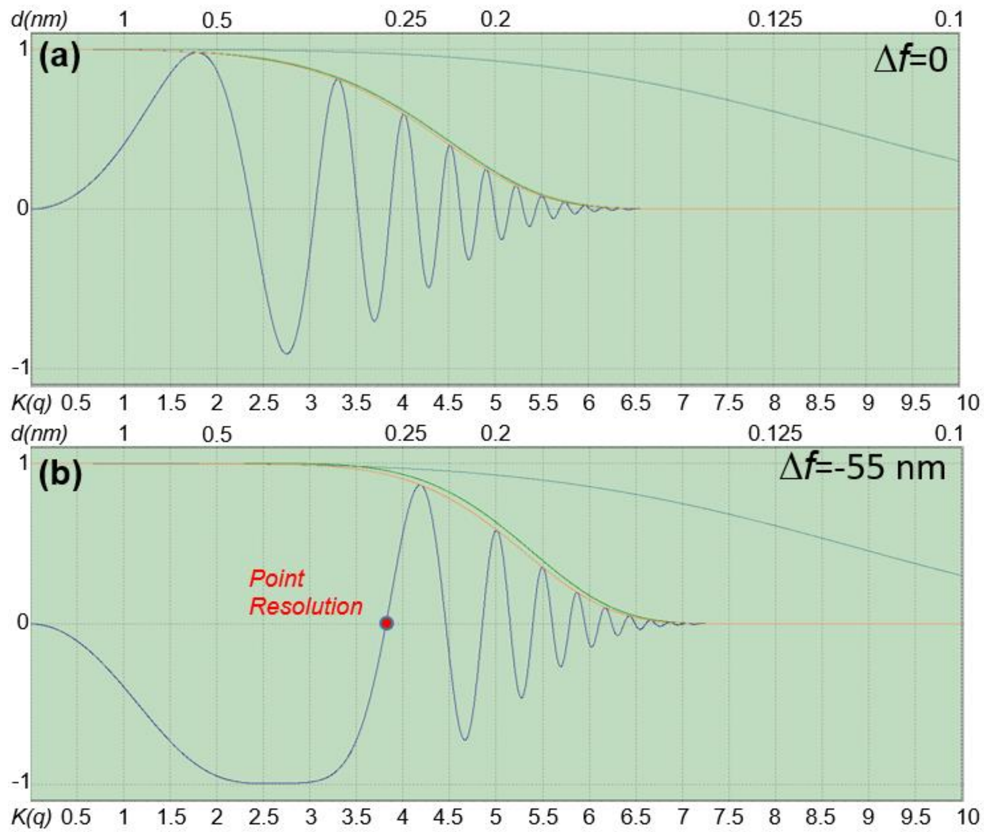

Figure 4: Examples of PCTF for an accelerating voltage of 200 kV and the coefficient C_s = 1.2 mm. (a) In-focus (Δf = 0 nm), (b) Scherzer focus ((Δf = -55 nm) The image is created by ctfExplorer [26].

Figure 4a, b compared the typical CTF diagrams for defocus = 0 and defocus = -55 nm respectively for the conditions of accelerating voltage of 200 kV and the coefficient C_s = 1.2 mm. The function values oscillate giving the maximum image contrast at CFTmax and no contrast when CFT = 0.

When the CTF is positive, the atoms present bright, while dark when it is negative. The first crossover with x-axis in the CTF is defined as point resolution of the crystal structure image, below this resolution, direct interpretation of high-resolution TEM images of weak phase objects is possible, meaning that in this region all atoms will appear dark on a bright background if it is underfocus, as Figure 4b shows. Our aim is to maximize the width and depth of the region between 0 and the point resolution [25]. Scherzer found this can be optimized by fine-tuning the defocus to achieve an optimal balance of the effect of spherical aberration and electron wavelength [24], and this defocus is called Scherzer defocus. The 1.2 times Scherzer defocus is seen as best defocus to take HRTEM. In the condition described above, Scherzer defocus is -55 nm after calculation.

2.1.5.4 Spatial resolution

Spatial resolution describes the ability to distinguish between closely spaced objects. In the context of transmission electron microscopy (TEM), spatial resolution refers to the minimum distance between two points on a sample that can be resolved in an image.

The resolution of TEM can be described by equation 2.1 [27]. However, the spatial resolution of TEM is affected by various factors, including aberrations, which are imperfections in the electron optical system that led to deviations from ideal imaging.

The two main types of aberrations in TEM are spherical aberration and chromatic aberration. Spherical aberration arises from the fact that electrons passing through a lens are refracted differently depending on their distance from the optical axis. This can result in a blurring of the image, which reduces the spatial resolution. Nevertheless, modern TEMs employ advanced aberration correctors that compensate for spherical aberration and improve spatial resolution. Thon ring can be seen as the rotation of CTF around y-axis. The aberration correctors are applied to make the thon ring more symmetrical to achieve better CTF condition [28].

Chromatic aberration, on the other hand, occurs because electrons of different energies have different wavelengths. As they pass through the lens system, they are refracted at different angles, causing blurring and a loss of contrast in the image. Chromatic aberration can be minimized by using monochromators to produce a beam of electrons with a narrow energy spread range of electrons [29].

2.1.6 In situ environmental TEM (ETEM)

2.1.6.1 Differential gas system

As Figure 2 shows, for this thesis, an ETEM (Titan 80–300 kV) equipped with a differential pumping system and an image aberration corrector (FEI Europe, Netherlands) from DTU Nanolab is applied [30]. This Titan ETEM is designed and equipped with a gas system, which can provide various kinds of gases such as O_2, H_2, H_2O, N_2 and CO with partial pressures from 10E-6 mbar to 26 mbar. One can control the needle valves and mass flow controllers to mix two or more kinds of these gases and fix the partial pressures for experiments. The gas system has high-pressure mode, ca 1-15 mbar and low-pressure mode, ca 10E-5 to 10E-2 mbar.

After shift to ETEM mode, the sample region is first pumped to 10E-3 mbar by using a turbo molecular pump (TMP1), then another TMP2 is added above/below the sample region to pump the pressure to 10E-6 mbar, finally an ion getter pump (IGP) closer to the monochromator region is pumped to 10E-9 mbar. The mass flow controllers are added to control the gas inlet.

In high-pressure mode, the needle is fully open, and the gas is directly controlled by the gas flow controller. The pressure is measured by a Barocel Rressure Transducer, BOC EDWARDS. One can directly use the mass flow controller to adjust the flows to inlet one or mixed gases.

In low-pressure mode, a constant pressure is maintained in the gas inlet system to form a higher-pressure reservoir, then the pressure in the sample region is adjusted using a needle valve between the gas inlet system and the sample region. The pressure is measured by a Wide Range Gauge, BOC EDWARDS.

The mix of different gases from different modes are also achievable if we mix the water vapor with other gases because there is an extra water inlet channel with a separate needle valve. In this thesis, by mixing H_2 and H_2O vapor, low oxygen partial pressures were successfully achieved, and the values can be derived by simple thermodynamics calculation. The experiments were mainly carried out in three different gas environments: (a) 3 mbar O_2, (b) a H_2/H_2O mixture with partial pressure ratio of 0.003 (total pressure 5 mbar) and (c) a H_2/H_2O with partial pressure ratio of 0.8 (total pressure 3 mbar).

The (a) 3 mbar O_2 and (c) H_2/H_2O with partial pressure ratio of 0.8 (total pressure 3 mbar) can be created by using high-pressure mode. For the first one, we adjust the gas flow controller to 2 ml $(min)^{-1}$, and then it will automatically give the pressure around 3 mbar. For the latter one, we first

inlet 2 ml $(min)^{-1}$ of H_2, and the pressure will reach around 1.2 mbar. Then we open the needle valve of the H_2O channel to make the total pressure reach 3 mbar, and thus the H_2/H_2O with partial pressure ratio of 0.8 can be reached. For (b) a H_2/H_2O mixture with partial pressure ratio of 0.003 (total pressure 5 mbar) the low-pressure mode is applied. Firstly, we build the H_2 high pressure reservoir of 60 mbar in the gas inlet system, and then we control the needle valve to make the pressure of H_2 reach 2E-2 mbar, and then we use the needle valve of the water channel to make the total pressure reach 5 mbar, and thus the pressure ratio of H_2 and H_2O can be 0.003 [31].

2.1.6.2 Dens lightning holder

For the *in situ* ETEM experiments, the DENS solutions Lightning holder is applied. The matched MEMS chip integrates heating and biasing functions together. The holder is a double tilt holder, by which we can do the β-tilt to make the sample lamella perpendicular to the electron beam. While we do the EDS measurement, we can also α-tilt to make the signal better collected by the EDS detector.

As Figure 5a,b shows, for the MEMS Lightning chip, the Mo microheater is encapsulated with silicon nitride (Si_3N_4) to prevent it from interacting with the sample and gas atmosphere, so the heater can work in the oxygen without the oxidation of Mo. While the Pt chip electrodes are deposited on top of the suspended SiNx without encapsule, which make sure the current collector of our cell can directly connect to the Pt electrodes. Figure 5b shows the position of heater spiral and Pt electrodes on the chip.

For the temperature control of 4 heating and 2 biasing chips, a closed-loop feedback system was created in order to enable the accurate temperature read-out while keeping it stable. As a result, the temperature to be delivered around the sample can be accurately controlled, as two contacts supply the current that heats up the microheater, while the other two contacts act as read-out the temperature delivered to the specimen. The temperature is determined by measuring the resistance of the Mo heater, which changes as a function of temperature [32]. For the biasing of the chip, the holder and the chip can supply up to 100 V inside the holder, which is large enough for the SOC test [32].

2.1.6.3 Instrument connection

In this work, there are two kinds of instrument connection styles applied. One is for the EIS-TEM measurements, and the other is for the heating-biasing experiments.

For EIS-TEM experiments, a split wire is used which splits the signals to heating and biasing. Here the biasing wire is connected to an external potentiostat (Gamry Femostat), which is controlled by an external computer with Gamry software to conduct the EIS measurement. The heating is connected following the pure heating experiment style from the Dens solution (which is detailed described in the manual).

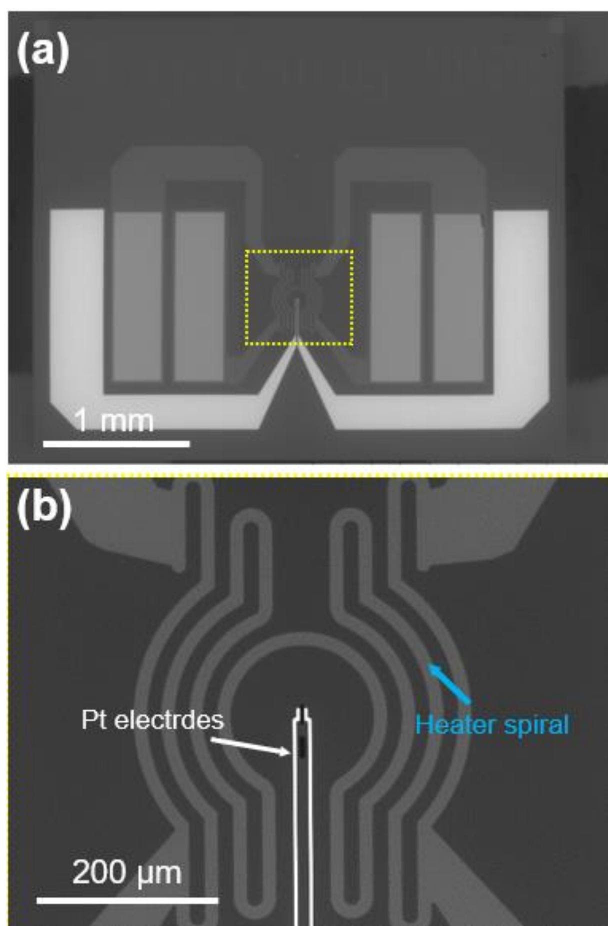

For heating-biasing experiment, we accept the heating-biasing connection style from the Dens solution with 4 heating electrodes and 2 biasing electrodes. Here, a Keithely box provided with the holder is used for the biasing signal. With this connection style, if we add positive bias in the Keitheley, the right Pt electrode on the chip is giving the negative voltage while the left is positive if the chip is put as Figure 5b shows with two Pt electrodes come from the “bottom”. This means if we make a symmetric cell structure as presented in chapter 4 and chapter 6, the upper layer in the image will be negative biased while the lower one is positive biased if we put positive number in the Keitheley box.

Figure 5: (a) The overview of Dens lightning MEMS chip, and (b) the zoom-in image of yellow rectangle region in (a)

2.1.7 SEM

SEM has similar basic principles to STEM. However, due to its application on the large thick sample, no electrons can penetrate through the entire sample and normally there is no detector underneath the sample. Meanwhile, the SEM has a large depth of field controlled by the aperture size and focus of the electrons, which allows a larger region in the specimen to be in focus at one time [33].

2.1.7.1 Working voltage

Compared with STEM, the working voltage of SEM is much lower. The typical accelerating voltage of SEM is between 0 and 30 kV. The electrons in the beam have lower energy, which means they penetrate only a few nanometers or micrometers into the sample before being scattered or absorbed by the atoms in the sample depending on the material and voltage [27]. This is ideal for imaging the surface topography and morphology of the sample, as the electrons are mostly reflected from the surface, providing high-resolution images [34].

2.1.7.2 Detectors

Different detectors such as secondary electron detector (collect SE2), in lens secondary electron detector (collect SE1), back scattered electron detector and in lens back-scattered electron detector can be installed in the SEM chamber and above the sample. In this work, the SEMs (Zeiss Ultra/Merlin) and Crossbeam (also has SEM function) from DTU energy were mainly applied, also for the SEM-EDS maps and spectrums [34].

2.1.7.3 Sample preparation

Samples for SEM must be conductive or coated with a conductive layer (e.g. C/gold) to prevent charging effects. In this thesis, all the pellets sample are first polished and coated with 8 nm gold before imaging to avoid charging [35].

2.1.8 Electron energy loss spectroscopy (EELS)

After interaction with the sample, some electrons are elastically scattered, and some electrons inelastically. Electron Energy Loss Spectroscopy (EELS) collect the information from the latter. By examining the energy distribution of all the electrons that were inelastically scattered, valuable insights can be gained about the local environment of the atomic electrons. This, in turn, can provide information about the physical and chemical properties of the specimen [36,37].

2.1.8.1 EELS spectrometer

The EELS signal is commonly collected by using a Gatan magnetic prism spectrometer, which is positioned underneath the imaging chamber of a (S)TEM. Most energy-loss electrons can be collected because they are scattered in a small angle, and the collection angle is also very small. The spectrometer's magnetic field separates the electrons and focuses them into a dispersion plane, where their position corresponds to their energy loss (ΔE). This dispersion pattern can be detected using a Gatan's imaging filter (GIF) [38,39].

2.1.8.2 Zero Loss Peak (ZLP)

Figure 6 presents a schematic illustration of a typical EELS spectra. From the left to the right on the spectra, Zero Loss Peak (ZLP) at 0 eV is formed by the elastically scattered electrons, which is the most intense peak, reflecting the stability and energy spread of the electron gun, recognized by its full width at half maximum (FWHMs). During alignment, the spectrometer is adjusted to focus as well as possible to eliminate the broadening of ZLP.

2.1.8.3 Plasmon Peak

The next region is the plasmon peak. The Plasmon peak describes the charge oscillations of the "free electron gas" which are often delocalized. In some solids, particularly metals, the bonding electrons behave as a free electron gas. When an incident electron moves through this gas, plasmons are generated. The energy of plasmons increases with electron density, allowing EELS spectra in the low-loss range to be utilized for estimating the density of free electrons [40]. The density of valence electrons can change by the change of the temperature, and this change can be revealed by the shift of the plasmon peak in different temperatures [41].

ZLP and Plasmon peaks can be referred as the low loss region reflecting the solid-state properties, and the low loss region extends from 0 to around 50 eV. The low loss region contributes the main background of core loss edges [27,42].

The data of the low loss region can also be used to calculate the thickness of the specimen, for example, by the EELS log-ratio method, as the following equation shows:

$$\mathrm{N} = \frac{t}{\lambda} = \ln\left(\frac{I_t}{I_0}\right) \tag{2.6}$$

where the t is specimen thickness in units of nm, λ the inelastic mean free path (nm), I_t is the total intensity of the entire spectrum, I_0 is the intensity of the zero loss peak, and N is mean number of inelastic scattering events per incident electron. λ is affected by average atomic number Z, Primary energy E_0 (keV), collection angle β (mrad), relativistic factor F according to the following equations [43,44]:

$$\lambda = \frac{106F(E_0/E_m)}{\ln(2\beta E_0/E_m)} \tag{2.7}$$

$$E_m = 7.6Z^{0.36} \tag{2.8}$$

$$\mathrm{F} = \frac{1+E_0/1022}{(1+E_0/511)^2}, \tag{2.9}$$

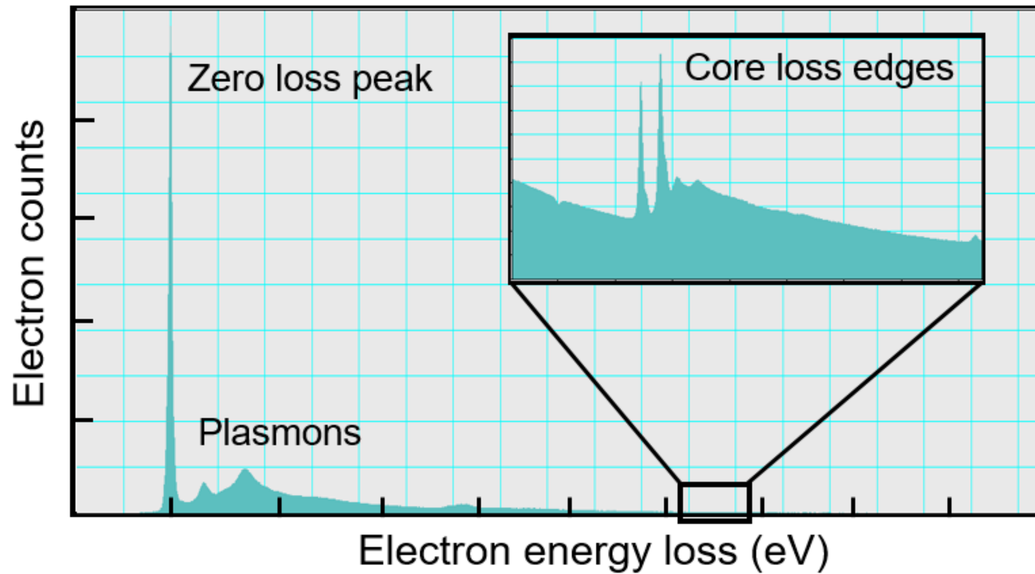

Figure 6: A typical EELS spectra

2.1.8.4 Core Loss Edges

For the core loss region, the energy loss range is normally from 50 eV to thousands of eV, and the main features are core loss edges which provide the elemental information. The core loss region reflects the atomic characters of the sample. When a beam of electrons with energy E_0 hit the shell electrons, they will lose the energy ΔE and deflected at a small angle, by which the shell electrons are excited, and jump from starting shell to final one by using some energy E_B, and gained momentum E_{kin}, in this case $\Delta E = E_B + E_{kin}$. [27], and this information can be read from the core loss edges.

The near edge fine structure (ELNES) is within the first 30-40 eV above the edge threshold, which provides information about band structure (density of unoccupied states), and extended fine structure (EXELFS) reflects atom-specific radial distribution of the surrounding atoms and the ejected electron during ionization. Their shapes strongly depend on the electronic functions in the electron transitions. For example, the inelastic collisions between incident electrons and K-shell electrons of free atoms generate sharp, saw-tooth like edges [45].

2.1.9 Energy dispersive spectroscopy (EDS)

Two kinds of x-rays can be generated during the electron interacting with core shell electrons and atom nucleus, which are characteristic x-rays and Bremsstrahlung. Bremsstrahlung and Characteristic radiation differ in that Bremsstrahlung X-rays generate a continuous X-ray spectrum,

while characteristic X-rays are produced at distinct narrow energy bands. EDS mainly analyze the characteristic x-rays, which is generated by relaxation of excited atoms [33].

Bremsstrahlung X-ray is a type of electromagnetic radiation that results from the deceleration of the electrons as it gets deflected by an atomic nucleus. The loss of the energy from the electrons will generate X-ray, as it usually has a continuous spectrum., and the higher the energy the electron has, the bremsstrahlung become more intense [46].

While the characteristic x-ray is generated when the material is bombarded with electrons, causing the electron to be ejected from the inner shell, leaving behind a vacant energy level known as a core hole. The outer shell electrons then fall into the inner shell, resulting in the emission of quantized photons with energy levels equivalent to the difference between the higher and lower energy levels. Each element has a unique set of energy levels, so the emission of X-rays produces frequencies characteristic of that element [47]. By collecting and analyzing those signals, the element can be identified by the location of the peaks in the spectrum, and the concentration of the element is indicated by the strength of the signal.

2.1.9.1 Artifacts

For the detection of X-rays. Firstly, the signals from the SEM/TEM holder and chamber may contribute to the spectra, and the possible contaminations such as carbon elements need to be excluded. Secondly, the detector of X-rays is usually made of Si, and Si detector can generate a voltage pulse as a function of energy of X-rays. After signal amplification, the energy value can be displayed as Gaussian peak where the intensity can represent the counts of X-rays with specific energy. However, after the X-rays interaction with Si, some of the X-rays lose 1.74 keV because Si Kα is around 1.74 keV. This makes extra peaks that are shifted 1.74 keV lower than the expected positions, called escape peaks. Meanwhile, the internal fluorescence peak at 1.74 keV in the EDS spectra can also generate during the interaction between X-rays and Si. Thirdly, if two X-rays enter the detector simultaneously, it will cause summed energies of the peaks, which is possible for any combination of two peaks from different elements, but mainly happen for the major elements [48].

2.1.9.2 Data analysis of EDS spectra

One can analyze the EDS spectra by following steps: 1) Find the most intense peak and start to find the peak from higher energies; 2) If the high intensity peak like Kα (or Lα and Mα) matches with reference, then check if other lines are at expected positions for the same elements and with

the expected relative intensities. 3) Check if the peaks overlap with the peaks from other possible elements. 4) Check the non-identified peaks and the minor peaks, and exclude the effects of artifacts.

2.2 The solid oxide cell (SOC)

Electrochemical cells transform the energy released from chemical reactions into electrical energy note as galvanic cell, and conversely, electrical energy can be utilized to drive electrochemical reaction note as electrolytic cell. Among the diverse array of electrochemical cells, one can find batteries, fuel cells, and electrolytic cells etc. An electrochemical cell consists of two half-cells whereby, each half-cell consists of an electrode interacting with either gas environments or solutions. A full cell is formed by connecting two half-cells both ionically and electrically. In one of the half-cells, electrons are discharged through an oxidation process. These electrons then travel through the external circuit and reach another half-cell, where suitable reduction reactions occur [49].

A typical electrochemical cell includes several parts such as electrodes and electrolyte. The anode is where oxidation reaction takes place, while the cathode is where the reduction reaction takes place. The electrolyte between the electrodes allows the ion conduction. There is a major difference between galvanic cells and electrolytical cells. For example, the reactions that happen in galvanic cells are usually spontaneous, while it is non-spontaneous in electrolytic cells [50].

If we use the concept of the galvanic cell and electrolytic cell to the solid oxide cells which can convert the energy between gas fuels and electricity, then they are solid oxide fuel cell (SOFC) or called solid oxide electrolytic cell (SOEC) respectively. For the electrolyte, it is usually made dense and used for ionic conduction and electrical insulation. For the electrodes, they are made porous to allow the gas flow, and it normally contain the electronic conductor, ionic conductor because the reaction happen at gas-electronic conductor-ionic conductor triple phase boundaries (TPBs) in the electrode regions close to the electrolyte which we note electrode-electrolyte interface [51].

2.2.1 Working principles of SOEC and SOFC

The principles of SOEC and SOFC are illustrated respectively by Figure 7 [52], here we use the reaction among H_2, O_2, H_2O as an example. In H_2, O_2, H_2O atmospheres, and the overall reaction that takes place can be described as:

$$H_2O(g) \rightleftharpoons H_2(g) + 1/2O_2(g), \quad (2.10)$$

In SOFC mode, as Figure 7a shows, the H_2 molecules are oxidized at the fuel electrode (anode) side, and lose electrons, while O_2 molecules are reduced at the oxygen electrode (cathode) side and get electrons. The oxygen ion from reduction diffuses through the dense electrolyte and react with H_2, and then form H_2O at the fuel electrode side. In this process, the electrons go through the outer circuit and drive work. The reactions on both sides can be expressed as:

Oxygen electrode side : $O_2 + 2e^- \rightarrow O^{2-}$ (ORR)

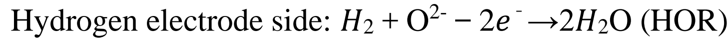

Hydrogen electrode side: $H_2 + O^{2-} - 2e^- \rightarrow 2H_2O$ (HOR)

In SOEC mode, as Figure 7b shows, by applying the potential/current, water vapor can be reduced into H_2 at the fuel electrode side, and the leftover O^{2-} diffuses through electrolyte, and is oxidized at the oxygen electrode side. The flow of electrons needs a driving force (potential) outside of the cell. The reactions on both sides can be expressed as:

Oxygen electrodes side: $O^{2-} \rightarrow O_2 + 2e^-$ (OER)

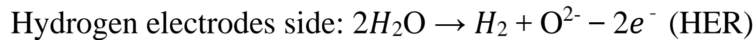

Hydrogen electrodes side: $2H_2O \rightarrow H_2 + O^{2-} - 2e^-$ (HER)

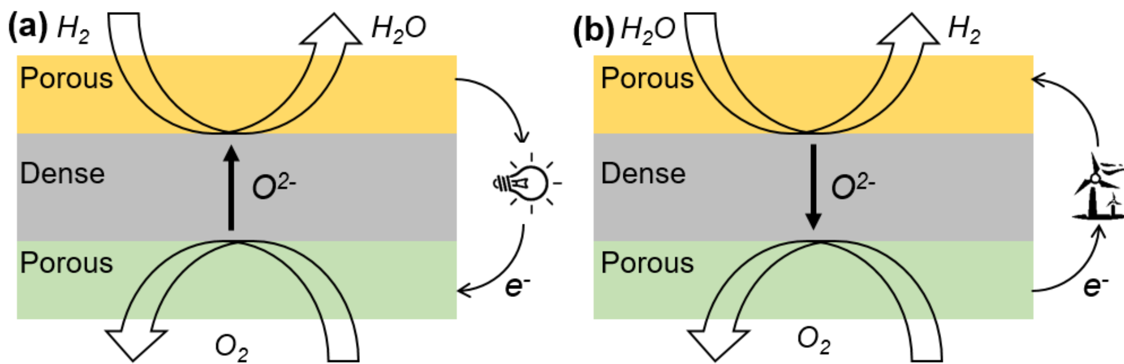

Figure 7: Schematic illustration of working principle of SOFC (a) and SOEC (b)

2.2.2 Thermodynamics of SOC

Thermodynamics is the study of energy transformation from one state to another, and it plays a vital role in comprehending the performance of SOFC/SOEC. By employing fundamental thermodynamic concepts, one can forecast the potential, temperature, pressure, volume, and moles of a cell system. Here are the Nernst equation and Gibbs free energy for the cells related to the thermodynamics which can be used to forecast the performance of the cell [53-55].

The relationship between Gibbs free energy of reaction (ΔG) of the cell reaction and ideal equilibrium electrical voltage (E_{mf}, electromotive force) can be described by the equation [56]:

$$-\Delta G = n \cdot F \cdot E_{mf}, \tag{2.11}$$

where n is the number of electrons transferred in the total reaction, and F is Faraday constant.

$$\Delta G = \Delta G_0 + RTlnK, \tag{2.12}$$

Where ΔG_0 is the Standard Gibbs free energy of the reaction dependent on the reaction species, and K is the constant in the law of mass action associated with the conditions of those reaction species. R represents the universal gas constant, and T denotes the temperature in Kelvin. Therefore, the Nernst equation in H_2, O_2, and H_2O atmospheres can be described as:

$$E_{mf} = E_0 + \frac{RT}{nF} ln \frac{P_{H_2O}}{P_{H_2}\sqrt{P_{O_2}}}, \tag{2.13}$$

where P_{H_2O}, P_{H_2}, and P_{O_2} are pressures of H_2O, H_2 and O_2 gases respectively. E_0 is the standard electrode potential, while E represents the cell potential at non-standard conditions.

For example, SOFC fed by H_2 and O_2, at standard conditions (25 °C and 1 atm pressure), the E is 1.23 V, with H_2 and O_2 access to the fuel and oxygen electrodes respectively [53].

2.3 Electrochemical impedance spectroscopy (EIS)

Electrochemical impedance spectroscopy (EIS) is a powerful method to study electrochemical systems [57,58]. EIS works by applying an oscillating voltage/current (usually ranging from 0.01 to 1,000,000 Hz) and collecting the response current/voltage. By fitting the data with an equivalent electric circuit model (ECM) of the electrochemical system, one can obtain the contributions of different processes in the reaction. As Figure 8 shows, in an EIS measurement, an AC potential or current is applied on the electrochemical system, and the response signal is collected.

EIS measurements are normally carried out by using a small excitation signal, which will be non-destructive to the system equilibrium. In a linear system, after interaction with electrochemical system, the frequency of the signal will not change while its phase may shift. During the fitting of EIS data, the interaction between electrochemical system and input signals can be exemplified by the electric elements exhibiting different block/through performances for the current with different

frequency domain. For example, in high frequency range, the capacitor (C) can be seen as connective, while in low frequency range, it can be seen as cut off.

For EIS test on the electrochemical system, the excitation potential and output current can be expressed as:

$$E(t) = E_0 \sin(\omega t) \tag{2.14}$$

$$I(t) = I_0 \sin(\omega t + \varphi) \tag{2.15}$$

where E_0 and I_0 are the amplitudes of the potential and current respectively. φ is phase shift, ω is radial frequency, and

$$\omega = 2\pi f \tag{2.16}$$

where f is the frequency, and t is the time.

So, the impedance can be described by Ohm's law, and the impedance Z can be expressed by:

$$Z(\omega) = \frac{E(t)}{I(t)} = \frac{E_0 \sin(\omega t)}{I_0 \sin(\omega t + \varphi)} \tag{2.17}$$

In the complex plane,

$$Z(\omega) = |Z| \cos\varphi + |Z| \sin\varphi = Z_{Re} + jZ_{Im} \tag{2.18}$$

Where j is the imaginary unit, and Z_{Re} and Z_{Im} are the real part and imaginary part of the impedance respectively. Therefore, the measured EIS data can be presented in a so-called Nyquist Plot by plotting them as the X- and Y-axis, respectively.

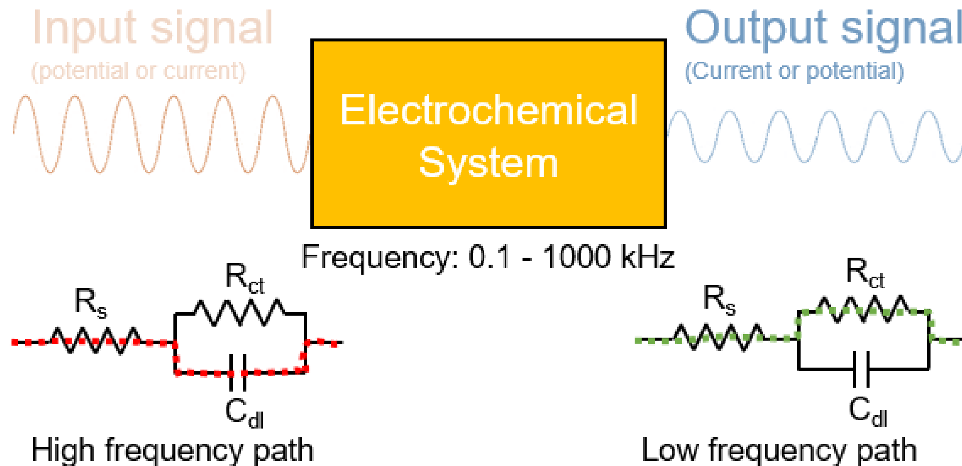

Figure 8: Schematic illustration of EIS principles and the current flow of elements in different frequency domain [59]

Figure 9 presents a typical EIS Nyquist plot of an SOC in the complex plane. Interpreting EIS data requires a proper electrical circuit model composed of various elements, such as resistor (R), capacitor (C), inductor (L) and CPE element. Assigning physical or chemical processes to different electrical elements can be achieved through experience or the creation of mathematical modeling.

For example, in a SOC system, there is the transport resistance representing the resistance of ionic conduction during operation, which is noted by *Rs* element. The electrochemical reactions take place in the electrodes during operation such as surface exchange reactions between active regions and gas environments, the gas diffusion, or the gas conversion can be described by several R-CPE elements denoted as ($R\text{-}CPE_1$), ($R\text{-}CPE_2$) and ($R\text{-}CPE_3$), and those are in series with *Rs*. An electrical circuit model (ECM) of these processes is presented in Figure 9 [60].

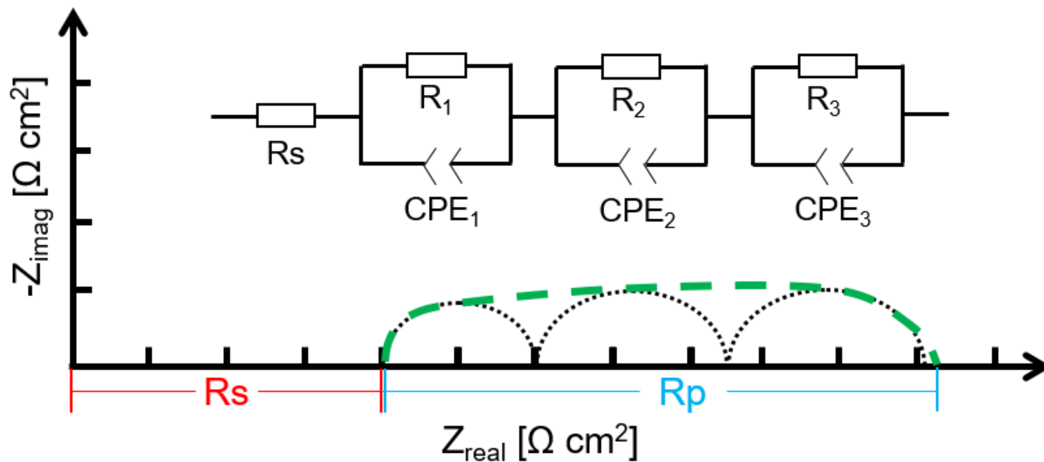

Figure 9: A simplified typical EIS spectra for the test on the SOC

2.4 Focused ion-beam scanning electron microscopy (FIB-SEM)

A FIB-SEM system combines a focused ion beam (FIB) with an SEM, which is a very powerful tool in the TEM sample preparation. This instrument works at high vacuum around 10E-6 mbar as in the SEM [61]. In addition to the normal function of SEM, the ion sources are added for the milling, deposition, and imaging. Through a micro-manipulator, lift-out and mounting of micro a sample is also achievable [62]. The ion source can be ionized Gallium accelerated by electric field and focused by the electric lens. For the Plasma FIB (such as Helios Hydra DualBeam), the ion source can be expanded to Xe, N, O and Ar. The high maximum current of plasma makes it possible for

high throughput milling process for large volume characterization and avoid the possible Ga injection contamination [63,64].

For the ion beam imaging, the accelerated ions will hit the target materials and sputter out the atoms. At the same time, the inelastic scattering will release the phonons and secondary electrons, and the electron signals can be captured by the detectors for imaging [65].

For the metal deposition, the gas injection system (GIS) can normally provide different precursors of deposition materials such as Pt, W and C. The high energy ion beam can break the bonds of molecules absorbed on the target surface, leave the deposition materials, and release the rest part of hydrocarbon (I-beam deposition). The electrons can also be used for the deposition, called E-beam deposition. However, the electrons are not effective for breaking the bonds, leaving more carbon in the deposited sample [66].

For the sample manipulation, a micromanipulator is normally equipped in the chamber to manipulate the sample, which can be controlled to move in x/y/z direction in a precise step. This tool is vital in the lift-out and attachment processes of the TEM sample to the target position.

2.5 Pulsed laser deposition (PLD)

Pulsed laser deposition (PLD) is one of the physical vapor deposition techniques which is widely used in the thin film growth of ceramic and metal materials [67]. It uses high-energy laser pulses to vaporize the surface of a solid target inside a vacuum chamber and condenses the vapor on a substrate to form a thin film up to a few micrometers in thickness. As Figure 10 shows, a typical PLD instrument contains a chamber. Inside the PLD chamber, a target holder and a substrate holder are placed against each other. A heater and thermocouple are placed in the substrate holder and the pulsed laser beam [68].

For conventional PLD, during the deposition, the UV light with a wavelength of 248 or 193 nm are generated by krypton fluoride (KrF) or argon fluoride (ArF) excimer lasers respectively, go through the window on the chamber wall, and hit the target from a certain angle. This causes ablation and producing a plume containing the materials containing many species including atoms, molecules, electrons, ions, but those have stoichiometry similar to that of the target [69]. This is one of the main advantages of PLD. The plume species then either interact with the gas environment or/and deposit on the target to form the film. Because of the high energy of ablated particles, they

can promote surface diffusion with no damage of substrate, and thus crystalline or single crystal film can be grown [70].

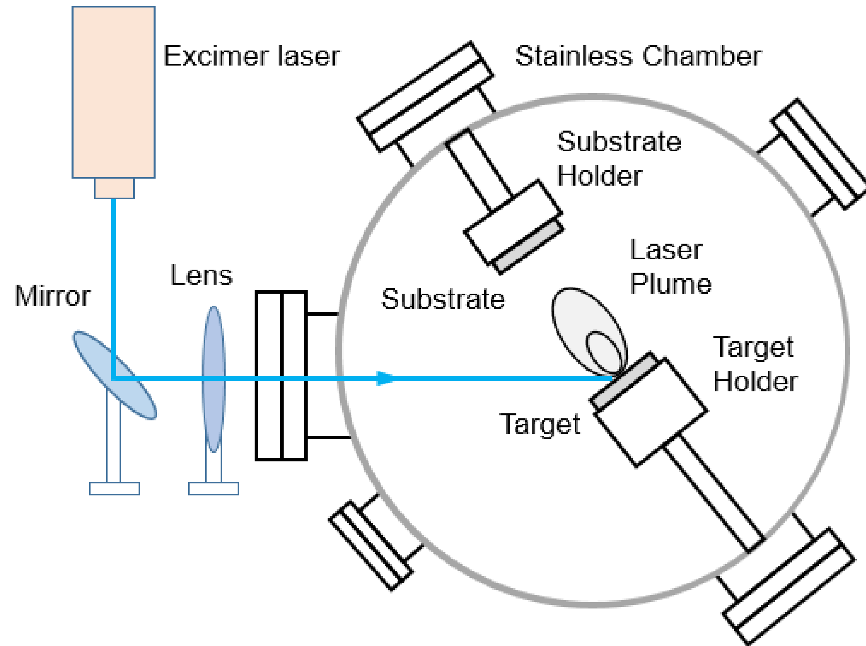

Figure 10: Schematic diagram of a pulsed laser deposition system

For the deposition, the nucleation and film growth depend on serval parameters, such as the laser energy with is strongly related with the deposition flux and the nucleation density of the film. The surface temperature of the substrate which can be controlled by the heater and measured by the thermocouple, the roughness of the substrate, and the background gas conditions. It is possible to control microstructures of the film in a wide range, from the sample produced can be amorphous, dense porous, by properly selecting laser operating conditions [71,72]. In this thesis, the oxygen atmosphere is applied in the chamber, and the substrates are heated at high temperature to grow the dense CGO, LSC and YSZ, the detailed information of experiments are presented in chapter 6.

References

1 Zhou, W., Apkarian, R., Wang, Z. L. & Joy, D. in *Scanning Microscopy for Nanotechnology: Techniques and Applications* (eds Weilie Zhou & Zhong Lin Wang) 1-40 (Springer New York, 2007).

2 Inkson, B. J. in *Materials Characterization Using Nondestructive Evaluation (NDE) Methods* (eds Gerhard Hübschen, Iris Altpeter, Ralf Tschuncky, & Hans-Georg Herrmann)

17-43 (Woodhead Publishing, 2016).

3 Williams, D. B. & Carter, C. B. in *Transmission Electron Microscopy: A Textbook for Materials Science* (eds David B. Williams & C. Barry Carter) 3-17 (Springer US, 1996).

4 Akhtar, K., Khan, S. A., Khan, S. B. & Asiri, A. M. in *Handbook of Materials Characterization* (ed Surender Kumar Sharma) 113-145 (Springer International Publishing, 2018).

5 Ngo, P. D. in *Failure Analysis of Integrated Circuits: Tools and Techniques* (ed Lawrence C. Wagner) 205-215 (Springer US, 1999).

6 Ruska, E. The development of the electron microscope and of electron microscopy. *Reviews of Modern Physics* 59, 627-638, doi:10.1103/RevModPhys.59.627 (1987).

7 Rayleigh. XXXI. Investigations in optics, with special reference to the spectroscope. *The London, Edinburgh, and Dublin Philosophical Magazine and Journal of Science* 8, 261-274, doi:10.1080/14786447908639684 (1879).

8 Mahmoud, B. H. *et al.* Impact of Long-Wavelength UVA and Visible Light on Melanocompetent Skin. *Journal of Investigative Dermatology* 130, 2092-2097, doi:https://doi.org/10.1038/jid.2010.95 (2010).

9 Thompson, A. C. & Vaughan, D. *X-ray data booklet*. Vol. 8 (Lawrence Berkeley National Laboratory, University of California Berkeley, CA, 2001).

10 de Broglie, L. *Recherches sur la théorie des Quanta*, Migration - université en cours d'affectation, (1924).

11 Stefan, R. *de Broglie wavelength of fast electrons*, <https://virtuelle-experimente.de/en/elektronenbeugung/wellenlaenge/de-broglie-relativistisch.php> (

12 Kuwahara, M. *et al.* Development of spin-polarized transmission electron microscope. *Journal of Physics: Conference Series* 298, 012016, doi:10.1088/1742-6596/298/1/012016 (2011).

13 Wagner, J. B., Cavalca, F., Damsgaard, C. D., Duchstein, L. D. L. & Hansen, T. W. Exploring the environmental transmission electron microscope. *Micron* 43, 1169-1175, doi:https://doi.org/10.1016/j.micron.2012.02.008 (2012).

14 Williams, D. B. & Carter, C. B. in *Transmission Electron Microscopy: A Textbook for Materials Science* (eds David B. Williams & C. Barry Carter) 73-89 (Springer US, 2009).

15 van der Mast, K. D. Field emission, developments and possibilities. *J. Microsc.*. 130, 309-324, doi:https://doi.org/10.1111/j.1365-2818.1983.tb04551.x (1983).

16 Mastronarde, D. N. Automated electron microscope tomography using robust prediction of specimen movements. *Journal of Structural Biology* 152, 36-51, doi:https://doi.org/10.1016/j.jsb.2005.07.007 (2005).

17 Mayer, J., Giannuzzi, L. A., Kamino, T. & Michael, J. TEM Sample Preparation and FIB-Induced Damage. *MRS Bull.* 32, 400-407, doi:10.1557/mrs2007.63 (2007).

18 Franken, L. E., Grünewald, K., Boekema, E. J. & Stuart, M. C. A. A Technical Introduction to Transmission Electron Microscopy for Soft-Matter: Imaging, Possibilities, Choices, and Technical Developments. *Small* 16, 1906198, doi:https://doi.org/10.1002/smll.201906198 (2020).

19 Williams, D. B. & Carter, C. B. in *Transmission Electron Microscopy: A Textbook for Materials Science* (eds David B. Williams & C. Barry Carter) 141-171 (Springer US, 2009).

20 van Huis, M. A. & Friedrich, H. in *Nanoparticles: Workhorses of Nanoscience* (ed Celso de Mello Donegá) 191-221 (Springer Berlin Heidelberg, 2014).

21 Bustillo, K. C. *et al.* 4D-STEM of Beam-Sensitive Materials. *Accounts of Chemical Research* 54, 2543-2551, doi:10.1021/acs.accounts.1c00073 (2021).

22 Williams, D. B. & Carter, C. B. in *Transmission Electron Microscopy: A Textbook for Materials Science* (eds David B. Williams & C. Barry Carter) 115-126 (Springer US, 2009).

23 Williams, D. B. & Carter, C. B. in *Transmission Electron Microscopy: A Textbook for Materials Science* (eds David B. Williams & C. Barry Carter) 371-388 (Springer US, 2009).

24 Williams, D. B. & Carter, C. B. in *Transmission Electron Microscopy: A Textbook for Materials Science* (eds David B. Williams & C. Barry Carter) 389-405 (Springer US, 2009).

25 Williams, D. B. & Carter, C. B. in *Transmission Electron Microscopy: A Textbook for Materials Science* (eds David B. Williams & C. Barry Carter) 483-509 (Springer US, 2009).

26 Sidorov, M. V. *Home of ctfExplorer*, <http://www.maxsidorov.com/ctfexplorer/index.htm> (2002).

27 Liao, Y. in *An Online Book* (An Online Book, Northwestern University, 2006).

28 Tanaka, N. Present status and future prospects of spherical aberration corrected TEM/STEM for study of nanomaterials∗. *Science and Technology of Advanced Materials* 9, 014111, doi:10.1088/1468-6996/9/1/014111 (2008).

29 Linck, M. *et al.* Chromatic Aberration Correction for Atomic Resolution TEM Imaging from 20 to 80 kV. *Physical Review Letters* 117, 076101, doi:10.1103/PhysRevLett.117.076101 (2016).

30 Hansen, T. W., Wagner, J. B., Jinschek, J. R. & Dunin-Borkowski, R. E. The Titan Environmental Transmission Electron Microscope: Specifications, Considerations and

First Results. *Microsc. microanal.* 15, 714-715, doi:10.1017/S1431927609097396 (2009).

31 Ma, Z. *et al.* Electrochemical Impedance Spectroscopy Integrated with Environmental Transmission Electron Microscopy. *Small Methods* n/a, 2201713, doi:https://doi.org/10.1002/smtd.202201713 (2023).

32 Garza, H. H. P. *et al.* in *2017 19th International Conference on Solid-State Sensors, Actuators and Microsystems (TRANSDUCERS).* 2155-2158.

33 Goodhew, P. J., John, H. & John, H. *Electron Microscopy and Analysis (3rd ed.)*. (CRC Press, 2000).

34 Goldstein, J. I. *et al.* in *Scanning Electron Microscopy and X-Ray Microanalysis* (eds Joseph I. Goldstein *et al.*) 65-91 (Springer New York, 2018).

35 Echlin, P. in *Handbook of Sample Preparation for Scanning Electron Microscopy and X-Ray Microanalysis* (ed Patrick Echlin) 247-298 (Springer US, 2009).

36 Hofer, F., Schmidt, F. P., Grogger, W. & Kothleitner, G. Fundamentals of electron energy-loss spectroscopy. *IOP Conference Series: Materials Science and Engineering* 109, 012007, doi:10.1088/1757-899X/109/1/012007 (2016).

37 Egerton, R. F. *Electron energy-loss spectroscopy in the electron microscope*. (Springer Science & Business Media, 2011).

38 Helmut, K. & Ludwig, R. in *Transmission Electron Microscopy: Physics of Image Formation* 416-455 (Springer New York, 2008).

39 Essers, E. *et al.* Energy resolution of an Omega-type monochromator and imaging properties of the MANDOLINE filter. *Ultramicroscopy* 110, 971-980, doi:https://doi.org/10.1016/j.ultramic.2010.02.009 (2010).

40 Stephens, A. P. Quantitative microanalysis by electron energy-loss spectroscopy: Two corrections. *Ultramicroscopy* 5, 343-349, doi:https://doi.org/10.1016/0304-3991(80)90038-8 (1980).

41 Chmielewski, A., Ricolleau, C., Alloyeau, D., Wang, G. & Nelayah, J. Nanoscale temperature measurement during temperature controlled in situ TEM using Al plasmon nanothermometry. *Ultramicroscopy* 209, 112881, doi:https://doi.org/10.1016/j.ultramic.2019.112881 (2020).

42 Williams, D. B. & Carter, C. B. in *Transmission Electron Microscopy: A Textbook for Materials Science* (eds David B. Williams & C. Barry Carter) 699-713 (Springer US, 2009).

43 Malis, T., Cheng, S. C. & Egerton, R. F. EELS log-ratio technique for specimen-thickness measurement in the TEM. *Journal of Electron Microscopy Technique* 8, 193-200, doi:https://doi.org/10.1002/jemt.1060080206 (1988).

44 Egerton, R. F. in *Electron Energy-Loss Spectroscopy in the Electron Microscope* (ed R. F. Egerton) 231-291 (Springer US, 2011).

45 Egerton, R. F. in *Electron Energy-Loss Spectroscopy in the Electron Microscope* (ed R. F. Egerton) 423-426 (Springer US, 2011).

46 L'Annunziata, M. F. in *Handbook of Radioactivity Analysis (Second Edition)* (ed Michael F. L'Annunziata) 1-121 (Academic Press, 2003).

47 Jenkins, R. & De Vries, J. L. in *Practical X-Ray Spectrometry* (eds R. Jenkins & J. L. De Vries) 1-25 (Macmillan Education UK, 1970).

48 Goldstein, J. I. *et al.* in *Scanning Electron Microscopy and X-Ray Microanalysis* (eds Joseph I. Goldstein *et al.*) 209-234 (Springer New York, 2018).

49 Mosher, M. & Kelter, P. in *An Introduction to Chemistry* (eds Michael Mosher & Paul Kelter) 853-902 (Springer International Publishing, 2023).

50 Ahmad, Z. in *Principles of Corrosion Engineering and Corrosion Control* (ed Zaki Ahmad) 9-56 (Butterworth-Heinemann, 2006).

51 Sammes, N. M. *et al.* in *Handbook of Climate Change Mitigation* (eds Wei-Yin Chen, John Seiner, Toshio Suzuki, & Maximilian Lackner) 1703-1727 (Springer US, 2012).

52 Jensen, S. H., Larsen, P. H. & Mogensen, M. Hydrogen and synthetic fuel production from renewable energy sources. *International Journal of Hydrogen Energy* 32, 3253-3257, doi:https://doi.org/10.1016/j.ijhydene.2007.04.042 (2007).

53 Mogensen, M. B. in *Seminar at Idaho National Laboratory* (Seminar at Idaho National Laboratory, Idaho National Laboratory, 2010).

54 Winkler, W. in *High Temperature Solid Oxide Fuel Cells - Fundamentals, design and Applications* (eds Subhash C. Singhal & Kevin Kendall) 53-82 (Elsevier, 2003).

55 Lindiwe, K. in *Thermodynamics and Energy Engineering* (ed Vizureanu Petrică) Ch. 1 (IntechOpen, 2019).

56 Winkler, W. & Nehter, P. in *Modeling Solid Oxide Fuel Cells: Methods, Procedures and Techniques* (eds Roberto Bove & Stefano Ubertini) 13-50 (Springer Netherlands, 2008).

57 Lasia, A. in *Modern Aspects of Electrochemistry* (eds B. E. Conway, J. O'M Bockris, & Ralph E. White) 143-248 (Springer US, 2002).

58 Instruments, G. Basics of electrochemical impedance spectroscopy. *G. Instruments, Complex impedance in Corrosion*, 1-30 (2007).

59 Alex, P. (ed Peroff Alex) (PINE Research, PINE Research, 2023).

60 Lang, M., Auer, C., Eismann, A., Szabo, P. & Wagner, N. Investigation of solid oxide fuel cell short stacks for mobile applications by electrochemical impedance spectroscopy.

Electrochimica Acta 53, 7509-7513, doi:https://doi.org/10.1016/j.electacta.2008.04.047 (2008).

61 Steve, R. & Robert, P. A review of focused ion beam applications in microsystem technology. *J. Micromech. Microeng.* 11, 287, doi:10.1088/0960-1317/11/4/301 (2001).

62 Rajput, N. S. & Luo, X. in *Micromanufacturing Engineering and Technology (Second Edition)* (ed Yi Qin) 61-80 (William Andrew Publishing, 2015).

63 Giannuzzi, L. & Smith, N. TEM Specimen Preparation with Plasma FIB Xe+ Ions. *Microsc. microanal.* 17, 646-647, doi:10.1017/S1431927611004107 (2011).

64 Eder, K. *et al.* A multi-ion plasma FIB study: Determining ion implantation depths of Xe, N, O and Ar in tungsten via atom probe tomography. *Ultramicroscopy* 228, 113334, doi:https://doi.org/10.1016/j.ultramic.2021.113334 (2021).

65 Li, P. *et al.* Recent advances in focused ion beam nanofabrication for nanostructures and devices: fundamentals and applications. *Nanoscale* 13, 1529-1565, doi:10.1039/D0NR07539F (2021).

66 Langford, R. M., Wang, T. X. & Ozkaya, D. Reducing the resistivity of electron and ion beam assisted deposited Pt. *Microelectron. Eng.* 84, 784-788, doi:https://doi.org/10.1016/j.mee.2007.01.055 (2007).

67 Fujioka, H. in *Handbook of Crystal Growth (Second Edition)* (ed Thomas F. Kuech) 365-397 (North-Holland, 2015).

68 Orita, M. *et al.* Pulsed laser deposition system for producing oxide thin films at high temperature. *Review of Scientific Instruments* 72, 3340-3343, doi:10.1063/1.1384449 (2001).

69 Lowndes, D. H., Geohegan, D. B., Puretzky, A. A., Norton, D. P. & Rouleau, C. M. Synthesis of Novel Thin-Film Materials by Pulsed Laser Deposition. *Science* 273, 898-903, doi:10.1126/science.273.5277.898 (1996).

70 Nur, O. & Willander, M. in *Low Temperature Chemical Nanofabrication* (eds Omer Nur & Magnus Willander) 49-86 (William Andrew Publishing, 2020).

71 Metev, S. & Meteva, K. Nucleation and growth of laser-plasma deposited thin films. *Applied Surface Science* 43, 402-408, doi:https://doi.org/10.1016/0169-4332(89)90247-X (1989).

72 Christen, H. M. & Eres, G. Recent advances in pulsed-laser deposition of complex oxides. *Journal of Physics: Condensed Matter* 20, 264005, doi:10.1088/0953-8984/20/26/264005 (2008).

Chapter 3: Literature review

In situ TEM is a powerful technique that allows for the analysis of structural and elemental properties by simulating experimental conditions through the application of various stimuli [1]. For gas-solid experiments in TEM, there are generally two routes to achieve a gas environment around the TEM sample, which were proposed as early as 30s [2-4]. In the first route, the gas is contained between two electron transparent windows. It was realized very early in 1960s [5]. After 2000s, people have been developing microelectromechanical systems (MEMS) chip-based TEM holders with windows to contain the gas [6]. The second route is to use environmental TEM (ETEM), which introduces gas directly into the TEM chamber. The differential pumping by turbo molecular pumps is applied to pump the gas leaked from sample region through special small apertures, and the pumping speed will be over the leakage speed [7-9].

The advantage of the ETEM is that it will not sacrifice the resolution of the TEM due to introduction of cell window membrane, and standard heating holders can be directly used. Nowadays, ETEMs can be equipped with a field emission gun (FEG) [10,11], and can also be equipped with an aberration corrector, monochromator, energy filter for electron energy-loss spectroscopy and energy dispersive X-ray spectrometer [12].

In this work, we use an ETEM, and we aim to combine in-situ TEM with the three different stimuli: heating, electrical polarization and a gas environment.

In this chapter, I will briefly review the development of the heating, biasing and combined heating-biasing experiments in the TEM with reactive gases and present the current status and challenges. This starts from the TEM heating experiments in reactive gases, then TEM electrochemical biasing experiment in gases, and in situ heating and biasing experiment. Finally, I will briefly review publications related to the interpretation of EIS results which helps to understand the electrochemical data we derived for our samples.

3.1 TEM heating experiments in reactive gasses

The type of heating TEM holders include holders with a furnace such as the heating holders from Gatan [13], or Hummingbird [14], and the MEMS chip-based heating holders such as DENS solution wildfire [15].

To the best of our knowledge, no scientific publications prior to the present work show the combination of heat, gas and electrical polarization on a solid oxide cell. There are, however, a few ETEM studies with focus on the solid oxide cell or its components.

Ni-YSZ is a common fuel electrode which provides the anodic catalytic activity of reducing the fuel gas in SOFC [16]. The Gatan Inconel heating holder can heat the sample furnace up to 1000 °C, by which Q. Jeangros and coworkers investigated the redox cycle of a commercially applied Ni-YSZ fuel electrode in a Titan ETEM. The microstructure evolution and reduction/oxidation mechanism are studied by heating the Ni-YSZ sample in oxygen and hydrogen atmospheres in the ETEM [17]. A NanoEX™-i/v sample holder with MEMS microheater can provide the precise and stable temperature of 1300°C [18]. Junko Matsuda and coworkers used heating function of this holder and conducted the experiments in a Titan ETEM to follow the redox cycling of Ni-ScSZ anode, studied the Ni oxidation, NiO reduction mechanisms, and volumetric and morphological change of Ni during the redox reactions [19].

CGO is commonly applied in SOC as the buffer layer between oxygen electrode and electrolyte and is also a material that the present work focussed on [20]. FEI Tecnai F20 field-emission ETEM with the differential pumping system can reach the high resolution of 0.13 nm in 4 mbar H_2 [21]. Peter A. Crozier and coworker applied a Gatan Inconel heating holder in this ETEM, studied the dynamic changes of cerium-based oxide nanoparticles during redox processes. Their work revealed the phase formation the reconstruction of specific crystal plane at 730 °C in hydrogen. In the same study, CGO nanoparticles with fluorite structures are found easier to be reduced compared with pyrochlore structures in hydrogen atmosphere [22]. Mingyun Zhu and coworkers used the Protochips fusion heating holder and MEMS E-chips to study the thermal stability of CeO_2 nanoflowers in vacuum and oxygen atmospheres by a Titan ETEM. The sintering and decomposition in oxygen, and the phase transition from CeO_2 to Ce_2O_3, and sublimating in a higher temperature in vacuum are revealed [23].

The aim of the present work is to develop a method for studying solid oxide model cells in operando, i.e. during cell operation. Such studies have not been presented before, but multilayer cell structures have previously been studied in the TEM with observations of the interfaces at high temperature. Takaaki Shimura and coworkers studied the interface diffusion phenomena of CGO-YSZ sintered at high temperature by in situ/ex situ TEM. Their study showed delamination

between YSZ and CGO during sintering if both YSZ can CGO are fixed rigidly on the chip [24]. Another example is Fabrizio Gaulandris et al. who also elucidated cation diffusion and Co oxidation states at the interfaces in a model SOFC in oxygen as a function of temperature [25,26].

The examples above show that solid oxide cells and their components can be studied in reactive gassed and elevated temperatures. What is missing in the examples above in order to study the materials and cells in operando, i.e. during relevant electrochemical conditions, thie addition of an applying an electrical polarization.

3.2 In situ biasing experiments in gases

To apply an electrical polarization, a so-called TEM biasing holder is needed, such as the "Nanofactory Instrument" AFM-TEM holder [27] or Hummingbird Scientific's in-situ electrical biasing holder. These holders have mainly been used for ion battery research, and mostly in vacuum, for the characterization of materials [28-34] and cell configurations [35-37], revealing reaction mechanisms such as intercalation, alloying, and conversion, and their corresponding structural evolutions [27,38,39]. However, these holders do not include a heater element and can therefore not be used for studying solid oxide cells in operando where elevated temperatures are needed.

Recently, combined heating-biasing holders were developed, and today these holders are commercially available. One of the first attempts to develop and apply a combined heating-biasing holder was in a study with focus on redox reactions and ionic conduction of a Pt-CGO-W cell in oxygen by Amir H Tavabi and coworkers through a Hitachi HF-2000 cold-FEG TEM with a homemade ETEM system and a special holder with electrodes and a Ta ribbon heater. The authors combined off-axis electron holography and EELS to follow the oxidation state in different atmospheres and different temperatures [40]. The published work from this group, however, only presented results from experiments that combined heat and gas, while the addition of an applied electrical potential to the cells was not presented.

Another attempt was made by Fabrizio Gualandris and coworkers of our group. They tried to achieve electrochemical operando TEM on a symmetric cell Pt-LSC-YSZ-LSC-STN cell fabricated from PLD. The combination of heating, gas, and biasing was presented at the IMC19 conference, but the electrochemical operando results were not published because the group suspected that the electrochemical measurements where influence by leak currents between the chip electrodes and heater membrane of the heating-biasing chip from Protochips.

3.2.1 Interpretation of EIS response signal

In this work, the interpretation of EIS signals is very important. Our FIB prepared sample are prepared from single material pellets or PLD prepared films. They can be made with well-defined sample geometry, composition, orientation, and crystallinity [41]. Since the interpretation of EIS signal from nano cells has not been reported before, here I briefly review some excellent works related to the EIS interpretation of PLD sample, which can be important reference.

Gun Tae Kim and coworkers prepared $La_2NiO_{4+\delta}$ films on both sides of a YSZ (100) single crystal, with gold meshes serving as current collectors, and tested in the oxygen atmosphere. The impedance spectra showed oxygen ion conduction of YSZ, interfacial resistance between the thin film and YSZ, and surface reaction properties of the thin-film electrode in different frequency domains. Because of the thin film geometry, the reaction rate is not limited by gas diffusion, and the surface reaction properties represented by the low frequency domains are not affected by a gas gradient. The surface exchange coefficient of the thin PLD film was consistent with that of a bulky ceramic sample [42]. This shows that EIS results from model cells prepared from PLD can be related to bulk samples.

William C. Chueh and coworkers deposited Sm doped ceria on both side of YSZ, and used Pt metal as current collectors, and tested in the reducing atmosphere. The chemical capacitance values after considering interfacial effects can be derived [43]. Christoph Riedl and coworkers deposited lanthanum strontium ferrite (LSF) films with or without Pt doping on a YSZ single crystal substrate. They found that the surface exchange reaction gave higher resistance compared to the transport resistance because of excellent transport performance of those films [44].

Generally speaking, the interpretation of EIS spectra of model cells needs to consider the contributions of charge species transport, such as ions and electrons (which are reflected in the high-frequency domain), the contribution of surface reactions (which is evident in the low-frequency domain), as well as other possibilities such as chemical capacitance, interfacial resistance/capacitance or gas diffusion processes. In addition, for the measurements, one may also need to consider the potential contributions that may arise from the counter electrodes, the test set-up, or other factors that could impact the EIS measurement.

References

1 Koh, A. L., Lee, S. C. & Sinclair, R. in *Controlled Atmosphere Transmission Electron Microscopy: Principles and Practice* (eds Thomas Willum Hansen & Jakob Birkedal Wagner) 3-43 (Springer International Publishing, 2016).

2 Marton, L. La microscopie electronique des objets biologiques. *Bull. Acad. Roy. Med. Belg* 21, 600-617 (1935).

3 Ruska, E. Beitrag zur übermikroskopischen Abbildung bei höheren Drucken. *Kolloid-Zeitschrift* 100, 212-219, doi:10.1007/BF01519549 (1942).

4 Abrams, I. M. & McBain, J. W. A Closed Cell for Electron Microscopy. *Journal of Applied Physics* 15, 607-609, doi:10.1063/1.1707475 (1944).

5 Heide, H. G. ELECTRON MICROSCOPIC OBSERVATION OF SPECIMENS UNDER CONTROLLED GAS PRESSURE. *Journal of Cell Biology* 13, 147-152, doi:10.1083/jcb.13.1.147 (1962).

6 Creemer, J. F. *et al.* Atomic-scale electron microscopy at ambient pressure. *Ultramicroscopy* 108, 993-998, doi:https://doi.org/10.1016/j.ultramic.2008.04.014 (2008).

7 Takahashi, N. *et al.* High Temperature Furnace for the Electron Microscope. *Journal of Electron Microscopy* 4, 16-23, doi:10.1093/oxfordjournals.jmicro.a051220 (1956).

8 Hashimoto, H., Tanaka, K. & Yoda, E. A Specimen Treating Device at High Temperature for the Electron Microscope. *Journal of Electron Microscopy* 6, 8-11, doi:10.1093/oxfordjournals.jmicro.a051258 (1958).

9 Gai, P. L. Environmental high resolution electron microscopy of gas-catalyst reactions. *Top. Catal.* 8, 97-113, doi:10.1023/A:1019192523483 (1999).

10 Hansen, P. L., Helveg, S. & Datye, A. K. in *Advances in Catalysis* Vol. 50 (eds Bruce C. Gates & Helmut Knzinger) 77-95 (Academic Press, 2006).

11 Hansen, T. W. *et al.* Atomic-Resolution in Situ Transmission Electron Microscopy of a Promoter of a Heterogeneous Catalyst. *Science* 294, 1508-1510, doi:10.1126/science.1064399 (2001).

12 Hansen, T. W., Wagner, J. B. & Dunin-Borkowski, R. E. Aberration corrected and monochromated environmental transmission electron microscopy: challenges and prospects for materials science. *Materials Science and Technology* 26, 1338-1344, doi:10.1179/026708310X12756557336355 (2010).

13 Xin, H. L. & Zheng, H. In Situ Observation of Oscillatory Growth of Bismuth Nanoparticles. *Nano Lett.* 12, 1470-1474, doi:10.1021/nl2041854 (2012).

14 Harutyunyan, A. R. *et al.* Preferential Growth of Single-Walled Carbon Nanotubes with

Metallic Conductivity. *Science* 326, 116-120, doi:10.1126/science.1177599 (2009).

15 Cui, W. *et al.* Direct observation of cation diffusion driven surface reconstruction at van der Waals gaps. *Nature Communications* 14, 554, doi:10.1038/s41467-023-35972-9 (2023).

16 Hauch, A., Brodersen, K., Chen, M. & Mogensen, M. B. Ni/YSZ electrodes structures optimized for increased electrolysis performance and durability. *Solid State Ionics* 293, 27-36, doi:https://doi.org/10.1016/j.ssi.2016.06.003 (2016).

17 Jeangros, Q. *et al.* In situ redox cycle of a nickel–YSZ fuel cell anode in an environmental transmission electron microscope. *Acta Mater.* 58, 4578-4589, doi:https://doi.org/10.1016/j.actamat.2010.04.019 (2010).

18 Mele, L. *et al.* A MEMS-based heating holder for the direct imaging of simultaneous in-situ heating and biasing experiments in scanning/transmission electron microscopes. *Microscopy Research and Technique* 79, 239-250, doi:https://doi.org/10.1002/jemt.22623 (2016).

19 Matsuda, J. *et al.* In situ transmission electron microscopic observations of redox cycling of a Ni–ScSZ cermet fuel cell anode. *Microscopy* 67, 251-258, doi:10.1093/jmicro/dfy025 (2018).

20 Constantin, G. *et al.* Efficiency of a dense thin CGO buffer layer for solid oxide fuel cell operating at intermediate temperature. *Solid State Ionics* 249-250, 98-104, doi:https://doi.org/10.1016/j.ssi.2013.07.004 (2013).

21 Sharma, R., Crozier, P. A., Marx, R. & Weiss, K. An Environmental Transmission Electron Microscope for In-Situ Observation of Chemical Processes at the Nanometer Level. *Microsc. microanal.* 9, 912-913, doi:10.1017/S1431927603444565 (2003).

22 Crozier, P. A., Wang, R. & Sharma, R. In situ environmental TEM studies of dynamic changes in cerium-based oxides nanoparticles during redox processes. *Ultramicroscopy* 108, 1432-1440, doi:https://doi.org/10.1016/j.ultramic.2008.05.015 (2008).

23 Zhu, M. *et al.* Combining in-situ TEM observations and theoretical calculation for revealing the thermal stability of CeO2 nanoflowers. *Nano Research* 15, 1319-1326, doi:10.1007/s12274-021-3659-6 (2022).

24 Shimura, T., Miyazaki, Y., Nakayama, Y., Takeguchi, M. & Shikazono, N. Characterization of inter-diffusion phase between gadolinium-doped ceria and yttria-stabilized zirconia during high-temperature sintering by in-situ and ex-situ transmission electron microscopy observations. *Solid State Ionics* 342, 115058, doi:https://doi.org/10.1016/j.ssi.2019.115058 (2019).

25 Gualandris, F. *et al.* In Situ TEM Analysis of a Symmetric Solid Oxide Cell in Oxygen and Vacuum – Cation Diffusion Observations. *ECS Transactions* 75, 123, doi:10.1149/07542.0123ecst (2017).

26 Gaulandris, F., Kuhn, L. T., Wagner, J. B., Sanna, S. & Simonsen, S. B. Co oxidation state at LSC-YSZ interface in model solid oxide electrochemical cell. *Solid State Ionics* 359, 115531, doi:https://doi.org/10.1016/j.ssi.2020.115531 (2021).

27 Ma, Z. *et al.* All roads lead to Rome: Sodiation of different-stacked SnS2. *Nano Energy* 67, 104276, doi:https://doi.org/10.1016/j.nanoen.2019.104276 (2020).

28 Huang, J. Y. *et al.* In Situ Observation of the Electrochemical Lithiation of a Single SnO2 Nanowire Electrode. *Science* 330, 1515-1520, doi:10.1126/science.1195628 (2010).

29 Li, N. & Su, D. In-situ structural characterizations of electrochemical intercalation of graphite compounds. *Carbon Energy* 1, 200-218, doi:https://doi.org/10.1002/cey2.21 (2019).

30 Niu, J. *et al.* In Situ Observation of Random Solid Solution Zone in LiFePO4 Electrode. *Nano Lett.* 14, 4005-4010, doi:10.1021/nl501415b (2014).

31 Wan, J. *et al.* In Situ Transmission Electron Microscopy Observation of Sodiation–Desodiation in a Long Cycle, High-Capacity Reduced Graphene Oxide Sodium-Ion Battery Anode. *Chem. Mat.* 28, 6528-6535, doi:10.1021/acs.chemmater.6b01959 (2016).

32 Asayesh-Ardakani, H. *et al.* In Situ TEM Investigation of ZnO Nanowires during Sodiation and Lithiation Cycling. *Small Methods* 1, 1700202, doi:https://doi.org/10.1002/smtd.201700202 (2017).

33 Wu, K. *et al.* In situ TEM and half cell investigation of sodium storage in hexagonal FeSe nanoparticles. *Chemical Communications* 55, 5611-5614, doi:10.1039/C9CC02107H (2019).

34 Li, Q. *et al.* Intermediate phases in sodium intercalation into MoS2 nanosheets and their implications for sodium-ion batteries. *Nano Energy* 38, 342-349, doi:https://doi.org/10.1016/j.nanoen.2017.05.055 (2017).

35 Wang, Z. *et al.* In Situ STEM-EELS Observation of Nanoscale Interfacial Phenomena in All-Solid-State Batteries. *Nano Lett.* 16, 3760-3767, doi:10.1021/acs.nanolett.6b01119 (2016).

36 Gong, Y. *et al.* In Situ Atomic-Scale Observation of Electrochemical Delithiation Induced Structure Evolution of LiCoO2 Cathode in a Working All-Solid-State Battery. *Journal of the American Chemical Society* 139, 4274-4277, doi:10.1021/jacs.6b13344 (2017).

37 Gong, Y. *et al.* Three-dimensional atomic-scale observation of structural evolution of cathode material in a working all-solid-state battery. *Nature Communications* 9, 3341, doi:10.1038/s41467-018-05833-x (2018).

38 Lu, X., Bogart, T. D., Gu, M., Wang, C. & Korgel, B. A. In Situ TEM Observations of Sn-Containing Silicon Nanowires Undergoing Reversible Pore Formation Due to Fast Lithiation/Delithiation Kinetics. *The Journal of Physical Chemistry C* 119, 21889-21895,

doi:10.1021/acs.jpcc.5b06386 (2015).

39 Xu, F. *et al.* In situ TEM probing of crystallization form-dependent sodiation behavior in ZnO nanowires for sodium-ion batteries. *Nano Energy* 30, 771-779, doi:https://doi.org/10.1016/j.nanoen.2016.09.020 (2016).

40 Tavabi, A. H., Arai, S., Muto, S., Tanji, T. & Dunin-Borkowski, R. E. In Situ Transmission Electron Microscopy of Ionic Conductivity and Reaction Mechanisms in Ultrathin Solid Oxide Fuel Cells. *Microsc. microanal.* 20, 1817-1825, doi:10.1017/S143192761401349X (2014).

41 Rupp, J. L. M., Scherrer, B., Schäuble, N. & Gauckler, L. J. Time–Temperature–Transformation (TTT) Diagrams for Crystallization of Metal Oxide Thin Films. *Advanced Functional Materials* 20, 2807-2814, doi:https://doi.org/10.1002/adfm.201000377 (2010).

42 Kim, G. T., Wang, S., Jacobson, A. J., Yuan, Z. & Chen, C. Impedance studies of dense polycrystalline thin films of La2NiO4+δ. *Journal of Materials Chemistry* 17, 1316-1320, doi:10.1039/B616101D (2007).

43 Chueh, W. C. & Haile, S. M. Electrochemical studies of capacitance in cerium oxide thin films and its relationship to anionic and electronic defect densities. *Physical Chemistry Chemical Physics* 11, 8144-8148, doi:10.1039/B910903J (2009).

44 Riedl, C. *et al.* Performance modulation through selective, homogenous surface doping of lanthanum strontium ferrite electrodes revealed by in situ PLD impedance measurements. *Journal of Materials Chemistry A* 10, 2973-2986, doi:10.1039/D1TA08634K (2022).

Chapter 4: Experimental requirements for high temperature solid state electrochemical TEM experiments

Zhongtao Ma, Christodoulos Chatzichristodoulou, Waynah Lou Dacayan, Kristian Speranza Mølhave, Francesco Maria Chiabrera, Thomas Erik Lyck Smitshuysen, Christian Danvad Damsgaard, Søren Bredmose Simonsen

Z. Ma, C. Chatzichristodoulou, W. L. Dacayan, F. M. Chiabrera, S. B. Simonsen
DTU Energy, Fysikvej, Kgs. Lyngby, 2800, Denmark
E-mail: sobrs@dtu.dk

K.S.Mølhave, T. E. L. Smitshuysen, C. D. Damsgarrd
DTU Nanolab, Ørsteds Plads, Kgs. Lyngby, 2800, Denmark

Keywords: ETEM, in situ, EIS, SOC, CGO, LSC

Abstract

In this paper, we present and discuss the experimental requirements for conducting solid-state electrochemical TEM experiments in general, including sample preparation, electrochemical measurements, failure factors, and possibilities for optimizations. Particularly, we describe the methodology of performing reliable electrochemical impedance spectroscopy measurements in reactive gasses and at elevated temperatures for both single materials and for solid oxide cells. The presented examples include impedance measurements of electronic conductors, an ionic conductor, and a mixed ionic and electronic conductor, all materials typically applied in solid oxide fuel and electrolysis cells. It is shown how transport properties and surface exchange properties can be measured by impedance spectroscopy in the TEM of materials with nanoscale dimensions. Simultaneously with the electrochemical measurements are the structural and elemental evolution directly observed via TEM and STEM imaging and spectroscopy. The ability to perform both the electrochemical and structural/elemental characterization in the same experiment and at the nanoscale makes it possible to directly link the electrochemical performance to the material

properties. These methods can have broad applicability in developing materials and structures for solid oxide cells, solid state batteries, thermal electrical devices and other solid state electrochemical devices.

1 Introduction

In situ and operando transmission electron microscopy (TEM) has proved its potential with its high spatial resolution in real-time characterization of nano-scale samples under various conditions and stimuli, like thermal, electrical and reactive gas environments [1-17]. In particular, the combination of environmental TEM (ETEM) and heating holders have made it possible to reveal the dynamics and mechanisms of solid-gas reactions at the nano and even atomic scale [18-21].

Recently, MEMS chip-based TEM holders have opened new possibilities for combinations of more stimuli in one experimental process [22,23]. One of these new fields is the simultaneous application of heating and electrical biasing [24-27]. An ETEM combined with such a heating-biasing holder makes it possible to study solid state electrochemical reactions at elevated temperatures in reactive gasses [Chapter 5]. Important examples of high-temperature solid state electrochemical technologies are the green energy conversion technologies solid oxide electrolysis and fuel cells (SOEC and SOFC).

We predict that high temperature solid state electrochemical TEM investigations will become increasingly important for the further development of these green energy technologies. In this article, we will discuss the experimental requirements for such experiments. As an example, we will focus on the solid oxide electrolysis cell (SOEC) and relevant materials. This P2X technology is particularly interesting by being the most efficient type of electrolysis cell and can be expected to play a critical role in green energy infrastructures [28].

The case of SOEC is chosen, not because it is easy to adapt this for the *operando* TEM experiments compared to other energy conversion technologies. On the contrary, this is very challenging. For example, SOECs have a complex layered 3D structure consisting of current collectors, porous electrodes (anode and cathode) and a gas tight electrolyte [29,30]. The materials of these components are combinations of hard, brittle ceramics and metals [31]. The cells are operated at elevated temperatures (typically 800 °C or above) in reactive gasses (typically H_2O, H_2, O_2, CO_2, CO) and under electrical polarization [32,33]. The electrochemical reactions take place at interfaces or triple

phase boundaries for which the chemical states, crystal structures and morphologies are known to depend on operation conditions [34,35].

The capabilities of the (S)TEM, electron diffraction, EELS, EDS, for analyzing the nano-scale structural and compositional dynamics motivates the application of *operando* TEM investigations of SOEC, but the demand for downscaling the cell dimensions for TEM analysis leads to challenges, such as a) designing a cell with relevant materials and suitable dimensions, b) designing a sample preparation routine with minimal risk of contamination or damage to the sample, c) ensuring sufficient electrical contact between the sample and chip electrodes d) avoiding loss of electrical contact or sample fracture as a result of thermal expansion when the temperature is elevated, e) ensuring that the electrochemical measurements represent the sample and are not dominated by the system around the sample and f) ensuring that the effects from the electron beam are negligible in the electrochemical, image and spectroscopy data.

In the present work, we will show how these challenges can be overcome for two types of samples: 1) single materials such as: a) Yttrium stabilized zirconia (YSZ) which is a pure ionic conductor , b) Nb doped $SrTiO_3$ (STN) and Pt which are electronic conductors, and c) Gd doped ceria (CGO) which behaves as mixed ionic and electronic conductor in reducing atmospheres, and 2) a full symmetric model SOEC cell with a YSZ electrolyte, CGO electrodes, and Pt and STN current collectors with three different cell geometries. The details of the experiments are described in the Materials and Methods section, and the challenges and solutions are discussed in the Results and Discussion section.

2 Materials and Methods

2.1 Materials and cell preparation

The single material CGO sample was fabricated by compressing the $Ce_{0.9}Gd_{0.1}O_{1.95-\delta}$ (CGO) powder (Solvay) by a 10 mm diameter stainless steel mold with a uniaxial pressure of 3 MPa followed by isostatic pressing at 325 MPa. Afterwards, the compressed pellet was sintered at 1500 °C in air for 12 h and slowly cooled to room temperature at a rate of 0.5 °C min^{-1}. The geometrical density of the sample was between 94 and 97% of the theoretical density [36]. The YSZ and STN samples were prepared from single crystals directly purchased from Crystec, GmBH. The Pt sample was prepared by Ga FIB-SEM ion-beam deposition.

In order to form a model SOEC cell with a layered structure, the cell was grown via pulsed-laser deposition (PLD) using a KrF excimer laser (248 nm; LPX 305, Coherent, Inc.) on Nb (0.5 wt. %) doped $SrTiO_3$ (001) single crystal substrate (Crystec, GmBH). The cell is symmetric with a 150 nm thick ZrO_2 with 8 mol % Y_2O_3 doping ($(ZrO_2)_{0.92}(Y_2O_3)_{0.08}$) electrolyte and approx. 100 nm thick electrodes consisting of CeO_2 doped with 10 at. % Gadolinia ($Ce_{0.9}Gd_{0.1}O_{1.95}$). Theoretically, the strain between the STN and CGO layers is 1.45 % and 5.51 % between YSZ and CGO. According to XRD theta-2theta scans of the model cell, the lattice constants are 5.4 Å and 5.2 Å for CGO and YSZ, respectively. Phi-scan around the [111] peak shows a 45° difference between the CGO and YSZ [111] peaks and the STN [111] peak. The surface roughness of the final CGO layer is 1.45 nm as determined by AFM over a 5 µm × 5 µm area.

2.2 TEM sample preparation

Our sample preparation processes are achieved by employing a Crossbeam (ZEISS, 1540XB) and a DENS solutions FIB Stub 3.0. The Omniprobe micromanipulator system need to reach the sample from the top of the stub. We modified the shape of needle with an arc to avoid the possible crash between the needle and the chip top edge during the needle insertion as shown in Figure S1. For all samples, the lamellas were mounted on a heating-biasing MEMS chip (DENS Lightning, 4 contacts for heating, 2 for biasing) as presented in Figure 1. As for a standard FIB-SEM sample lift-out process, 1 µm thick layer of Pt is deposited to protect the top sample surface.

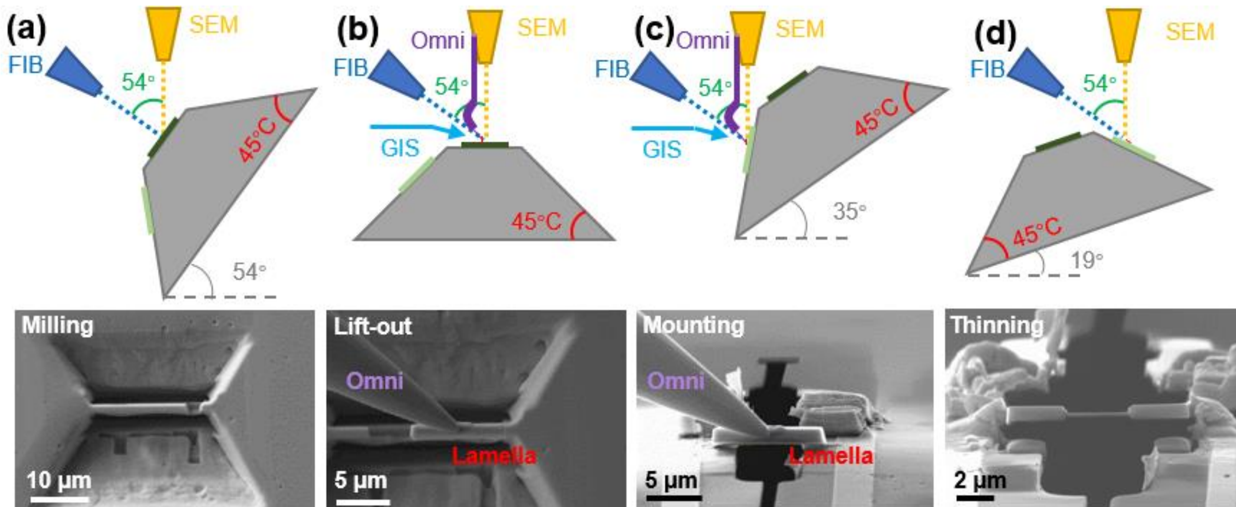

Figure 1: Geometries and relative positions in the FIB-SEM chamber during the sample preparation process. (a) Milling to create the sample lamella. The sample surface is normal to the ion beam; (b) Lift-out. The lamella is vertical; (c) Mounting. The chip surface is 80° from the

horizontal plane. There is a 10° angle between the lamella surface and the chip surface; (d) Thinning. The lamella surface is parallel to the ion beam.

Figure 1a-d illustrates the relative positions of different parts in the preparation process. In Figure 1a, the sample surface is normal to the ion beam with stage tilt to 54°. Two deep trenches are milled to form the lamella, and a standard J shape undercut is made for the lift-out process (Figure 1b) with the stage tilt back to 0. The lamella is vertical to the horizontal plane before lift-out. When mounting the lamella at the chip, the stage is tilted 35° and there is a 10° angle between the lamella and the chip surface (Figure 1c). The 10° angle is needed to be able to perform a final thinning of the lamella after mounting on the chip. For the final thinning process, the stage is rotated 180° and tilted 19° to make the lamella surfaces parallel to the FIB (Figure 1d). All the detailed steps are described in Table 1.

Table 1: Steps of lamella preparation onto a MEMS chip

#	Step name	Stage position		Milling and Deposition parameters						
		Rotation / °	Tilt / °	Milling area top length / µm	Milling area bottom length / µm	Milling area Height / µm	Current / pA	Time / min	Pt GIS	Voltage / kV
0	**Chip trench milling**	0	9				500		Out	30
1	**Pt protection layer**	0	54	20	20	1	200	2	In	30
2	**Trench top**	0	54	30	20	15	5000	20	Out	30
3	**Trench bottom**	0	54	20	30	15	5000	20	Out	30
4	**J shape cut**	0	0				1000		Out	30
5	**Needle connect**	0	0	1.5	1.5	1.5	20	1.5	In	30
6	**Lift-out – cut free**	0	0	1.5	1.5	3	500	1	Out	30
7	**Attaching to chip**	0	35	2	2	1.5	50	2	In	30
8	**Free the needle**	0	35	2	2	1	500	1	Out	30
9	**Circuit Pt deposition**	0	15				50	10	In	30
10	**Thinning front side**	180	21	4	4	2	500	10	Out	30
11	**Thinning back side**	180	17	4	4	2	500	10	Out	30
12	**Cut trenches for lamella/cell**	0	-1				500	10	Out	30
13	**Final thinning front side**	180	21	4	4	0.5	50	10	Out	30
14	**Final thinning back side**	180	17	4	4	0.5	50	10	Out	30
15	**Final polishing front side**	180	24	10	10	5	50	10	Out	5
16	**Final polishing back side**	180	14	10	10	5	50	10	Out	5

2.3 Electrochemical TEM

The electrochemical investigations were carried out in an ETEM (FEI, Titan 80–300 kV) equipped with a differential pumping system and an image aberration corrector [37], where the sample is exposed to the reactive gases O_2, H_2 and H_2O vapor. By mixing H_2 and H_2O with different pressure ratios, low oxygen partial pressures were achieved. The experiments were carried out in three different gas environments: (a) 3 mbar O_2, (b) a 5 mbar H_2/H_2O with pressure ratio of 0.003, and

(c) 3 mbar H_2/H_2O with pressure ratio of 0.8. The temperature ramping rate was 50 °C/min and TEM imaging and electrochemical impedance spectroscopy (EIS) measurements were carried out at each temperature ranging from RT to 800 °C after 3 min waiting time for the system to stabilize. A potentiostat (Gamry FAS2 Femtostat) was connected to the TEM holder (DENS Lightning) to add electrical bias signal on the electrodes of the chip. Two-probe EIS measurements were carried out with an amplitude of 20 mV and frequency range from 100 kHz to 0.1 Hz.

Because of the small dimensions of the TEM sample, uninteded disturbances such as static electricity or e.g. connection of the TEM holder to an instrument with a different grounding level can destroy the sample. The procedure we have applied to minimize the risk of this type of sample failure is one where no cables are connected, no equiptment is grounded or turned on after the sample is mounted in the holder. The procedure is: Before connecting the cable to the TEM holder, all other eqiuptment are connected and grounded to the same ground. The TEM holder is then connected and the potentiostat is turned on. The operator is grounded to the same ground as the equiptment with a wrist band, and finally the MEMS chip with the sample is mounted in the TEM holder.

3 Results and discussion

In this work the methodology of high-temperature solid state electrochemical TEM is presented and the method of electrochemical impedance spectroscopy TEM (EIS-TEM) is introduced. The method is exemplified by two different types of TEM samples: a) single materials, allowing us to investigate the transport and surface/structure evolution as a function of temperature, gas environment and applied electrical potentials and b) solid oxide cells, allowing us to observe chemical and structural changes at the cell interfaces while also analyzing its electrochemical performance. In particular, the structural and compositional evolution at interfaces can be linked directly with experimental conditions and electrochemical measurements. As a representative example, we present a Pt-CGO-YSZ-CGO-STN model cell.

3.1 TEM sample preparation routine

One major challenge when conducting in situ or operando research with MEMS chips is the process of preparing and mounting the sample. Our group attempted to use an ultramicrotome to cut thin samples of model SOEC/SOFC cells, but despite being able to produce thin lamellas of these hard and brittle materials, the overall cell structure and individual layers suffered from

fractures [38]. An alternative solution is the use of FIB-SEM, which has been proven to be an effective method for preparing cells for TEM analysis. The routine we have developed is described in detail in section 2.2 in this article. A key advantage of FIB-SEM is that it allows the simultaneous deposition of metals such as Pt or W to build circuits on the sample, enabling electrical testing [39]. In the following section we discuss considerations related to the FIB-SEM instrument and to the deposition of Pt.

3.1.1 FIB-SEM geometry

It is important to take into account the geometry of the instrument chamber. This includes the angle between the electron beam and ion beam, the position and shape of the Omniprobe needle and gas injection system (GIS), and the structures/dimensions of the stub used for lift-out and mounting processes.

For instance, the angle between the electron beam and ion beam varies in different systems. In the FEI system and JEOL MultiBeam, it is 52° [39,40], while in the ZEISS system it is 54° [41]. The internal structures of the instrument chamber, such as the position of the detectors, can also vary. To create a successful sample, one may need to modify the positions of the GIS nozzle or the Omniprobe needle in the FIB-SEM chamber to meet the desired position.

In the absence of a special stub and modified Omni-needle, the sample can be mounted on the chip with multiple lift-out processes. Firstly, the sample is transferred to an intermediate omnigrid. Then, after tilting the stage, the sample can be transferred to the MEMS chip placed on a 45-degree stub. However, in our experiment, we were able to mount the sample on the MEMS chip with only one lift-out process by using a special stub (DENS solutions FIB Stub 3.0) and a modified Omniprobe transfer needle, as described in the experimental part of this article.

3.1.2 Creating electrical contact

Ion or electron beam deposited Pt or other metals can be used for establishing electrical contact between the sample and chip electrodes.

The advantage of ion beam deposition compared to electron beam deposition is that it typically yields more conductive layers, and allows faster formation of thick layers [42]. The conductivity and proportion of Pt to hydrocarbon precursor in the deposited layer will vary depending on the ion beam current [43]. The higher the ion beam current, the greater the conductivity of the deposited Pt [44]. The main disadvantage of ion beam deposition in this context is a higher degree of Pt overspray,

i.e., thin layers of Pt deposited in other regions than where the beam is focused. The Pt overspray may form pathways for leak currents.

The Pt overspray at the TEM sample can be removed by thinning and final polishing with the FIB after ion-beam deposition. Electron deposition forms less overspray, which can be important for samples where post deposition thinning is not possible. The main disadvantages of electron deposited Pt is that the deposition process is slower, while it yields a higher hydrocarbon content and lower conductivity [45].

It may be desired to remove the hydrocarbon component from the deposited Pt layer before in situ/operando experiments. An example of this is reported in our recent publication where the pores in the deposited Pt were used for gas transport [Chapter 5]. One method to remove the hydrocarbon component is to treat the sample in a few mbar of O_2 at approx. 500 °C for 5 minutes or more.

In a recent publication, the properties of ion deposited Pt as electrical contacting material in operando electron microscopy experiments is discussed in more detail [Appendix 2].

3.2 Background Resistance and Capacitance

It is important to know the resistance and capacitance of the empty MEMS chip to be able to determine to what extent these will influence the actual measurements of the sample mounted on the chip. Figure 2 a and b presents an SEM image of an empty MEMS chip at two different magnifications.

We have measured the resistance and capacitance of several empty chips by EIS. The measurements were conducted in air. To describe the resistance and capacitance the impedance spectra were fitted with an electrical circuit model (ECM) consisting of a resistor, R_s, and a *CPE* element referred to as *CPE-shunt* in parallel. It is expected that the resistance is mainly contributed by the SiN membrane between the Pt electrodes on the chip, and that the capacitance can be from the chip, holder, and wires [Chapter 5]. Figure 3 presents the measured resistance as function of temperature of an empty chip in air (black stars). According to the figure the resistance of a new empty chip remains high, over 100 Gohm, from room temperature to 800 °C.

A used empty chip was also measured. This is a chip that has undergone multiple sample mounting processes of different samples, and which was exposed to several heating-cooling cycles.

According to Figure 3 the resistance of the used empty chip (blue open stars) becomes significantly lower than the new empty chip as the temperature is raised. The reason for the lower resistance of the used chip is most likely that the SiN membrane between the chip electrodes has been contaminated with Pt overspray from Pt deposition, hydrocarbons from the air, and/or from redeposited sample material during FIB thinning.

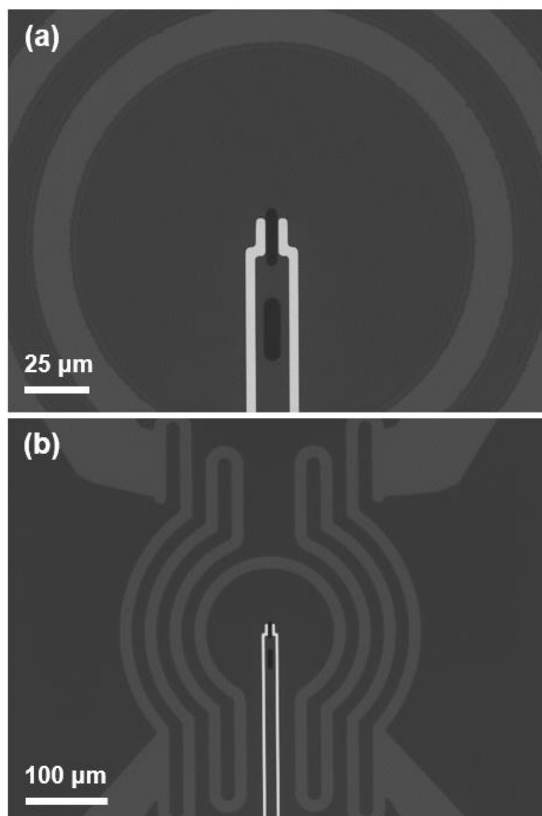

Figure 2: (a-b) SEM images of the heating biasing chips used in the present work. The brightest features are Pt electrodes for biasing. The less bright pattern with circular shapes is a Mo heater spiral. the Mo heater spiral is encapsulated in a 400 μm thick SiN membrane. Pt electrodes are supported by the SiN membrane, but is not encapsulated.

Figure 4a-b shows an example of a used chip with a layer of such contamination. In Figure 4a the contamination layer is observed as a bright contrast region, and the EDS map in Figure 4b shows that this layer consists of Pt. This chip was plasma cleaned for 10 min after which the contamination layer became visible in the electron SEM images. This suggests that the Pt-organic compounds from the gas injection system have condensed on the SiN membrane during Pt deposition. Irradiating with an electron or ion beam or using plasma cleaning can decompose these compounds into Pt nanoparticles. Similarly, Figure 4c shows the same type of contamination on a sample after ion-beam Pt deposition. The area of this contamination region is approx. 80 μm in diameter.

As Figure 4a-b shows, plasma cleaning is not a feasible method for cleaning this type of contamination. Instead, the condensed Pt-precursor compounds can be removed by using the chip heater element to elevate the temperature to evaporate the compounds from the SiN surface. This process should be carried out before beam exposure. For the same reason it is recommended to minimize the SEM scanning time or area during sample preparation in the FIB-SEM to prevent decomposition of any Pt-precursor material adsorbed at the surface of the MEMS chip.

Another source of contamination is hydrocarbon molecules adsorbed on the chip/sample surface when it is exposed to air outside the microscope. This can lead to carbon building up on the surface during exposure to the electron beam. The carbon is electrically conductive and can cause leak currents over the membrane or sample. This type of contamination can be removed by heating the chip to around 500°C in an oxidizing environment.

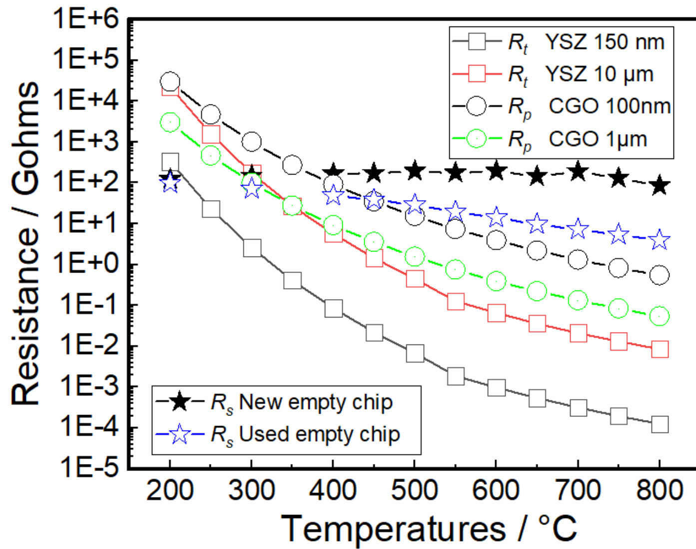

Figure 3: The figure presents measured resistances for a new and a used empty MEMS chip (DENS solutions). Theoretical transport resistance, R_t of YSZ with the length in the direction of the current, l = 150 nm or 10 µm and the cross section area of A = 100 nm x 5 µm compared with the theoretical surface exchange resistance, R_p of CGO electrodes with l = 100 nm or 1 µm and A = 100 nm x 5 µm. The calculated resistance values for these dimensions of CGO are based on measurements in a gas environment with H_2-to-H_2O ratio of 0.8 [Chapter 5].

Another method to mitigate the effects of contamination, whether it is Pt overspray, hydrocarbon contamination or redeposited material from the FIB-SEM work, is to further separate the chip electrodes by cutting a long trench between the electrodes with the FIB. An example of such a trench is shown on the chip presented in Figure 4a-b. From the images it can be seen that the trench in this example is slightly too short compared to the contaminated area, and in hindsight should have been made longer. When the trench is sufficiently long it reduces the likelihood of leak currents along the surface of the chip.

According to Figure 3, the resistance of used chips can be significantly lower than of new chips, and to ensure precise electrochemical measurement of the target sample, it is recommended to measure the resistance of the same chip two times: a) before mounting the sample to confirm that its resistance is high enough and b) after conducting experiments. In the latter case, the sample can be disconnected, and the background resistance measured again. By considering the chip's

contribution, the resistance of the sample can be corrected by subtracting the current that may leak through the chip.

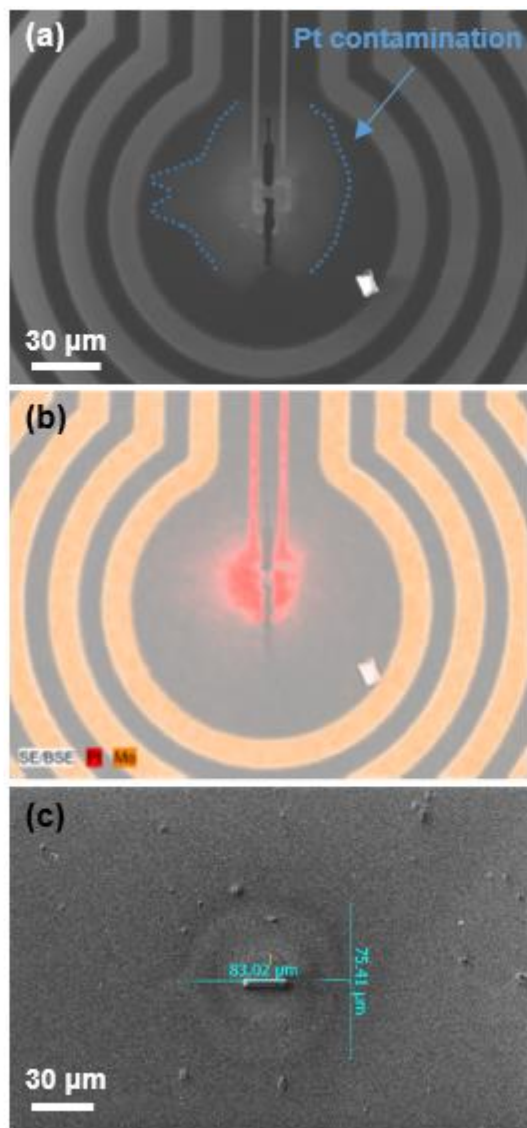

Figure 4: (a) SEM image of the chip after it has undergone mounting processes and plasma cleaning. The region contaminated with platinum (Pt) is marked by a blue dotted line, (b) SEM-EDS map that shows the distribution of Pt (red) and molybdenum (Mo) signals (orange), and (c) SEM image of a PLD sample before lift-out. Pt precursor contamination is observed in a circular pattern around the ion beam deposited Pt.

While the user would prefer the resistance of the empty chip to be as high as possible, the capacitance of the entire connected system, i.e., the chip, TEM holder and wires connected to the potentiostat, should be as low as possible. For the system used for our measurements, the measured capacitance is constant and stable as a function of temperature with the value $3.8 \cdot 10^{-11}$ F. The value is the same when using a new and a used empty chip. The contribution to the capacitance is likely mainly from the wires in and connected to the TEM holder. The capacitance value from the present system is small enough compared to typical capacitive contributions expected for SOFC/SOEC TEM samples, such as surface capacitance and chemical capacitance [Chapter 5].

To confirm the consistency of the resistance and capacitance values measured in air, the EIS measurements were repeated for a new chip in the ETEM in 3 mbar of H_2/H_2O with a gas pressure ratio of 0.8 and in 3 mbar O_2. In both gas environments similar resistance and capacitance values were obtained.

3.3 Sample fracture

One of the main challenges when conducting solid state electrochemical TEM experiments at elevated temperatures is the thermal expansion and contraction of the materials during heating and cooling processes. This can result in variations in the electrical contact resistance and even in loss of electrical contact between the sample and the chip electrodes [Appendix 2]. It can also result in fracture of the sample and delamination of the deposited Pt.

Figure 5 shows an example of a sample that was broken by heating it in the ETEM. As can be observed from the figure, a crack has formed from one of the 90-degree corners in the sample. We have observed that cracks often start at sharp corners, and that the problem with crack formation can be reduced by adjusting the geometry so that sharp corners are modified with the FIB into more rounded shapes.

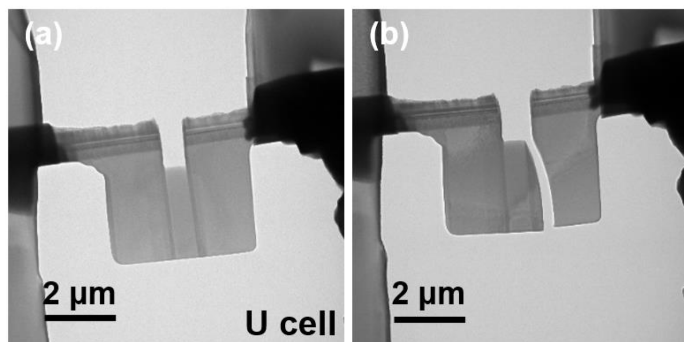

Figure 5: (a) TEM image of CGO-YSZ-CGO U cell (U cell will be introduced in detail later in this paper); (b) TEM image of the U cell after one cycle of heating and cooling.

3.4 Influence of electron beam

An important question to address is if the electron beam will influence the EIS measurements when conducting EIS-TEM experiments. Figure 6 presents an experiment where the electron beam covered different regions of an ion beam deposited Pt sample and/or the Pt electrodes on the MEMS chip while conducting the EIS measurement in 2 mbar O_2. Figure 6c shows the position and area of the beam for each EIS measurement. The results show that exposing the Pt electrodes or the sample to the electron beam does not influence the EIS measurement (Figure 6a). This means that it is possible to record EIS spectra and TEM images simultaneously.

On the other hand, it is well-known that an electron beam can cause structural changes, so-called beam damage in a TEM sample [46] and for this reason the beam current density and total dose should always be kept as low as possible while still being able to record the needed information. This is particularly important for in situ and operando experiments where the same region of the sample is exposed to the electron beam several times [11].

It can be expected that beam damage to the sample will influence the EIS measurements. Figure 6b shows EIS measurements from the same sample as in Figure 6a, but after deliberately inducing beam damage to the sample by focusing the beam to a small spot on the sample in 3 min. TEM images clearly revealed structural changes in the ion beam deposited Pt (Figure 6d, e). Consistently, Figure 6b show significantly larger arcs in the Nyquist plots compared to Figure 6a. This shows that this beam induced structural change led to a significant increase in the sample resistance. Again after beam damage, there was no significant difference in the EIS spectra recorded with or without the electron beam.

Due to the risk of beam damage, we usually blank the beam during our EIS-TEM measurements, and only expose the sample to the electron beam in the short time frame it requires to record images, diffraction patterns or spectroscopy data.

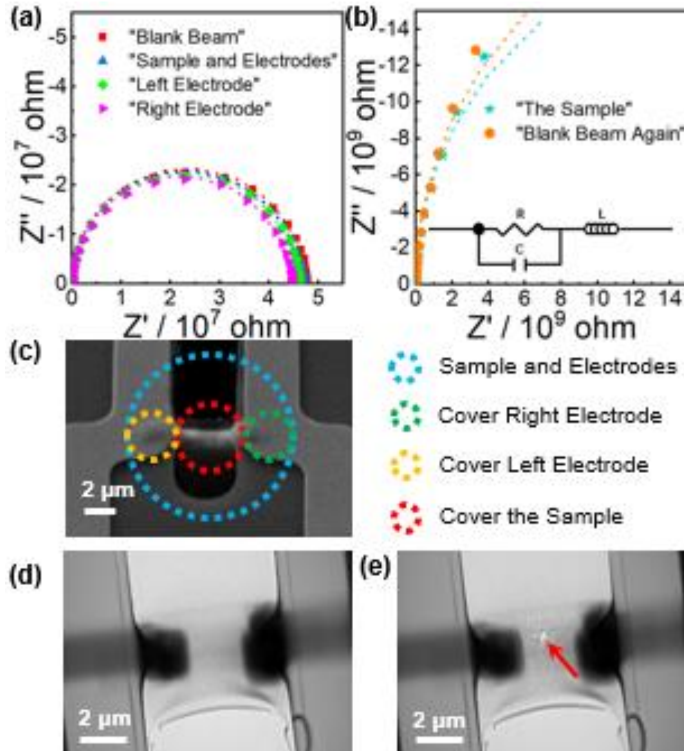

Figure 6: (a) EIS measurements at the conditions: The electron beam is blanked (red squares), covers the sample and both chip electrodes (blue triangle), covers left electrode (green tilted square) and covers only right electrode (purple triangle). (b) EIS measurements from the same sample, after beam damage. The EIS measurements with the beam covering sample and blanked. (c) The positions and areas of the electron beam at the thin film Pt sample. (d-e) The thin film Pt sample (d) before and (e) after exposure of a focused beam for 3 min. The red arrow indicates the focusing point.

3.5 EIS-TEM measurements of single materials

To demonstrate the EIS-TEM method applied on single materials, we have chosen three different types of conductors 1) electronic conductors, Pt and STN, 2) an ionic conductor, YSZ, and 3) a mixed ionic and electronic conductor, CGO.

3.5.1 Electronic conductors

The simplest case is EIS-TEM measurements on an electronic conductor. This type of sample only requires sufficient electrical connection to the chip electrodes. This will allow electrons from one chip electrode to be transported through the electronic conductor by an applied voltage to reach the other chip electrode.

STN is an example of an electronic conductor. Figure 7a and 7c present an STN sample mounted on the heating-biasing MEMS chip. Examples of Nyquist plots of EIS data and the fitted ECM are shown in Figure 7b. For a purely electronic conductor, a typical EIS spectrum would exhibit a straight line parallel to the y axis with a fixed intercept on the x axis, which corresponds to its transport resistance, R_t. However, the presence of the resistance from the TEM holder and wires, the shunt capacitance described in section 3.2, will influence the shape of the EIS spectra. Therefore, we can anticipate a single arc in the Nyquist plot with the second intercept representing the transport properties. The Nyquist plots in Figure 7b are consistent with this expectation.

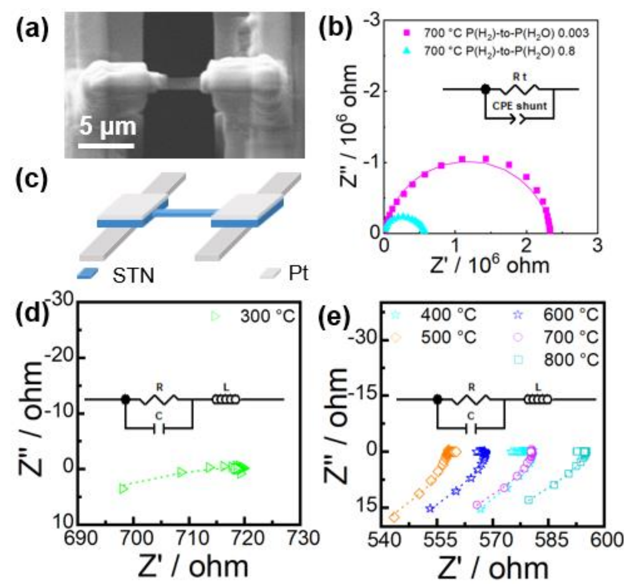

Figure 7: (a) SEM image, (c) schematic diagram, and (b) EIS spectra recorded in the ETEM of STN sample mounted on heating-biasing MEMS chip. The EIS spectra are all recorded at 700 °C in a mixture of H_2 and H_2O with the pressure ratio of 0.003 and 0.8 as indicated for each sample. (d-e) Nyquist plot of EIS-TEM data of an ion beam deposited Pt thin film. The spectra are recorded from 300 °C to 800 °C in 2 mbar O_2 [Appendix 2].

From the measured dimensions of the central part of the STN sample, we can calculate by ohm's law that the transport resistivity at 700 °C is 6.7 ohm cm in 3 mbar H_2/H_2O with gas pressure ratio of 0.003, and 1.5 ohm cm in 5 mbar H_2/H_2O with gas pressure ratio of 0.8. According to the measurements, the STN demonstrates higher electrical conductivity in a more reducing environment, which is in accordance with previous reports and can be attributed to an increased concentration of electrons [47].

Another example of an electronic conductor is ion beam deposited Pt. In a recent publication we investigate the temperature dependence of ion-deposited Pt in vacuum and in O_2 and show that the EIS-TEM measurement agree with previously reported results [Appendix 2].

Figure 7d-e show Nyquist plots from EIS-TEM measurements of a Pt thin film sample, deposited between the electrodes of the MEMS chip, recorded from 300 °C to 800 °C. The ECM model used for fitting the data is also presented. Compared to the measurements of the empty chip showing a resistance of tens or hundreds of GΩ (Figure 3), and of the STN in the range of MΩ, the resistance of the Pt is in the kΩ range. From the discussion of the EIS-TEM results for the STN sample one would expect the appearance of a capacitive semicircle in the Nyquist plot due to the contributions of the Pt film resistance and the shunt capacitance. However, the EIS measurements of the Pt film do not show a semi-circle as observed for the STN sample, and we found that the data could only be fitted well if an inductance element, L is added in series with the sample R_t and the shunt capacitance, C in the ECM. The absence of the capacitive semicircle is due to the magnitude of the film resistance being much smaller (approx. 10^3 times) than the capacitive impedance even at the highest frequencies of the measurement (100 kHz), resulting in effectively short circuiting the shunt capacitance. On the other hand, the EIS data reflect a component of inductance in this case. From the fitted data the inductance values are around 0.0002 H. The inductance is likely due to the influence of the experimental equipment such as the wires, chips, and the sample holder. We found that the values of the inductance are stable from 25 °C to 850 °C for this sample. Therefore, it may be beneficial to consider the inductance contribution when fitting low resistance measurements.

Furthermore, Figure 7d, e shows that the resistance of ion beam-deposited Pt changes as a function of temperature. This has been reported before and shown to be related to changes in the Pt nanostructure [Appendix 2].

3.5.2 Ionic conductors

The situation is more complicated for the case of ionic conductors where the electronic current at the electrodes needs to be converted to ions that are then transported through the ionic conductor. This conversion involves a surface exchange reaction that takes place at the triple phase boundary (TPBs) between the electronic conductor, the ionic conductor and the gas phase. The TPB is the active region in the vicinity of which the reaction occurs, driven by the applied polarization.

Therefore, the surface exchange reaction resistance, R_p will depend on the length of the TPB. The measured total resistance in the EIS-TEM experiment will be the sum of R_t and R_p, where the latter depends on the TPB.

When preparing the EIS-TEM sample of an ionic conductor one should consider how to control the TPB length. One approach to making a well-defined TPB length is to prepare the sample as a layered cell, like those presented in section 3.6 below. Another approach is to mount the ion conducting material directly on the chip and connect it to the chip electrodes by ion beam-deposited metal similar to the STN sample. The example presented in this section follows the latter approach.

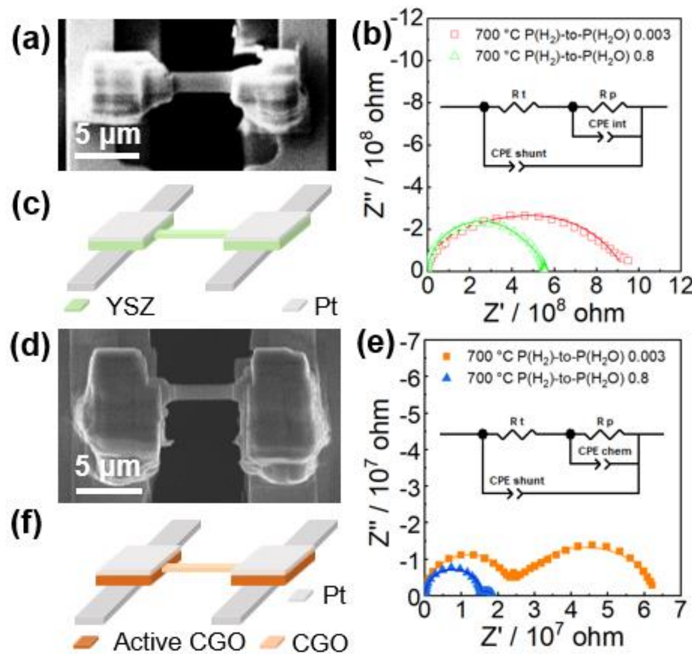

Figure 8: (a,d) SEM images, (c,f) schematic diagrams, and (b,e) EIS spectra recorded in the ETEM of YSZ and CGO samples mounted on heating-biasing MEMS chips. The EIS spectra are all recorded at 700 °C in a mixture of H_2 and H_2O with the pressure ratio of 0.003 and 0.8 as indicated for each sample.

The ionic conductor in this case is YSZ which conducts oxygen ions at elevated temperatures. Ion beam-deposited Pt connects the YSZ to the chip electrodes, and therefore the TPB is defined by the contact zone for YSZ, Pt and gas. A challenge of this approach of depositing the electronic conductor is that the TPB length is not very well-defined. Firstly, the exact shape and dimensions of the deposited material can be difficult to control. Secondly, the deposited material has a complex nanostructure and is mixed with hydrocarbons and ions from the FIB [Appendix 2]. The hydrocarbons are removed if the sample is heated to 500 °C in the presence of oxygen [Appendix 2], resulting in Pt with a nanoporous structure. Our recent work indicates that the nanopores increase the TPB length compared to dense Pt by allowing gas diffusion in the pores

[Chapter 5]. However, it is not straight forward to control or to determine the pore volume, pore size and tortuosity of the deposited Pt.

Figure 9 presents STEM images of a lamella prepared from ion beam-deposited Pt as a function of temperature in H_2/H_2O. The figure demonstrates that heat treatment in a reducing environment is a method for removing the pores in ion beam-deposited Pt to achieve a dense Pt contact. This is one route for making the TPB more well-defined, but shorter compared to the porous structure. The use of this method prior to the actual EIS-TEM measurements is only feasible for samples that can tolerate a reducing environment at such high temperatures.

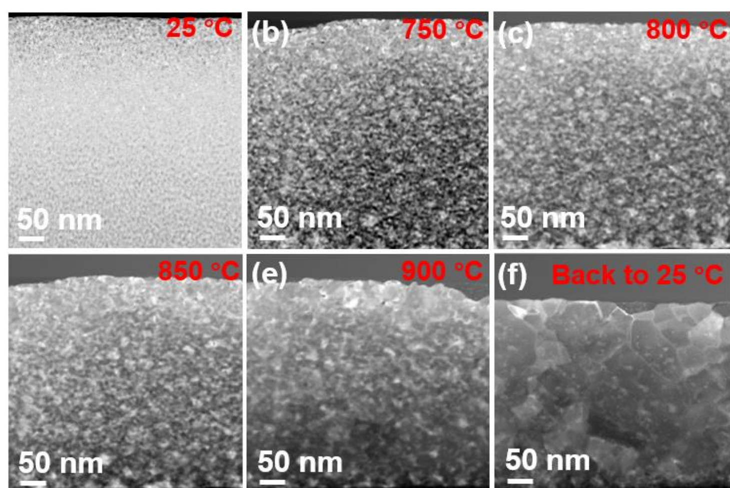

Figure 9: STEM-HAADF images of cross-sections of Pt samples at different temperatures in 3 mbar H_2/H_2O with gas pressure ratio of 0.8

Figure 8a-c presents EIS-TEM results for a YSZ sample contacted to the chip electrodes with ion beam deposited Pt. In this case, a heat treatment in 2 mbar O_2 at 500 °C was carried out to remove hydrocarbon and create pores in the ion beam-deposited Pt to maximize the TBP length. The EIS spectra were recorded at 700 °C in the two different gas ratio mixtures of H_2 and H_2O.

For a pure ionic conductor two arcs can be expected in the Nyquist plot, one in the high frequency range representing ionic transport and another in the lower frequency range representing the surface exchange reaction at the TPBs. In the environment with H_2-to-H_2O ratio of 0.003, the EIS spectrum in the Nyquist plot appears as a squeezed semi-circle suggesting there are likely more than one processes superimposed. The spectrum can be fitted well with an ECM representing two arcs from two processes, which is consistent with the expectation. The same ECM could fit well the EIS spectrum recorded in the environment with H_2-to-H_2O ratio of 0.8, i.e., with lower oxygen partial pressure.

For the gas ratio of 0.8, the obtained R_p, represented by the second arc, is approx. 1/3 of that in the ratio of 0.003, while the first arc, representing R_t, shows similar values in both gas environments. This result is expected, since the R_t should depend on temperature, but not on the oxygen partial

pressure within the range employed here, whereas R_p depends on the gas environment and decreases with increasing H_2 concentration as expected [48].

3.5.3 Mixed conductors

In the case of mixed electronic and ionic conductors (MIECs), some electrons will be converted to ions through surface exchange reactions as described for the ionic conductors and transported as ions through the MIEC, while some electrons will directly leak through the sample as described for the electronic conductors.

If the electronic conductivity of the MIEC is sufficiently high and/or the nanoporous structure of the current collector sufficiently fine, the surface exchange reaction will not be limited to the TPB, but will extend to the sample surface S exposed to the gas environment in the vicinity of the current collector. For the MIEC it should be considered how far the active surface extends from the TPB. The important parameters are: a) the gas environment and temperature which control the degree of electronic conductivity. b) sample geometry, in thin sample regions, e.g., the part of the sample that is so thin that it can be studied in the TEM, fewer electrons may flow to the surface sites due to the higher resistance compared to thicker parts of the sample, e.g., the side parts that are connected to the electrodes. Samples with such thin regions in the center and thicker regions connected to the MEMS chip electrodes are presented in Figure 8d-f. c) the polarization strength.

It is not trivial via a-c to determine to what extent each surface of the sample contributes to the surface exchange reaction, but in general the thicker side parts will be more active, and thin central part less active [Chapter 5]. This is illustrated schematically in Figure 8f. For R_t, it is the thin region that mainly contributes.

An example of a MIEC is CGO in gas environments with a low oxygen partial pressure. Figure 8d-f presents EIS-TEM results for a CGO sample at 700 °C in two different gas ratio mixtures of H_2 and H_2O. Like the ionic conductor, we can expect to observe two arcs in each EIS spectra, with the first arc representing R_t and the second representing the surface exchange reaction. As anticipated, the EIS spectra presented in Figure 7h both have two arcs, and the arc representing R_p decreases with decreasing oxygen partial pressure. In our recently published work, we have presented a detailed EIS-TEM analysis of such CGO samples which shows that the absolute resistivity values and activation energies match very well with literature values for bulk materials [Chapter 5].

3.6 Cell design

So far, we have described the EIS-TEM method applied on single materials. Now we will focus on the method applied on a more complex sample: the solid oxide cell. The cell could represent an SOEC or an SOFC.

The choice of cell to study can go in two different directions: a) industrial type cells or b) model cells. Studying industrial cells offers a direct link between the fundamental study in the TEM and the industrial application [49], while the advantage of the model cell approach is that the cell complexity can be downscaled to allow for investigations of few selected scientific questions.

Figure 10 presents a symmetric CGO/YSZ/CGO cell, corresponding to a model SOEC with a state-of-the-art YSZ electrolyte and two CGO electrodes. When electrically polarized, at elevated temperatures in O_2, it would simulate the oxygen electrode of an SOEC at one electrode, and simultaneously, the oxygen electrode of an SOFC at the other electrode. Similar symmetric cells can be made for studying the hydrogen electrodes of SOECs and SOFCs. Using a symmetrical cell design eliminates the need to separate fuel and oxygen gasses, which is challenging in an ETEM.

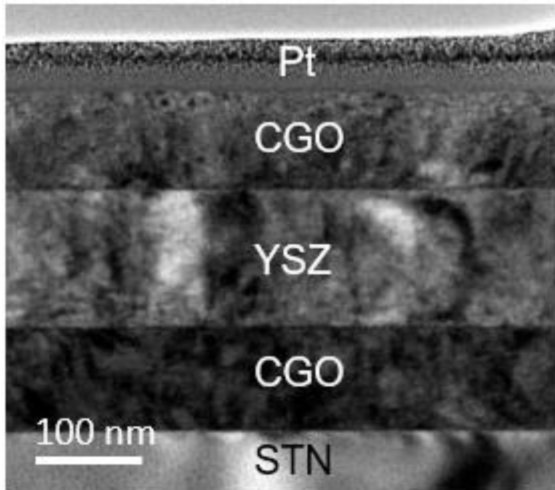

Figure 10: TEM image of a CGO-YSZ-CGO model cell. The top part is coated with Pt. The STN and Pt function as current collectors.

In this case, the model cell electrodes are dense, contrary to industrial cells with porous electrodes to allow for gas transport. Electrode porosity is not necessary when the cell is thinned for TEM use, since the gasses have access above and below the cell. The fully dense electrodes make the cell less fragile and the TPB lengths and interface areas well-defined. The latter is needed when converting EIS measurements of resistance, R (Ω), into geometry independent parameters such as resistivity, ρ (Ω cm) and conductivity, σ (S/cm) for comparison with reference experiments.

R_t is in series with R_p, and these two make up the total resistance. One can adjust the total resistance by controlling the thickness of the electrolyte and electrode layers.

The present model cell was designed using theoretical calculations to determine the appropriate thicknesses for each cell layer material. The layer thicknesses were chosen based on the expected total resistance, which should be within a range that can be measured using the available equipment and significantly below the resistance of the empty MEMS chip.

The use of pulsed laser deposition (PLD) for preparing the model cell allows for fine-tuning the thickness of the individual cell layers and adjusting the expected resistance, R for each layer. The small cross-section areas, A of a TEM sample necessarily lead to relatively high measured transport resistances, R_t, which scales inversely with A.

$$R_t = \rho \frac{l}{A}, \tag{1}$$

where l is the length in the direction of the current, corresponding to the layer thickness, and ρ the resistivity.

An industrial state-of-the-art YSZ electrolyte typically has a thickness of approx. 10 μm [50,51]. Figure 3 which showed the resistance of an empty chip also presents the calculated ionic R_t for a TEM sample of YSZ with a thickness of 10 μm compared to 150 nm as used in the present model cell. Firstly, the figure shows that the resistance of the YSZ is significantly lower than that of the empty chip which makes an EIS-TEM measurement of the YSZ sample feasible. Secondly Figure 3 shows that the layer thickness of YSZ will strongly influence the measured R_t.

Now focusing on the cell electrodes, in our case CGO, it is important to consider R_p which is inversely proportional to the active surface area [Chapter 5].

$$R_p = \frac{r_p}{S}, \tag{2}$$

where r_p is the area specific surface exchange resistance.

By increasing S, R_p can be reduced if necessary. In an industrial cell, this can be achieved through infiltration or by altering the porosity of the electrodes [52]. In a reducing environment, the CGO in the Pt-CGO-YSZ-CGO-STN model cell shows mixed ionic and electronic behavior as discussed in section 3.5.3, and S is the entire CGO electrode surface. Therefore, the CGO layer thickness controls R_p.

Figure 3 compares the calculated R_p for a 100 nm and a 1 μm thick CGO electrode in 3 mbar of H_2/H_2O with a pressure ratio of 0.8. The figure shows that while R_t (exemplified with YSZ)

decreases with decreasing layer thickness, the trend is opposite for R_p. For CGO electrodes in the given gas environment the surface exchange resistance will become comparable to the resistance of the chip if the CGO layer thickness is too small. The figure indicates that EIS-TEM measurements of the present CGO-YSZ-CGO cell are not feasible at temperatures below 400 °C.

3.7 Cell geometries

There are many ways a model cell like the one presented in Figure 10 can be shaped by the FIB and connected to the MEMS chip electrodes. We will here present a few geometries and discuss them.

The most intuitive geometry is perhaps to connect the current collectors directly to the electrodes of the chip. We call this the "H-cell" and Figure 11a shows an example of how the cell is mounted. Advantages of this geometry is that it is feasible to ensure electrical contact along the entire width of the current collectors, while the actual cell (electrodes and electrolyte) is positioned in the window for electron transparency. Compared to the other geometries, the H-cell is also relatively simple. However, the preparation procedure for the H-cell can be quite challenging because it requires rotation of the lamella by 90° after the lift-out. In our case, we used an omnigrid as an intermediate carrier. Two lift-outs were performed, first transferring the lamella to the omnigrid, rotating it by 90° outside the FIB-SEM system, and then performing a second lift-out to mount the cell on the chip. Another challenge is that the ion beam is parallel to the cell interfaces after the cell is mounted on the chip. When thinning the cell to approximately 100 nm, the different layers in the cell will likely be milled at different rates. Because of this, there is a risk of damaging the sample. An example is shown in Figure S2a and b, where a crack in the center of the cell formed after the thinning process.

It can be an advantage instead to mount the cell on the chip so that the cell layers are normal to the ion beam. However, the cell should still only be connected to the chip electrodes via the cell current collectors. A geometry that satisfies these requirements is what we call the “Z-cell”, presented in Figure 11b. The Z-cell does not require rotation of the sample and can therefore be prepared with just one lift-out step. Electrical short circuiting is avoided by cutting trenches at different positions on the lamella. The current path is represented by yellow dashed lines in Figure 11.

Introducing a conductive ceramic substrate, such as STN, as a current collector may contribute additional resistance and yield inhomogeneous electrode polarization. To avoid the impact of

introducing other current collectors than Pt, one can adopt the structure we call the "U-cell" to realize a CGO-YSZ-CGO cell structure. A layer of CGO can be deposited directly on the YSZ substrate, followed by one lift-out step, and cutting the geometry for the electrical circuits (Figure 11c).

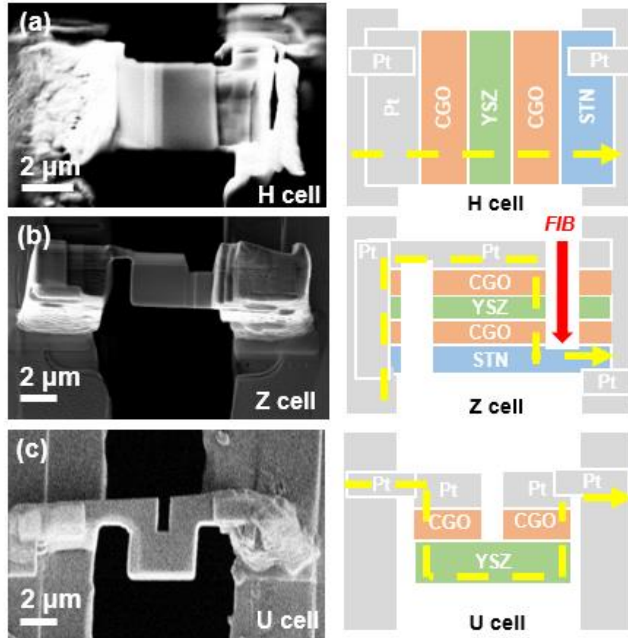

Figure 11: SEM images and corresponding schematic diagrams of three cell geometries: "H-cell", "Z-cell" and "U-cell." The yellow arrows indicate the direction of the current path.

For high temperature EIS-TEM experiments, the sample should be able to withstand heating and cooling cycles. Our experiments have shown that the Z-cell is robust enough to withstand several heating and cooling cycles in different gas environments and pressures without breaking. This may be due to the plastic deformation ability of the metallic Pt neck in the upper left corner [53]. Contrary to the Z-cell, the U-cell appears to be less robust to heating and cooling cycles because the weakness of central part due to stress concentration of ceramics. An example of this was given by Figure 5 showing a U-cell before and after one heating and cooling cycle. However, the U-cell structure is still feasible for low temperature applications, for example for solid state battery research.

3.8 EIS-TEM results from a cell

In Figure 12a, a STEM image of a Pt-CGO-YSZ-CGO-STN Z-cell structure is presented, showcasing the lamella and cell structure mounted on the chip electrodes. Figure 12b presents examples of EIS results from this cell obtained in two different environments: 3 mbar O_2 and 5 mbar of H_2/H_2O with a pressure ratio of 0.8.

The corresponding ECM is also presented. In this case, the transport resistance, denoted as R_t, is mainly contributed by YSZ, while the surface exchange reaction on CGO can be represented by R_p in parallel with the interface capacitance, *CPEint* (or chemical capacitance, *CPEchem*). All the contributions from the sample are parallel with the *CPEshunt* from the holder and wires.

As can be expected, it was found that the total resistance of the Pt-CGO-YSZ-CGO-STN structure is significantly higher in an oxidizing environment than in a reducing atmosphere. The R_t is very small in this configuration, so the EIS spectra only shows one arc from surface exchange resistance R_p.

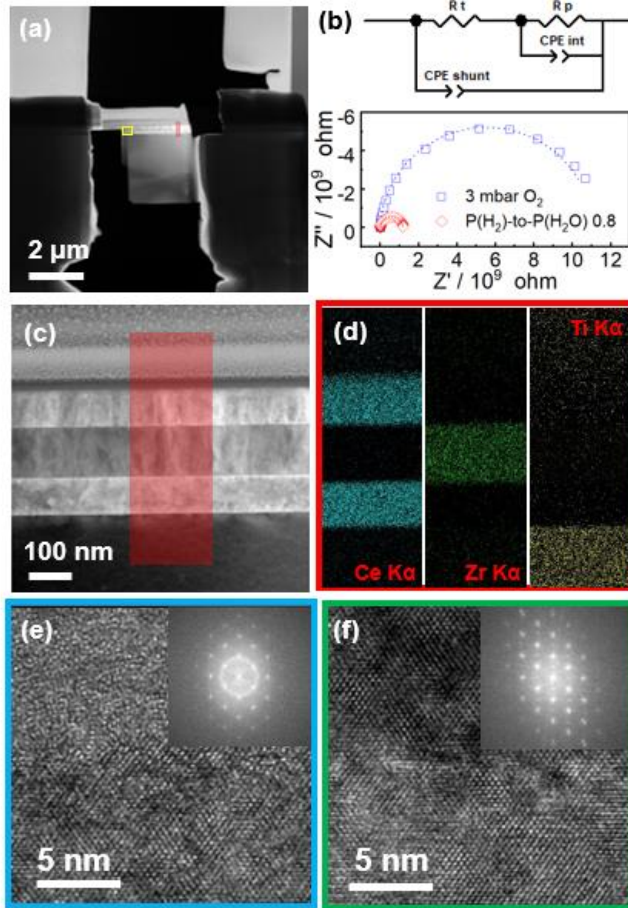

Figure 12: (a) STEM-HAADF image of a cell mounted on the chip. The cell layers from top to bottom being Pt, CGO, YSZ, CGO, and STN. (b) EIS spectra of the Pt-CGO-YSZ-CGO-STN structure at 500°C in environments of 3 mbar O_2 and H_2/H_2O with a gas ratio of 0.8. (c) Close-up STEM image of the cell. (d) EDS maps of the region marked with a red rectangle in (c), with the corresponding signals for detecting Ce, Zr, and Ti elements noted in the figure. (e) and (f) HRTEM images showing the interfaces of Pt-CGO and CGO-YSZ respectively.

Figure 12c shows the different layers in the cell, with layer thicknesses of 105 nm, 150 nm, and 110 nm for the lower CGO, YSZ, and top CGO layer, respectively. Figures 10d present corresponding EDS maps of the Ce, Zr, and Ti elements from CGO, YSZ and STN respectively. These results indicate that the elements are uniformly distributed in the layers.

The interfaces between layers are particularly important in electrochemical devices [56-61]. Figures 12e, f present HRTEM images of the interfaces between Pt-CGO and CGO-YSZ. The lattice fringes and corresponding FFT results confirm the amorphous structure of Pt and the fluorite structures of both CGO and YSZ [54].

Obviously, the parameter space that can be varied for such a cell in the EIS-TEM experiment (temperature, gas environment, electrical polarization) is large but presenting a detailed exploration of this parameter space is beyond the scope of the present work. The intention here is

to provide examples of the type of data that can be obtained with EIS-TEM for a full SOEC model cell. The results illustrate the high quality of the cell in terms of layer homogeneity and crystallinity. The results also show that it is indeed possible to conduct EIS measurements on a model SOEC cell in reactive gasses and at elevated temperatures while recording spectroscopy data and HRTEM images of the interfaces.

4 Conclusion

In this work we have addressed the most important experimental requirements and challenges for conducting high-temperature solid-state electrochemical TEM experiments. The experiments are performed by combining an ETEM, with a MEMS chip-based heating-biasing TEM holder and a Potentiostat for electrochemical measurements that can measure resistances in the GΩ range. Different approaches to sample preparation were presented for single materials and full solid oxide model cells. It was shown that it is feasible to prepare samples by FIB-SEM, where the sample was thinned after mounting it on a heating-biasing MEMS chip and connected to the electrodes with ion beam deposited Pt. The possible influence from the resistance and capacitance of the MEMS chip was discussed. It was found that contamination of the chip during sample preparation can significantly lower the chip resistance. Strategies for minimizing the problem with contamination were presented, as well as a strategy to minimize the risk of sample fracture during heating-cooling cycles.

Emphasis is put on the combination of electrochemical impedance spectroscopy with TEM (EIS-TEM). The feasibility of performing EIS-TEM experiments for all types of conductors (electronic, ionic and mixed) is proven, as well as for full solid oxide model cells in a variety of gasses and at elevated temperatures. For each type of sample, the specific experimental requirements are discussed and tested solutions are presented.

The ability to combine electrochemical measurements with structural and compositional characterization in the same experiment is shown. This will make it possible to directly link the electrochemical performance to the material properties which can have broad applicability for solid oxide cells, solid state batteries, and other solid state electrochemical devices.

Acknowledgement

This project has received funding from the European Research Council (ERC) under the European Union’s Horizon 2020 research and innovation programme (grant agreement No 850850).

References

1 Sinclair, R. & Parker, M. A. High-resolution transmission electron microscopy of silicon re-growth at controlled elevated temperatures. *Nature* 322, 531-533, doi:10.1038/322531a0 (1986).

2 Holloway, K. & Sinclair, R. High-resolution and in situ tem studies of annealing of Ti-Si multilayers. *Journal of the Less Common Metals* 140, 139-148, doi:https://doi.org/10.1016/0022-5088(88)90376-1 (1988).

3 Kamino, T. & Saka, H. A newly developed high resolution hot stage and its application to materials characterization. *Microsc. Microanal. Microstruct.* 4, 127-135 (1993).

4 Kamaladasa, R. J. *et al.* In Situ TEM Imaging of Defect Dynamics under Electrical Bias in Resistive Switching Rutile-TiO2. *Microsc. microanal.* 21, 140-153, doi:10.1017/S1431927614013555 (2015).

5 Haas, B., Rouvière, J.-L., Boureau, V., Berthier, R. & Cooper, D. Direct comparison of off-axis holography and differential phase contrast for the mapping of electric fields in semiconductors by transmission electron microscopy. *Ultramicroscopy* 198, 58-72, doi:https://doi.org/10.1016/j.ultramic.2018.12.003 (2019).

6 Baker, R. T. K., Thomas, C. & Thomas, R. B. Continuous observation of the particle size behavior of platinum on alumina. *Journal of Catalysis* 38, 510-513, doi:https://doi.org/10.1016/0021-9517(75)90120-7 (1975).

7 Baker, R. T. K., Thomas, R. B. & Wells, M. Controlled atmosphere electron microscopy studies of graphite gasification—The catalytic influence of vanadium and vanadium pentoxide. *Carbon* 13, 141-145, doi:https://doi.org/10.1016/0008-6223(75)90271-7 (1975).

8 Crozier, P. A. & Datye, A. K. in *Studies in Surface Science and Catalysis* Vol. 130 (eds Avelino Corma, Francisco V. Melo, Sagrario Mendioroz, & José Luis G. Fierro) 3119-3124 (Elsevier, 2000).

9 Hansen, P. L. *et al.* Atom-Resolved Imaging of Dynamic Shape Changes in Supported Copper Nanocrystals. *Science* 295, 2053-2055, doi:10.1126/science.1069325 (2002).

10 Helveg, S. *et al.* Atomic-scale imaging of carbon nanofibre growth. *Nature* 427, 426-429, doi:10.1038/nature02278 (2004).

11 Simonsen, S. B. *et al.* Direct Observations of Oxygen-induced Platinum Nanoparticle Ripening Studied by In Situ TEM. *Journal of the American Chemical Society* 132, 7968-7975, doi:10.1021/ja910094r (2010).

12 Crozier, P. A. & Chenna, S. In situ analysis of gas composition by electron energy-loss spectroscopy for environmental transmission electron microscopy. *Ultramicroscopy* 111, 177-185, doi:https://doi.org/10.1016/j.ultramic.2010.11.005 (2011).

13 Chenna, S. & Crozier, P. A. Operando Transmission Electron Microscopy: A Technique for Detection of Catalysis Using Electron Energy-Loss Spectroscopy in the Transmission Electron Microscope. *ACS Catalysis* 2, 2395-2402, doi:10.1021/cs3004853 (2012).

14 Jinschek, J. R. Advances in the environmental transmission electron microscope (ETEM) for nanoscale in situ studies of gas–solid interactions. *Chemical Communications* 50, 2696-2706, doi:10.1039/C3CC49092K (2014).

15 Simonsen, S. B., Wang, Y., Jensen, J. O. & Zhang, W. Coarsening of carbon black supported Pt nanoparticles in hydrogen. *Nanotechnology* 28, 475710, doi:10.1088/1361-6528/aa91a8 (2017).

16 Hansen, T. W., Wagner, J. B. & Dunin-Borkowski, R. E. Aberration corrected and monochromated environmental transmission electron microscopy: challenges and prospects for materials science. *Materials Science and Technology* 26, 1338-1344, doi:10.1179/026708310X12756557336355 (2010).

17 Luo, C., Wang, C., Wu, X., Zhang, J. & Chu, J. In Situ Transmission Electron Microscopy Characterization and Manipulation of Two-Dimensional Layered Materials beyond Graphene. *Small* 13, 1604259, doi:https://doi.org/10.1002/smll.201604259 (2017).

18 Chenna, S., Banerjee, R. & Crozier, P. A. Atomic-Scale Observation of the Ni Activation Process for Partial Oxidation of Methane Using In Situ Environmental TEM. *ChemCatChem* 3, 1051-1059, doi:https://doi.org/10.1002/cctc.201000238 (2011).

19 Resasco, J., Dai, S., Graham, G., Pan, X. & Christopher, P. Combining In-Situ Transmission Electron Microscopy and Infrared Spectroscopy for Understanding Dynamic and Atomic-Scale Features of Supported Metal Catalysts. *The Journal of Physical Chemistry C* 122, 25143-25157, doi:10.1021/acs.jpcc.8b03959 (2018).

20 Helveg, S. & Hansen, P. L. Atomic-scale studies of metallic nanocluster catalysts by in situ high-resolution transmission electron microscopy. *Catalysis Today* 111, 68-73, doi:https://doi.org/10.1016/j.cattod.2005.10.019 (2006).

21 Hui, F. *et al.* Understanding the structural evolution of Au/WO2.7 compounds in hydrogen atmosphere by atomic scale in situ environmental TEM. *Nano Research* 13, 3019-3024, doi:10.1007/s12274-020-2966-7 (2020).

22 Pérez Garza, H. H. *et al.* in *European Microscopy Congress 2016: Proceedings* 237-238.

23 Perez-Garza, H. H. *et al.* in *2016 Ieee 11th Annual International Conference on Nano/Micro Engineered and Molecular Systems International Conference on Nano-Micro Engineered and Molecular Systems NEMS* (Ieee, 2016).

24 Berthier, R., Nail, C., Carabasse, C., Molas, G. & Cooper, D. In Situ Biasing of Conductive Bridge Resistive Memory Devices Observed in a Transmission Electron Microscope. *Microsc. microanal.* 23, 1452-1453, doi:10.1017/S1431927617007929 (2017).

25 Pérez Garza, H. H. *et al.* in *European Microscopy Congress 2016: Proceedings* 237-238 (2016).

26 Product News. *Microscopy Today* 26, 48-50, doi:10.1017/S1551929518000949 (2018).

27 Mele, L. *et al.* A MEMS-based heating holder for the direct imaging of simultaneous in-situ heating and biasing experiments in scanning/transmission electron microscopes. *Microscopy Research and Technique* 79, 239-250, doi:https://doi.org/10.1002/jemt.22623 (2016).

28 Hauch, A. *et al.* Recent advances in solid oxide cell technology for electrolysis. *Science* 370, eaba6118, doi:10.1126/science.aba6118 (2020).

29 Wang, Q., Ricote, S. & Chen, M. Oxygen electrodes for protonic ceramic cells. *Electrochimica Acta* 446, 142101, doi:https://doi.org/10.1016/j.electacta.2023.142101 (2023).

30 Kiebach, R. *et al.* Stability of La0.6Sr0.4Co0.2Fe0.8O3/Ce0.9Gd0.1O2 cathodes during sintering and solid oxide fuel cell operation. *Journal of Power Sources* 283, 151-161, doi:https://doi.org/10.1016/j.jpowsour.2015.02.064 (2015).

31 Bishop, S. R. *et al.* Chemical Expansion: Implications for Electrochemical Energy Storage and Conversion Devices. *Annual Review of Materials Research* 44, 205-239, doi:10.1146/annurev-matsci-070813-113329 (2014).

32 Nishida, R. *et al.* High-performance electrodes for reversible solid oxide fuel cell/solid oxide electrolysis cell: Ni–Co dispersed ceria hydrogen electrodes. *RSC Advances* 4, 16260-16266, doi:10.1039/C3RA47089J (2014).

33 Xiao, J., Xie, Y., Liu, J. & Liu, M. Deactivation of nickel-based anode in solid oxide fuel cells operated on carbon-containing fuels. *Journal of Power Sources* 268, 508-516, doi:https://doi.org/10.1016/j.jpowsour.2014.06.082 (2014).

34 Tanasini, P. *et al.* Experimental and Theoretical Investigation of Degradation Mechanisms by Particle Coarsening in SOFC Electrodes. *Fuel Cells* 9, 740-752, doi:https://doi.org/10.1002/fuce.200800192 (2009).

35 Ding, D., Li, X., Lai, S. Y., Gerdes, K. & Liu, M. Enhancing SOFC cathode performance by surface modification through infiltration. *Energy & Environmental Science* 7, 552-575, doi:10.1039/C3EE42926A (2014).

36 Chatzichristodoulou, C. *et al.* Enhanced reducibility and electronic conductivity of Nb or W doped Ce0.9Gd0.1O1.95−δ. *Solid State Ionics* 269, 51-56, doi:https://doi.org/10.1016/j.ssi.2014.11.011 (2015).

37 Hansen, T. W., Wagner, J. B., Jinschek, J. R. & Dunin-Borkowski, R. E. The Titan Environmental Transmission Electron Microscope: Specifications, Considerations and First Results. *Microsc. microanal.* 15, 714-715, doi:10.1017/S1431927609097396 (2009).

38 Gaulandris, F. *In situ transmission electron microscopy on operative electrochemical cells* PhD thesis, Technical University of Denmark, (2017).

39 Zintler, A. *et al.* FIB based fabrication of an operative Pt/HfO2/TiN device for resistive switching inside a transmission electron microscope. *Ultramicroscopy* 181, 144-149, doi:10.1016/j.ultramic.2017.04.008 (2017).

40 Vijayan, S., Jinschek, J. R., Kujawa, S., Greiser, J. & Aindow, M. Focused Ion Beam Preparation of Specimens for Micro-Electro-Mechanical System-based Transmission Electron Microscopy Heating Experiments. *Microsc. microanal.* 23, 708-716, doi:10.1017/s1431927617000605 (2017).

41 Desbois, G. *et al.* Cryogenic vitrification and 3D serial sectioning using high resolution cryo-FIB SEM technology for brine-filled grain boundaries in halite: first results. *Geofluids* 8, 60-72, doi:https://doi.org/10.1111/j.1468-8123.2007.00205.x (2008).

42 Chappanda, K. N., Batra, N. M., Holguin-Lerma, J. A., Costa, P. M. F. J. & Younis, M. I. Fabrication and Characterization of MWCNT-Based Bridge Devices. *IEEE Transactions on Nanotechnology* 16, 1037-1046, doi:10.1109/TNANO.2017.2742149 (2017).

43 Liu, L.-j. & Wang, J.-j. in *2001 6th International Conference on Solid-State and Integrated Circuit Technology. Proceedings (Cat. No.01EX443).* 1087-1090 vol.1082.

44 Tao, T., Ro, J., Melngailis, J., Xue, Z. & Kaesz, H. D. Focused ion beam induced deposition of platinum. *Journal of Vacuum Science & Technology B: Microelectronics Processing and Phenomena* 8, 1826-1829, doi:10.1116/1.585167 (1990).

45 Langford, R. M., Wang, T. X. & Ozkaya, D. Reducing the resistivity of electron and ion beam assisted deposited Pt. *Microelectron. Eng.* 84, 784-788, doi:https://doi.org/10.1016/j.mee.2007.01.055 (2007).

46 Egerton, R. F., Li, P. & Malac, M. Radiation damage in the TEM and SEM. *Micron* 35, 399-409, doi:https://doi.org/10.1016/j.micron.2004.02.003 (2004).

47 Irvine, J. T. S., Slater, P. R. & Wright, P. A. Synthesis and electrical characterisation of the perovskite niobate-titanates, Sr1−x/2Ti1−xNbxO3−δ. *Ionics* 2, 213-216, doi:10.1007/BF02376024 (1996).

48 Kek, D., Mogensen, M. & Pejovnik, S. A Study of Metal (Ni, Pt, Au)/Yttria-Stabilized Zirconia Interface in Hydrogen Atmosphere at Elevated Temperature. *Journal of The Electrochemical Society* 148, A878, doi:10.1149/1.1383069 (2001).

49 Jeangros, Q. *et al.* Benefits of Nanoscale Operando Experiments in Environmental Transmission Electron Microscopy for Solid Oxide Fuel Cell Devices. *Microsc. microanal.* 28, 814-816, doi:10.1017/S1431927622003658 (2022).

50 Zarabi Golkhatmi, S., Asghar, M. I. & Lund, P. D. A review on solid oxide fuel cell durability: Latest progress, mechanisms, and study tools. *Renewable and Sustainable*

Energy Reviews 161, 112339, doi:https://doi.org/10.1016/j.rser.2022.112339 (2022).

51 Zhang, J., Ricote, S., Hendriksen, P. V. & Chen, Y. Advanced Materials for Thin-Film Solid Oxide Fuel Cells: Recent Progress and Challenges in Boosting the Device Performance at Low Temperatures. *Advanced Functional Materials* 32, 2111205, doi:https://doi.org/10.1002/adfm.202111205 (2022).

52 Vohs, J. M. & Gorte, R. J. High-Performance SOFC Cathodes Prepared by Infiltration. *Advanced Materials* 21, 943-956, doi:https://doi.org/10.1002/adma.200802428 (2009).

53 Darling, A. The elastic and plastic properties of the platinum metals. *Platinum Metals Review* 10, 14-19 (1966).

54 Manning, P. S., Sirman, J. D. & Kilner, J. A. Oxygen self-diffusion and surface exchange studies of oxide electrolytes having the fluorite structure. *Solid State Ionics* 93, 125-132, doi:https://doi.org/10.1016/S0167-2738(96)00514-0 (1996).

Supporting information

Experimental requirements for high temperature solid state electrochemical TEM experiments

Zhongtao Ma, Christodoulos Chatzichristodoulou, Waynah Lou Dacayan, Kristian Speranza Mølhave, Francesco Maria Chiabrera, Thomas Erik Lyck Smitshuysen, Christian Danvad Damsgaard, Søren Bredmose Simonsen

Z. Ma, C. Chatzichristodoulou, W. L. Dacayan, F. M. Chiabrera, S. B. Simonsen

DTU Energy, Fysikvej, Kgs. Lyngby, 2800, Denmark
E-mail: sobrs@dtu.dk

K.S.Mølhave, T. E. L. Smitshuysen, C. D. Damsgarrd
DTU Nanolab, Ørsteds Plads, Kgs. Lyngby, 2800, Denmark

Figure S1

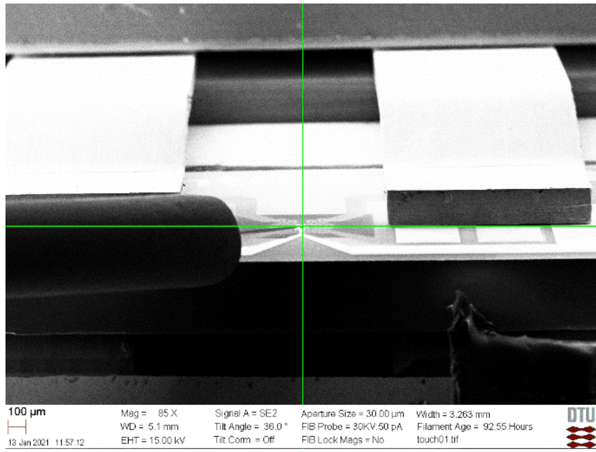

Figure S1: the image showing the needle is blocked by the chip edge

Figure S2

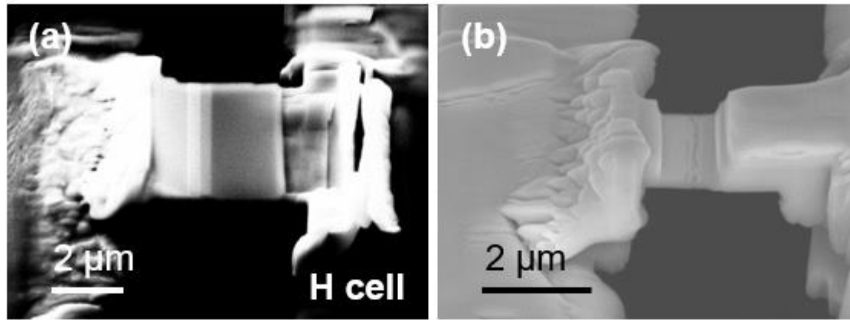

Figure S2: (a) the SEM image of Pt-CGO-YSZ-CGO-STN of H-cell after mounting process; (b) the H-cell is cracked due to the different milling rate of different layers of materials.

Chapter 5: Electrochemical Impedance Spectroscopy integrated with Environmental Transmission Electron Microscopy

(This Chapter has been published on Small Methods, paper shown in Appendix 1, license shown in Appendix 3)

*Zhongtao Ma †, Waynah Lou Dacayan †, Christodoulos Chatzichristodoulou, Kristian Speranza Mølhave, Francesco Maria Chiabrera, Wenjing Zhang, Søren Bredmose Simonsen**

Z. Ma, W. L. Dacayan, C. Chatzichristodoulou, F. M. Chiabrera, S. B. Simonsen

DTU Energy, Fysikvej, Kgs. Lyngby, 2800, Denmark
E-mail: sobrs@dtu.dk

K.S.Mølhave
DTU Nanolab, Ørsteds Plads, Kgs. Lyngby, 2800, Denmark

W. Zhang

DTU Environment, Bygningstorvet, Kgs. Lyngby, 2800, Denmark

Keywords: ETEM, operando, EIS, SOEC, SOFC, CGO

Abstract

The concept of combining electrical impedance spectroscopy (EIS) with environmental TEM (ETEM) is demonstrated by testing a specially designed micro gadolinia-doped ceria (CGO) sample in reactive gasses (O_2 and H_2/H_2O), at elevated temperatures (RT - 800 °C) and with applied electrical potentials. The EIS-TEM method provides structural and compositional information with direct correlation to the electrochemical performance. It is demonstrated that reliable EIS measurements can be achieved in the TEM for a sample with nano-scale dimensions. Specifically, the ionic and electronic conductivity, the surface exchange resistivity and the volume specific chemical capacitance are in good agreement with results from more standardized electrochemical tests on macroscopic samples. CGO is chosen as test material due to its relevance for solid oxide electrochemical reactions where its electrochemical performance depends on temperature and gas environment. As expected, the results show increased conductivity and lower surface exchange resistance in H_2/H_2O gas mixtures where the oxygen partial pressure is low

compared to experiments in pure O_2. The developed EIS-TEM platform is an important tool in promoting our understanding of nanoscale processes for green energy technologies, e.g. solid oxide electrolysis/fuel cells, batteries, thermoelectric devices etc.

1 Introduction

The efficiency of green energy technologies such as P2X (including electrolysis), fuel cells, and batteries directly depends on reaction rates in the involved electrochemical reactions. These again depend on the structure and composition of the component materials. [1] Comparison of electrochemical tests with post-mortem microscopy investigations shows that structural and compositional evolution at the nanoscale are the main reasons for efficiency losses. [2] To accelerate the implementation of particularly P2X and fuel cell technologies in the green energy infrastructure, a detailed understanding of the correlation between electrochemistry and structure/composition is needed so that efficient degradation mitigation strategies can be developed.

Post-mortem microscopy has led to important developments in all areas of energy technologies. However, results from post-mortem characterization only represent the end-result from the entire electrochemical process history, including the effects of various gas environments, polarizations, temperature ramps, as well as possible effects from sample preparation for microscopy. In order to directly link a given electrochemical stimuli (e.g. reactant composition, temperature, electrical polarization) with the structure/composition change of the material in its active state, we need to develop a new *operando* characterization method that provides real time electrochemical measurements with atomic level structure characterization under relevant conditions.

One group of methods with a potential to give insight into nano-structure/composition of materials in their active state is *in situ/operando* TEM. These methods allow for structure and composition investigations at high spatial resolution while exposing the sample to various selected stimuli, e.g. controlled atmospheres, [3] elevated temperature, [4] applied stress, [5] electrical polarization [6] or combinations of these.

On the other hand, an electrochemical method that can give information about the electrochemical response of the functional materials under operating conditions is electrochemical impedance spectroscopy (EIS). This has been widely used due to its nondestructive nature, high sensitivity, and ability to study and distinguish between surface/interface and bulk processes. [7]

Electrochemical TEM investigations are already carried out at room temperature in vacuum or in liquid phase, particularly with focus on battery materials. [8] Recently, attempts have been made to expand the electrochemical TEM capabilities to include *operando* experiments with focus on the solid oxide fuel and electrolysis cells (SOFC and SOEC) [9] requiring at least three stimuli: electrical potentials, reactive gases and elevated temperatures. Today, chip-based heating-biasing TEM holders are commercially available (e.g. Protochips Fusion, DENS solutions Lightning, Hummingbird Scientific MEMS Heating Biasing, Thermo Fisher Scientific NanoEX). The combination of such holders and an environmental TEM (ETEM) offers the possibility to study the three stimuli combined.

Preparing and conducting high temperature solid state electrochemical TEM with relevance to SOEC or SOFC is far from trivial. Here, a few of the challenges are listed: First, solid oxide electrochemical cells have complex layered structures composed of a mixture of metals and hard, brittle ceramics. These need to be thinned to electron transparency and mounted on the heating-biasing chips while ensuring mechanical stability and sufficient electrical contact to the biasing electrodes of the chip. Second, fracture of the sample or loss of electrical contract must be avoided, taking into consideration the thermal expansion of the sample and the chip components during heating. Most importantly, the currents in the chip heater must not interfere with the electrochemical measurements and should be well separated from the sample. The combination of relatively high resistivity, ρ, for the ceramic materials under investigation and the extraordinary small dimensions of a typical TEM sample leads to very high measured resistances often in the GΩ range. It is therefore crucial to minimize the unavoidable leak currents through the chip components.

Before high temperature solid state electrochemical TEM can exploit its full potential, it is crucial to establish that these challenges can be solved in a manner that reliable electrochemical measurements can be performed in the TEM. This we do in the present work. We present a combined EIS-TEM analysis of $Ce_{0.9}Gd_{0.1}O_{1.95-\delta}$ (CGO), which is a popular SOEC and SOFC electrolyte-electrode barrier layer material and is commonly used as a multi-functional component in the composite electrodes of the cell. [10] CGO is a good material for testing the reliability of EIS measurements because its various electrochemical properties (ionic conductivity, electronic conductivity, activity for surface-gas exchange reactions), which are dependent on temperature and the gas environment, can be measured with EIS and are well documented.

The results from this work show that the combined EIS and TEM (EIS-TEM) measurements agree with reference experiments with larger CGO samples. The EIS-TEM method also allows for establishing a direct link between the electrochemical activity and the nano-scaled structure and composition of the material. The method is not limited to investigations of SOECs/SOFCs, but can also be useful for linking functionality and structure/composition in studies of batteries, thermoelectric devices, catalysis, corrosion, etc.

This paper presents EIS-TEM measurements on a CGO sample with nanoscale dimensions. The temperature and pO_2 dependence of the ionic and electronic conductivity, as well as its surface exchange resistivity in O_2 and H_2/H_2O atmospheres, and its volume specific chemical capacitance in H_2/H_2O, are measured. The influence of Pt porosity is studied and finally the result are shown to be reproducible.

2 Results and Discussion

2.1 Structure of the CGO sample

Figure 1a shows an overview of the chip geometry while Figure 1b presents how the CGO sample was mounted on top of the chip. It can be observed from the latter that the sample consists of two thick side parts and a thinner central part with a thickness of ca. 100 nm (according to EELS log-ratio analysis [11]). The thick side parts (Figure 1b) are connected to the chip electrodes and the thin central part spans over the hole in the center of the chip shown in Figure 1a.

The corresponding SEM-EDS map in Figure 1c shows that most of the top surface area of the side parts is covered with ion-deposited Pt. On the other hand, there is no trace of Pt on top of the thinned central CGO part, as well as on a small portion of the top surfaces of the two thick side parts and on their side surfaces. Pt is also not expected on their entire bottom surface of the sample (not visible, but with access to gas phase due to the 10° tilt between the CGO sample and the chip).

The TEM image of the thinned central part in Figure 1e shows its dimensions and reveals a single grain boundary between two micrometer sized grains. The presence of a single grain boundary is consistent with the grain size of few micrometers observed in the CGO pellet (Figure 1d). Measurements on the HRTEM image (Figure 1f) of the region marked by a red square in Figure 1e are consistent with the crystal structure of $Ce_{0.9}Gd_{0.1}O_{1.95-\delta}$ with the space group Fm3m observed at zone axis $[0\bar{1}1]$. [12]

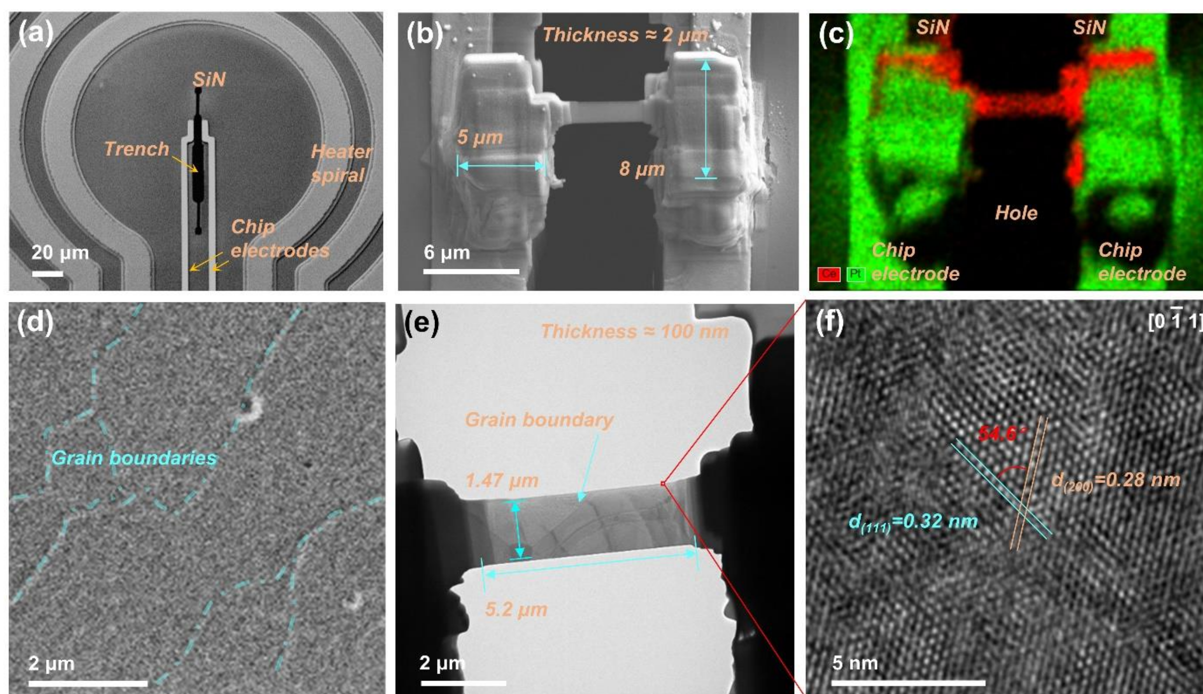

Figure 1: CGO sample mounted on a heating-biasing chip. (a) SEM image showing the center of an empty heating-biasing chip; (b) SEM image of the sample connected to the Pt electrodes of the chip; (c) SEM-EDS map of (b) recorded at 15 kV, red color representing the Ce Lα-peak, green the Pt Mα peak; (d) ion-beam image of the CGO pellet; (e) TEM image of center part of (b); (f) HRTEM image, including crystal analysis of the region in (e) indicated by a red square.

2.2 Morphology and Oxidation state

Figure 2 presents an image series of the grain boundary region at temperatures from 200 °C to 800 °C, in H_2/H_2O gas environment. As could be expected from previous studies, [13] no morphological changes were observed as a response to the elevated temperature (or as a response to electron beam exposure or EIS measurements). Specifically, the sample stayed fully dense (i.e. no pores developed), the interface between the sample and air (and between the two grains) stayed straight and smooth, and no new structures were formed such as nanoparticle generating on the surface. The changes in contrast in the images can be attributed to the displacement of the sample position along the direction of the electron beam caused by thermal expansion. The sample is also stable in the O_2 environment.

It is expected that the Ce oxidation state in the CGO will be Ce^{4+} in the oxygen environment, while the amount of Ce^{3+} increases in the reducing environments, especially at the CGO surface where reduction initiates. This was confirmed by EELS Ce M_5-to-M_4 white line ratio analysis, where spectra measured in O_2 and in H_2/H_2O with ratio 0.8 showed Ce^{4+} in the central part of the thin CGO, and an increased amount of Ce^{3+} ca. 10 nm near the CGO surface This is consistent with EELS analysis of pure ceria (See Supplementary information sect. 5). [14]

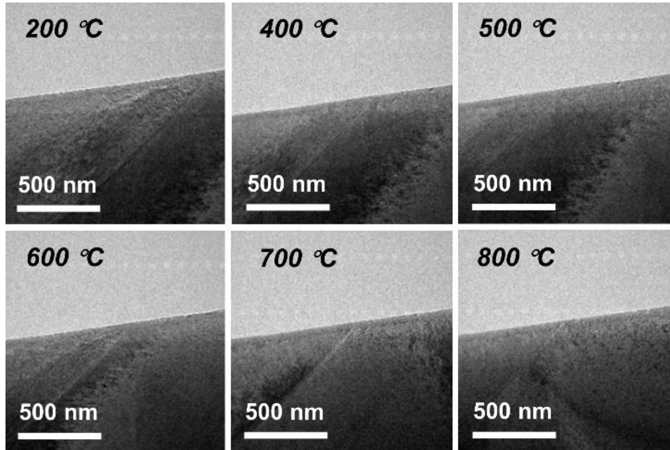

Figure 2: *In situ* TEM images of the CGO sample in H_2/H_2O with partial pressure ratio of 0.8 as a function of temperature.

2.3 EIS electrical circuit model

Figure 3 presents Nyquist plots of the EIS data recorded in the three gas environments at temperatures from 500 °C to 800 °C. All spectra can be separated into two arcs. The electrical circuit model (ECM) presented in Figure 3 is used to fit the two arcs. These include resistances, R_t and R_p and constant phase elements, CPE_{shunt}, CPE_{int} and CPE_{chem}. The topology of the ECM and each of its elements is described in the following.

The CPE_{shunt} corresponds to the shunt capacitance from the electrical circuit on the MEMS chip, the TEM holder wires, and the cables connecting to the potentiostat. This is connected in parallel to the entire sample and all its contributions. The value of the CPE_{shunt} deduced from the measurements carried out with a sample matches indeed the capacitance recorded for an empty chip at each temperature from 500 °C-800 °C, i.e., ca. $3.8 \cdot 10^{-11}$ F.

The high frequency arc starts at the origin of the real and imaginary axes at high frequencies and can be ascribed to ohmic transport through the central thin CGO part.

For a mixed conductor, such as CGO, the ohmic transport resistance, R_t is related to the movement of ions and electrons in the material, and therefore R_t has both an ionic and an electronic component as will be discussed in detail later. The transport resistance is denoted by R_t in the electrical circuit model (ECM). In principle, the ECM model should also include the bulk capacitance of the sample

in parallel with R_t. For the present sample dimensions, the expected bulk capacitance is approx. $7.5 \cdot 10^{-18}$ F m^{-1}, negligible in comparison to CPE_{shunt}, and therefore not included in the ECM.

The second arc can be associated to several possible contributions including transport barriers at grain boundaries, [15] gas diffusion and gas conversion contributions [16] or the surface exchange reaction. The grain boundary resistance [17] will be negligible for the present micrometer sized sample with large grains, having only a few grain boundaries (only one visible in the central part (Figure 1e)), and its expected capacitance (ca. 10^{-13} F, see Supplementary information sect. 6) [18] is smaller than the measured shunt capacitance (ca. 10^{-11} F). Considering the small sample dimensions and the extremely small currents incited in it (ca. 10^{-10} A), gas concentration impedances are also negligible. [16] The low frequency arc is therefore ascribed to the surface exchange reaction resistance, denoted by R_p. It is coupled to the gas-solid interface capacitance and the chemical capacitance of CGO, denoted by CPE_{int} and CPE_{chem}, respectively, in the ECM (Figure 3).

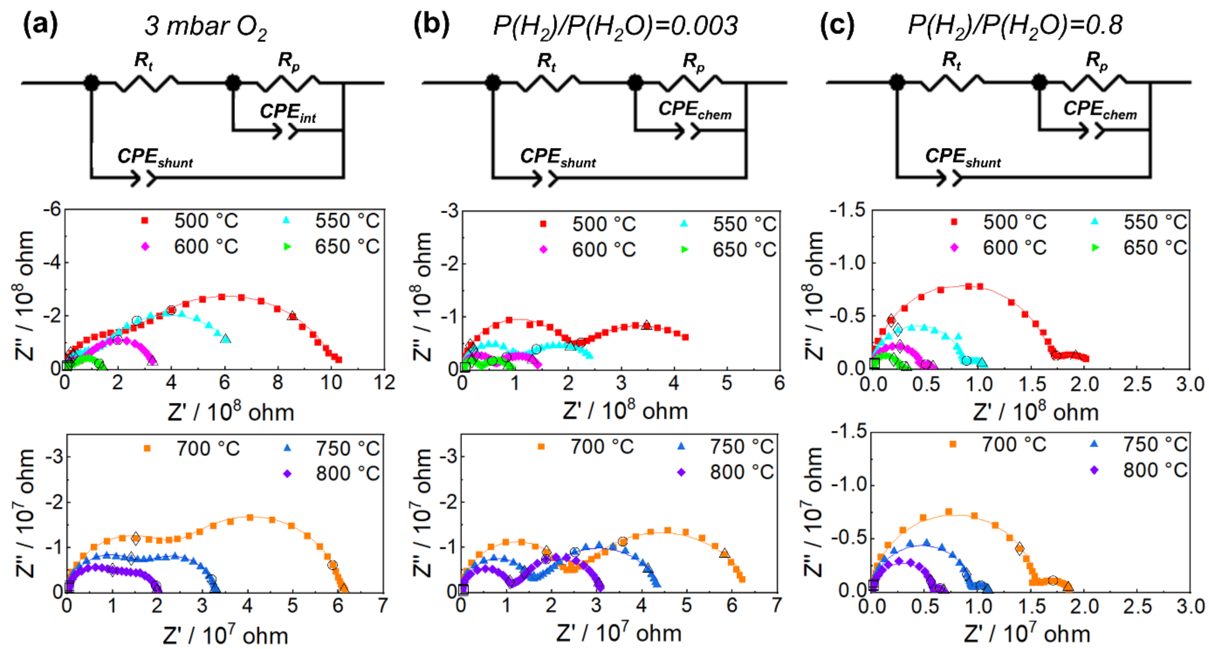

Figure 3: EIS spectra (symbols) and fittings (lines) recorded in (a) O_2 (3 mbar) and in a H_2/H_2O with partial pressure ratio of (b) 0.003 (total pressure 5 mbar) and (c) 0.8 (total pressure 3 mbar); 10 kHz (square), 100 Hz (diamond), 1 Hz (circle), 0.1 Hz (triangle) are noted on the spectra, with hollow symbols; ECM used for fitting the data are presented at the top for each gas composition.

The ECM in Figure 3a is used to fit all spectra recorded in O_2, with CPE_{chem} of CGO being negligible, due to the very small concentration of small polarons (as discussed in Supplementary section 5) and CPE_{int} being dominant. In H_2/H_2O, on the other hand, CPE_{chem} of CGO is expected to form a substantial contribution, which increases with increasing temperature and H_2-to-H_2O ratio to values substantially larger than CPE_{int}. [19]

From Figure 3, for all gas environments, it can be observed that the magnitude of both the first and second arc decreases as a function of temperature, indicating thermally activated processes as indeed expected for both the transport and surface reaction. This is also in line with a negligible gas concentration contribution that would be nearly temperature independent.

2.4 EIS data analysis

Both the conductivity and the surface exchange reaction of CGO depend on the gas environment. Figure 4 presents a schematic illustration of the differences for our CGO TEM sample in O_2 and H_2/H_2O. The overall chemical reaction formulae are different in the two cases. Also, in O_2, CGO is a pure ionic conductor which limits the active surface close to the region of the electron conducting Pt current collector. In the H_2/H_2O environment electrons are transported through the side parts of CGO thereby allowing the entire CGO surface to be active.

In this section we will therefore analyze the transport and surface exchange resistance from the EIS measurements in each type of gas environment separately, starting with the O_2 environment.

Using the following equation and the dimensions of the thinned central part of the sample, the total conductivity, σ_t, consisting of contributions from both ionic and electronic conductivity, can be calculated from R_t.

$$\sigma_t = \frac{1}{R_t}\frac{l}{w \cdot t}, \qquad (1)$$

where l, w and t are the length, width and thickness of the thin central part of the sample, respectively. Notice that only the thin central part is considered for calculating σ_t since it contributes to over 98% of the total transport resistance (see supplementary information, sect. 7). Figure 5a presents σ_t as function of temperature in O_2, and is compared with reference data from bulk polycrystalline CGO in air. [20] From the slope of the fitted line in Figure 5a, an activation energy of $E_a = 0.7$ eV was determined, which is consistent with literature values: In 3 mbar O_2 and 500-800 °C, CGO is primarily an ionic conductor, [17b, 21] and the determined E_a corresponds

to that for the ionic conductivity, σ_{ion}. The present EIS-TEM deduced σ_t values in O_2 agree closely with the reference data both with respect to E_a and to the absolute values for σ_t.

The resistance associated with the surface exchange reaction was also determined and compared to literature values. To quantify the area specific surface reaction resistance, we need to estimate the active CGO surface. For a pure ionic conductor, like CGO in 3 mbar O_2, the oxygen exchange is expected to take place in a localized reaction zone near the triple phase boundary (TPB) consisting of the ion conductor (CGO), the electron conductor (Pt) and the gas phase. For the present sample, the TPB will therefore be close to the Pt current collector as illustrated in Figure 4a (red dots). [12, 17a] As described in the experimental section, the Pt forms a nano-porous structure after the carbon removal pretreatment. Compared to a dense Pt, the nano-porous Pt will enhance the surface exchange reaction by an increased total TPB length. Perfect percolation through the nano-porous Pt cannot be expected and the surface exchange reaction will be prohibited where gas pores terminate before reaching the surface. This effect will be discussed later in this paper. The area specific surface reaction resistance, r_p, can therefore be calculated by using Equation 2.

$$r_p = R_p * S \, , \tag{2}$$

where S is the interface between CGO and the nanoporous Pt (around 92 μm^2). The result is presented as a function of temperature in Figure 5b in comparison with data from a dense CGO thin film model electrode tested in synthetic air. For the surface exchange reaction in O_2, E_a = 1.5 eV is deduced from the slope of Figure 5b for temperatures above 600 °C, a value that is close to the reference value of E_a = 1.7 eV for the CGO thin film electrode. [22] In the temperature range 500 - 600 °C, the slope clearly deviates from the straight line, possibly because the total resistance of the nano-scaled CGO sample approached the Giga-ohm regime where a current leak through the chip starts to influence the measurements.

We will now focus on the experiments carried out in the H_2/H_2O environment. The electronic conductivity, σ_{elec} in CGO, depends strongly on the oxygen partial pressure as described by Equation 3. [23]

$$\sigma_t = \sigma_{ion} + \sigma_{elec} = \sigma_{ion} + \sigma_{elec}^0 P_{O_2}^{-1/4} \, , \tag{3}$$

where σ^0_{elec} can be regarded as a constant for small deviations from oxygen stoichiometry. At low oxygen partial pressures CGO is therefore a mixed conductor with both oxygen vacancies and electrons as charge carriers.

Figure 5c presents σ_t as a function of oxygen partial pressure for the EIS-TEM measurements compared with reference data. The figure shows that σ_t increases with decreasing oxygen partial pressure, as expected according to Equation 3. Although the trend of σ_t is as expected, the absolute values deviate from the reference values. The σ_t measured at 700 °C and 750 °C matches well with the reference data at 600 °C and 700 °C, respectively. [23a] This could indicate an error in the measured temperature in the order of 50-100 °C which is higher than the 5% error on the temperature (corresponding to 35-38 °C for read out temperatures 700-750 °C) expected for these commercials MEMS chips. A possible explanation is a temperature gradient across the thin central part of the sample due to the relatively low thermal conductivity of CGO.

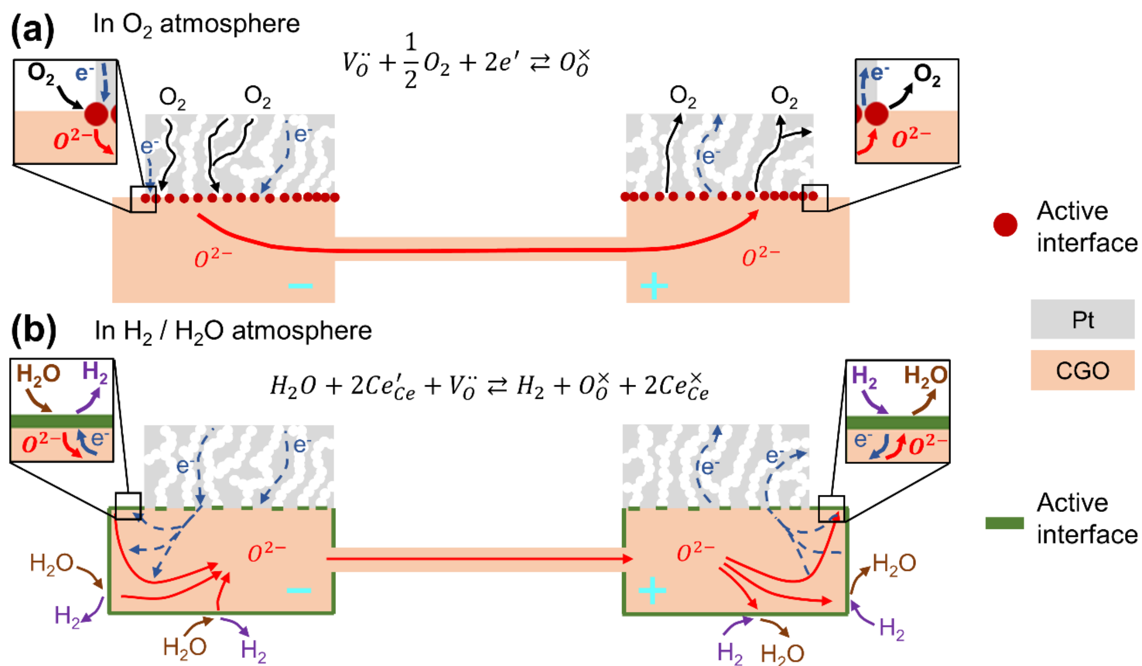

Figure 4: Illustration of active surface area for Pt-CGO as (a) pure ionic conductor and as (b) mixed electronic/ionic conductor. Arrows indicate direction of ions (red) and electrons (Navy). In the actual experiment, the flow direction alternates with the frequency of the imposed AC perturbation.

To assess this hypothesis, a temperature calibration experiment was conducted based on the melting point of Zn nanoparticles deposited on a similar CGO lamella. When ramping the temperature up in 3 mbar H_2 at a rate of 20 °C min^{-1}, the *in situ* TEM images showed Zn melting at a ca. 50 °C higher read out temperature in the center compared to the sides of the sample. (Figure S3). This confirms that the temperature off-set observed in Figure 5c is most likely due to a temperature gradient across the CGO lamella. Additional work, which is beyond the scope of the present work, is needed to accurately calibrate or calculate the absolute temperature in different positions of the TEM sample as function of nominal chip temperature.

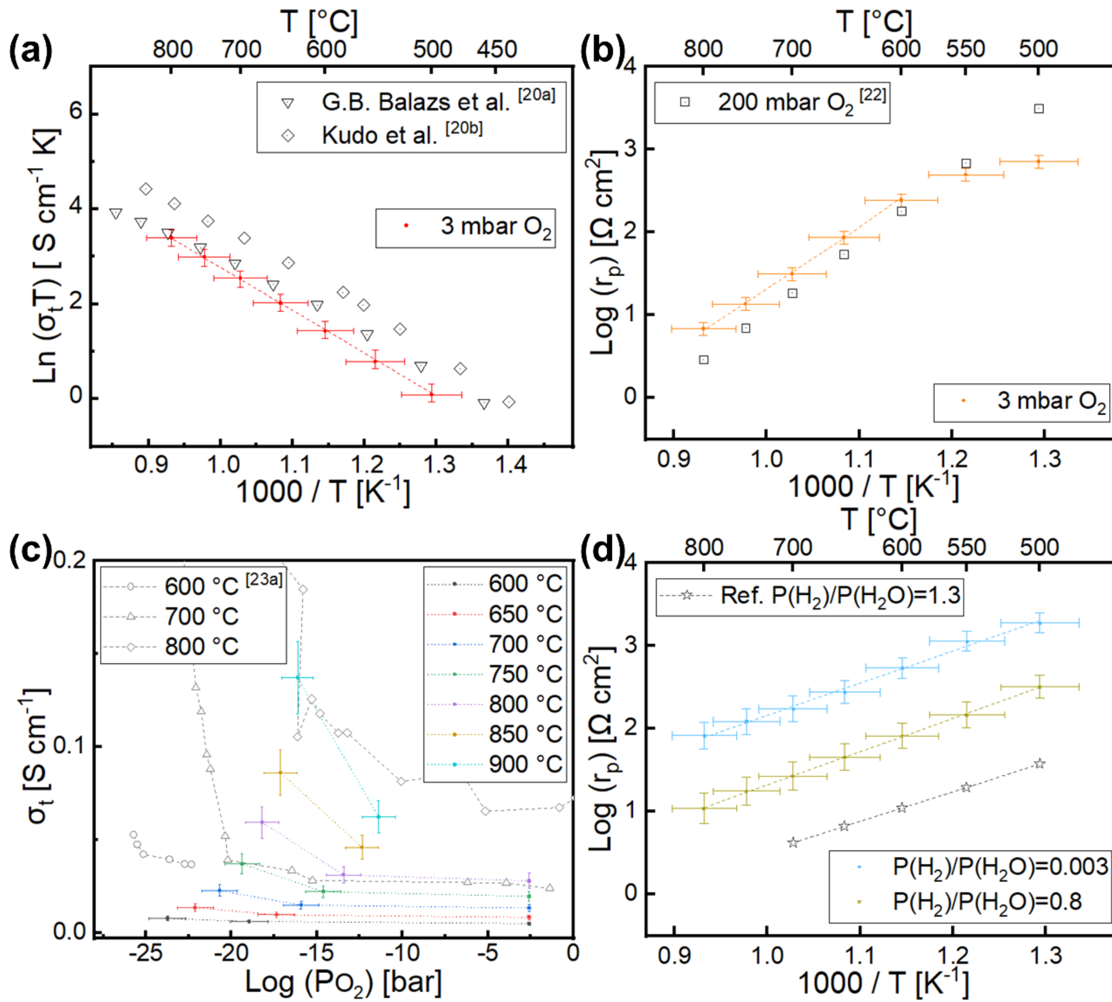

Figure 5: Electrochemical EIS-TEM measurements of CGO in different atmospheres. (a) Arrhenius plot of total conductivity in 3 mbar O_2 (red) and reference data for bulk polycrystalline CGO in air (black); [20] (b) Arrhenius plot of the surface reaction resistance in 3 mbar O_2 (orange), and reference data from a CGO thin film electrode in synthetic air (black); [22] (c) total conductivity

as a function of pO_2 (colored), and empty black symbols refer to reference data for polycrystalline CGO; [23a] (d) surface reaction resistance as function of temperature in H_2/H_2O atmospheres (blue, green), and reference data from a CGO thin film electrode in H_2/H_2O with partial pressure ratio of 1.3 (black). [24]

The thicker side parts of the sample are not expected to deviate substantially from the nominal chip temperature (around 5% of read out value), and therefore the surface reaction rates and associated capacitances determined by EIS are expected to reflect a fairly accurate temperature dependence.

For the mixed conducting CGO in H_2/H_2O environments, the surface exchange reaction takes place not only near the TPB, but on the entire CGO-gas interface, [17a] as illustrated in Figure 4b (green line). The total surface area (S) of both thick side parts of the CGO (261 μm^2) is therefore used in Equation 2 to calculate the area specific surface reaction resistance, r_p. The surface exchange resistance R_p determined from the second arc, however, is influenced by an electronic leak current through the thin central part of the MIEC CGO, i.e. not all the electrical current participates in the electrochemical reaction. This can be corrected using the following equation: [17a, 24]

$$R_p^{cor} = \frac{R_p R_{elec}}{R_{elec} - R_p} - R_{ion}, \quad (4)$$

where the ionic resistance, R_{ion}, represents the transport resistance recorded in O_2. The electronic resistance, R_{elec} is determined from, σ_{elec}, using the dimensions of the central part in Equation 1 and σ_{elec} is determined from σ_t and σ_{ion} via Equation 3. Finally r_p corrected for leak currents is calculated from R_p^{cor} using Equation 2. The effect of correcting for leak currents is shown in Figure S6.

Figure 5d shows the temperature dependence of the corrected r_p for CGO in H_2/H_2O with partial pressure ratio of 0.003 and 0.8. For both gas environments the measured E_a = 0.8 eV. This value is close to the reference value of 0.7 eV. [25] Also, the absolute values of r_p decrease with increasing H_2/H_2O ratio (Figure 5d), corresponding to a decreasing pO_2 and increasing electronic conductivity (Figure 5c). A number of studies suggest that the second electron transfer (likely coupled with the H-H association and desorption) is the rate-limiting step for the H_2 evolution reaction (HER) on ceria. [26] This will accelerate upon increasing the concentration of electronic charge carriers, resulting in reduced r_p upon increasing H_2/H_2O ratio as observed in the present experiment. A

decrease in r_p upon increasing H_2/H_2O ratio is also expected for the H_2 oxidation reaction (HOR). [27]

The volume-specific capacitance, which can be calculated from CPE_{chem} by using Brug et al.'s formula and geometry of the CGO sample is presented in Figure 6. [28] Considering the 2000 nm thick side parts, our results for 600 °C and 650 °C match well with the reference data of the film with similar thickness of 2241 nm. [19] Both of them follow the $P_{O_2}^{-1/4}$ dependence as expected, and this confirms that the capacitance is dominated by the chemical capacitance.

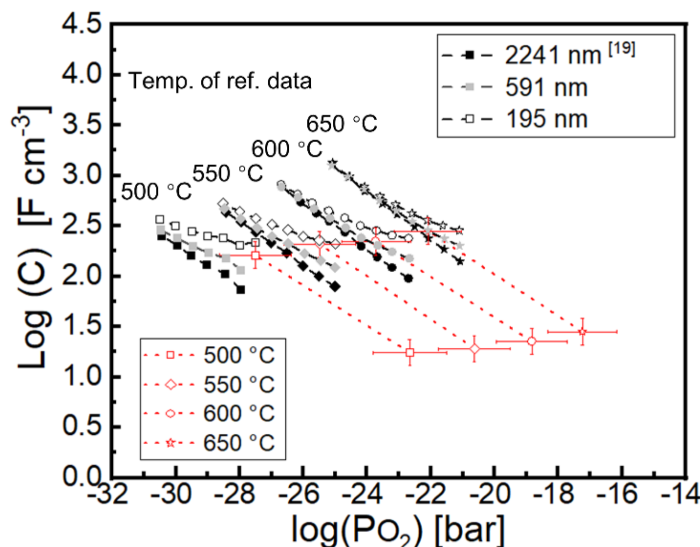

Figure 6: Volume-specific capacitance of the 2000 nm thick CGO side parts (red) as function of oxygen partial pressure and reference data from 2241 nm (black), 591 nm (grey) and 195 nm (black open symbols) CGO films at 500 °C, 550 °C, 600 °C, 650 °C, respectively. [19]

2.5 The effect of porous Pt

In order to explore the effect of the nano-porous Pt structure in the electrochemical measurements, the CGO sample was exposed to 900 °C in the reducing gas environment (An overview of all EIS-TEM processes for the sample is shown in the supplementary information, sect. 9). These conditions lead to Pt coarsening (Figure S2c), loss of percolating pore network for gas diffusion and thereby decreased TPB length. It can therefore be expected that the surface exchange resistance is increased, in particular for the reaction in oxygen where the surface reaction rate depends directly on the TPB. This effect was confirmed by comparison of EIS spectra recorded before and after coarsening (Figure 7a). The transport resistivity is rather similar (i.e. 35 Ω cm before and 39 Ω cm after) while the surface reaction resistance increased 74 times (to 492 Ω cm^2 from 7 Ω cm^2).

The effect of coarsening on the surface exchange reaction it is expected to be smaller in H_2/H_2O because here the entire CGO surface is active (as illustrated in Figure 4b). This is confirmed by the EIS spectra in Figure 7b. In H_2/H_2O with ratio of 0.8, the transport resistivity after coarsening

(19 Ω cm) is similar to the value measured before (17 Ω cm). The surface reaction resistance after coarsening (5 Ω cm^2) is only 2.5 times larger than before (2 Ω cm^2).

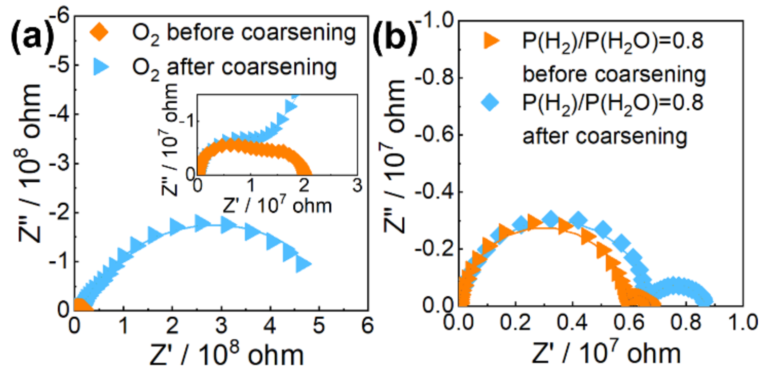

Figure 7: (a) EIS spectra recorded in 3 mbar O_2 at 800 °C before and after coarsening; (b) EIS spectra recorded in H_2/H_2O with partial pressure ratio of 0.8 at 800 °C before and after coarsening.

2.6 Reproducibility of test results

The analysis above shows that the Pt morphology determines the TPB and influences the surface exchange reaction resistance in O_2. For comparison, two additional CGO samples with a smaller Pt-CGO interface, and therefore shorter TPB, were produced and tested (Figure 8). In H_2/H_2O with gas pressure ratio 0.003, the area specific surface reaction resistance of the CGO sample 1 and 2 were compared and the absolute values agree well, deviating only by a factor of ca. 2 (Figure 8b). The transport resistivity deviates more, by a factor of ca. 5 (Figure 8c). This can be attributed to the different temperature distribution across the center part of the samples, as a consequence of the different sample geometries (Figure 1 and Figure 8a). The transport resistance is dominated by the thin central part which also happens to be the part influenced the most by the temperature gradient. CGO sample 3 is tested in both 3 mbar O_2 and H_2/H_2O with partial pressure ratio of 0.8. The activation energy and absolute values of the area specific surface reaction resistance match well with CGO sample 1 in both atmospheres (Figure 8d, e). The transport resistivity in H_2/H_2O with partial pressure ratio of 0.8 shows a relatively small deviation in the absolute value by a factor of 3 (Figure 8f). Again, this can be explained by the different temperature distributions across the two samples.

Overall, we observe good reproducibility with respect to both transport properties and surface exchange reaction resistances in O_2 and H_2/H_2O amongst the three samples (Figure 8), and any deviations can be rationalized by the somewhat different temperature distributions across the different samples. These results showcase the possibility to carry out *operando* EIS-TEM studies

on SOC samples and open up the path for the investigation of full cells to answer questions of great technological significance.

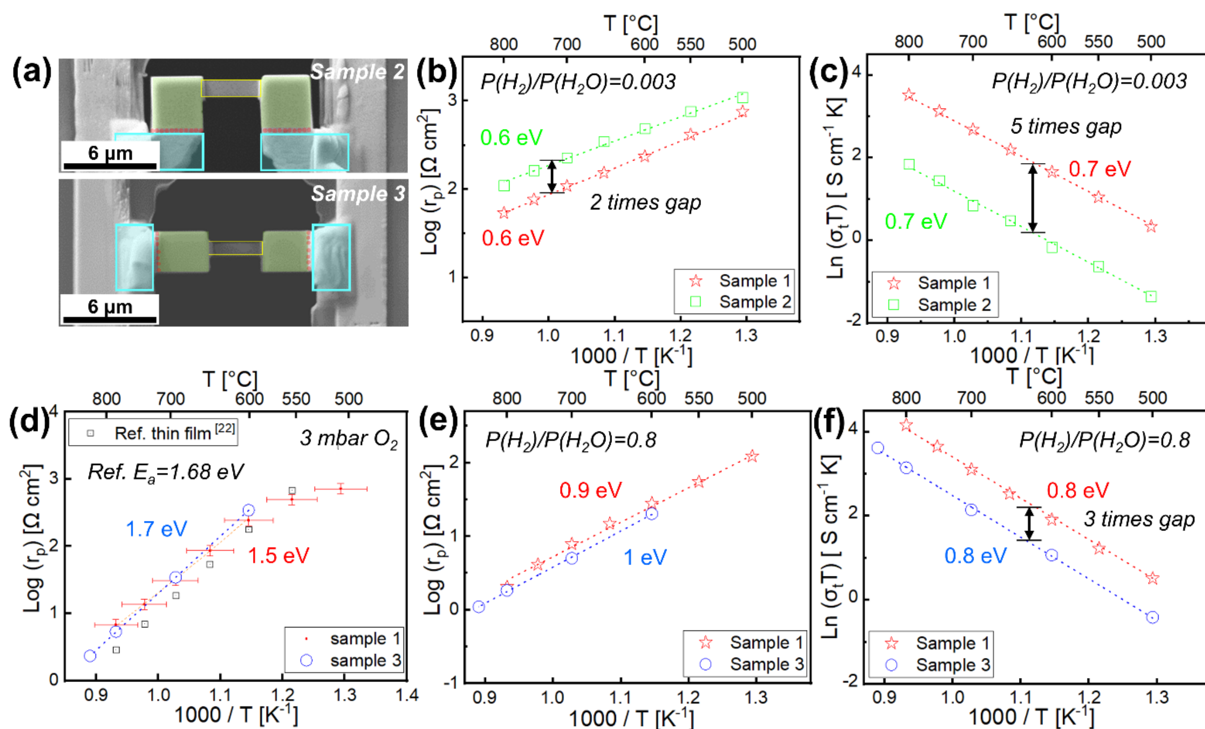

Figure 8: Comparison of electrochemical EIS-TEM measurements of CGO sample 2 and 3 in different atmospheres relative to CGO sample 1. (a) SEM images of sample 2 and 3; the thin central part, thick side parts, and deposited Pt are marked by yellow, green and cyan colors respectively. In H_2/H_2O atmospheres, the surface exchange reaction takes place at the surface of the side parts (green), while in oxygen atmosphere, the surface exchange reaction only take place at the Pt-CGO interface (red); (b) comparing the area specific surface reaction resistance of sample 1 and 2 in H_2/H_2O with gas partial pressure ratio of 0.003; (c) the total conductivity in H_2/H_2O with partial pressure ratio of 0.003 for sample 1 and 2; (d) the area specific surface reaction resistance of sample 1 and 3 in 3 mbar O_2, and reference data from a CGO thin film electrode in synthetic air (black); [22] (e) area specific surface reaction resistance in H_2/H_2O with partial pressure ratio of 0.8 for sample 1 and 3; (f) the total conductivity in H_2/H_2O with partial pressure ratio of 0.8 for sample 1 and 3.

3 Conclusion

The feasibility of operando EIS-TEM on solid state electrochemical cells operating in reactive gasses and elevated temperatures was demonstrated by measuring the temperature and pO2

dependence of the ionic and electronic conductivity of CGO, as well as its surface exchange resistivity in O_2 and H_2/H_2O atmospheres, and its volume specific chemical capacitance in H_2/H_2O.

A special sample structure was designed with thick side parts and a thin central part, by which one can separate the contributions of bulk charge transport and the surface reaction processes. The measured temperature and pO_2 dependent conductivity, surface exchange resistance, and chemical capacitance, as well as their activation energies and pO_2 exponents are found to agree well with reference data.

It can therefore be concluded that reliable EIS measurements can be performed in the TEM, even for the difficult case of hard, brittle ceramic materials which are thinned sufficiently for HRTEM analysis. The strength of *operando* EIS-TEM is that it allows us to simultaneously gain information on both the electrochemical behavior and the structure/composition of a material at the atomic level, in its active state.

With the purpose of determining the validity of the EIS measurements in the TEM, we have deliberately chosen operation conditions (temperatures, gas environments, polarizations) where the material was stable. The EIS-TEM method will be of particular importance in the investigation of dynamical changes of the structure and composition induced by the operating conditions. For such cases, the effect of the dynamical changes observed from the TEM can be directly compared to simultaneously recorded EIS spectra. Such a capability will be crucial for the further development in our understanding of the nanoscale processes such as degradation in a number of green energy technologies, e.g. electrolysis cells, fuel cells and batteries.

4 Experimental Methods

4.1 Sintered pellet preparation

Commercial ultra-high surface (UHS) area $Ce_{0.9}Gd_{0.1}O_{1.95-\delta}$ (CGO) powder was purchased from Solvay. The powder was compressed into pellets using a 10 mm diameter stainless steel mold at a uniaxial pressure of 3 MPa, followed by isostatic pressing at 325 MPa and sintering at 1500 °C in air for 12 h and slow cooling to room temperature at a rate of 0.5 K min^{-1}. The geometrical density of the pellets was between 94 and 97% of the theoretical density. [12]

4.2 TEM sample preparation

By using a focused Ga^+ ion beam (Crossbeam, ZEISS, 1540XB) and a micromanipulator (Kleindiek), TEM lamellas were prepared from the CGO pellet and were mounted on heating-

biasing chips (DENS lightning, with 4 contacts for heating, 2 contacts for biasing, and a through-hole window). To avoid any current leak along the surface of the chip due to Pt overspray, the two Pt electrodes of the chip were further separated by milling a long trench between them before mounting the TEM lamella (Figure 1 and S1). After the mounting process, the CGO lamellas have a 10° angle relative to the chip surface. Pt was ion-deposited to ensure electrical contact between the CGO lamella and the Pt electrodes at the chip. A final preparation step was thinning and polishing the central part of the lamella to allow for TEM analysis and to remove any Pt overspray from ion-deposition. [29] A result of such sample preparation is presented in Figure 1.

4.3 EIS-TEM experiments

The EIS-TEM experiments were carried out in an ETEM (Titan 80–300 kV) equipped with a differential pumping system and an image aberration corrector (FEI Europe, Netherlands). [30] The ETEM can host gases like O_2, H_2 and H_2O with partial pressures from 10^{-6} mbar to 26 mbar. With the use of needle valves and mass flow controllers, mixing of two or more of these gases can be achieved and the partial pressures can be controlled. For our experiments, low oxygen partial pressures were achieved by mixing H_2 and H_2O vapor. The experiments were carried out in three different gas environments: (a) 3 mbar O_2, (b) a H_2/H_2O mixture with partial pressure ratio of 0.003 (total pressure 5 mbar) and (c) a H_2/H_2O with partial pressure ratio of 0.8 (total pressure 3 mbar).

The electrochemical workstation (Gamry FAS2 Femtostat) used for two-probe EIS measurements was connected to the Pt electrodes of the chip via the TEM holder (DENS Lightning). EIS was performed by applying an alternating voltage amplitude of 20 mV in a frequency range from 100 kHz to 0.03 Hz.

Before EIS-TEM measurements, the samples were heated to 500 °C in the ETEM at 3 mbar O_2 for 5 min. This is to remove the amorphous carbon and its potential effects which is mixed with the Pt nanoparticles in the ion-deposited Pt. [29, 31] EELS analysis showed that the carbon edge was fully removed after this treatment, confirming that the treatment was sufficient to remove the carbon. After this, the Pt forms a nano-porous network with voids in the regions that previously contained carbon (Figure S2a-b).

EIS-TEM analysis were carried out while the temperature was held constant at 500-900 °C, in steps of 50 °C, after waiting for 3 min for the system to stabilize at each temperature. The total time spent on image acquisition and impedance measurement at each temperature was ca. 12 min.

For all *operando* TEM experiments, it is important to minimize possible effects of the electron beam. Therefore, a relatively low beam current density of 23 e $Å^{-2}s^{-1}$ or lower was used for TEM imaging, except for HRTEM which was recorded only once at RT. The beam was also blanked during temperature ramping and EIS analysis. No changes in the sample morphology or in the Ce oxidation state were observed as a result of beam exposure according to imaging and EELS analysis.

4.4 Error analysis

Errors on reported calculated data can come from the measurement of sample dimensions, gas pressure and temperature, and EIS recording and fitting. All these errors are considered and presented as error bars in the graphs. The details of the error analysis are presented in the supplementary information.

Acknowledgements

S.B.S planned and initiated the project. Z.M. and W.L.D contributed to development of the EIS-TEM experimental procedures. Z.M. prepared the TEM samples and conducted the *operando* EIS-TEM experiments and corresponding data analysis. Z.M., W.L.D, F.M.C., W.Z., S.B.S, C.C and K.S.M all contributed to the discussions for development of experimental method and of interpretation of the results. Z.M. and W.L.D prepared the figures. Z.M., W.L.D, S.B.S, C.C, K.S.M. F.M.C., and W.Z. wrote the manuscript and all the authors contributed to the discussion and revision of the manuscript.

This project has received funding from the European Research Council (ERC) under the European Union's Horizon 2020 research and innovation programme (grant agreement No 850850).

Received: ((will be filled in by the editorial staff))
Revised: ((will be filled in by the editorial staff))
Published online: ((will be filled in by the editorial staff))

References

[1] A. Hauch, R. Küngas, P. Blennow, A. B. Hansen, J. B. Hansen, B. V. Mathiesen, M. B. Mogensen, *Science* 2020, 370, eaba6118.

[2] a)L. Holzer, B. Iwanschitz, T. Hocker, B. Münch, M. Prestat, D. Wiedenmann, U. Vogt, P. Holtappels, J. Sfeir, A. Mai, T. Graule, *Journal of Power Sources* 2011, 196, 1279; b)S.-K. Jung, H. Gwon, J. Hong, K.-Y. Park, D.-H. Seo, H. Kim, J. Hyun, W. Yang, K. Kang, *Advanced Energy Materials* 2014, 4, 1300787; c)B.-K. Park, Q. Zhang, P. W. Voorhees, S. A. Barnett, *Energy & Environmental Science* 2019, 12, 3053.

[3] a)R. T. K. Baker, C. Thomas, R. B. Thomas, *Journal of Catalysis* 1975, 38, 510; b)R. T. K. Baker, R. B. Thomas, M. Wells, *Carbon* 1975, 13, 141; c) P. A. Crozier, A. K. Datye, in *Studies in Surface Science and Catalysis*, Vol. 130 (Eds: A. Corma, F. V. Melo, S. Mendioroz, J. L. G. Fierro), Elsevier, Granada, Spain 2000, Pages 3119-3124; d)P. L. Hansen, J. B. Wagner, S. Helveg, J. R. Rostrup-Nielsen, B. S. Clausen, H. Topsoe, *Science* 2002, 295, 2053; e)S. Helveg, C. López-Cartes, J. Sehested, P. L. Hansen, B. S. Clausen, J. R. Rostrup-Nielsen, F. Abild-Pedersen, J. K. Nørskov, *Nature* 2004, 427, 426; f)S. B. Simonsen, I. Chorkendorff, S. Dahl, M. Skoglundh, J. Sehested, S. Helveg, *Journal of the American Chemical Society* 2010, 132, 7968; g)P. A. Crozier, S. Chenna, *Ultramicroscopy* 2011, 111, 177; h)S. Chenna, P. A. Crozier, *ACS Catalysis* 2012, 2, 2395; i)J. R. Jinschek, *Chemical Communications* 2014, 50, 2696; j)S. B. Simonsen, Y. Wang, J. O. Jensen, W. Zhang, *Nanotechnology* 2017, 28, 475710.

[4] a)R. Sinclair, M. A. Parker, *Nature* 1986, 322, 531; b)K. Holloway, R. Sinclair, *Journal of the Less Common Metals* 1988, 140, 139; c)T. Kamino, H. Saka, *Microsc. Microanal. Microstruct.* 1993, 4, 127.

[5] a)M. Legros, *Comptes Rendus Physique* 2014, 15, 224; b)Y. Deng, R. Zhang, T. C. Pekin, C. Gammer, J. Ciston, P. Ercius, C. Ophus, K. Bustillo, C. Song, S. Zhao, H. Guo, Y. Zhao, H. Dong, Z. Chen, A. M. Minor, *Advanced Materials* 2020, 32, 1906105.

[6] a)R. J. Kamaladasa, A. A. Sharma, Y.-T. Lai, W. Chen, P. A. Salvador, J. A. Bain, M. Skowronski, Y. N. Picard, *Microsc. microanal.* 2015, 21, 140; b)B. Haas, J.-L. Rouvière, V. Boureau, R. Berthier, D. Cooper, *Ultramicroscopy* 2019, 198, 58.

[7] M. J. Jørgensen, M. Mogensen, *Journal of The Electrochemical Society* 2001, 148, A433.

[8] a)S. Basak, K. Dzieciol, Y. E. Durmus, H. Tempel, H. Kungl, C. George, J. Mayer, R.-A. Eichel, *Chemical Physics Reviews* 2022, 3, 031303; b)M. J. Williamson, R. M. Tromp, P. M. Vereecken, R. Hull, F. M. Ross, *Nature Materials* 2003, 2, 532; c)X. H. Liu, J. Y. Huang, *Energy & Environmental Science* 2011, 4, 3844.

[9] a)A. H. Tavabi, S. Arai, S. Muto, T. Tanji, R. E. Dunin-Borkowski, *Microsc. microanal.* 2014, 20, 1817; b)F. Gualandris, S. B. Simonsen, J. B. Wagner, S. Sanna, S. Muto, L. T. Kuhn, *ECS Transactions* 2017, 75, 123.

[10] a)S. H. Jo, P. Muralidharan, D. K. Kim, *Solid State Ionics* 2008, 178, 1990; b)T. Klemensø, J. Nielsen, P. Blennow, Å. H. Persson, T. Stegk, B. H. Christensen, S. Sønderby, *Journal of Power Sources* 2011, 196, 9459; c)J. Nielsen, T. Klemensø, P. Blennow, *Journal of Power Sources* 2012, 219, 305; d) E. M. Sala, N. Mazzanti, M. B. Mogensen, C. Chatzichristodoulou, *Solid State Ionics* 2022, 375, 115833.

[11] T. Malis, S. C. Cheng, R. F. Egerton, *Journal of Electron Microscopy Technique* 1988, 8, 193.

[12] C. Chatzichristodoulou, S. Ricote, S. P. V. Foghmoes, J. Glasscock, A. Kaiser, P. V. Hendriksen, *Solid State Ionics* 2015, 269, 51.

[13] a)V. Esposito, D. W. Ni, Z. He, W. Zhang, A. S. Prasad, J. A. Glasscock, C. Chatzichristodoulou, S. Ramousse, A. Kaiser, *Acta Mater.* 2013, 61, 6290; b)J. Chen, M. Ouyang, P. Boldrin, A. Atkinson, N. P. Brandon, *ACS Applied Materials & Interfaces* 2020, 12, 47564.

[14] a)B. Goris, S. Turner, S. Bals, G. Van Tendeloo, *ACS Nano* 2014, 8, 10878; b)S.-G. Frederik, *Master thesis: Improving durability of solid oxide cells by redox re-activation,* DTU Energy, DTU, Kgs. Lyngby, Feb, 2020; c)R. Sinclair, S. C. Lee, Y. Shi, W. C. Chueh, *Ultramicroscopy* 2017, 176, 200.

[15] a)X. Guo, R. Waser, *Progress in Materials Science* 2006, 51, 151; b)Y. Lin, S. Fang, D. Su, K. S. Brinkman, F. Chen, *Nature Communications* 2015, 6, 6824.

[16] P. Marmet, L. Holzer, J. G. Grolig, H. Bausinger, A. Mai, J. M. Brader, T. Hocker, *Physical Chemistry Chemical Physics* 2021, 23, 23042.

[17] a)W. Lai, S. M. Haile, *Journal of the American Ceramic Society* 2005, 88, 2979; b)X. Guo, W. Sigle, J. Maier, *Journal of the American Ceramic Society* 2003, 86, 77.

[18] D. Pérez-Coll, E. Céspedes, A. J. Dos santos-García, G. C. Mather, C. Prieto, *Journal of Materials Chemistry A* 2014, 2, 7410.

[19] W. C. Chueh, S. M. Haile, *Physical Chemistry Chemical Physics* 2009, 11, 8144.

[20] a)G. B. Balazs, R. S. Glass, *Solid State Ionics* 1995, 76, 155; b)T. Kudo, H. Obayashi, *Journal of The Electrochemical Society* 1975, 122, 142.

[21] C. Chatzichristodoulou, P. V. Hendriksen, *Physical Chemistry Chemical Physics* 2011, 13, 21558.

[22] N. Mazzanti, *in submission* 2022.

[23] a)S. Wang, T. Kobayashi, M. Dokiya, T. Hashimoto, *Journal of The Electrochemical Society* 2000, 147, 3606; b)M. Mogensen, N. M. Sammes, G. A. Tompsett, *Solid State Ionics* 2000, 129, 63.

[24] J. Jamnik, J. Maier, *Journal of The Electrochemical Society* 1999, 146, 4183.

[25] N. Mazzanti, *Ph.D thesis: Ceria-based thin film electrodes for sustainable hydrogen production,* DTU Energy, DTU, Kgs. Lyngby, Aug. 2021.

[26] a)Z. A. Feng, F. El Gabaly, X. Ye, Z.-X. Shen, W. C. Chueh, *Nature Communications* 2014, 5, 4374; b)T. Wu, Q. Deng, H. A. Hansen, T. Vegge, *The Journal of Physical Chemistry C* 2019, 123, 5507.

[27] Y. Choi, S. K. Cha, H. Ha, S. Lee, H. K. Seo, J. Y. Lee, H. Y. Kim, S. O. Kim, W. Jung, *Nature Nanotechnology* 2019, 14, 245.

[28] G. J. Brug, A. L. G. van den Eeden, M. Sluyters-Rehbach, J. H. Sluyters, *Journal of Electroanalytical Chemistry and Interfacial Electrochemistry* 1984, 176, 275.

[29] Y.-W. Lan, W.-H. Chang, Y.-C. Chang, C.-S. Chang, C.-D. Chen, *Nanotechnology* 2015, 26, 055705.

[30] T. W. Hansen, J. B. Wagner, J. R. Jinschek, R. E. Dunin-Borkowski, *Microsc. microanal.* 2009, 15, 714.

[31] L.-j. Liu, J.-j. Wang, presented at *2001 6th Int. Conf. on Solid-State and Integr. Circuit Technol. Proc. (Cat. No.01EX443)*, Shanghai, China, 22-25 Oct. 2001.

Supporting Information

Electrochemical Impedance Spectroscopy integrated with Environmental Transmission Electron Microscopy

*Zhongtao Ma †, Waynah Lou Dacayan †, Christodoulos Chatzichristodoulou, Kristian Speranza Mølhave, Francesco Maria Chiabrera, Wenjing Zhang, Søren Bredmose Simonsen**

Z. Ma, W. L. Dacayan, C. Chatzichristodoulou, F. M. Chiabrera, S. B. Simonsen

DTU Energy, Fysikvej, Kgs. Lyngby, 2800, Denmark

E-mail: sobrs@dtu.dk

K.S.Mølhave

DTU Nanolab, Ørsteds Plads, Kgs. Lyngby, 2800, Denmark

W. Zhang

DTU Environment, Bygningstorvet Building, Kgs. Lyngby, 2800, Denmark

1. Chip overview and the trench to minimize leak current

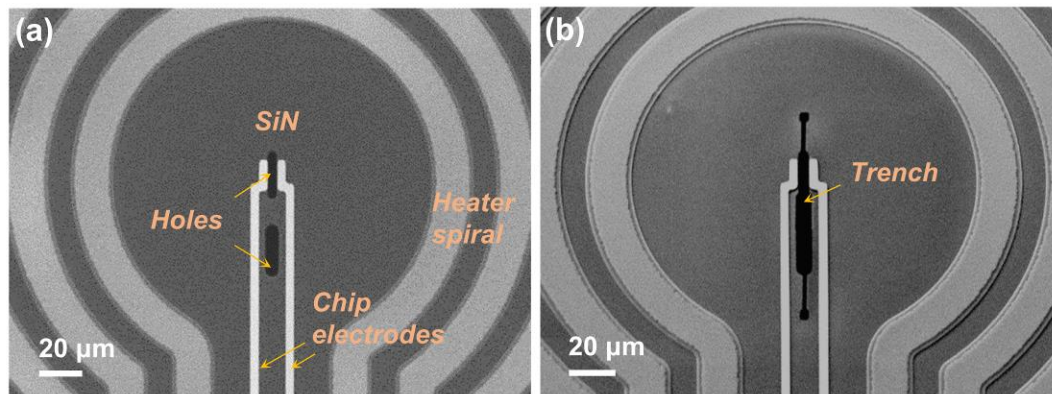

Figure S1: Images of empty chips before (a) and after (b) milling the extra trench to avoid current leaks.

2. Nanoporous structure of Pt current collector

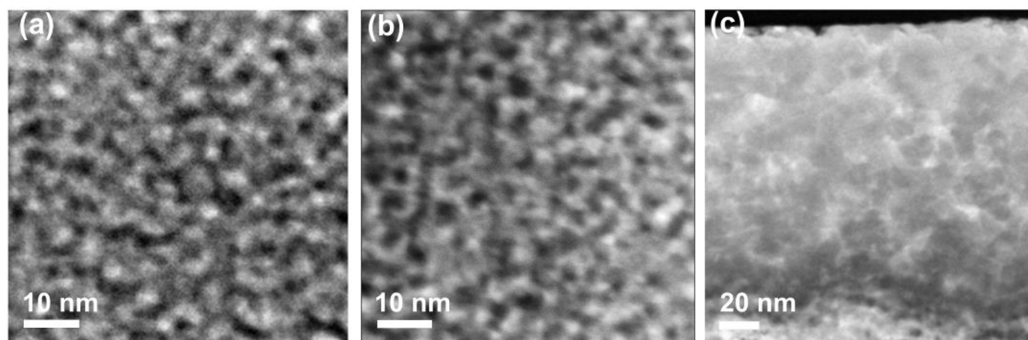

Figure S2: STEM-HAADF images of the ion-beam deposited Pt structure before (a) and after (b) removing the carbon at 500 °C. (c) STEM-HAADF image of ion-beam deposited Pt after treatment at 900 °C in H_2/H_2O with partial pressure ratio of 0.8.

3. Error analysis

Error bars for all quantitative values presented in graphs in the main article are calculated as propagated errors using the standard formula: [1]

$$\delta q = \sqrt{(\frac{\partial q}{\partial x}\delta x)^2 + \cdots + (\frac{\partial q}{\partial z}\delta z)^2}\,, \qquad \text{(S1)}$$

where q is any function of several variables x, …, z, and δq the propagated error.

3.1. Error estimates for TEM sample dimension

Sample dimensions visible in the TEM images were measured 10 times and the error is conservatively estimated as the difference between the maximum and the minimum. The error of the thin CGO region thickness was determined from the EELS log-ratio analysis [2] and we assume an error of 5 %. Absolute values are presented in Table S1.

3.2. Error estimates for gas pressures

For the measurements of gas pressures, the error comes from instrumental limitation. We used two gauges separately for the pressure above 1 mbar (Barocel Rressure Transducer, BOC EDWARDS) and below 1 mbar (Wide Range Gauge, BOC EDWARDS). Each gauge has a measurement uncertainty which was used for the error calculations. Values are presented in Table S1.

3.3. Error estimates for temperature measurements

For the error of temperature, measurement uncertainty of 5% according to specification from DENS solutions was used for error bars.

In addition to this we observed experimentally a temperature gradient across the TEM specimen in the following experiment: Zn nanoparticles were dispersed in ethanol, drop casted and dried in air on chip with a CGO sample with similar dimensions to the one presented in the main article. When ramping the temperature up in 3 mbar H_2 at a rate of 20 °C min^{-1}, the in situ TEM images showed that melting of Zn particles at the sides at a temperature of ca. 480 °C, and progressing to the center of the CGO lamella where the Zn particles are melting at ca 535 °C. From this we estimate that there is a temperature difference of ca. 50 °C between the center of the lamella and the side part of the CGO sample at the read out temperature of ca. 500 °C (Figure S3 and Video. S1). In the main article, the influence from the temperature gradient on the quantitative measurements is discussed.

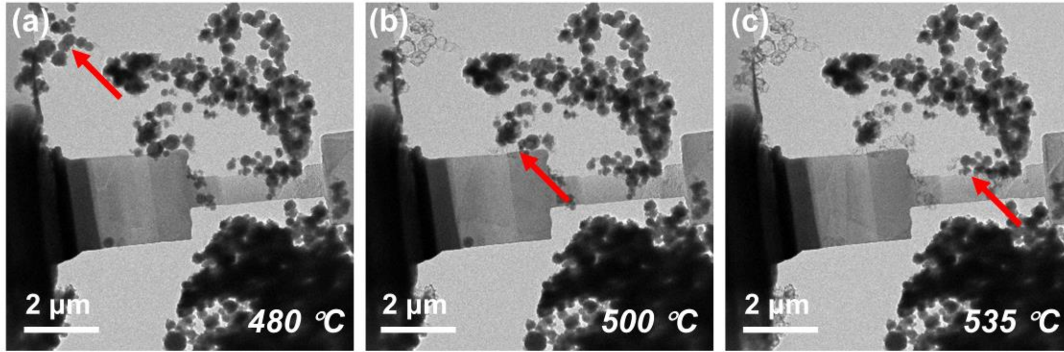

Figure S3: (a) the Zn nanoparticles on the chip's SiN_x top layer start to melt at the read out temperature of 480 °C; (b) the Zn nanoparticles on the side parts of CGO start to melt at the read out temperature of 500 °C; (c) the Zn nanoparticles on the center part of CGO start to melt at the read out temperature of 535 °C.

3.4. Error estimates for electrochemical measurements

Two EIS spectra were recorded at same condition, i.e. at 400°C in H_2/H_2O with gas partial pressure ratio of 0.003. The difference was 1 % and 12 % for the measurement of R_t and R_p respectively. 12 % is used as a conservative error estimate for both R_t and R_p for all experimental conditions.

Table S1. The actual values of errors for each variables

Variables	Errors
Central part length	0.05 μm
Central part width	0.05 μm
Central part thickness	5 nm
Side parts length	0.5 μm
Side parts width	1 μm
Side parts thickness	0.5 μm
Barocel Rressure Transducer	0.5 mbar
Wide Range Gauge	δP = 0.5 * P
Temperature	5%
Rt	12 %
Rp	12 %
CPE-Q	2 %
CPE-n	6 %

4. The method to acquire the ion-beam image presented in Figure 1d

The grains and grain boundaries are milled in a different rate when scanned under 200 pA ion beam. Ion beam imaging was used to make the grain boundaries visible on pellet. From the image one can roughly estimate the grain size.

5. Analysis of the Ce oxidation state

The Ce oxidation state can be analyzed via the Ce M5-to-M4 white line ratio analysis of EELS spectra. [3] Here, white line ratios are determined as described (considering the ratio of area of the Ce M5 and M4 peaks) in reference. [4] EELS spectra were recorded at two different positions of the central thin part of a CGO sample, a) ca. 10 nm from the edge and b) in the center.

5.1. EELS analysis at the edge of the central thin CGO part

EELS spectra were recorded in 3 mbar O_2 or H_2/H_2O with partial pressure ratio of 0.8. The Ce M_5-to-M_4 white line ratio analysis presented in Figure S4 shows that in 3 mbar O_2 the white line ratio is approx. 0.75, corresponding to Ce^{4+}. In H_2/H_2O with gas partial pressure ratio of 0.8, the ratio is approx. 0.9, indicating an increased content of Ce^{3+}.

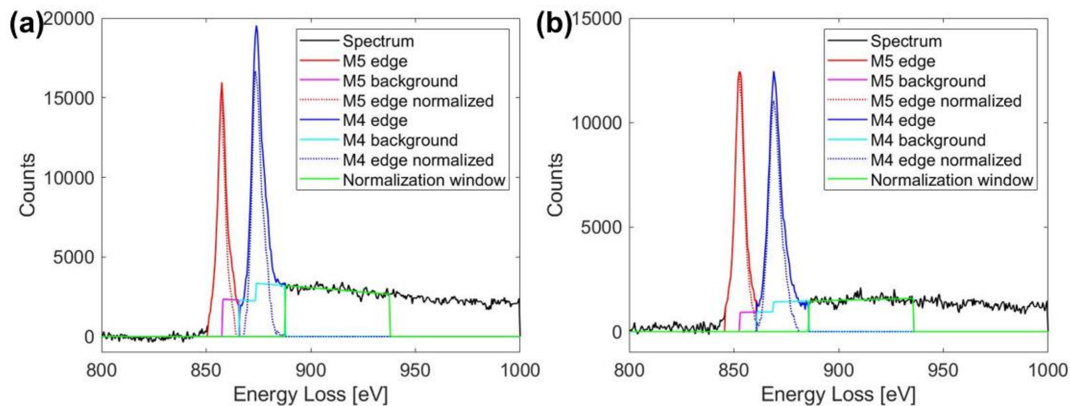

Figure S4: Analysis of Ce M_5-to-M_4 white line ratio of EELS spectra recorded at 600 °C in (a) 3 mbar O_2 and (b) 3 mbar H_2/H_2O with gas partial pressure ratio of 0.8.

5.2. EELS analysis at the center of the central thin CGO part

Figure S5 presents EELS spectra recorded in vacuum, and 3 mbar O_2 or H_2/H_2O with gas partial pressure ratios of 0.003 or 0.8 at different temperatures. The presented spectra show similar intensities of the Ce M_5 and M_4 white lines for all conditions. From Figure S5d it can be seen that the ratio is constant around 0.74, corresponding to Ce^{4+}.

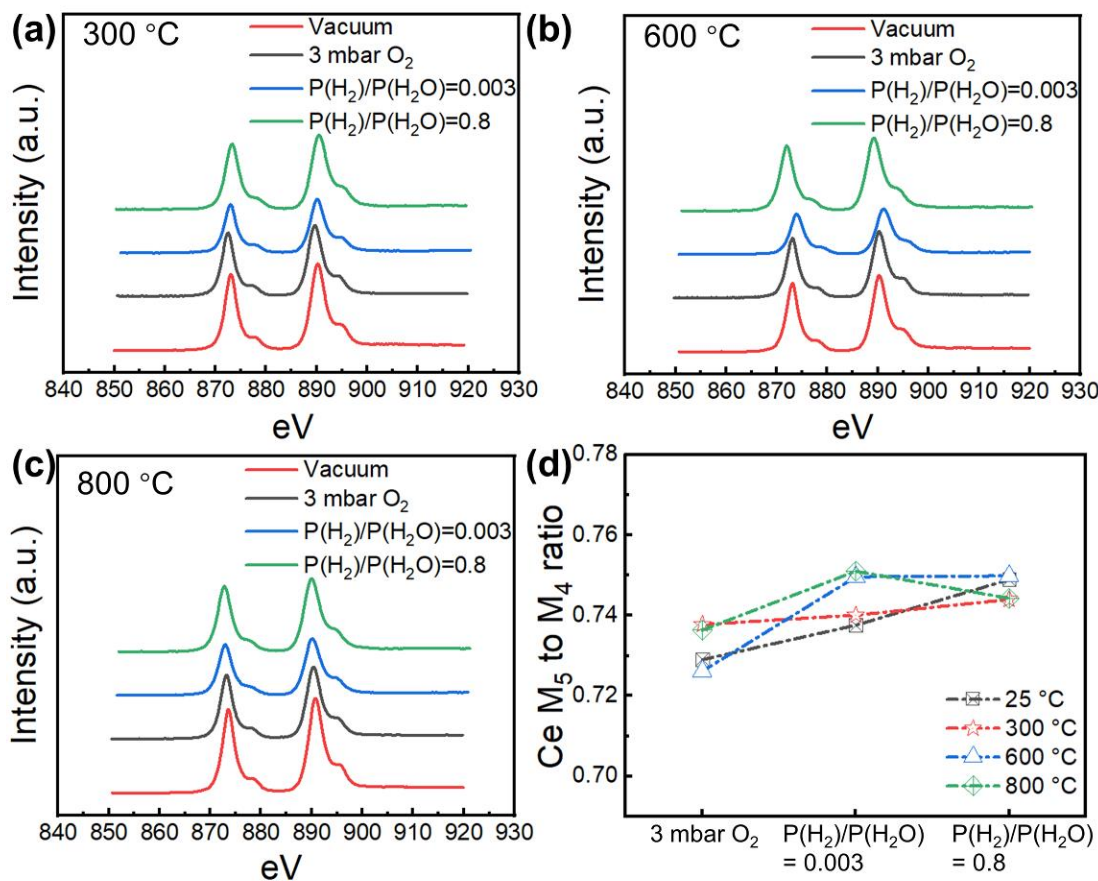

Figure S5: (a-c) EELS spectra at 300 °C, 600 °C and 800 °C in different atmospheres; (d) Ce $M_{4,5}$ white line ratio in 3 mbar O_2, H_2/H_2O with gas pressure ratio 0.003, and H_2/H_2O with gas partial pressure ratio of 0.8 atmospheres at different temperatures.

In conclusion, the EELS measurements at the center do not show an increased amount of Ce^{3+} in reducing environment, despite that a small increase is expected.

To evaluate if it is reasonable that the Ce^{3+} amount is not large enough to be measured by the EELS analysis everywhere in the thin CGO the following was considered:

5.2.1. 100 nm thin CGO

By using the measured electronic conductivity σ_e, one can calculate the concentration of Ce^{3+} atoms in a volume of 1 cm^3, $c_{Ce^{3+}}$ by using the following Equation S2: [5]

$$\sigma_e = e c_{Ce^{3+}} \mu_{eon} \quad \text{(S2)}$$

where e is the elementary charge of an electron, and μ_{eon} is the mobility of the electrons. For the latter we use values from the literature. [6] The ratio of Ce^{3+} to the total number of Ce atoms, $c_{Ce^{3+}}/c_{Ce}$ is calculated from $c_{Ce^{3+}}$ and the theoretical number of Ce atoms in the volume of 1 cm^3. The calculated values are shown in Tables S2 and S3. The tables show that the concentration of Ce^{3+} in the thin CGO is < 0.5 % even at 800 °C in the most reducing environment. This can explain why Ce^{3+} is not observed in the EELS analysis of the bulk part of the 100 nm thin CGO, but only at the edge where the concentration is expected to be higher.

Table S2. the $c_{Ce^{3+}}$ and $c_{Ce^{3+}}/c_{Ce}$ as function of temperature in 5 mbar of H_2/H_2O with partial pressure ratio of 0.003 by using mobility value from literature

Temp./°C	Mobility (μeon) / cm^2 V^{-1} s^{-1}	$c_{Ce^{3+}}$ / Atoms cm^{-3}	$c_{Ce^{3+}}/c_{Ce}$
500	0.001315433	2.1638E+18	9.59947E-05
550	0.001587667	3.55419E+18	0.000157668
600	0.001875396	4.53475E+18	0.000201159
650	0.002175652	4.65873E+18	0.000206657
700	0.00248575	5.00945E+18	0.000222211
750	0.002803294	6.47228E+18	0.000287081
800	0.003126181	7.42942E+18	0.000329521

Table S3. the $c_{Ce^{3+}}$ and $c_{Ce^{3+}}/c_{Ce}$ as function of temperature in 3 mbar of H_2/H_2O with partial pressure ratio of 0.8 by using mobility value from literature

Temp./°C	Mobility (μeon) / cm^2 V^{-1} s^{-1}	$c_{Ce^{3+}}$ / Atoms cm^{-3}	$c_{Ce^{3+}}/c_{Ce}$
500	0.001315433	4.16822E+18	0.000184902

550	0.001587667	6.86413E+18	0.000304456
600	0.001875396	1.14836E+19	0.000509247
650	0.002175652	1.80051E+19	0.000798218
700	0.00248575	2.87828E+19	0.001275415
750	0.002803294	4.72159E+19	0.002090507
800	0.003126181	7.48517E+19	0.003310044

5.2.2. Thick side parts of CGO

For comparison the Ce^{3+} concentration was also estimated for the thick side parts of the CGO TEM sample. By considering the chemical capacitance, one can calculate the $c_{Ce^{3+}}$ by using the following equation: [7]

$$C_{chem} = \frac{e^2}{k_B T}\left(\frac{1}{c_{Ce^{3+}}} + \frac{1}{2c_{dop}}\right)^{-1}, \quad \text{(S3)}$$

where e is elementary charge, k_B is Boltzmann constant, and c_{dop} is concentration of Gd in CGO. The concentration of $c_{Ce^{3+}}$ and $c_{Ce^{3+}}/c_{Ce}$ in the sample when exposed to H_2/H_2O with partial pressure ratio of 0.003 or 0.8, are given in Tables S4 and S5, respectively. The Ce^{3+} concentration is significantly higher in the thick side parts of the CGO compared to the thin central part.

Table S4. $c_{Ce^{3+}}$ and $c_{Ce^{3+}}/(c_{Ce^{3+}} + c_{Ce^{4+}})$ as function of temperature in 5 mbar of H_2/H_2O with partial pressure ratio of 0.003

Temp./°C	$c_{Ce^{3+}}$ / Atoms cm^{-3}	$c_{Ce^{3+}}/c_{Ce}$
500	7.26808E+18	0.000322368
550	8.46651E+18	0.000375503
600	1.06153E+19	0.000470759
650	1.4021E+19	0.000621702
700	1.74457E+19	0.000773437
750	2.29968E+19	0.001019289
800	2.97753E+19	0.001319332

Table S5. $c_{Ce^{3+}}$ and $c_{Ce^{3+}}/c_{Ce}$ as function of temperature in 3 mbar of H_2/H_2O with partial pressure ratio of 0.8

Temp./°C	$C_{Ce^{3+}}$ / Atoms cm^{-3}	$c_{Ce^{3+}}/c_{Ce}$
500	6.85868E+19	0.003033843
550	9.41849E+19	0.004161427
600	1.06094E+20	0.004685142
650	1.44304E+20	0.006361792
700	2.12059E+20	0.009320976
750	3.22634E+20	0.014112669
800	5.2089E+20	0.0225889

In both atmospheres, the concentration of small polarons, Ce^{3+}, is much smaller than $2c_{dop} = 5E + 21$, and therefore the first factor in equation S3 dominates. Since the concentration of Ce^{3+} is proportional to $P_{O_2}^{-1/4}$ for CGO within the range of O_2 partial pressures investigated here [7], the first term in equation S3 dominates also in 3 mbar O_2 and we can write:

$$C_{chem} = \frac{e^2}{k_B T}(\frac{1}{c_{Ce^{3+}}} + \frac{1}{2c_{dop}})^{-1} = \frac{e^2}{k_B T}(\frac{1}{c_{Ce^{3+}}})^{-1} = \frac{e^2 c_{Ce^{3+}}}{k_B T} \sim P_{O_2}^{-1/4} , \quad \text{(S4)}$$

The chemical capacitance therefore decreases by 1 order of magnitude for every 4 orders of magnitude of increase in O_2 partial pressure, and its value at 3 mbar O_2 will be approx. 10^{-13} F for the ~10^{-10} cm^3 volume of the sample used here. This value is two orders of magnitude smaller than the shunt capacitance of the system, and this contribution can therefore be neglected for the measurements carried out at 3 mbar O_2.

6. Grain boundary capacitance of the central thin CGO

We use the equations

$$C_B = \varepsilon_0 \varepsilon_r \frac{A}{L} , \quad \text{(S4)}$$

$$C_{gb} = \varepsilon_0 \varepsilon_r \frac{A}{L} \frac{d_g}{\delta_{gb}} , \quad \text{(S5)}$$

where C_B and C_{gb} are capacitances of bulk and grain boundary, respectively; ε_0 and ε_r are the permittivity of free space (8.85E-12 F m^{-1}) and the dielectric constant of CGO (ε_r = ca. 30), [8]

respectively; d_g and δ_{gb} are the average values of grain size and grain-boundary thickness, respectively; L is the length and A is the cross-sectional area of the thin central part of the sample. If d_g is 5.4 μm, and if we use the length of unit cell as a minimum for δ_{gb}, the grain boundary capacitance will be 7.5E-13 F, and the actual capacitance should be smaller than this.

7. Contribution to the resistance from the thin central part of the sample

The contribution to the total resistance from the thin central part of the sample, R_1 can be calculated from:

$$\frac{R_1}{R_1+R_2}, \qquad \text{(S6)}$$

where, R_2 is the resistance of the thick side parts. The resistance, R is related to the resistivity, ρ and sample dimension via:

$$R = \frac{\rho * l}{wt} \qquad \text{(S7)}$$

where l, w and t are length, width and thickness respectively.

For the central part:

$$R_1 = \frac{\rho * 5.2\ \mu m}{1.47\ \mu m * 0.1\ \mu m} \qquad \text{(S8)}$$

For the side parts:

$$R_2 = \frac{\rho * 5\ \mu m}{8\ \mu m * 2\ \mu m} * 2 \qquad \text{(S9)}$$

Substituting equations S8 and S9 in S6, it can be deduced that the central part contributes with more than 98 % of the total resistance. This value is even likely underestimated due to i) the presence of Pt on the top of the side part surface and ii) the slightly higher temperature on the side parts compared to the central part due to temperature gradients across the sample according to Figure S3.

8. Correction of electronic current leak

As Figure S6a shows, in H_2/H_2O with gas partial pressure ratio of 0.003 or 0.8, the activation energies are 0.60 eV and 0.93 eV, respectively. The EIS-TEM measurements are compared to a CGO thin film electrode in H_2/H_2O with gas partial pressure ratio of 1.3, [9] which has the activation energy of 0.71 eV. When the thin central part of ceria is partially reduced, an electronic leak current is expected through it, which results in an underestimation of the polarization resistance. This is corrected in Figure S6b.

After correction, the E_a are 0.77 eV and 0.79 eV in H_2/H_2O with partial pressure ratio of 0.003 and 0.8, respectively. Both values are close to the reference value of 0.71 eV.

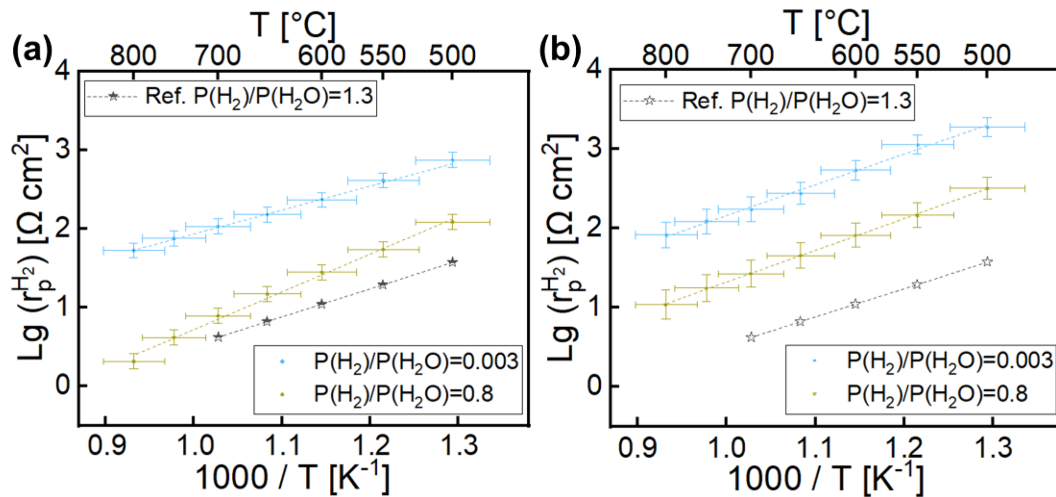

Figure S6: surface reaction resistance as function of temperature in reducing atmospheres (a) Before and (b) after removing the current leak.

9. Overview of the EIS-TEM experimental processes in different environments

The EIS-TEM experiment was conducted with the same CGO sample in the following sets of conditions in the specified order.

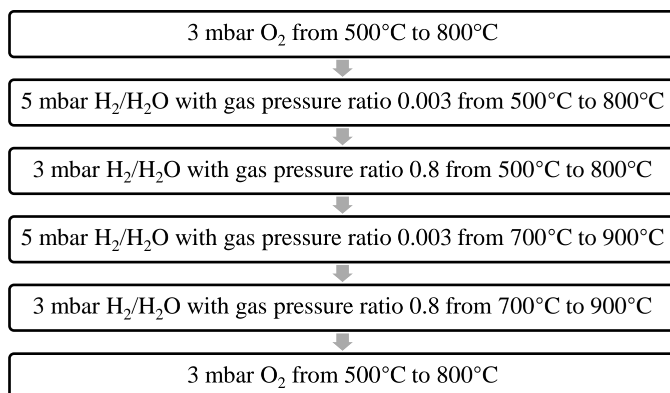

References

[1] J. R. Taylor, *Error Analysis: the Study of Uncertainties in Physical Measurements (2nd edn)*, University Science Books, Sausalito 1997.
[2] T. Malis, S. C. Cheng, R. F. Egerton, *Journal of Electron Microscopy Technique* 1988, 8, 193.
[3] R. F. Egerton, *Electron energy-loss spectroscopy in the electron microscope*, Springer Science & Business Media, 2011.
[4] D. H. Pearson, C. C. Ahn, B. Fultz, *Physical Review B* 1993, 47, 8471.
[5] S. Wang, T. Kobayashi, M. Dokiya, T. Hashimoto, *Journal of The Electrochemical Society* 2000, 147, 3606.
[6] B. C. H. Steele, *Solid State Ionics* 2000, 129, 95.
[7] W. C. Chueh, S. M. Haile, *Physical Chemistry Chemical Physics* 2009, 11, 8144.
[8] D. Pérez-Coll, E. Céspedes, A. J. Dos santos-García, G. C. Mather, C. Prieto, *Journal of Materials Chemistry A* 2014, 2, 7410.
[9] N. Mazzanti, *Ph.D thesis: Ceria-based thin film electrodes for sustainable hydrogen production,* DTU Energy, DTU, Kgs. Lyngby, Aug. 2021.

Chapter 6: High Temperature Electrochemical ETEM study on solid oxide cells

Zhongtao Ma, Christodoulos Chatzichristodoulou, Kristian Speranza Mølhave, Francesco Maria Chiabrera, Simone Sanna, Fabrizio Gaulandris, Søren Bredmose Simonsen

Abstract

We investigated the application of the high temperature EIS-TEM method and high temperature biasing TEM experiment. Through a special lift-out and mounting technique using FIB, a so-called Z cell geometry has been successfully prepared for CGO-YSZ-CGO cell and LSC-YSZ-LSC cell. For the first one, we applied EIS-TEM measurement, and our EIS test results are consistent with the literatures, which considered the transport performance of YSZ/CGO and surface exchange properties of CGO. This demonstrated the feasibility of high temperature EIS measurement of the Z cell geometry inside the ETEM. Next, we applied high temperature biasing-TEM on the LSC-YSZ-LSC cell. STEM-HAADF/ADF image followed the nano feature formation on the LSC layer under cathodic biasing in oxygen at different biasing voltage. STEM-EELS proved the existence of Co^{+2} under negative biasing at 700 °C. STEM-EDS line scan shows the big particles containing only Co as cation will form. After analyzing the HRTEM image, the phase can be phase on the LSC layers under negative biasing can decompose into Co_3O_4, La_2CoO_4, and other possible phases such as La_2O_3 and SrO. This demonstrates the feasibility of high temperature biasing experiments on the SOC model cell. In all, this paper proved the feasibility of high temperature electrochemical experiments.

1 Introduction

The rising energy demand and ever-increasing carbon emissions from fossil fuels prompt people to explore the application and research of sustainable energy technologies [1]. Among these technologies, SOFC/SOEC devices show great potential due to their high energy conversion efficiency, scalability, cleanliness, and quiet operation properties [2-4]. SOFC operates at high temperatures and can output electricity or thermal energy by using pure hydrogen or hydrocarbon fuels. On the other hand, SOEC can perform energy conversion in the opposite way to produce fuels. Considering these advantages, SOFC/SOEC will play a significant role in applications such as peak regulation for wind/solar power and ensuring a constant power supply.

However, the cost of SOC systems is still high, with a median system cost of around $2,450/kWnet in 2020 [2]. Additionally, the relatively high degradation rate of 1% per 1000 hours necessitates the gradual improvement of SOC systems through more rational design. There are several issues related to SOC that need to be addressed. For instance, in the case of perovskite LSCF or LSC cathode materials, their surface structure can change due to Sr element segregation on the surface, thereby affecting surface reaction kinetics during the ORR process [5]. The segregated Sr can further react with YSZ electrolyte, forming insulating $SrZrO_3$ [6], which affects the durability of SOC. In the case of the commonly applied anode material Ni-YSZ, one of the major concerns is the phenomenon of "Ostwald ripening," which leads to Ni coarsening [7]. This effect can reduce the triple-phase boundaries (TPBs) and electrical conductivity, contributing to Ni migration and depletion [4,8,9]. Moreover, poisoning caused by Cr [10], S [11], and Cl [12] can also occur on the materials used in SOC systems.

To understand the root causes of these problems and improve the performance of the cells, new characterization methods need to be applied. Advanced in situ techniques have been reported for probing and investigating the reaction properties on SOC electrodes [13,14]. For instance, the PLD model cell has been developed to study surface reaction properties [15]. In this model cell, a thin film working electrode with a defined geometry is exposed to the gas environment. This structure provides a good platform for in situ characterization tools such as in situ Raman [16] and in situ X-ray analysis [13,17,18]. Recently, in situ ETEM has been employed on SOC electrodes, facilitated by special holders and creative sample designs. For example, the formation/growth of phases/pores in Ni-YSZ microstructures during oxidation/reduction processes was observed in an oxygen environment up to 1000 °C [19]. Sr depletion and agglomeration on YSZ-LSC interfaces have been revealed [20].

Taking inspiration from previous remarkable achievements, we attempted to combine three types of stimuli in the ETEM: reactive gases, elevated temperatures, and electrical potentials. This approach allows us to simulate the practical working conditions of SOC under actual operation. To achieve this setup, we employed a heating and biasing MEMS chip inside the ETEM [21]. By combining the powerful capabilities of TEM with high-resolution structural characterization, we can directly observe important features that reflect reactions, such as pores, interface quality, nanoparticle generation, and structural displacement. Additionally, by an SEM-FIB system, we can prepare samples with defined dimensions and specifications that meet the requirements for

TEM observation. Furthermore, the ETEM is equipped with EELS and EDS, which enable us to analyze chemical properties such as changes in element valence and element distribution/migration.

In a previous work conducted by our group, we demonstrated the feasibility of operating EIS-TEM, which combines the capabilities of electrochemical impedance spectroscopy (EIS) and ETEM [22]. EIS, with its non-destructive nature, enables us to detect and understand the transport/reaction mechanisms of the electrochemical system by applying input/response electrical signals and fitting them with appropriate electric circuit models (ECMs). EIS-ETEM is particularly suitable and important for research on SOFC/SOEC systems operated at high temperatures and in various atmospheres.

In this paper, a miniaturized symmetric cell, Pt-CGO-YSZ-CGO-STN, is fabricated to study the individual contributions of CGO electrodes. An appropriate ECM is provided for fitting EIS data. The surface reaction mechanism and transport properties derived from EIS spectra are consistent with data from the literature. We demonstrate the feasibility of fabricating cell samples, which we refer to as "Z cell," using FIB-SEM, and conducting electrochemical tests inside the ETEM. Another symmetric Pt-LSC-YSZ-LSC-STN Z cell is fabricated to conduct an experiment where structural changes are induced in the LSC by an applied electrical potential. The structure and elemental composition of the LSC layer under cathodic biasing are revealed using HRTEM, STEM-EDS, and STEM-EELS. The Z cell geometry and high-temperature electrochemical TEM not only hold promise for making significant contributions to in situ ETEM research on SOC, ion batteries, and special materials or structures in terms of structural characterization and physical property measurement but also provide valuable information for device miniaturization, such as micro SOFCs (μ-SOFCs).

2 Experimental

2.1 PLD deposition and characterization

For the pulsed laser deposition (PLD) of the CGO-YSZ-CGO sandwiched structure, the targets were prepared by compressing and annealing high-purity commercial powders of 10 % mol Gd doped ceria (CGO10) and ZrO_2: 8% mol Y_2O_3 (8YSZ). Initially, a CGO thin film was deposited onto a (111)-oriented STN (STO + 0.7 % mol Nb_2O_5) single crystal measuring $5 \times 5 \times 0.5$ mm^3 (Crystech GmbH). Subsequently, the YSZ deposition was performed at 550 °C in an oxygen atmosphere of 5.0×10^{-3} mbar, then another layer of CGO film was sequentially deposited onto

the previously deposited YSZ thin film, resulting in a multi-layered structure. The deposition of the two layers of CGO was carried out at 600 °C in an oxygen atmosphere of 1.0×10^{-3} mbar. A 248 nm KrF excimer laser (Lambda-Physik COMPex Pro 210F) was used as the laser source, operating at a frequency of 10 Hz. The estimated laser fluence on the target was approximately 1.6 $J \cdot cm^{-2}$. The target-substrate distance was maintained at 15 mm. The resulting thin films exhibited homogeneity across a surface area of 5×5 mm^2 with a thickness of 1300 nm for CGO layers and 200 nm for YSZ layer.

The process for depositing an LSC-YSZ-LSC symmetric cell was similar. First, targets of $La_{0.6}Sr_{0.4}CoO_{3-\delta}$ (LSC) were prepared. Then, LSC layers and 8YSZ were then deposited on a single crystal STN substrate. For all layers, the deposition process utilized a 248 nm KrF excimer laser with a pulse duration of 25 ns. The laser operated at a constant laser fluence of 4 $J \cdot cm^{-2}$ and a frequency of 30 Hz. The deposition rate for LSC and YSZ was maintained at 0.01 nm per pulse. The substrate temperature was set to 500 ℃, and the oxygen partial pressure during deposition was maintained at 1×10^{-4} mbar.

The structural characterization of the PLD thin films was performed using X-ray diffraction (XRD) in θ-2θ mode and ω (rocking curve) scan. A homemade XRD system with a Cu Kα X-ray source was utilized for these purposes. The thin films exhibited very small surface roughness, as demonstrated by atomic force microscopy (AFM). The surface morphology of the thin films was examined using a Zeiss Ultra FEG SEM equipped with EDS.

2.2 symmetric cell fabrication

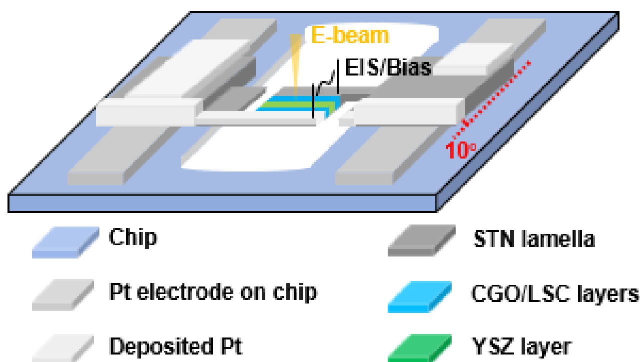

Figure 1: Schematic diagram of CGO-YSZ-CGO cell mounted on the chip

Trenches were milled in the SiN membrane of the chip to ensure that the current flows through the entire layered structure and not through the SiN.

TEM lamellas were milled and lifted out from the PLD sample with a CGO-YSZ-CGO-STN structure using a focused ion beam (ZEISS, 1540XB) and a micromanipulator (Kleindiek). Prior to the milling process, a 2 μm Pt layer was

deposited on the surface of CGO to protect the sample during milling and serve as the current collector for subsequent electrochemical measurements. After preparing the lamella, the lift-out process was conducted, and the lamella was mounted on heating-biasing chips (DENS lightning), which had four contacts for heating, two contacts for biasing, and a through-hole window. The CGO lamella was mounted at a 10° angle relative to the chip surface. Pt was then deposited using the ion beam to ensure the two Pt electrodes on the chip were connected to the two electrodes on the cell. Subsequently, two trenches were cut into the cell structure to establish the correct electrical circuits. The final thinning step in the sample preparation process made the lamella thin enough for TEM observations. The cell on top of the chip is illustrated in Figure 1. Further details of the sample preparation process are reported in our previous work [Chapter 4].

The preparation of the LSC-YSZ-LSC cell follows a similar process. However, our focus is on studying the properties of LSC-YSZ-LSC in an oxygen atmosphere, whereas the STN substrate exhibits high resistance in an oxidizing environment, which would significantly affect the electrochemical test [23]. To overcome this, during sample preparation, we directly connect the LSC layers with the Pt electrodes on the chip. This approach eliminates the influence of STN, ensuring accurate biasing signal of the LSC-YSZ-LSC cell without interference from the substrate.

2.3 electrochemical TEM experiments

2.3.1 ETEM experiment

The TEM work in this paper is conducted in an ETEM equipped with a differential gas pumping system (FEI, Titan 80–300 kV). Before performing the actual EIS-TEM/biasing-TEM measurements, all the samples were heated to 500 °C in the microscope in 3 mbar O_2 for 5 minutes. This step was necessary to remove the amorphous carbon that is mixed with the Pt nanoparticles in the ion-deposited Pt, and Pt-organic compounds condense on top of sample mounting region on the chip during sample preparation [Chapter 4-5]. EELS analysis confirmed that the carbon edge was eliminated after this treatment, thereby confirming the effectiveness of the process [Appendix 2]. Subsequently, the Pt formed a nano-porous network of nanoparticles with voids in the regions that previously contained carbon. This observation was supported by the STEM-ADF images [Chapter 5].

To minimize potential effects of the electron beam during all in situ ETEM experiments, it was important to use a relatively low beam current density of 23 e/(Å^{2}s) or lower for TEM imaging,

except for HRTEM images. Additionally, the beam was blanked during temperature ramping and EIS measurements. Imaging and EELS analysis revealed no changes in the sample morphology or the Ce oxidation state as a result of beam exposure.

2.3.2 In situ high temperature EIS-TEM measurement

The EIS-TEM experiments are detailed in our former work [Chapter 5]. Here, we provide a brief description. The wire connection style was determined through an "*in situ* heating experiment" using the DENS lightning holder. In this style, the wire is divided into heating and biasing wires. The heating is controlled by the Dens control box, while the biasing is connected to a Gamry potentiostat.

The EIS-TEM experiments were conducted by the ETEM and an electrochemical potentiostat. To achieve low oxygen partial pressures, H_2 and H_2O vapor were mixed using the gas control system within the ETEM. The EIS-TEM measurements of the CGO-YSZ-CGO cell were performed with a H_2/H_2O ratio of 0.8 (total pressure: 3 mbar).

The potentiostat (Gamry FAS2 Femtostat) used for two-probe EIS measurements was connected to the Pt electrodes of the chip via the TEM holder. An oscillating voltage amplitude of 20 mV and a frequency range from 100 kHz to 0.1 Hz were utilized. TEM imaging and EIS analysis were performed while maintaining at each temperature within the range of 500-850 °C, with the step of 50 °C. After hitting each temperature point, the temperature is kept constant 3 min before measurement to allow the system to stabilize. The total time allocated for image acquisition and impedance measurement at each temperature was approximately 10 minutes.

2.3.3 In situ high temperature Biasing-TEM measurement

The high-temperature electrochemical biasing experiments on the LSC-YSZ-LSC samples (two LSC-YSZ-LSC cells named sample 1 and sample 2) were conducted in 3 mbar O_2 within the ETEM. The "*in situ* heating/biasing experiment" wire connection style from the DENS solution manual was adopted. Instead of the Gamry, the standard Keithley box provided by DENS with the holder was attached to the holder. This was used to apply a constant electrical potential to the cell. In the Impulse software from DENS, if we input the positive biasing number, for this connection style, the LSC layer close to the Pt will be negatively polarized and the LSC close to the STN substrate will be positively polarized. In the experiment, the cell was directly heated to 700 °C at a ramping rate of 50 °C/min. Once the temperature stabilized, we in steps gradually increased the

applied potential from a small value up to 5 V. The applied potential values were 0.2 mV, 0.5 mV, 2 mV, 5 mV, 20 mV, 50 mV, 0.2 V, 0.5 V, 2 V, 3 V (sample 2), 4 V (sample 2) and 5 V (sample 1). For sample 1, the voltages below 5 V, we maintained each voltage for 5 minutes, while at 5 V, we stayed for 30 minutes to record the structural and elemental evolution. For sample 2, above -2 V, we maintained each voltage for 5 minutes, while at -2 V, -3 V and -4 V, we stay 20 minutes, 10 minutes and 8 minutes respectively.

2.3.4 EIS interpretation

The interpretation of EIS spectra requires a proper ECM to fit the derived EIS data, based on the physical reaction processes occurring on the electrodes during the measurements. J. Jamnik and J. Maier proposed an approximation model for the EIS of mixed ionic and electronic conductors, considering different conditions such as the general situation, ideal situation with selectively blocking electrodes, or real electrodes with possible electron irreversibility and ion leakage [24,25]. W. Lai and S. M. Haile applied this model to ceria to extract detailed electrical and thermodynamic properties at different temperatures and atmospheres [26].

In our cell, when reactive gases are present, the physical processes can be described by an ECM similar to our previous work [Chapter 5]. As shown in Figure 2, a shunt capacitance (CPE_{shunt}) is connected in parallel with all the contributions from the sample, which are introduced by the MEMS chip and the TEM holder setup [Chapter 5]. A transport resistance element (R_t) represents the ionic and electronic conduction, and it is in series with a surface reaction resistance element (R_p) that is parallel to a capacitance element. Regarding this capacitance element, in reducing atmospheres, the CGO layers exhibit mixed ionic and electronic conductor (MIEC) behavior, where the chemical capacitance dominates and is significantly larger than the interface capacitance [27]. Therefore, we utilize CPE_{chem} to fit the EIS data. The entire surface of CGO exposed to the reducing gas environment is electrochemically active and capable of undergoing surface exchange reactions due to its MIEC nature.

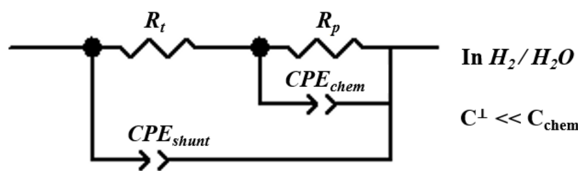

Figure 2 The ECM for fitting EIS of CGOYSZCGO cell in H_2/H_2O ratio of 0.8

3 Results and Discussion

3.1 Application 1: EIS test of Pt-CGO-YSZ-CGO-STN

3.1.1 Microstructural characterization of CGO-YSZ-CGO cell

Figure 3a presents the XRD θ-2θ scans of CGO-YSZ-CGO cell on STN substrate, showing the peaks of CGO, YSZ, and STN. The presence of the STN (001), CGO (002), and YSZ (002) peaks indicates that the layer structures exhibit a highly (001) oriented texture, suggesting the c-axis oriented growth of the CGO and YSZ thin films on the STN substrate. The sharp peaks confirm the good crystallographic quality of all three layers. The observed CGO peak expanding towards left can be attributed to lattice expanding as the thickness increasing.

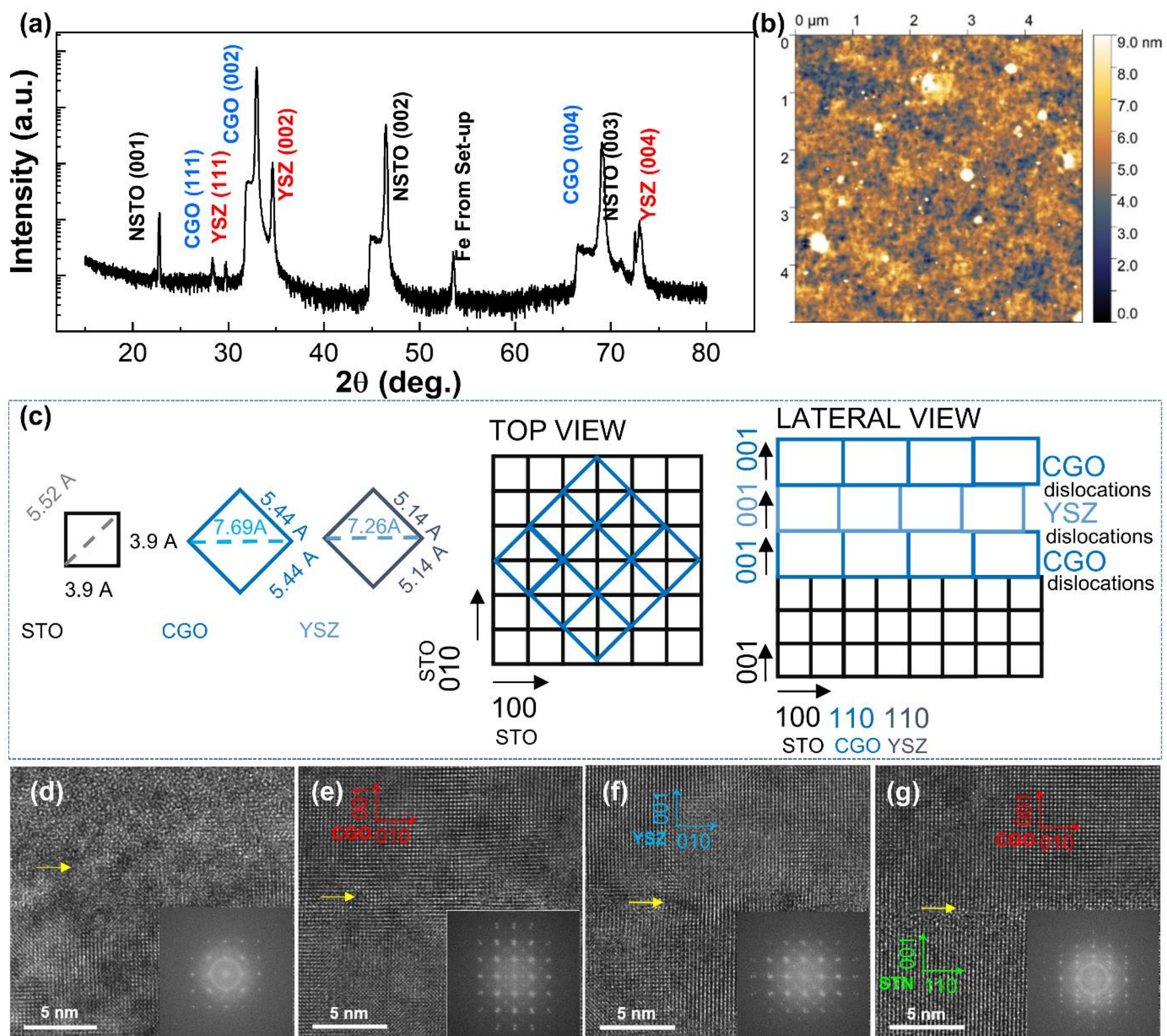

Figure 3: (a) XRD θ-2θ scan of the CGO-YSZ-CGO film, (b) AFM characterization of the surface of the CGO-YSZ-CGO film, (c) growth mechanisms of CGO and YSZ films on the STN substrate, (d) interface of Pt-CGO, (e) interface of CGO-YSZ (CGO layer between Pt and YSZ), (f) interface of YSZ-CGO (CGO layer between YSZ and STN), and (g) interface of CGO-STN; the yellow arrows note the interfaces.

The surface quality is evaluated for this 2.7 micro thick film by an AFM (Figure 3b), showing a low roughness of 9 nm on the top surface of 2nd layer. Figure 3c presents the cell parameters of perovskite STN, fluorite CGO, and fluorite YSZ. The length of the diagonal of the STN unit cell closely matches the cell length of both CGO and YSZ, satisfying the conditions for proper crystal growth. The growth of the CGO cubic cell can align with the STN cubic cell through a 45° rotation, as depicted in the top view and lateral view illustrations of the film structures after the deposition process. The lattice mismatch between the CGO layer and the STN substrate is 1.4 percent, while the lattice mismatch between the CGO layers and YSZ is 5.6 percent. These mismatches lead to the formation of dislocations near the interfaces, resulting in distorted lattice planes visible in high-resolution images. However, it is important to note that these defects do not extend into the bulk portions of the electrolyte or electrode.

HRTEM images in Figure 3d-g, showing the interfaces of Pt-CGO, CGO-YSZ, YSZ-CGO and CGO-STN, and the corresponding FFTs are inserted in the images. The excellent contacts in the interfaces with minimal misfits and dislocations ensure that they do not hinder the oxygen transfer process [28], and verify the excellent growth of the films, and the structure of polycrystalline Pt layer, and the single crystal CGO, YSZ and STN. Even after 2.7 microns of growth, the HRTEM images still prove the growth of the film following the [001] direction. This also means that the planes CGO and YSZ exposed to the gas environment are parallel to (100) planes, and the current is parallel to the [001] direction of CGO and YSZ layers when this cell is polarized in the experiment.

Figure 4a presents the Pt-CGO-YSZ-CGO-STN structure was mounted on the heating-biasing chip, with Pt and STN serving as the current collectors directly connected to the two Pt electrodes on the chip. To prevent current leakage through redeposition layer formed at the surface of YSZ during sample preparation, a parallelogram electrode configuration was used. The "Z cell" geometry was chosen due to its demonstrated cycling robustness, allowing multiple heating and cooling cycles without cracking [Chapter 4].

SEM-EDS maps of this cell, focusing on elements Pt-Mαβ, Si-Kα, Ce-Lα, and Sr-Lα, reveal the layer structure and confirm the uniform distribution of the elements. Following this measurement, the cell was further thinned to achieve electron transparency below 100 nm, enabling TEM characterization.

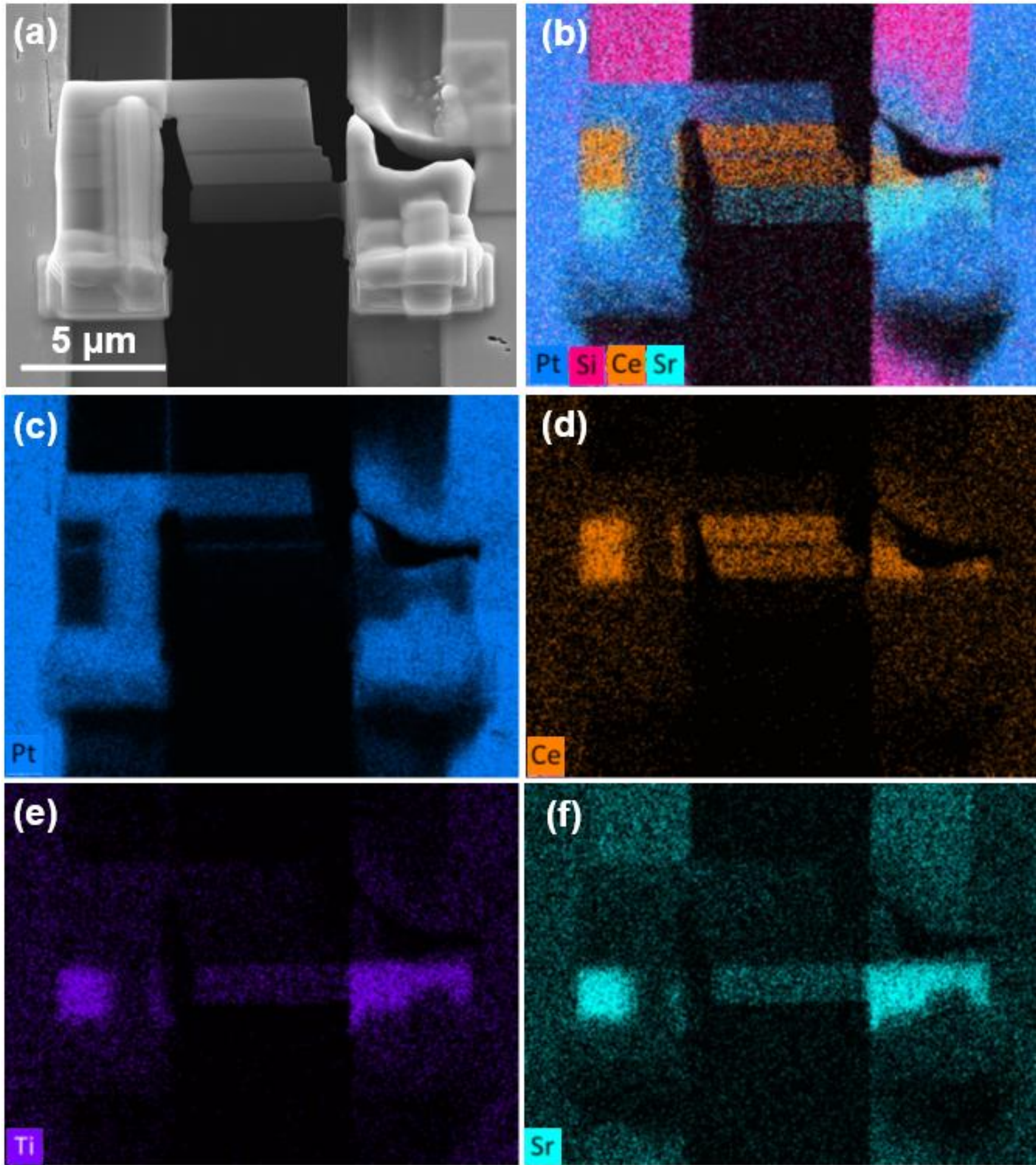

Figure 4: (a) SEM image of the CGO-YSZ-CGO cell mounted on the chip, along with

corresponding EDS mapping. (b) EDS mapping of elements Pt-Mαβ, Si-Kα, Ce-Lα, Sr-Lα, and (c-f) individual element mapping, respectively.

3.1.2 EIS test of Pt-CGO-YSZ-CGO-STN

The EIS spectra recorded at $P(H_2)/P(H_2O) = 0.8$, ranging from 500 °C to 850 °C, are presented in Figure 5a-b. All EIS spectra exhibit two arcs, and both arcs decrease as the temperature is increased, confirming a thermally activated electrochemical process. The first arc of the spectra can be attributed to the transport resistance, while the second arc represents the surface reaction property.

For the first arc, it is important to consider the dimensions of the YSZ electrolyte and CGO electrodes. The width (thickness in PLD sample) of top CGO layer (CGO1), YSZ, bottom CGO layer (CGO2) layers in the cell are 1.24 μm, 0.2 μm and 1.3 μm respectively. By EELS log ratio method [29], the average thickness of each layer is calculated to 0.14 um, 0.1 um and 0.06 um for CGO1, YSZ and CGO2 respectively. Considering the conductivities of YSZ and CGO derived from our test results for pure materials YSZ and CGO, the transport resistance contribution of CGO1, YSZ and CGO2 will be around 10%, 65% and 25%. However, the resistance of STN in this reducing atmosphere can be neglected.

By fitting it with the Arrhenius equation, we found that the activation energy of the transport resistance is approximately 0.72 eV, which is close to previous reports in the literature [Chapter 5] [30].

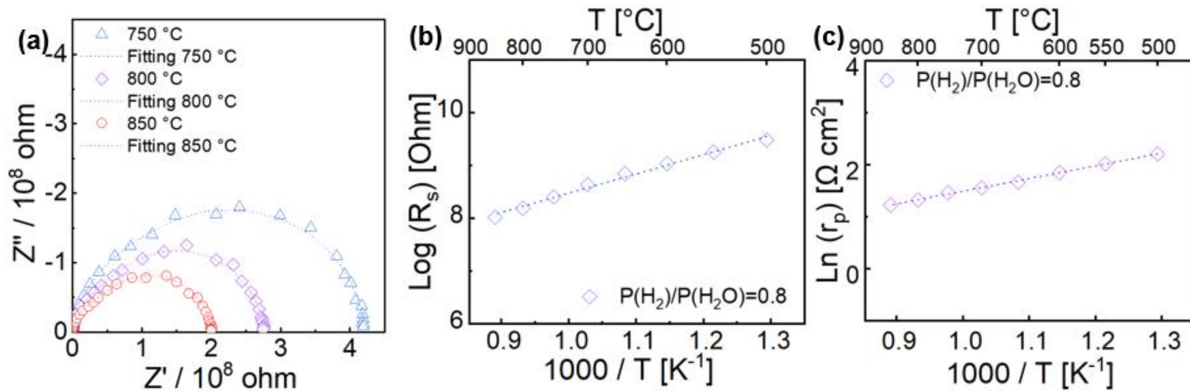

Figure 5: (a-b) EIS spectra of the cell structure recorded in an environment with $P(H_2)/P(H_2O)=0.8$, ranging from 500 °C to 850 °C. (b) The Arrhenius plot of the transport resistance R_s from the first arc of the spectra at different temperatures. (c) The Arrhenius plot fitting of the area-specific surface exchange resistance r_p from the second arc of the spectra at different temperatures.

Next, we consider the second arc, which is expected to represent the surface exchange resistance for CGO. In this reducing atmosphere H_2/H_2O ratio of 0.8, the entire surface of the CGO electrodes is considered active due to its mixed ionic and electronic conductive nature [Chapter 5]. After fitting the EIS spectra, we found that the activation energy for the second arc is approximately 0.5 eV. This value is lower than the expected 0.79 [Chapter 5]. Possibly, this can be ascribed to an electronic current leak through the narrow 0.2 μm YSZ electrolyte layer.

3.2 Application 2: High temperature biasing of Pt-LSC-YSZ-LSC-STN

Perovskite oxides, such as LSC, have been proven to be promising cathode materials for SOFCs due to their high conductivity and electrocatalytic nature [31,32]. However, the degradation mechanisms, such as Sr segregation during oxygen reduction and the reaction between LSC and YSZ electrolyte, still require further study [33,34]. The degradation mechanism of LSC under practical conditions needs to be studied further, particularly through *in situ* methods.

3.2.1 Structure characterization of the Pt-LSC-YSZ-LSC-STN cell

A symmetric LSC-YSZ-LSC cell is shown in Figure 6. Figure 6a displays a SEM image of the LSC-YSZ-LSC cell mounted on top of the DENS heating-biasing chip, with the two LSC layers directly connected to the two electrodes on the chip (which differs from the case of CGO-YSZ-CGO cell where the cell was connected via the Pt and STN). SEM-EDS maps of Pt Lα (b), Co-Kα (c), Y-Lα (d), Ti-Kα (e), and La-Kα (f) is shown in Figure 6, demonstrating the uniform distribution of elements and successful preparation of the cell structures. There is overlap between the Y-L, Pt-M and Sr-L, so here the Y map shows more than just the YSZ layer.

Figure 7a shows a TEM image of the cell. From top to bottom, the layers consist of Pt, LSC, YSZ, LSC, and STN, which follows the opposite sequence used for building the film by PLD. The circles indicate the positions where the SAEDs are recorded. SAEDs from the LSC and YSZ layers are shown in Figures 8(b), (e), and (h). LSC layer close to STN substrate shown in Figure 7h exhibits a single crystal where the crystal orientation is slightly deviating and with some amorphous phase contribution recognized by the SAED ring pattern. While the main contributions of YSZ layer and LSC layer built on the YSZ exhibit the polycrystalline nature shown in Figure 7b and e respectively. From data in Figure b and h, the main phase can be identified as LSC material with lattice distance

of 0.286 nm for {200} and 0.2 nm for {110}, while there are also some contributions from small amounts of CoO identified by 0.248 nm for {111} and 0.21 nm for {200} through measuring the SAED patterns.

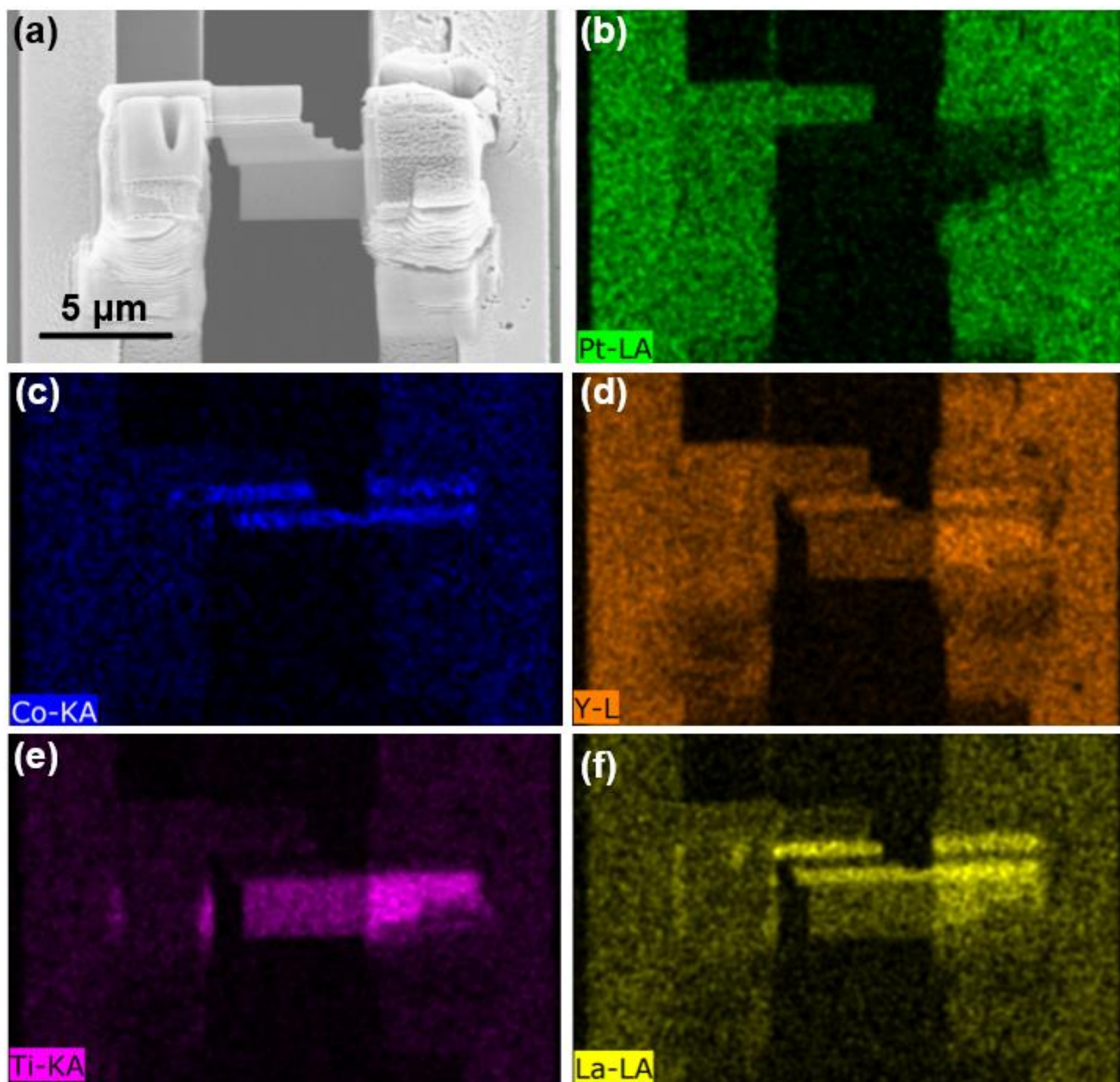

Figure 6: SEM image (a) of the LSC-YSZ-LSC cell mounted on the chip, with corresponding SEM-EDS maps showing elements of Pt-Lα (b), Co-Kα (c), Y-L (d), Ti-Kα (e), and La-Kα (f).

Figures 7c, d, f, and g present HRTEM images of the Pt-LSC, LSC-YSZ, YSZ-LSC, and LSC-STN interfaces respectively, from which LSC exhibits a Pm-3m cubic perovskite structure, YSZ shows an Fm-3m fluorite structure, and STN exhibits a cubic perovskite structure.

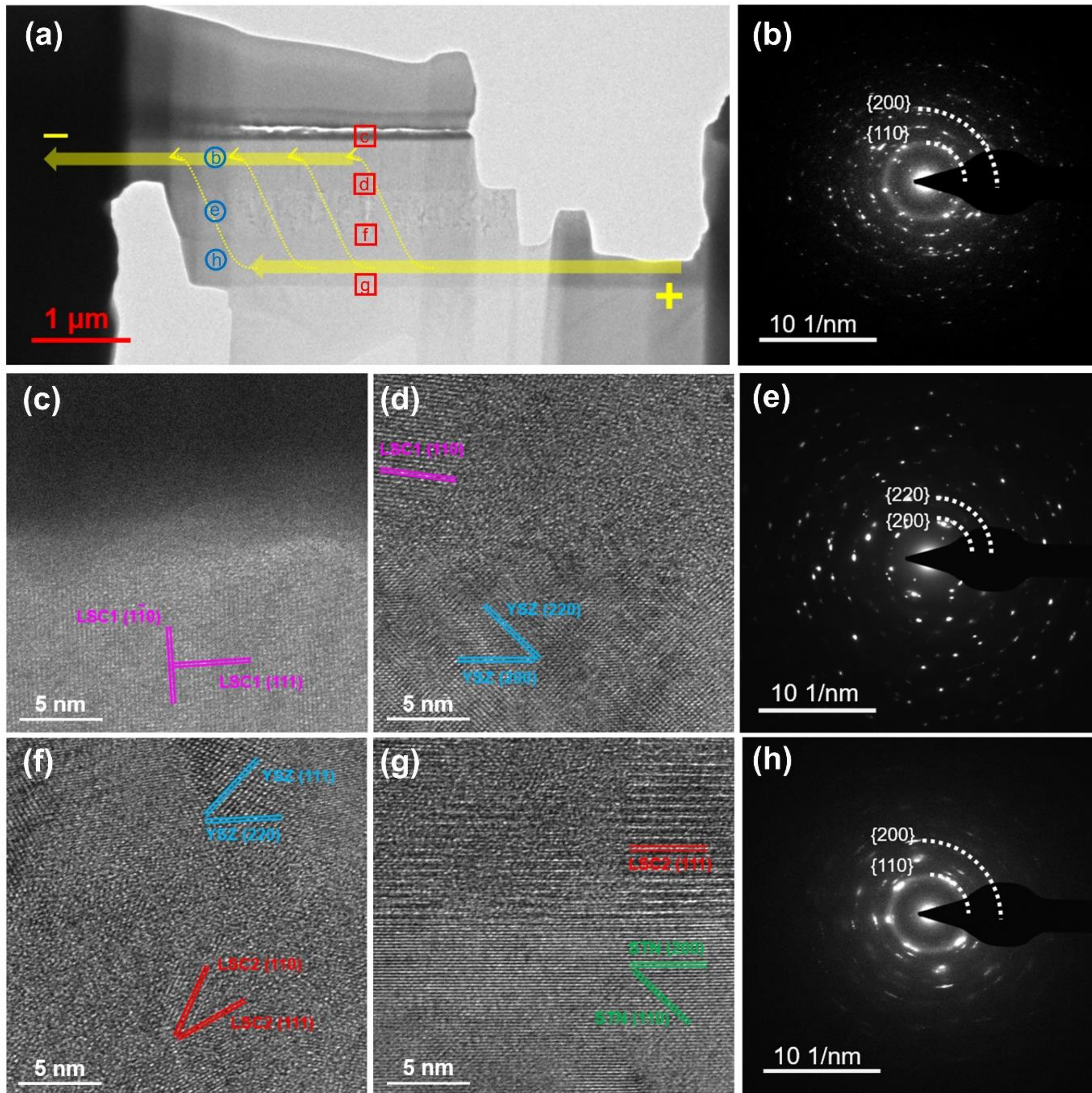

Figure 7: (a) TEM image of the Pt-LSC-YSZ-LSC-STN structure. SAED patterns of the YSZ and LSC layers are shown in (b), (e), and (h). HRTEM images depict the interfaces of Pt-LSC in (c), LSC-YSZ in (d), YSZ-LSC in (f), and LSC-STN in (g) respectively.

3.2.2 Biasing experiment of LSC-YSZ-LSC cell

3.2.2.1 in situ STEM imaging

The yellow arrow in Figure 7a shows the flow of current in the LSC-YSZ-LSC cell sample 1 during the in situ biasing experiment. The top LSC is set to be under negative electric potential, while the bottom layer is set to be under positive electric potential.

The main purpose of the experiment is to showcase that it is possible to induce cell degradation via electrical polarization within the current operando TEM methodology. Unusual high potentials above 1 V were applied to the cell in order to induce accelerated degradation in electrodes.

Figure 8 presents the resistance as a function of applied voltage from 20 mV to 5 V at 700 °C in 3 mbar O_2 (sample 1). The plot shows that the resistance decreases as the voltage increases, particularly when the voltage increases from 0.5 V to 5 V. The current density under 5 V voltage is 2800 A/cm^2. The decrease of the resistance can be ascribed to the structural and compositional change due to the large voltage, and when the voltage is over 2V, this drop become more obvious, which is consistent with the obvious structure change after applying the high voltage described later in this Chapter.

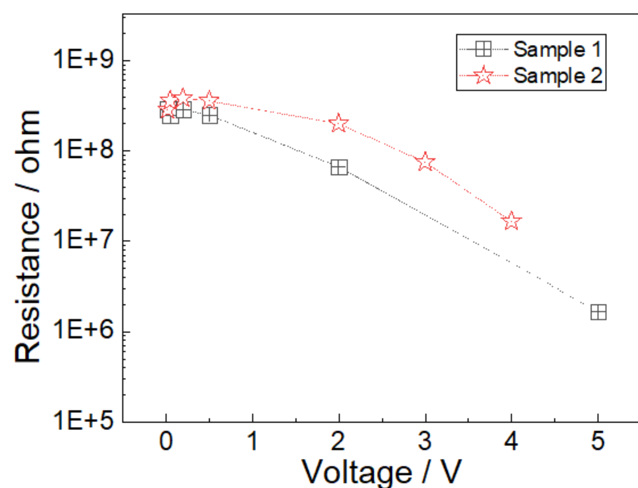

Figure 8: The relationship between the applied voltage on the cell and the corresponding resistance calculated using Ohm's law.

STEM-HAADF images were used to track the morphological evolution of the LSC-YSZ-LSC cells. Figure 9a displays the cell at 700 °C in 3 mbar O_2 before applying any electric potential. The structure appears highly dense and uniform. The sample was at 700 °C for 5 minutes before the STEM image was recorded. No cracks or other feature formations are observed in the cell structure. There are no voids or cracks present around the interface, which remains clean. No amorphous phase or interfacial layer has formed between the two materials. Additionally, there is no evidence of element segregation or accumulation at the interface, this will be present later in this paper.

After applying a 0.5 V voltage for 5 minutes, as shown in Figure 9b, there are no obvious feature formations in the layer structures. However, upon increasing the voltage to 2 V and maintaining it for 5 minutes, as shown in Figure 9c, small nano features start to form at the bottom of the top LSC layer close to YSZ. Subsequently, upon further increasing the voltage to 5 V and maintaining it for 10 minutes, the regions with nano features propagate further into the top LSC layer, and the degradation layer gradually becomes wider as function of time (d-f). The observed nano features

that form in the top LSC layer continues to expand, and the nano features grow and merge. At 5 V delamination between YSZ and the lower LSC layer is also observed as a thin dark line between the two layers (d-f). The cell is, however, still electrically well connected as no increase in resistance was observed.

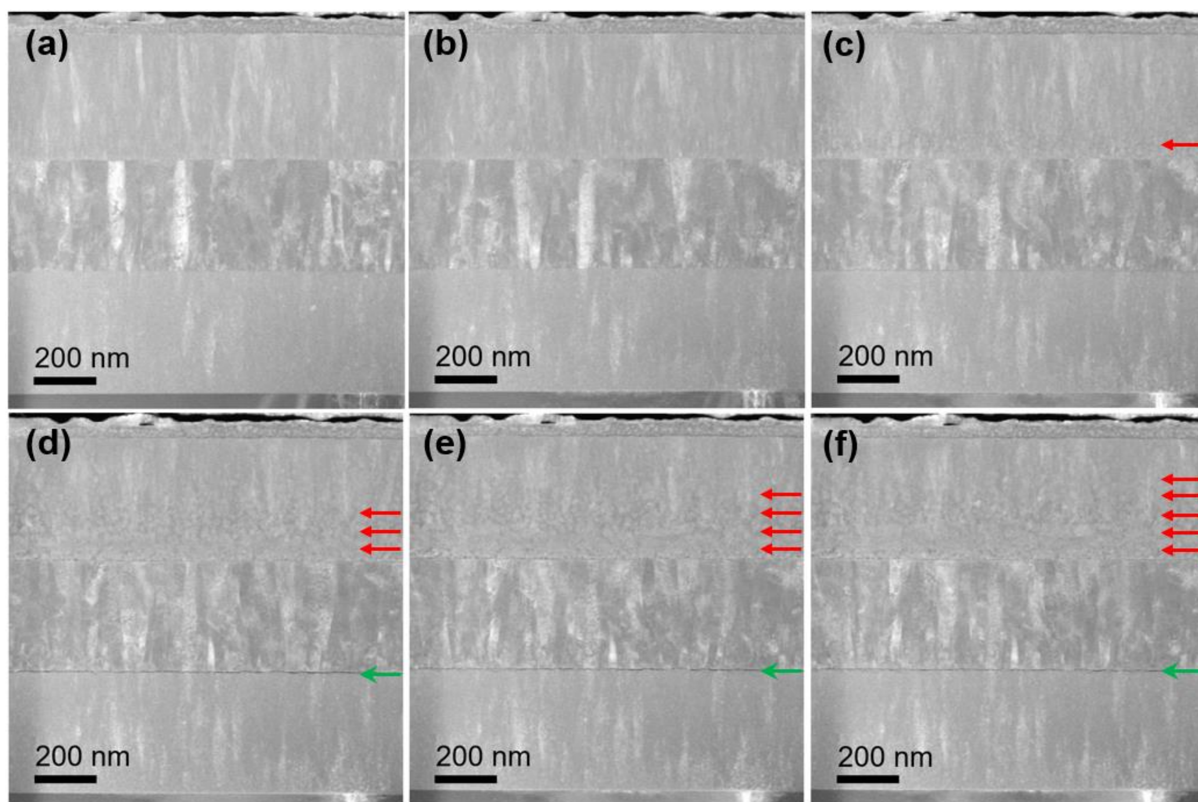

Figure 9: STEM-HAADF images of the LSC-YSZ-LSC cell (sample 1) at 700 °C in 3 mbar O_2 with different biasing conditions. (a) 0 V for 5 min; (b) 0.5 V for 5 min; (c) 2 V for 5 min; (d)5 V for 10 min; (e) 5 V for 20 min; (f) 5 V for 30 min.

For comparison, a second LSC-YSZ-LSC cell was prepared and mounted to the chip in a similar way as shown above. All dimensions of this cell were identical to the first cell, although minor deviations can occur, such as small variation in thickness and width. Also, the experimental conditions (700 °C and 3 mbar O_2) were identical, except that the second cell was polarized positively at the top LSC layer and negatively at the lower LSC layer.

Figure 8 presents the resistance as a function of applied voltage from 20 mV to 4 V at 700 °C in 3 mbar O_2 (sample 2). The initial resistance is almost identical to that of the first cell and the resistance decreases in a similar manner as a function of applied voltage, although slightly less.

For the second cell with reversed polarization, the nano features appear at the lower LSC layer as expected (Figure 10). They start to show on the YSZ-LSC interface with -2 V biasing for 4 min, similar to the first cell. After 20 min the region with nano features extends to the entire LSC layer (Figure 10c). Increasing the applied potential to 3 V and 4 V leads to increased sizes of the nano features (Figure 10d-f. It can be observed that the features close to the YSZ-LSC interface has the largest sizes.

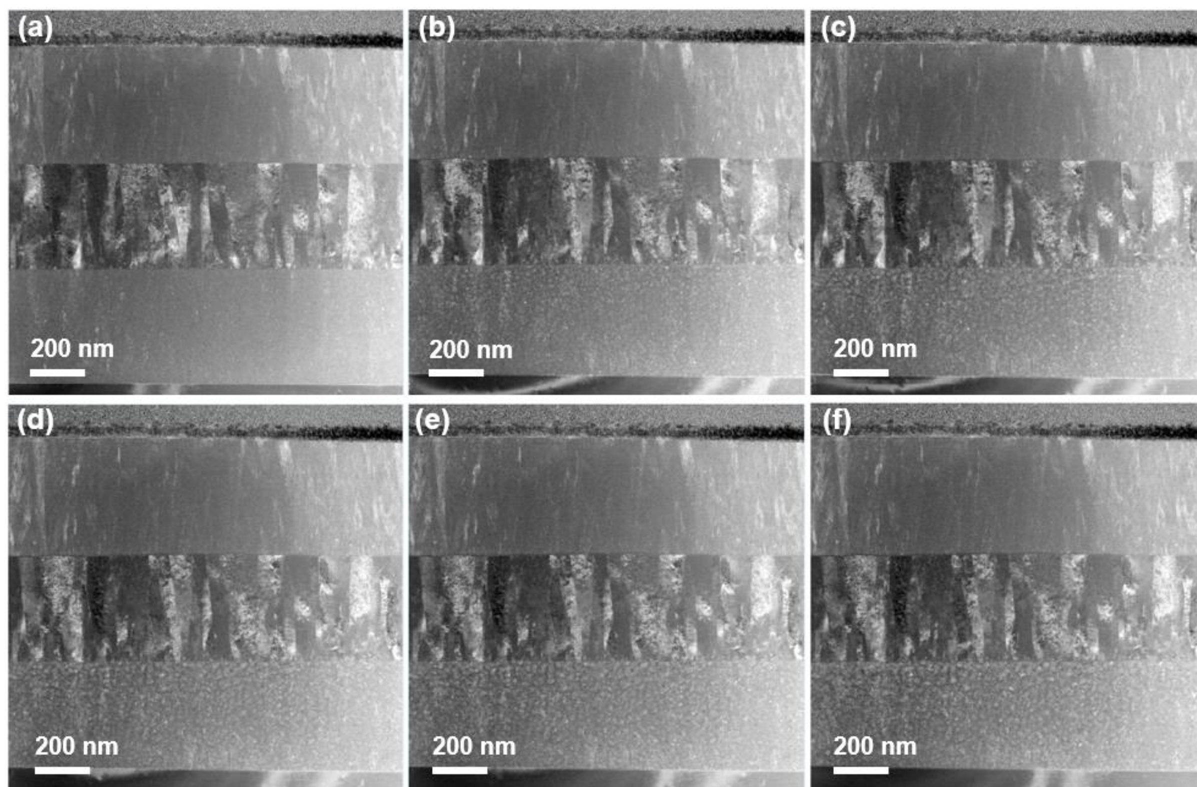

Figure 10: STEM-ADF images of LSC-YSZ-LSC cell (sample 2) at 700 °C in 3 mbar O_2 with different biasing conditions. (a) 0 V for 10 min; (b) -2 V for 4 min; (c) -2 V for 20 min; (d) -3 V for 8 min; (e) -3 V for 10min; (f) -4V for 8 min.

Shrinkage of LSC layer under negative biasing has also been revealed for LSC-YSZ-LSC sample 1 and sample 2 from the images in Figure 9 and 10. For the sample 1, before and after the biasing experiment at 700 °C, the width of top LSC layer decreased 2.4 %. For sample 2, the bottom LSC layer decreased 6 %. While the layers under positive biasing in these two samples did not change.

3.2.2.2 in situ STEM-EELS following valence state of Co and La at 700 °C

Due to the limitations of instruments, we are not able to capture the signal of Sr by STEM-EELS. However, the valence state of Co and La are followed in the oxygen atmosphere under different biasing conditions at 700 °C. The positions recording the EELS spectra are noted in Figure 11c. In this image, the layers from Pt to STN current collectors are presented from the left to the right. Figure 11a shows the spectra after biasing experiment. Figure 11b compared the intensity ratio of Co L_2/L_3 and La M_4/M_5 in the corresponding positions.

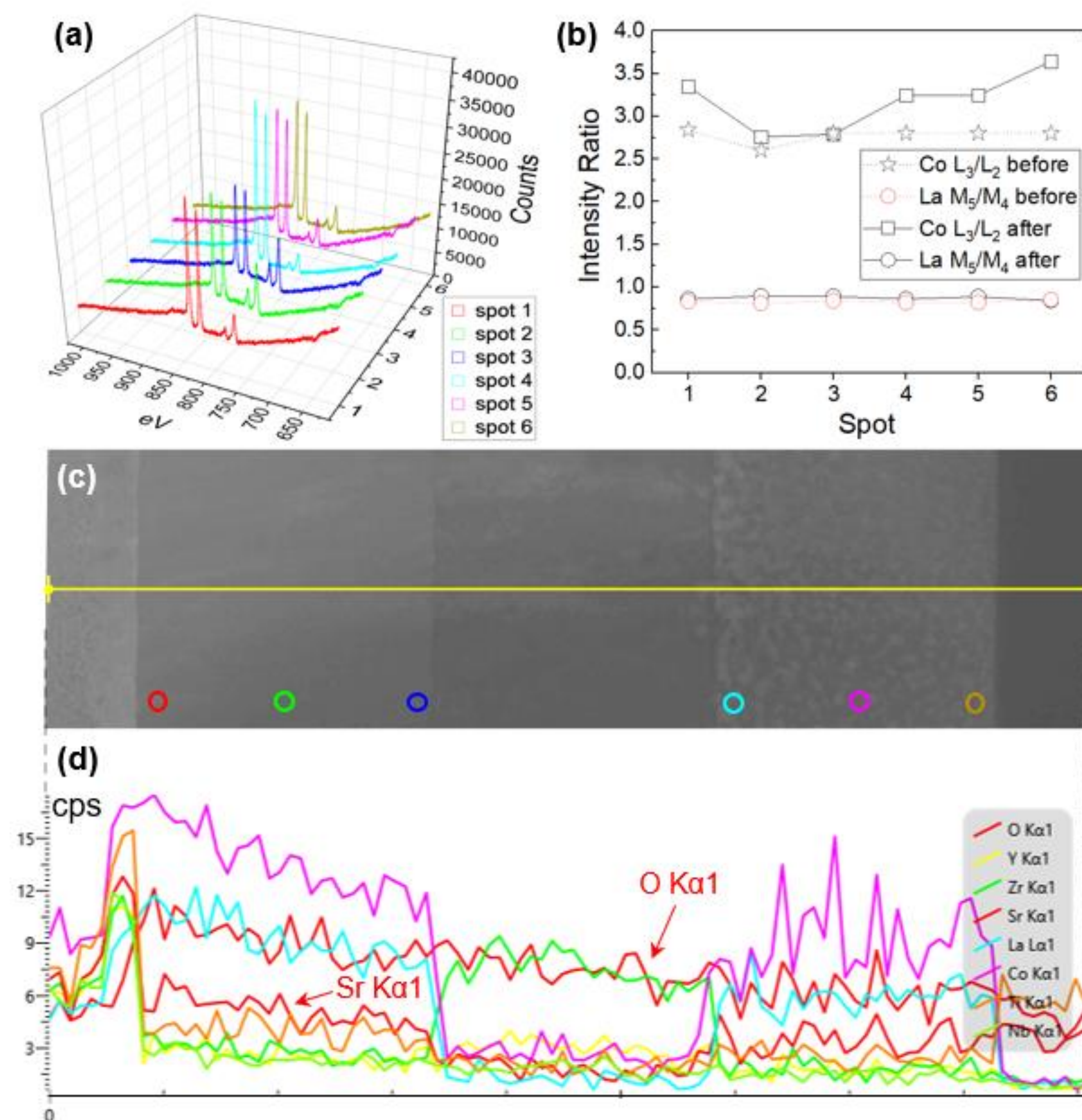

Figure 11: (a) Comparing the STEM-EELS spectra of top LSC layer and bottom LSC layer after the cathodic biasing; (b) Comparing the intensity ratio of Co L_2/L_3 and La M_4/M_5 of different spots before and during biasing at 700 °C in 3 mbar O_2; (c) STEM-HAADF image showing the spots of STEM-EELS point scan and the position of STEM-EDS line scan; (d) STEM-EDS line scan of LSC-YSZ-LSC cell at 700 °C after biasing experiments.

Note that the STEM-EELS are recorded under the biasing. For the LSC-YSZ-LSC sample 2, comparing the spots 2, 3 and spots 4, 5, the valence state of Co elements in the bottom LSC layer is obviously lower than the top LSC layer, meaning the Co are reduced under negative biasing. The intensity ratio for spot 6 closest to the STN current collector shows highest intensity ratio of 3.6, consistent with the +2 Co reported before [35,36]. However, the valence state of La remain constant for different spots, around 0.84-0.89, which is closed to the previously reported values [37]. In contrast, the same LSC-YSZ-LSC sample before biasing shows uniform Co and La valence states distribution, as presented in Figure 11b.

3.2.2.3 in situ STEM-EDS following the quantity of La, Co and Sr at 700 °C

Figure 11d shows STEM-EDS line scans recorded at room temperature after electrical polarization experiment. The results show that after around 30 min cathodic polarization on the bottom LSC in the LSC-YSZ-LSC sample 2, the signal of Co shows several big peaks, which indicates that Co elements have agglomerated and formed some big particles. The peaks from other elements, La and Sr, are not following the same trend as Co, which indicates that the new phase only contains Co cation elements. There is a small peak from Sr around the YSZ-LSC interface to the right side in Figure 11d (lower LSC electrode), which could indicate an enrichment and diffusion of Sr to the YSZ-LSC interface under cathodic polarization. There are, however, also other small variations in the Sr signal in the lower LSC electrode after cathodic polarization and further studies is necessary to determine the Sr distribution in more detail.

3.2.2.4 post-mortem SAED structural analysis after reaction

To study the structure of the nano features or phase formed during the reaction, we captured SAED patterns for different regions of the LSC-YSZ-LSC sample in vacuum at RT after removing the oxygen and without taking the sample out from TEM.

The SAED pattern in Figure 12a shows a diffraction ring pattern of the bottom LSC layer before cathodic polarization. After cathodic polarization, the structure of bottom LSC layer has changed

a lot, and its single crystal nature has gone replaced by the polycrystalline formation by comparing Figure 12a, b. In the same figure, the SAED rings can match with the crystal planes of LSC, Co_3O_4 [38], La_2CoO_4 [39] and CoO [41]. For the Co_3O_4, the large Co peak with new phase with Co as the only one cation from STEM-EDS and the unique lattice distance of 0.48 of {111} confirm its existence. For the La_2CoO_4, the unique lattice distance of 0.37 nm displaying the {101} planes confirm its existence. For the CoO and LSC, although all its lattice distances for each crystal plane can be found in this SAED pattern, while some of them are overlapped with other phase such as Co_3O_4 and La_2CoO_4. Considering the STEM-EELS white ratio data, after the high temperature biasing experiment, the Co valence state has changed a lot for the entire bottom LSC layer, so here most of the LSC phase can be confirmed as decomposed.

The existence of La_2O_3 has also been confirmed by earlier report [33]. However, here due to the overlapping of the SAED ring, we are not able to confirm this. And the existence of the {012} with lattice distance of 0.23 nm cannot be found in the SAED pattern [40]. One possible reason for this can be the growth of La_2O_3 single crystal has a specific orientation and therefore we may miss the reflection of {012}.

Combining the result of STEM-EELS data and SAED we confirm the existence of cobalt oxide with Co^{+2} in the LSC layer under negative biasing. However, some of cobalt oxide may have been oxidized to Co_3O_4 upon the negative biasing has been removed in oxygen at 700 ° C. We could not find evidence of the existence of SrO in the SAED pattern of the center of the bottom LSC layer as has been previously reported [42]. The earlier report indicates that the use of polarization can prompt Sr segregation and diffusion towards the biased LSC-YSZ interface, resulting in the formation of a layer enriched with Sr [33]. Figure 12 c,d comparing the SAED pattern for YSZ and YSZ-LSC interface after reaction. However, the lattice distance of YSZ and SrO are very closed to each other, so it is very difficult to determine whether the diffraction ring is caused by breaking of YSZ or formation of new phase SrO. In order to further reveal the migration of Sr element, better spectra techniques such as more precise STEM-EELS or STEM-EDS mappings may be necessary.

For the two tested LSC-YSZ-LSC cell, the LSC electrodes which were positively polarized no new phases were observed. The LSC phase and valence state remains constant, which can be ascribed to the fact that positive polarization can suppress the Sr segregation, as reported before [5].

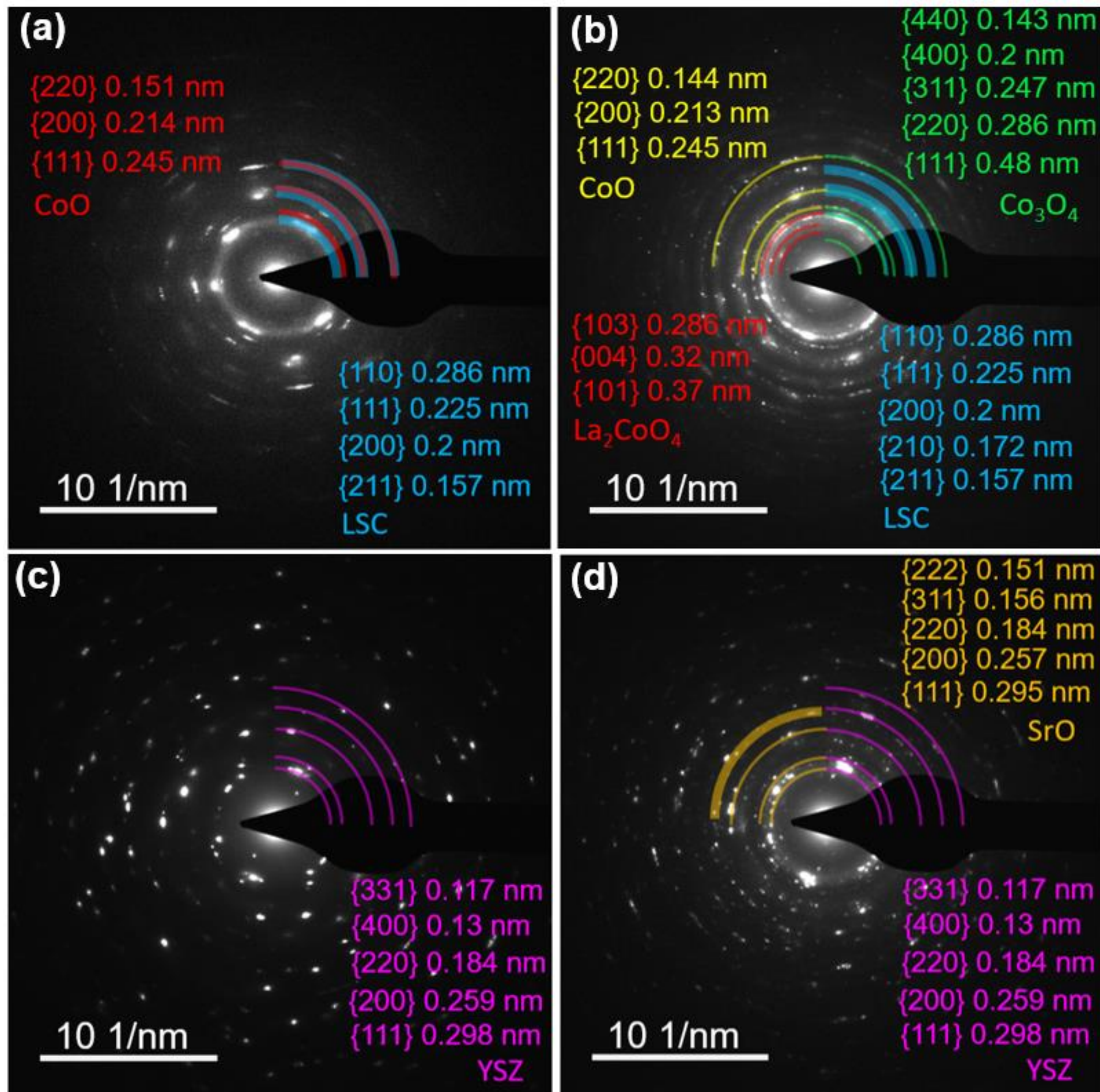

Figure 12: SAED pattern of (a) before biasing experiment and (b) after biasing experiment in the center of bottom LSC layer after cathodic biasing at 700° C in oxygen, (c) the SAED pattern of YSZ center, and (d) the SAED pattern of the YSZ-LSC interface.

4 Conclusion

1) We have combined heat, bias, and gas atmosphere in an ETEM, and applied it to a model solid oxide cell structure for the first time. We have shown that it is possible to measure EIS spectra

from such a cell and that it is possible to induce degradation in a cell by applying a constant relatively high electric potential.

2) We propose to prepare the cell as Z cell geometry for this type of experiment, which can be adapted to high temperature electrochemical ETEM. The structure can be prepared by FIB-SEM milling and mounting on top of the heating/biasing chip and can be thinned to a thickness suitable for TEM observation. The structure uses an ion deposited Pt as the current collector, and the experimental results prove that the structure can obtain stable electrochemical measurement results.

3) We performed high-temperature EIS-TEM measurement on CGO-YSC-CGO symmetrical cell, both the absolute value and activation energy of transport resistance and surface exchange resistance are consistent with those reported in the literature.

4) We conducted a high-temperature constant electrical polarization experiment on symmetric LSC-YSZ-LSC cells. The results suggests that LSC decomposed into Co_3O_4 and La_2CoO_4, or other possible phases as La_2O_3, CoO and SrO.

5) The current density through the LSZ-YSZ-LSC cell at 700 °C and 5 V biasing is 2.8E5 mA/cm^2. The experiment shows that the solid oxide model cell with a Z cell geometry can withstand such a high current density without showing strong leak currents.

References

1 IEA. World Energy Outlook 2022. (IEA, Paris, 2022).

2 Whiston, M. M. *et al.* Meeting U.S. Solid Oxide Fuel Cell Targets. *Joule* 3, 2060-2065, doi:https://doi.org/10.1016/j.joule.2019.07.018 (2019).

3 Singhal, S. C. & Kendall, K. in *High Temperature and Solid Oxide Fuel Cells* (eds Subhash C. Singhal & Kevin Kendall) 1-22 (Elsevier Science, 2003).

4 Trini, M. *et al.* Comparison of microstructural evolution of fuel electrodes in solid oxide fuel cells and electrolysis cells. *Journal of Power Sources* 450, 227599, doi:https://doi.org/10.1016/j.jpowsour.2019.227599 (2020).

5 Koo, B. *et al.* Sr Segregation in Perovskite Oxides: Why It Happens and How It Exists. *Joule* 2, 1476-1499, doi:https://doi.org/10.1016/j.joule.2018.07.016 (2018).

6 Karimaghaloo, A. *et al.* Nanoscale Surface and Interface Engineering of Solid Oxide Fuel Cells by Atomic Layer Deposition. *International Journal of Precision Engineering and Manufacturing-Green Technology* 6, 611-628, doi:10.1007/s40684-019-00090-9 (2019).

7 Jiao, Z., Takagi, N., Shikazono, N. & Kasagi, N. Study on local morphological changes of nickel in solid oxide fuel cell anode using porous Ni pellet electrode. *Journal of Power Sources* 196, 1019-1029, doi:https://doi.org/10.1016/j.jpowsour.2010.08.047 (2011).

8 Zarabi Golkhatmi, S., Asghar, M. I. & Lund, P. D. A review on solid oxide fuel cell durability: Latest progress, mechanisms, and study tools. *Renewable and Sustainable Energy Reviews* 161, 112339, doi:https://doi.org/10.1016/j.rser.2022.112339 (2022).

9 Khan, M. Z. *et al.* A simplified approach to predict performance degradation of a solid oxide fuel cell anode. *Journal of Power Sources* 391, 94-105, doi:https://doi.org/10.1016/j.jpowsour.2018.04.080 (2018).

10 Yokokawa, H. *et al.* Achievements of NEDO Durability Projects on SOFC Stacks in the Light of Physicochemical Mechanisms. *Fuel Cells* 19, 311-339, doi:https://doi.org/10.1002/fuce.201800187 (2019).

11 Xiong, Y. *et al.* Sulfur Poisoning of SOFC Cathodes. *Journal of The Electrochemical Society* 156, B588, doi:10.1149/1.3090169 (2009).

12 Haga, K., Shiratori, Y., Ito, K. & Sasaki, K. Chlorine Poisoning of SOFC Ni-Cermet Anodes. *Journal of The Electrochemical Society* 155, B1233, doi:10.1149/1.2980521 (2008).

13 Liu, M., Lynch, M. E., Blinn, K., Alamgir, F. M. & Choi, Y. Rational SOFC material design: new advances and tools. *Materials Today* 14, 534-546, doi:https://doi.org/10.1016/S1369-7021(11)70279-6 (2011).

14 Sala, E. M. *et al.* Unravelling the role of dopants in the electrocatalytic activity of ceria towards CO2 reduction in solid oxide electrolysis cells. *Physical Chemistry Chemical Physics* 25, 3457-3471, doi:10.1039/D2CP05157E (2023).

15 Guan, Z., Chen, D. & Chueh, W. C. Analyzing the dependence of oxygen incorporation current density on overpotential and oxygen partial pressure in mixed conducting oxide electrodes. *Physical Chemistry Chemical Physics* 19, 23414-23424, doi:10.1039/C7CP03654J (2017).

16 Pomfret, M. B. *et al.* Hydrocarbon Fuels in Solid Oxide Fuel Cells: In Situ Raman Studies of Graphite Formation and Oxidation. *The Journal of Physical Chemistry C* 112, 5232-5240, doi:10.1021/jp711312p (2008).

17 Liu, D.-J. & Almer, J. Phase and strain distributions associated with reactive contaminants inside of a solid oxide fuel cell. *Appl. Phys. Lett.* 94, 224106, doi:10.1063/1.3148362 (2009).

18 Stierle, A. & Molenbroek, A. M. Novel In Situ Probes for Nanocatalysis. *MRS Bull.* 32, 1001-1009, doi:10.1557/mrs2007.208 (2007).

19 Jeangros, Q. *et al.* In situ redox cycle of a nickel–YSZ fuel cell anode in an environmental transmission electron microscope. *Acta Mater.* 58, 4578-4589, doi:https://doi.org/10.1016/j.actamat.2010.04.019 (2010).

20 Gualandris, F. *et al.* In Situ TEM Analysis of a Symmetric Solid Oxide Cell in Oxygen and Vacuum – Cation Diffusion Observations. *ECS Transactions* 75, 123, doi:10.1149/07542.0123ecst (2017).

21 Pérez Garza, H. H. *et al.* in *European Microscopy Congress 2016: Proceedings* 237-238 (2016).

22 Ma, Z. *et al.* Electrochemical Impedance Spectroscopy Integrated with Environmental Transmission Electron Microscopy. *Small Methods* n/a, 2201713, doi:https://doi.org/10.1002/smtd.202201713 (2023).

23 Irvine, J. T. S., Slater, P. R. & Wright, P. A. Synthesis and electrical characterisation of the perovskite niobate-titanates, Sr1−x/2Ti1−xNbxO3−δ. *Ionics* 2, 213-216, doi:10.1007/BF02376024 (1996).

24 Macdonald, J. R. Theory of space‐charge polarization and electrode‐discharge effects. *The Journal of Chemical Physics* 58, 4982-5001, doi:10.1063/1.1679086 (2003).

25 Jamnik, J. & Maier, J. Treatment of the Impedance of Mixed Conductors Equivalent Circuit Model and Explicit Approximate Solutions. *Journal of The Electrochemical Society* 146, 4183, doi:10.1149/1.1392611 (1999).

26 Lai, W. & Haile, S. M. Impedance Spectroscopy as a Tool for Chemical and Electrochemical Analysis of Mixed Conductors: A Case Study of Ceria. *Journal of the American Ceramic Society* 88, 2979-2997, doi:https://doi.org/10.1111/j.1551-2916.2005.00740.x (2005).

27 Nenning, A., Holzmann, M., Fleig, J. & Opitz, A. K. Excellent kinetics of single-phase Gd-doped ceria fuel electrodes in solid oxide cells. *Materials Advances* 2, 5422-5431, doi:10.1039/D1MA00202C (2021).

28 Pergolesi, D. *et al.* Tensile Lattice Distortion Does Not Affect Oxygen Transport in Yttria-Stabilized Zirconia–CeO2 Heterointerfaces. *ACS Nano* 6, 10524-10534, doi:10.1021/nn302812m (2012).

29 Malis, T., Cheng, S. C. & Egerton, R. F. EELS log-ratio technique for specimen-thickness measurement in the TEM. *Journal of Electron Microscopy Technique* 8, 193-200, doi:https://doi.org/10.1002/jemt.1060080206 (1988).

30 Vendrell, X. & West, A. R. Electrical Properties of Yttria-Stabilized Zirconia, YSZ Single Crystal: Local AC and Long Range DC Conduction. *Journal of The Electrochemical Society* 165, F966, doi:10.1149/2.0881811jes (2018).

31 Tsipis, E. V. & Kharton, V. V. Electrode materials and reaction mechanisms in solid oxide fuel cells: a brief review. *Journal of Solid State Electrochemistry* 12, 1367-1391, doi:10.1007/s10008-008-0611-6 (2008).

32 Samson, A., Søgaard, M., Knibbe, R. & Bonanos, N. High Performance Cathodes for Solid Oxide Fuel Cells Prepared by Infiltration of La0.6Sr0.4CoO3−δ into Gd-Doped Ceria. *Journal of The Electrochemical Society* 158, B650, doi:10.1149/1.3571249 (2011).

33 He, S. *et al.* A FIB-STEM Study of Strontium Segregation and Interface Formation of Directly Assembled La0.6Sr0.4Co0.2Fe0.8O3-δ Cathode on Y2O3-ZrO2 Electrolyte of Solid Oxide Fuel Cells. *Journal of The Electrochemical Society* 165, F417, doi:10.1149/2.0151807jes (2018).

34 Chen, K. *et al.* Polarization-Induced Interface and Sr Segregation of in Situ Assembled La0.6Sr0.4Co0.2Fe0.8O3−δ Electrodes on Y2O3–ZrO2 Electrolyte of Solid Oxide

Fuel Cells. *ACS Applied Materials & Interfaces* 8, 31729-31737, doi:10.1021/acsami.6b11665 (2016).

35 Wang, Z. L., Yin, J. S. & Jiang, Y. D. EELS analysis of cation valence states and oxygen vacancies in magnetic oxides. *Micron* 31, 571-580, doi:https://doi.org/10.1016/S0968-4328(99)00139-0 (2000).

36 Wang, Z. L. & Yin, J. S. Cobalt valence and crystal structure of La0.5Sr0.5CoO2.25. *Philosophical Magazine B* 77, 49-65, doi:10.1080/13642819808206382 (1998).

37 Manoubi, T., Colliex, C. & Rez, P. Quantitative electron energy loss spectroscopy on M45 edges in rare earth oxides. *Journal of Electron Spectroscopy and Related Phenomena* 50, 1-18, doi:https://doi.org/10.1016/0368-2048(90)80001-Q (1990).

38 Kotousova, I. S. & Polyakov, S. M.

39 Kajitani, T., Hosoya, S., Hiraga, K. & Fukuda, T. Tetragonal-Orthorhombic Phase Transition of La2CoO4-x. *Journal of the Physical Society of Japan* 59, 562-570, doi:10.1143/JPSJ.59.562 (1990).

40 Gökhan Ünlü, C. *et al.* Structure and magnetic properties of (La1−xFex)FeO3 (x = 0, 0.25, 0.50) perovskite. *Journal of Alloys and Compounds* 784, 1198-1204, doi:https://doi.org/10.1016/j.jallcom.2019.01.047 (2019).

41 Sasaki, S., Fujino, K., Tak, Eacute & Uchi, Y. X-Ray Determination of Electron-Density Distributions in Oxides, MgO, MnO, CoO, and NiO, and Atomic Scattering Factors of their Constituent Atoms. *Proceedings of the Japan Academy, Series B* 55, 43-48, doi:10.2183/pjab.55.43 (1979).

42 Verbraeken, M. C., Suard, E. & Irvine, J. T. S. Structural and electrical properties of calcium and strontium hydrides. *Journal of Materials Chemistry* 19, 2766-2770, doi:10.1039/B820173K (2009).

Chapter 7: Conclusion

In conclusion, this study aimed to transform the environmental transmission electron microscope (ETEM) sample chamber into a versatile electrochemical laboratory capable of providing different gas atmospheres for in situ observations of materials. We demonstrated the feasibility of applying a focused ion beam (FIB) system to prepare pure material samples as well as cell samples for in situ biasing including electrochemical impedance spectroscopy (EIS) measurements. In the first chapter of results, we present the points that need to be taken care of in solid-state electrochemical TEM experiments, including sample preparation, electrochemical measurement, failure factors, and recommended optimization methods. We provide examples of typical EIS spectra for both pure materials and cell structures. The pure materials include pure electronic conductor STN, pure ionic conductor YSZ, and mixed ionic and electronic conductor CGO. By creating a thin region in the center of the sample and leaving side parts with big and bulky size, we were able to separate information on sample transport properties mainly contributed by central part and surface exchange performance mainly contributed by side parts. With measurements on the cell samples, we were able to directly observe interfacial structures between layers and track related structural evolution and elemental migration. The results indicate that the FIB system is a useful tool for the preparation of samples for in situ ETEM experiments.

Furthermore, pure CGO samples were used as a demonstration model to verify the feasibility of testing electrochemical impedance spectroscopy in the transmission electron microscope. It was found that under reducing conditions, this sample is a classic mixed ionic-electronic conductor, while under oxidizing conditions, it is a pure ionic conductor. We obtained the ionic conductivity, electronic conductivity, and surface exchange resistance of the CGO samples in both oxygen and hydrogen/water vapor mixed gas atmospheres. The numerical values of these variables and their activation energies from fitting of arrenius equation were found to be consistent with those reported in previous literatures. This demonstrates the effectiveness and feasibility of applying in situ EIS in the transmission electron microscope for studying the electrochemical properties of materials.

Lastly, we investigated the application of the EIS-TEM method on cell samples. We prepared the Z cell through a special lift-out technique using FIB and tested the cells under hydrogen gas atmospheres at different temperatures. For the CGO-YSZ-CGO sample, we applied EIS-TEM

measurement, and our EIS test results are consistent with the we expected. All the spectra contain two arcs, which can be considered the transport performance of YSZ and surface exchange properties of CGO. This demonstrated the feasibility of high temperature EIS-TEM experiment of the Z cell structure in different gas environments. Next, we applied high temperature biasing-TEM on the LSC-YSZ-LSC cell. STEM-HAADF/ADF image followed the nano feature formation on the LSC layer under cathodic biasing in oxygen at different biasing voltage. STEM-EELS proved the existence of Co^{+2} under negative biasing at 700 °C. STEM-EDS line scan shows the big particles containing only Co as cation will form. After analyzing the HRTEM image, the phase can be phase on the LSC layers under negative biasing can decompose into Co_3O_4, La_2CoO_4, and other possible phases such as La_2O_3 and SrO. This demonstrates the feasibility of high temperature biasing experiments on the SOC model cell.

Chapter 8: Outlook

Regarding the development progress of the EIS-TEM method, there are still some points that can be further improved, mainly focusing on the improvement of cell structure, considering that the methods for testing pure materials are relatively mature.

Firstly, one side of our Z cell structure is Pt deposited by FIB, and the other side is STN. This is because our cell structure needs to be deposited on the STN substrate. However, the introduction of STN causes the asymmetry of the cell structure, leading to issues such as the very high resistance of the STN substrate material under oxygen atmosphere, resulting in an increase in the transport resistance in the EIS spectra we obtained in the oxidation environment. Ideally, the STN layer should be cut off by FIB, and a layer of Pt should be deposited on the cut cross-section. Using the same Pt deposition parameters, Pt with the same properties can be obtained, thereby constructing a perfect Pt-cell-Pt structure, as shown in Figure 1.

The preparation of this type of sample can be divided into the following steps: lift-out the cut lamella onto a needle tip, as Figure 2a; Rotate the needle tip 180 degrees outside the electron microscope, as Figure 2b, Cut off the STN substrate on the upper side, as Figure 2c, and deposit a layer of Pt on top as Figure 2d. After rough thinning, the sample is then transferred to the chip, and the processes afterwards similar to cell preparation is performed, resulting in a completely symmetric Pt-cell-Pt structure.

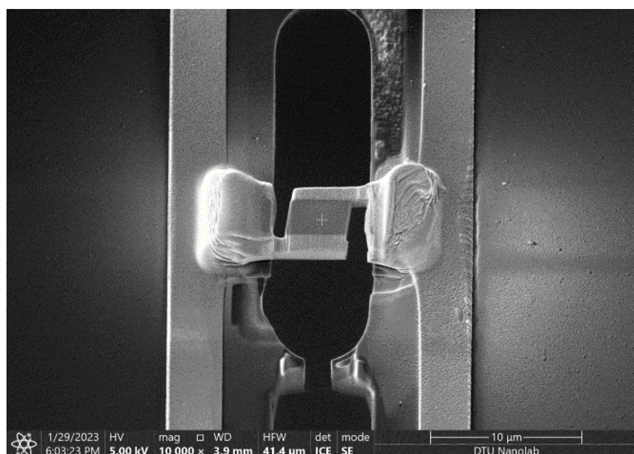

Figure 1: the Pt-CGO-Pt symmetric cell structure

At the same time, the sample preparation can be carried out on the in-situ heating stage in the FIB because, when constructing the Pt conductive circuit, the Pt-organics sprayed from the GIS will be condense on the surface of the chip. After radiation of the ion beam, electron beam or plasma, Pt nanoparticles will form and may potentially cause chip short-cut. Therefore, in-situ heating can be performed before cutting and thinning after spraying Pt to evaporate the Pt-organic deposited on the surface of the chip inside the SEM-TEM, thereby reducing the potential short circuit caused by the formation of Pt nanoparticles.

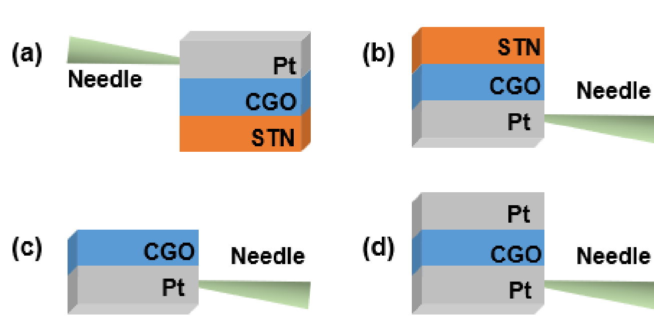

Figure 2: the sample preparation process of Pt-CGO-Pt nano cell

Appendix 1: *Small Methods - 2023 - Ma - Electrochemical Impedance Spectroscopy Integrated with Environmental Transmission Electron*

small methods
www.small-methods.com

Check for updates

Electrochemical Impedance Spectroscopy Integrated with Environmental Transmission Electron Microscopy

*Zhongtao Ma, Waynah Lou Dacayan, Christodoulos Chatzichristodoulou, Kristian Speranza Mølhave, Francesco Maria Chiabrera, Wenjing Zhang, and Søren Bredmose Simonsen**

The concept of combining electrical impedance spectroscopy (EIS) with environmental transmission electron microscopy (ETEM) is demonstrated by testing a specially designed micro gadolinia-doped ceria (CGO) sample in reactive gasses (O_2 and H_2/H_2O), at elevated temperatures (room temperature—800 °C) and with applied electrical potentials. The EIS-TEM method provides structural and compositional information with direct correlation to the electrochemical performance. It is demonstrated that reliable EIS measurements can be achieved in the TEM for a sample with nanoscale dimensions. Specifically, the ionic and electronic conductivity, the surface exchange resistivity, and the volume-specific chemical capacitance are in good agreement with results from more standardized electrochemical tests on macroscopic samples. CGO is chosen as a test material due to its relevance for solid oxide electrochemical reactions where its electrochemical performance depends on temperature and gas environment. As expected, the results show increased conductivity and lower surface exchange resistance in H_2/H_2O gas mixtures where the oxygen partial pressure is low compared to experiments in pure O_2. The developed EIS-TEM platform is an important tool in promoting the understanding of nanoscale processes for green energy technologies, e.g., solid oxide electrolysis/fuel cells, batteries, thermoelectric devices, etc.

1. Introduction

The efficiency of green energy technologies such as P2X (including electrolysis), fuel cells, and batteries directly depends on reaction rates in the involved electrochemical reactions. These again depend on the structure and composition of the component materials.[1] Comparison of electrochemical tests with post-mortem microscopy investigations shows that structural and compositional evolution at the nanoscale is the main reasons for efficiency losses.[2] To accelerate the implementation of particularly P2X and fuel cell technologies in the green energy infrastructure, a detailed understanding of the correlation between electrochemistry and structure/composition is needed so that efficient degradation mitigation strategies can be developed.

Post-mortem microscopy has led to important developments in all areas of energy technologies. However, results from post-mortem characterization only represent the end result from the entire electrochemical process history, including the effects of various gas environments, polarizations, temperature ramps, as well as possible effects from sample preparation for microscopy. In order to directly link a given electrochemical stimuli (e.g., reactant composition, temperature, electrical polarization) with the structure/composition change of the material in its active state, we need to develop a new operando characterization method that provides real-time electrochemical measurements with atomic level structure characterization under relevant conditions.

One group of methods with a potential to give insight into nanostructure/composition of materials in their active state is in situ/operando TEM. These methods allow for structure and composition investigations at high spatial resolution while exposing the sample to various selected stimuli, e.g., controlled atmospheres,[3] elevated temperature,[4] applied stress,[5] electrical polarization[6] or combinations of these.

On the other hand, an electrochemical method that can give information about the electrochemical response of the functional materials under operating conditions is electrochemical impedance spectroscopy (EIS). This has been widely used due

Z. Ma, W. L. Dacayan, C. Chatzichristodoulou, F. M. Chiabrera, S. B. Simonsen
DTU Energy
Fysikvej, 2800 Kgs. Lyngby, Denmark
E-mail: sobrs@dtu.dk

K. S. Mølhave
DTU Nanolab
Ørsteds Plads, 2800 Kgs. Lyngby, Denmark

W. Zhang
DTU Environment
Bygningstorvet, 2800 Kgs. Lyngby, Denmark

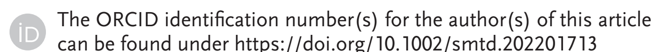
The ORCID identification number(s) for the author(s) of this article can be found under https://doi.org/10.1002/smtd.202201713

© 2023 The Authors. Small Methods published by Wiley-VCH GmbH. This is an open access article under the terms of the Creative Commons Attribution-NonCommercial-NoDerivs License, which permits use and distribution in any medium, provided the original work is properly cited, the use is non-commercial and no modifications or adaptations are made.

DOI: 10.1002/smtd.202201713

23669608, 0, Downloaded from https://onlinelibrary.wiley.com/doi/10.1002/smtd.202201713 by Danish Technical Knowledge, Wiley Online Library on [01/06/2023]. See the Terms and Conditions (https://onlinelibrary.wiley.com/terms-and-conditions) on Wiley Online Library for rules of use; OA articles are governed by the applicable Creative Commons License

to its nondestructive nature, high sensitivity, and ability to study and distinguish between surface/interface and bulk processes.[7]

Electrochemical TEM investigations are already carried out at room temperature in a vacuum or in liquid phase, particularly with focus on battery materials.[8] Recently, attempts have been made to expand the electrochemical TEM capabilities to include operando experiments with focus on the solid oxide fuel and electrolysis cells (SOFC and SOEC)[9] requiring at least three stimuli: electrical potentials, reactive gases, and elevated temperatures. Today, chip-based heating-biasing TEM holders are commercially available (e.g., Protochips Fusion, DENS solutions Lightning, Hummingbird Scientific MEMS Heating Biasing, Thermo Fisher Scientific NanoEX). The combination of such holders and an environmental TEM (ETEM) offers the possibility to study the three stimuli combined.

Preparing and conducting high-temperature solid state electrochemical TEM with relevance to SOEC or SOFC is far from trivial. Here, a few of the challenges are listed: First, solid oxide electrochemical cells have complex layered structures composed of a mixture of metals and hard, brittle ceramics. These need to be thinned to electron transparency and mounted on the heating-biasing chips while ensuring mechanical stability and sufficient electrical contact to the biasing electrodes of the chip. Second, fracture of the sample or loss of electrical contract must be avoided, taking into consideration the thermal expansion of the sample and the chip components during heating. Most importantly, the currents in the chip heater must not interfere with the electrochemical measurements and should be well separated from the sample. The combination of relatively high resistivity, ρ, for the ceramic materials under investigation and the extraordinarily small dimensions of a typical TEM sample leads to very high measured resistances often in the GΩ range. It is therefore crucial to minimize the unavoidable leak currents through the chip components.

Before high-temperature solid state electrochemical TEM can exploit its full potential, it is crucial to establish that these challenges can be solved in a manner that reliable electrochemical measurements can be performed in the TEM. This we do in the present work. We present a combined EIS-TEM analysis of $Ce_{0.9}Gd_{0.1}O_{1.95\text{-}\delta}$ (CGO), which is a popular SOEC and SOFC electrolyte–electrode barrier layer material and is commonly used as a multi-functional component in the composite electrodes of the cell.[10] CGO is a good material for testing the reliability of EIS measurements because its various electrochemical properties (ionic conductivity, electronic conductivity, activity for surface-gas exchange reactions), which are dependent on temperature and the gas environment, can be measured with EIS and are well documented.

The results from this work show that the combined EIS and TEM (EIS-TEM) measurements agree with reference experiments with larger CGO samples. The EIS-TEM method also allows for establishing a direct link between the electrochemical activity and the nanoscaled structure and composition of the material. The method is not limited to investigations of SOECs/SOFCs, but can also be useful for linking functionality and structure/composition in studies of batteries, thermoelectric devices, catalysis, corrosion, etc.

This paper presents EIS-TEM measurements on a CGO sample with nanoscale dimensions. The temperature and pO_2 dependence of the ionic and electronic conductivity, as well as its surface exchange resistivity in O_2 and H_2/H_2O atmospheres, and its volume-specific chemical capacitance in H_2/H_2O, are measured. The influence of Pt porosity is studied and finally the result is shown to be reproducible.

2. Results and Discussion

2.1. Structure of the CGO Sample

Figure 1a shows an overview of the chip geometry while Figure 1b presents how the CGO sample was mounted on top of the chip. It can be observed from the latter that the sample consists of two thick side parts and a thinner central part with a thickness of ≈100 nm (according to EELS log-ratio analysis[11]). The thick side parts (Figure 1b) are connected to the chip electrodes and the thin central part spans over the hole in the center of the chip shown in Figure 1a.

The corresponding SEM-EDS map in Figure 1c shows that most of the top surface area of the side parts is covered with ion-deposited Pt. On the other hand, there is no trace of Pt on top of the thinned central CGO part, as well as on a small portion of the top surfaces of the two thick side parts and on their side surfaces. Pt is also not expected on their entire bottom surface of the sample (not visible, but with access to gas phase due to the 10° tilt between the CGO sample and the chip).

The TEM image of the thinned central part in Figure 1e shows its dimensions and reveals a single-grain boundary between two micrometer-sized grains. The presence of a single-grain boundary is consistent with the grain size of few micrometers observed in the CGO pellet (Figure 1d). Measurements on the HRTEM image (Figure 1f) of the region marked by a red square in Figure 1e are consistent with the crystal structure of $Ce_{0.9}Gd_{0.1}O_{1.95\text{-}\delta}$ with the space group *Fm*3*m* observed at zone axis $[0\bar{1}1]$.[12]

2.2. Morphology and Oxidation State

Figure 2 presents an image series of the grain boundary region at temperatures from 200 °C to 800 °C, in H_2/H_2O gas environment. As could be expected from previous studies,[13] no morphological changes were observed as a response to the elevated temperature (or as a response to electron beam exposure or EIS measurements). Specifically, the sample stayed fully dense (i.e., no pores developed), the interface between the sample and air (and between the two grains) stayed straight and smooth, and no new structures were formed such as nanoparticle generating on the surface. The changes in contrast in the images can be attributed to the displacement of the sample position along the direction of the electron beam caused by thermal expansion. The sample is also stable in the O_2 environment.

It is expected that the Ce oxidation state in the CGO will be Ce^{4+} in the oxygen environment, while the amount of Ce^{3+} increases in the reducing environments, especially at the CGO surface where reduction initiates. This was confirmed by EELS Ce M_5-to-M_4 white line ratio analysis, where spectra measured in O_2 and in H_2/H_2O with ratio 0.8 showed Ce^{4+} in the central part of the thin CGO, and an increased amount of Ce^{3+} ≈10 nm near the CGO surface This is consistent with EELS analysis of pure ceria (see Section S5, Supporting Information).[14]

 © 2023 The Authors. Small Methods published by Wiley-VCH GmbH

23669608, 0, Downloaded from https://onlinelibrary.wiley.com/doi/10.1002/smtd.202201713 by Danish Technical Knowledge, Wiley Online Library on [01/06/2023]. See the Terms and Conditions (https://onlinelibrary.wiley.com/terms-and-conditions) on Wiley Online Library for rules of use; OA articles are governed by the applicable Creative Commons License

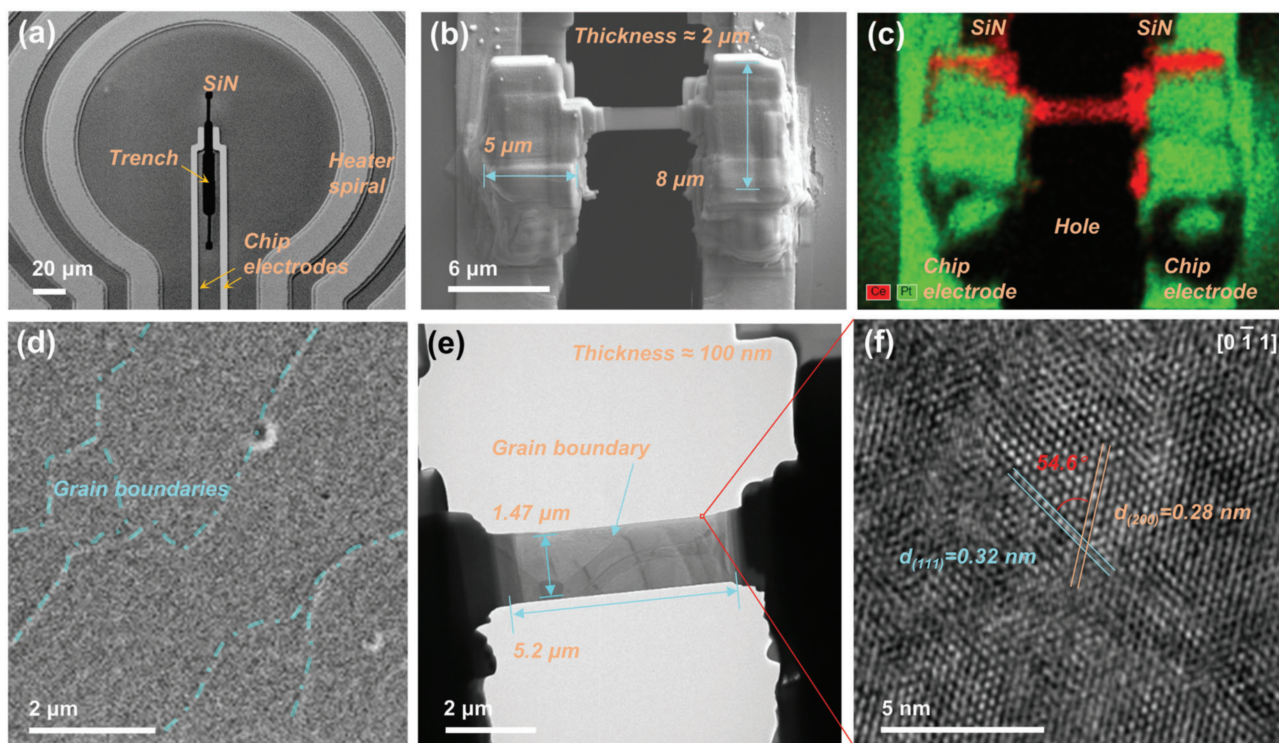

Figure 1. CGO sample mounted on a heating-biasing chip. a) SEM image showing the center of an empty heating-biasing chip; b) SEM image of the sample connected to the Pt electrodes of the chip; c) SEM-EDS map of (b) recorded at 15 kV, red color representing the Ce Lα-peak, green the Pt Mα peak; d) ion-beam image of the CGO pellet; e) TEM image of center part of (b); f) HRTEM image, including crystal analysis of the region in (e) indicated by a red square.

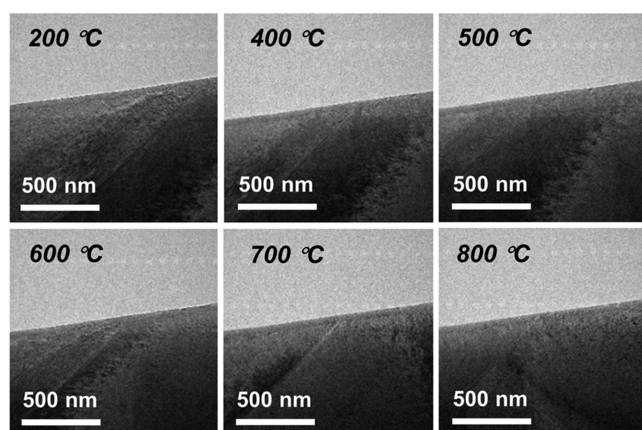

Figure 2. In situ TEM images of the CGO sample in H_2/H_2O with partial pressure ratio of 0.8 as a function of temperature.

2.3. EIS Electrical Circuit Model

Figure 3 presents Nyquist plots of the EIS data recorded in the three gas environments at temperatures from 500 °C to 800 °C. All spectra can be separated into two arcs. The electrical circuit model (ECM) presented in Figure 3 is used to fit the two arcs. These include resistances, R_t and R_p and constant phase elements, CPE_{shunt}, $CPE_{int,}$ and CPE_{chem}. The topology of the ECM and each of its elements is described in the following.

The CPE_{shunt} corresponds to the shunt capacitance from the electrical circuit on the MEMS chip, the TEM holder wires, and the cables connecting to the potentiostat. This is connected in parallel to the entire sample and all its contributions. The value of the CPE_{shunt} deduced from the measurements carried out with a sample matches indeed the capacitance recorded for an empty chip at each temperature from 500 °C to 800 °C, i.e., $\approx 3.8 \times 10^{-11}$ F.

The high-frequency arc starts at the origin of the real and imaginary axes at high frequencies and can be ascribed to ohmic transport through the central thin CGO part.

For a mixed conductor, such as CGO, the ohmic transport resistance, R_t is related to the movement of ions and electrons in the material, and therefore R_t has both an ionic and an electronic component as will be discussed in detail later. The transport resistance is denoted by R_t in the electrical circuit model (ECM). In principle, the ECM model should also include the bulk capacitance of the sample in parallel with R_t. For the present sample dimensions, the expected bulk capacitance is approximately 7.5×10^{-18} F m^{-1}, negligible in comparison to CPE_{shunt}, and therefore not included in the ECM.

The second arc can be associated with several possible contributions including transport barriers at grain boundaries,[15] gas diffusion and gas conversion contributions[16] or the surface exchange reaction. The grain boundary resistance[17] will be negligible for the present micrometer-sized sample with large grains, having only a few grain boundaries (only one visible in the central part (Figure 1e), and its expected capacitance ($\approx 10^{-13}$ F, see

 © 2023 The Authors. Small Methods published by Wiley-VCH GmbH

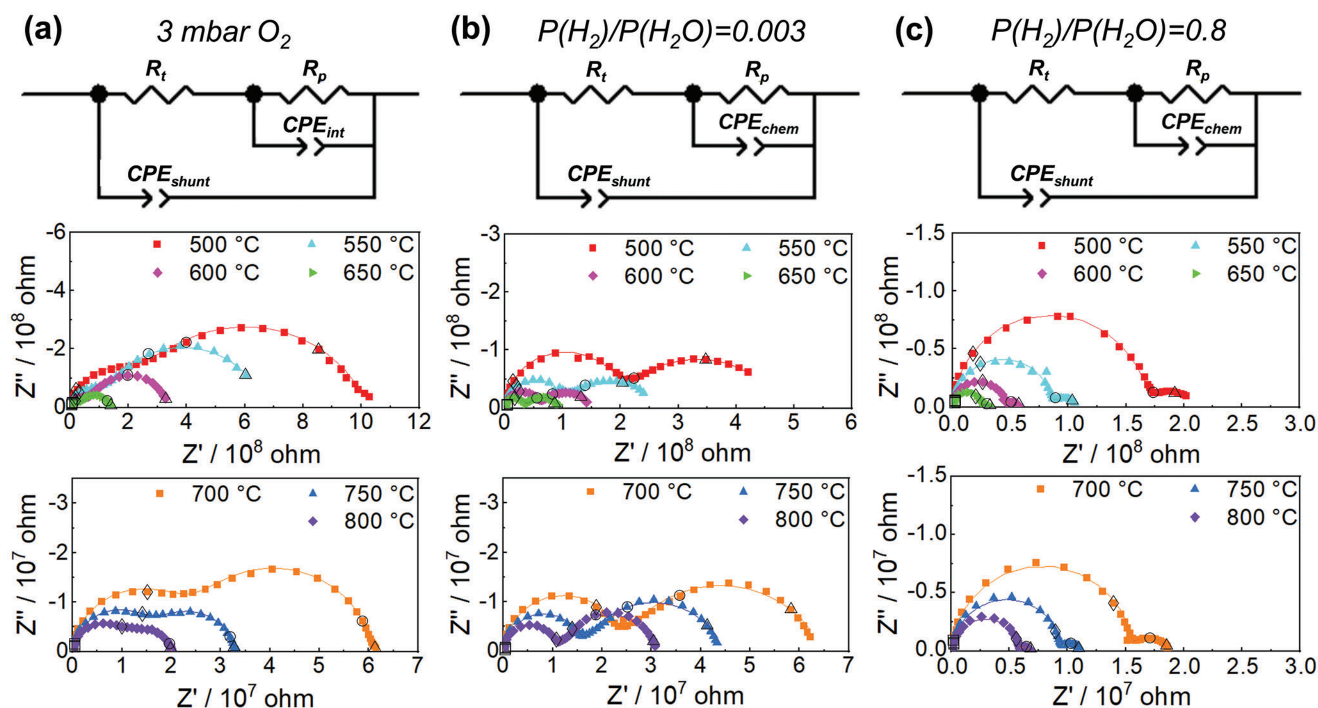

Figure 3. EIS spectra (symbols) and fittings (lines) recorded in a) O_2 (3 mbar) and in a H_2/H_2O with partial pressure ratio of b) 0.003 (total pressure 5 mbar) and c) 0.8 (total pressure 3 mbar); 10 kHz (square), 100 Hz (diamond), 1 Hz (circle), 0.1 Hz (triangle) are noted on the spectra, with hollow symbols; ECM used for fitting the data are presented at the top for each gas composition.

Section S6, Supporting Information)[18] is smaller than the measured shunt capacitance ($\approx 10^{-11}$ F). Considering the small sample dimensions and the extremely small currents incited in it ($\approx 10^{-10}$ A), gas concentration impedances are also negligible.[16] The low-frequency arc is therefore ascribed to the surface exchange reaction resistance, denoted by R_p. It is coupled to the gas–solid interface capacitance and the chemical capacitance of CGO, denoted by CPE_{int} and CPE_{chem}, respectively, in the ECM (Figure 3).

The ECM in Figure 3a is used to fit all spectra recorded in O_2, with CPE_{chem} of CGO being negligible, due to the very small concentration of small polarons (as discussed in Section S5, Supporting Information) and CPE_{int} being dominant. In H_2/H_2O, on the other hand, CPE_{chem} of CGO is expected to form a substantial contribution, which increases with increasing temperature and H_2-to-H_2O ratio to values substantially larger than CPE_{int}.[19]

From Figure 3, for all gas environments, it can be observed that the magnitude of both the first and second arc decreases as a function of temperature, indicating thermally activated processes as indeed expected for both the transport and surface reaction. This is also in line with a negligible gas concentration contribution that would be nearly temperature independent.

2.4. EIS Data Analysis

Both the conductivity and the surface exchange reaction of CGO depend on the gas environment. **Figure 4** presents a schematic illustration of the differences for our CGO TEM sample in O_2 and H_2/H_2O. The overall chemical reaction formulae are different in the two cases. Also, in O_2, CGO is a pure ionic conductor which limits the active surface close to the region of the electron-conducting Pt current collector. In the H_2/H_2O environment electrons are transported through the side parts of CGO thereby allowing the entire CGO surface to be active.

In this section we will therefore analyze the transport and surface exchange resistance from the EIS measurements in each type of gas environment separately, starting with the O_2 environment.

Using the following equation and the dimensions of the thinned central part of the sample, the total conductivity, σ_t, consisting of contributions from both ionic and electronic conductivity, can be calculated from R_t.

$$\sigma_t = \frac{1}{R_t} \frac{l}{w \cdot t} \tag{1}$$

where l, w and t are the length, width and thickness of the thin central part of the sample, respectively. Notice that only the thin central part is considered for calculating σ_t since it contributes to over 98% of the total transport resistance (see Section S7, Supporting Information). **Figure 5**a presents σ_t as a function of temperature in O_2, and is compared with reference data from bulk polycrystalline CGO in air.[20] From the slope of the fitted line in Figure 5a, an activation energy of E_a = 0.7 eV was determined, which is consistent with literature values: In 3 mbar O_2 and 500–800 °C, CGO is primarily an ionic conductor,[17b,21] and the determined E_a corresponds to that for the ionic conductivity, σ_{ion}. The present EIS-TEM deduced σ_t values in O_2 agree closely with the

 © 2023 The Authors. Small Methods published by Wiley-VCH GmbH

23669608, 0, Downloaded from https://onlinelibrary.wiley.com/doi/10.1002/smtd.202201713 by Danish Technical Knowledge, Wiley Online Library on [01/06/2023]. See the Terms and Conditions (https://onlinelibrary.wiley.com/terms-and-conditions) on Wiley Online Library for rules of use; OA articles are governed by the applicable Creative Commons License

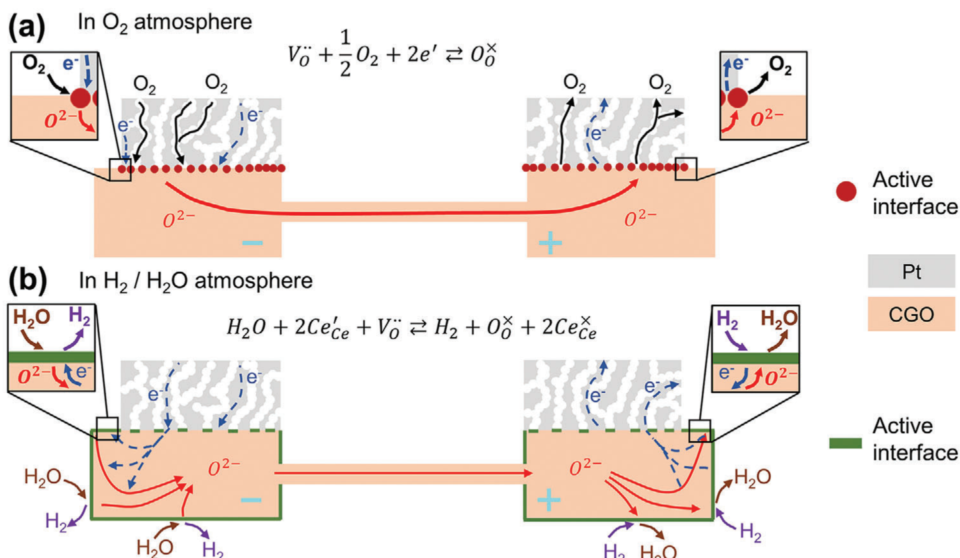

Figure 4. Illustration of active surface area for Pt-CGO as a) pure ionic conductor and as b) mixed electronic/ionic conductor. Arrows indicate the direction of ions (red) and electrons (Navy). In the actual experiment, the flow direction alternates with the frequency of the imposed AC perturbation.

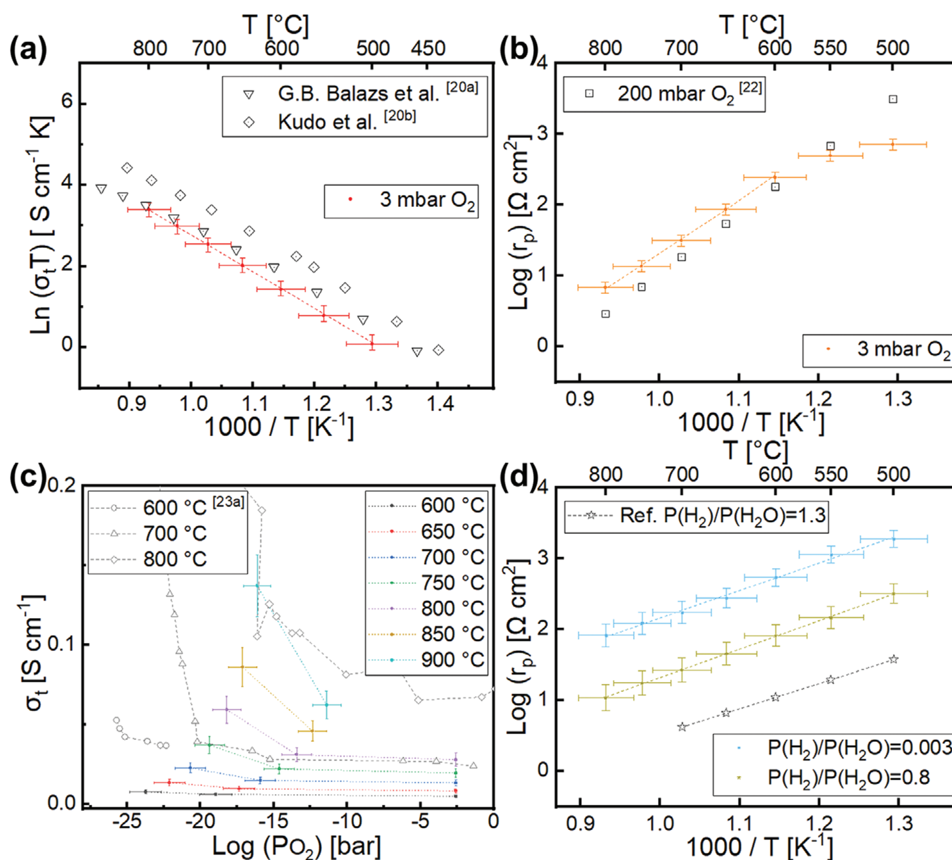

Figure 5. Electrochemical EIS-TEM measurements of CGO in different atmospheres. a) Arrhenius plot of total conductivity in 3 mbar O_2 (red) and reference data for bulk polycrystalline CGO in air (black);[20] b) Arrhenius plot of the surface reaction resistance in 3 mbar O_2 (orange), and reference data from a CGO thin film electrode in synthetic air (black);[22] c) total conductivity as a function of pO_2 (colored), and empty black symbols refer to reference data for polycrystalline CGO;[23a] d) surface reaction resistance as function of temperature in H_2/H_2O atmospheres (blue, green), and reference data from a CGO thin film electrode in H_2/H_2O with partial pressure ratio of 1.3 (black).[24]

© 2023 The Authors. Small Methods published by Wiley-VCH GmbH

23669608, 0, Downloaded from https://onlinelibrary.wiley.com/doi/10.1002/smtd.202201713 by Danish Technical Knowledge, Wiley Online Library on [01/06/2023]. See the Terms and Conditions (https://onlinelibrary.wiley.com/terms-and-conditions) on Wiley Online Library for rules of use; OA articles are governed by the applicable Creative Commons License

reference data both with respect to E_a and to the absolute values for σ_t.

The resistance associated with the surface exchange reaction was also determined and compared to literature values. To quantify the area-specific surface reaction resistance, we need to estimate the active CGO surface. For a pure ionic conductor, like CGO in 3 mbar O_2, the oxygen exchange is expected to take place in a localized reaction zone near the triple phase boundary (TPB) consisting of the ion conductor (CGO), the electron conductor (Pt) and the gas phase. For the present sample, the TPB will therefore be close to the Pt current collector as illustrated in Figure 4a (red dots).[12,17a] As described in the experimental section, the Pt forms a nano-porous structure after the carbon removal pretreatment. Compared to a dense Pt, the nanoporous Pt will enhance the surface exchange reaction by an increased total TPB length. Perfect percolation through the nanoporous Pt cannot be expected and the surface exchange reaction will be prohibited where gas pores terminate before reaching the surface. This effect will be discussed later in this paper. The area-specific surface reaction resistance, r_p, can therefore be calculated by using Equation 2.

$$r_p = R_p * S \quad (2)$$

where S is the interface between CGO and the nanoporous Pt (around 92 µm^2). The result is presented as a function of temperature in Figure 5b in comparison with data from a dense CGO thin film model electrode tested in synthetic air. For the surface exchange reaction in O_2, E_a = 1.5 eV is deduced from the slope of Figure 5b for temperatures above 600 °C, a value that is close to the reference value of E_a = 1.7 eV for the CGO thin film electrode.[22] In the temperature range 500– 600 °C, the slope clearly deviates from the straight line, possibly because the total resistance of the nanoscaled CGO sample approached the Giga-ohm regime where a current leak through the chip starts to influence the measurements.

We will now focus on the experiments carried out in the H_2/H_2O environment. The electronic conductivity, σ_{elec} in CGO, depends strongly on the oxygen partial pressure as described by Equation 3.[23]

$$\sigma_t = \sigma_{ion} + \sigma_{elec} = \sigma_{ion} + \sigma_{elec}^0 P_{O_2}^{-1/4} \quad (3)$$

where σ_{elec}^0 can be regarded as a constant for small deviations from oxygen stoichiometry. At low oxygen partial pressures, CGO is therefore a mixed conductor with both oxygen vacancies and electrons as charge carriers.

Figure 5c presents σ_t as a function of oxygen partial pressure for the EIS-TEM measurements compared with reference data. The figure shows that σ_t increases with decreasing oxygen partial pressure, as expected according to Equation 3. Although the trend of σ_t is as expected, the absolute values deviate from the reference values. The σ_t measured at 700 °C and 750 °C matches well with the reference data at 600 °C and 700 °C, respectively.[23a] This could indicate an error in the measured temperature in the order of 50–100 °C which is higher than the 5% error on the temperature (corresponding to 35–38 °C for read-out temperatures 700–750 °C) expected for these commercials MEMS chips. A possible explanation is a temperature gradient across the thin central part of the sample due to the relatively low thermal conductivity of CGO.

To assess this hypothesis, a temperature calibration experiment was conducted based on the melting point of Zn nanoparticles deposited on a similar CGO lamella. When ramping the temperature up in 3 mbar H_2 at a rate of 20 °C min^{-1}, the in situ TEM images showed Zn melting at a ≈50 °C higher read-out temperature in the center compared to the sides of the sample (Figure S3 and Video S1, Supporting Information). This confirms that the temperature off-set observed in Figure 5c is most likely due to a temperature gradient across the CGO lamella. Additional work, which is beyond the scope of the present work, is needed to accurately calibrate or calculate the absolute temperature in different positions of the TEM sample as a function of nominal chip temperature.

The thicker side parts of the sample are not expected to deviate substantially from the nominal chip temperature (around 5% of read out value), and therefore the surface reaction rates and associated capacitances determined by EIS are expected to reflect a fairly accurate temperature dependence.

For the mixed conducting CGO in H_2/H_2O environments, the surface exchange reaction takes place not only near the TPB, but on the entire CGO–gas interface,[17a] as illustrated in Figure 4b (green line). The total surface area (S) of both thick side parts of the CGO (261 µm^2) is therefore used in Equation 2 to calculate the area-specific surface reaction resistance, r_p. The surface exchange resistance R_p determined from the second arc, however, is influenced by an electronic leak current through the thin central part of the MIEC CGO, i.e., not all the electrical current participates in the electrochemical reaction. This can be corrected using the following equation:[17a,24]

$$R_p^{cor} = \frac{R_p R_{elec}}{R_{elec} - R_p} - R_{ion} \quad (4)$$

where the ionic resistance, R_{ion}, represents the transport resistance recorded in O_2. The electronic resistance, R_{elec} is determined from, σ_{elec}, using the dimensions of the central part in Equation 1 and σ_{elec} is determined from σ_t and σ_{ion} via Equation 3. Finally r_p corrected for leak currents is calculated from R_p^{cor} using Equation 2. The effect of correcting for leak currents is shown in Figure S6 (Supporting Information).

Figure 5d shows the temperature dependence of the corrected r_p for CGO in H_2/H_2O with partial pressure ratio of 0.003 and 0.8. For both gas environments the measured E_a = 0.8 eV. This value is close to the reference value of 0.7 eV.[25] Also, the absolute values of r_p decrease with increasing H_2/H_2O ratio (Figure 5d), corresponding to a decreasing pO_2 and increasing electronic conductivity (Figure 5c). A number of studies suggest that the second electron transfer (likely coupled with the H-H association and desorption) is the rate-limiting step for the H_2 evolution reaction (HER) on ceria.[26] This will accelerate upon increasing the concentration of electronic charge carriers, resulting in reduced r_p upon increasing H_2/H_2O ratio as observed in the present experiment. A decrease in r_p upon increasing H_2/H_2O ratio is also expected for the H_2 oxidation reaction (HOR).[27]

The volume-specific capacitance, which can be calculated from CPE_{chem} by using Brug et al.'s formula and geometry of the CGO sample is presented in **Figure 6**.[28] Considering the 2000 nm

© 2023 The Authors. Small Methods published by Wiley-VCH GmbH

23669608, 0, Downloaded from https://onlinelibrary.wiley.com/doi/10.1002/smtd.202201713 by Danish Technical Knowledge, Wiley Online Library on [01/06/2023]. See the Terms and Conditions (https://onlinelibrary.wiley.com/terms-and-conditions) on Wiley Online Library for rules of use; OA articles are governed by the applicable Creative Commons License

23669608, 0, Downloaded from https://onlinelibrary.wiley.com/doi/10.1002/smtd.202201713 by Danish Technical Knowledge, Wiley Online Library on [01/06/2023]. See the Terms and Conditions (https://onlinelibrary.wiley.com/terms-and-conditions) on Wiley Online Library for rules of use; OA articles are governed by the applicable Creative Commons License

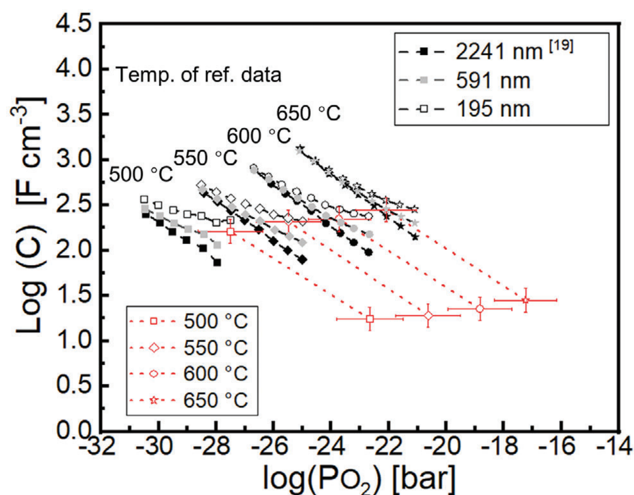

Figure 6. Volume-specific capacitance of the 2000 nm thick CGO side parts (red) as function of oxygen partial pressure and reference data from 2241 nm (black), 591 nm (gray), and 195 nm (black open symbols) CGO films at 500 °C, 550 °C, 600 °C, 650 °C, respectively.[19]

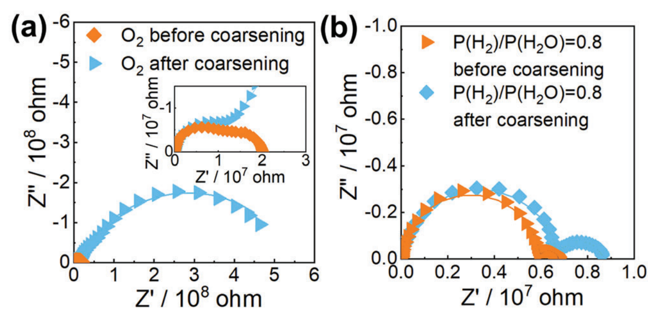

Figure 7. a) EIS spectra recorded in 3 mbar O_2 at 800 °C before and after coarsening; b) EIS spectra recorded in H_2/H_2O with partial pressure ratio of 0.8 at 800 °C before and after coarsening.

thick side parts, our results for 600 °C and 650 °C match well with the reference data of the film with a similar thickness of 2241 nm.[19] Both of them follow the $P_{O_2}^{-1/4}$ dependence as expected, and this confirms that the capacitance is dominated by the chemical capacitance.

2.5. The Effect of Porous Pt

In order to explore the effect of the nanoporous Pt structure in the electrochemical measurements, the CGO sample was exposed to 900 °C in the reducing gas environment (An overview of all EIS-TEM processes for the sample is shown in Section S9, Supporting Information). These conditions lead to Pt coarsening (Figure S2c, Supporting Information), loss of percolating pore network for gas diffusion and thereby decreased TPB length. It can therefore be expected that the surface exchange resistance is increased, in particular for the reaction in oxygen where the surface reaction rate depends directly on the TPB. This effect was confirmed by a comparison of EIS spectra recorded before and after coarsening (**Figure 7**a). The transport resistivity is rather similar (i.e., 35 Ω cm before and 39 Ω cm after) while the surface reaction resistance increased 74 times (to 492 Ω cm^2 from 7 Ω cm^2).

The effect of coarsening on the surface exchange reaction it is expected to be smaller in H_2/H_2O because here the entire CGO surface is active (as illustrated in Figure 4b). This is confirmed by the EIS spectra in Figure 7b. In H_2/H_2O with ratio of 0.8, the transport resistivity after coarsening (19 Ω cm) is similar to the value measured before (17 Ω cm). The surface reaction resistance after coarsening (5 Ω cm^2) is only 2.5 times larger than before (2 Ω cm^2).

2.6. Reproducibility of Test Results

The analysis above shows that the Pt morphology determines the TPB and influences the surface exchange reaction resistance in O_2. For comparison, two additional CGO samples with a smaller Pt-CGO interface, and therefore shorter TPB, were produced and tested (**Figure 8**). In H_2/H_2O with gas pressure ratio 0.003, the area-specific surface reaction resistance of the CGO sample 1 and 2 were compared and the absolute values agree well, deviating only by a factor of ≈2 (Figure 8b). The transport resistivity deviates more, by a factor of ≈5 (Figure 8c). This can be attributed to the different temperature distributions across the center part of the samples, as a consequence of the different sample geometries (Figures 1 and 8a). The transport resistance is dominated by the thin central part which also happens to be the part influenced the most by the temperature gradient. CGO sample 3 is tested in both 3 mbar O_2 and H_2/H_2O with a partial pressure ratio of 0.8. The activation energy and absolute values of the area-specific surface reaction resistance match well with CGO sample 1 in both atmospheres (Figure 8d,e). The transport resistivity in H_2/H_2O with a partial pressure ratio of 0.8 shows a relatively small deviation in the absolute value by a factor of 3 (Figure 8f). Again, this can be explained by the different temperature distributions across the two samples.

Overall, we observe good reproducibility with respect to both transport properties and surface exchange reaction resistances in O_2 and H_2/H_2O amongst the three samples (Figure 8), and any deviations can be rationalized by the somewhat different temperature distributions across the different samples. These results showcase the possibility to carry out operando EIS-TEM studies on SOC samples and open up the path for the investigation of full cells to answer questions of great technological significance.

3. Conclusion

The feasibility of operando EIS-TEM on solid-state electrochemical cells operating in reactive gasses and elevated temperatures was demonstrated by measuring the temperature and pO_2 dependence of the ionic and electronic conductivity of CGO, as well as its surface exchange resistivity in O_2 and H_2/H_2O atmospheres, and its volume-specific chemical capacitance in H_2/H_2O.

A special sample structure was designed with thick side parts and a thin central part, by which one can separate the contributions of bulk charge transport and the surface reaction processes. The measured temperature and pO_2-dependent conductivity, surface exchange resistance, and chemical capacitance, as well as their activation energies and pO_2 exponents are found to agree well with reference data.

© 2023 The Authors. Small Methods published by Wiley-VCH GmbH

23669608, 0, Downloaded from https://onlinelibrary.wiley.com/doi/10.1002/smtd.202201713 by Danish Technical Knowledge, Wiley Online Library on [01/06/2023]. See the Terms and Conditions (https://onlinelibrary.wiley.com/terms-and-conditions) on Wiley Online Library for rules of use; OA articles are governed by the applicable Creative Commons License

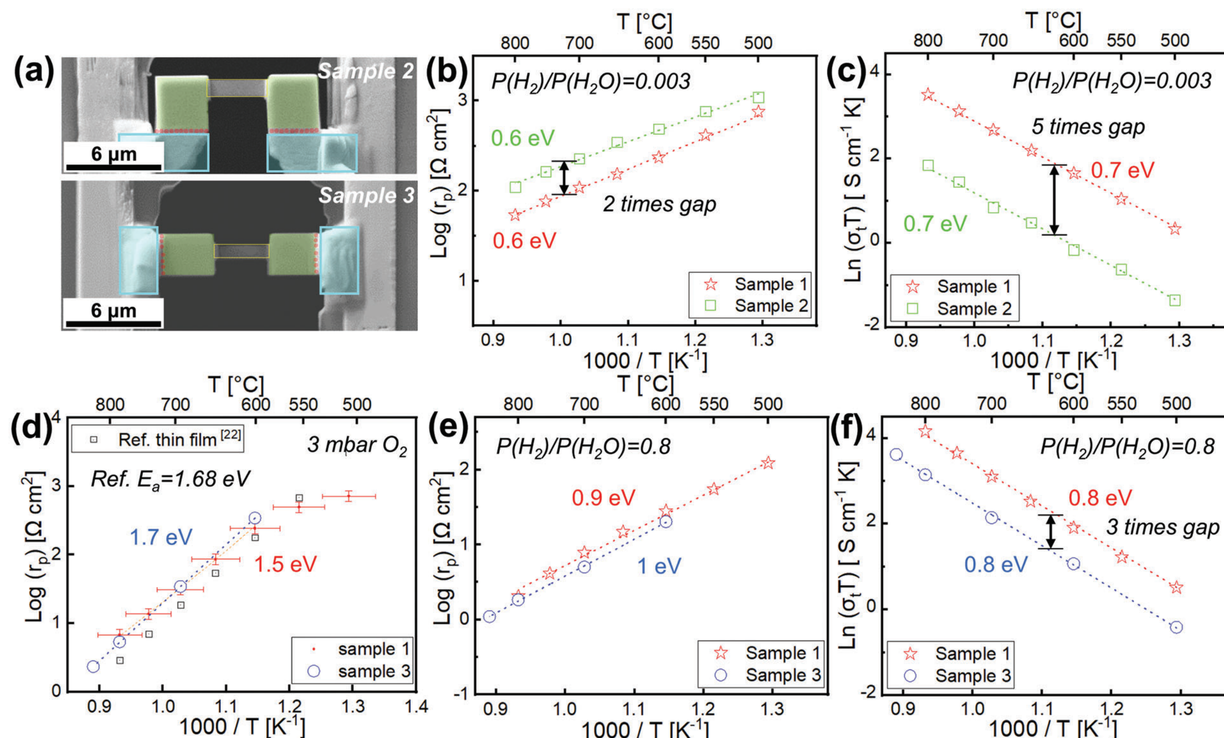

Figure 8. Comparison of electrochemical EIS-TEM measurements of CGO samples 2 and 3 in different atmospheres relative to CGO sample 1. a) SEM images of samples 2 and 3; the thin central part, thick side parts, and deposited Pt are marked by yellow, green and cyan colors respectively. In H_2/H_2O atmospheres, the surface exchange reaction takes place at the surface of the side parts (green), while in oxygen atmosphere, the surface exchange reaction only take place at the Pt-CGO interface (red); b) comparing the area specific surface reaction resistance of sample 1 and 2 in H_2/H_2O with gas partial pressure ratio of 0.003; c) the total conductivity in H_2/H_2O with partial pressure ratio of 0.003 for sample 1 and 2; d) the area specific surface reaction resistance of sample 1 and 3 in 3 mbar O_2, and reference data from a CGO thin film electrode in synthetic air (black);[22] e) area-specific surface reaction resistance in H_2/H_2O with partial pressure ratio of 0.8 for samples 1 and 3; f) the total conductivity in H_2/H_2O with partial pressure ratio of 0.8 for sample 1 and 3.

It can therefore be concluded that reliable EIS measurements can be performed in the TEM, even for the difficult case of hard, brittle ceramic materials which are thinned sufficiently for HRTEM analysis. The strength of operando EIS-TEM is that it allows us to simultaneously gain information on both the electrochemical behavior and the structure/composition of a material at the atomic level, in its active state.

With the purpose of determining the validity of the EIS measurements in the TEM, we have deliberately chosen operation conditions (temperatures, gas environments, polarizations) where the material was stable. The EIS-TEM method will be of particular importance in the investigation of dynamical changes of the structure and composition induced by the operating conditions. For such cases, the effect of the dynamical changes observed from the TEM can be directly compared to simultaneously recorded EIS spectra. Such a capability will be crucial for the further development in our understanding of the nanoscale processes such as degradation in a number of green energy technologies, e.g., electrolysis cells, fuel cells, and batteries.

4. Experimental Section

Sintered Pellet Preparation: Commercial ultrahigh surface (UHS) area $Ce_{0.9}Gd_{0.1}O_{1.95-\delta}$ (CGO) powder was purchased from Solvay. The powder was compressed into pellets using a 10 mm diameter stainless steel mold at a uniaxial pressure of 3 MPa, followed by isostatic pressing at 325 MPa and sintering at 1500 °C in air for 12 h and slow cooling to room temperature at a rate of 0.5 K min^{-1}. The geometrical density of the pellets was between 94 and 97% of the theoretical density.[12]

TEM Sample Preparation: By using a focused Ga^+ ion beam (Crossbeam, ZEISS, 1540XB) and a micromanipulator (Kleindiek), TEM lamellas were prepared from the CGO pellet and were mounted on heating-biasing chips (DENS lightning, with 4 contacts for heating, 2 contacts for biasing, and a through-hole window). To avoid any current leak along the surface of the chip due to Pt overspray, the two Pt electrodes of the chip were further separated by milling a long trench between them before mounting the TEM lamella (Figure 1 and Figure S1, Supporting Information). After the mounting process, the CGO lamellas have a 10° angle relative to the chip surface. Pt was ion-deposited to ensure electrical contact between the CGO lamella and the Pt electrodes at the chip. A final preparation step was thinning and polishing the central part of the lamella to allow for TEM analysis and to remove any Pt overspray from ion deposition.[29] A result of such sample preparation is presented in Figure 1.

EIS-TEM Experiments: The EIS-TEM experiments were carried out in an ETEM (Titan 80-300 kV) equipped with a differential pumping system and an image aberration corrector (FEI Europe, Netherlands).[30] The ETEM can host gases like O_2, H_2 and H_2O with partial pressures from 10^{-6} to 26 mbar. With the use of needle valves and mass flow controllers, the mixing of two or more of these gases can be achieved and the partial pressures can be controlled. For our experiments, low oxygen partial pressures were achieved by mixing H_2 and H_2O vapor. The experiments were carried out in three different gas environments: a) 3 mbar O_2, b) a H_2/H_2O mixture with partial pressure ratio of 0.003 (total pressure 5 mbar), and c) a H_2/H_2O with partial pressure ratio of 0.8 (total pressure 3 mbar).

© 2023 The Authors. Small Methods published by Wiley-VCH GmbH

The electrochemical workstation (Gamry FAS2 Femtostat) used for two-probe EIS measurements was connected to the Pt electrodes of the chip via the TEM holder (DENS Lightning). EIS was performed by applying an alternating voltage amplitude of 20 mV in a frequency range from 100 kHz to 0.03 Hz.

Before EIS-TEM measurements, the samples were heated to 500 °C in the ETEM at 3 mbar O_2 for 5 min. This is to remove the amorphous carbon and its potential effects, which is mixed with the Pt nanoparticles in the ion-deposited Pt.[29,31] EELS analysis showed that the carbon edge was fully removed after this treatment, confirming that the treatment was sufficient to remove the carbon. After this, the Pt forms a nano-porous network with voids in the regions that previously contained carbon (Figure S2a,b, Supporting Information).

EIS-TEM analysis was carried out while the temperature was held constant at 500–900 °C, in steps of 50 °C, after waiting for 3 min for the system to stabilize at each temperature. The total time spent on image acquisition and impedance measurement at each temperature was ≈12 min.

For all operando TEM experiments, it is important to minimize possible effects of the electron beam. Therefore, a relatively low beam current density of 23 e $Å^{-2}$ s^{-1} or lower was used for TEM imaging, except for HRTEM which was recorded only once at RT. The beam was also blanked during temperature ramping and EIS analysis. No changes in the sample morphology or in the Ce oxidation state were observed as a result of beam exposure according to imaging and EELS analysis.

Error Analysis: Errors on reported calculated data can come from the measurement of sample dimensions, gas pressure and temperature, and EIS recording and fitting. All these errors are considered and presented as error bars in the graphs. The details of the error analysis are presented in the Supporting Information.

Supporting Information

Supporting Information is available from the Wiley Online Library or from the author.

Acknowledgements

Z.M. and W.L.D. contributed equally to this work. S.B.S. planned and initiated the project. Z.M. and W.L.D. contributed to development of the EIS-TEM experimental procedures. Z.M. prepared the TEM samples and conducted the operando EIS-TEM experiments and corresponding data analysis. Z.M., W.L.D., F.M.C., W.Z., S.B.S, C.C., and K.S.M. all contributed to the discussions for the development of experimental method and of interpretation of the results. Z.M. and W.L.D. prepared the figures. Z.M., W.L.D., S.B.S., C.C., K.S.M., F.M.C., and W.Z. wrote the manuscript and all the authors contributed to the discussion and revision of the manuscript. This project was received funding from the European Research Council under the European Union's Horizon 2020 research and innovation programme (grant agreement No 850850).

Conflict of Interest

The authors declare no conflict of interest.

Data Availability Statement

The data that support the findings of this study are openly available at https://doi.org/10.11583/DTU.22347127.v1.

Keywords

CGO, EIS, ETEM, operando, SOEC, SOFC

Received: December 29, 2022
Revised: February 27, 2023
Published online:

[1] A. Hauch, R. Küngas, P. Blennow, A. B. Hansen, J. B. Hansen, B. V. Mathiesen, M. B. Mogensen, *Science* **2020**, *370*, eaba6118.
[2] a) L. Holzer, B. Iwanschitz, T. Hocker, B. Münch, M. Prestat, D. Wiedenmann, U. Vogt, P. Holtappels, J. Sfeir, A. Mai, T. Graule, *J. Power Sources* **2011**, *196*, 1279; b) S.-K. Jung, H. Gwon, J. Hong, K.-Y. Park, D.-H. Seo, H. Kim, J. Hyun, W. Yang, K. Kang, *Adv. Energy Mater.* **2014**, *4*, 1300787; c) B.-K. Park, Q. Zhang, P. W. Voorhees, S. A. Barnett, *Energy Environ. Sci.* **2019**, *12*, 3053.
[3] a) R. T. K. Baker, C. Thomas, R. B. Thomas, *J. Catal.* **1975**, *38*, 510; b) R. T. K. Baker, R. B. Thomas, M. Wells, *Carbon* **1975**, *13*, 141; c) P. A. Crozier, A. K. Datye, in *Studies in Surface Science and Catalysis*, Vol. *130* (Eds: A. Corma, F. V. Melo, S. Mendioroz, J. L. G. Fierro), Elsevier, Granada, Spain **2000**, p. 3119; d) P. L. Hansen, J. B. Wagner, S. Helveg, J. R. Rostrup-Nielsen, B. S. Clausen, H. Topsoe, *Science* **2002**, *295*, 2053; e) S. Helveg, C. López-Cartes, J. Sehested, P. L. Hansen, B. S. Clausen, J. R. Rostrup-Nielsen, F. Abild-Pedersen, J. K. Nørskov, *Nature* **2004**, *427*, 426; f) S. B. Simonsen, I. Chorkendorff, S. Dahl, M. Skoglundh, J. Sehested, S. Helveg, *J. Am. Chem. Soc.* **2010**, *132*, 7968; g) P. A. Crozier, S. Chenna, *Ultramicroscopy* **2011**, *111*, 177; h) S. Chenna, P. A. Crozier, *ACS Catal.* **2012**, *2*, 2395; i) J. R. Jinschek, *Chem. Commun.* **2014**, *50*, 2696; j) S. B. Simonsen, Y. Wang, J. O. Jensen, W. Zhang, *Nanotechnology* **2017**, *28*, 475710.
[4] a) R. Sinclair, M. A. Parker, *Nature* **1986**, *322*, 531; b) K. Holloway, R. Sinclair, *J. Less-Common Met.* **1988**, *140*, 139; c) T. Kamino, H. Saka, *Microsc., Microanal., Microstruct.* **1993**, *4*, 127.
[5] a) M. Legros, *C. R. Phys.* **2014**, *15*, 224; b) Y. Deng, R. Zhang, T. C. Pekin, C. Gammer, J. Ciston, P. Ercius, C. Ophus, K. Bustillo, C. Song, S. Zhao, H. Guo, Y. Zhao, H. Dong, Z. Chen, A. M. Minor, *Adv. Mater.* **2020**, *32*, 1906105.
[6] a) R. J. Kamaladasa, A. A. Sharma, Y.-T. Lai, W. Chen, P. A. Salvador, J. A. Bain, M. Skowronski, Y. N. Picard, *Microsc. Microanal.* **2015**, *21*, 140; b) B. Haas, J.-L. Rouvière, V. Boureau, R. Berthier, D. Cooper, *Ultramicroscopy* **2019**, *198*, 58.
[7] M. J. Jørgensen, M. Mogensen, *J. Electrochem. Soc.* **2001**, *148*, A433.
[8] a) S. Basak, K. Dzieciol, Y. E. Durmus, H. Tempel, H. Kungl, C. George, J. Mayer, R.-A. Eichel, *Chem. Phys. Rev.* **2022**, *3*, 031303; b) M. J. Williamson, R. M. Tromp, P. M. Vereecken, R. Hull, F. M. Ross, *Nat. Mater.* **2003**, *2*, 532; c) X. H. Liu, J. Y. Huang, *Energy Environ. Sci.* **2011**, *4*, 3844.
[9] a) A. H. Tavabi, S. Arai, S. Muto, T. Tanji, R. E. Dunin-Borkowski, *Microsc. Microanal.* **2014**, *20*, 1817; b) F. Gualandris, S. B. Simonsen, J. B. Wagner, S. Sanna, S. Muto, L. T. Kuhn, *ECS Trans.* **2017**, *75*, 123.
[10] a) S. H. Jo, P. Muralidharan, D. K. Kim, *Solid State Ionics* **2008**, *178*, 1990; b) T. Klemensø, J. Nielsen, P. Blennow, Å. H. Persson, T. Stegk, B. H. Christensen, S. Sønderby, *J. Power Sources* **2011**, *196*, 9459; c) J. Nielsen, T. Klemensø, P. Blennow, *J. Power Sources* **2012**, *219*, 305; d) E. M. Sala, N. Mazzanti, M. B. Mogensen, C. Chatzichristodoulou, *Solid State Ionics* **2022**, *375*, 115833.
[11] T. Malis, S. C. Cheng, R. F. Egerton, *J. Electron. Microsc. Tech.* **1988**, *8*, 193.
[12] C. Chatzichristodoulou, S. Ricote, S. P. V. Foghmoes, J. Glasscock, A. Kaiser, P. V. Hendriksen, *Solid State Ionics* **2015**, *269*, 51.
[13] a) V. Esposito, D. W. Ni, Z. He, W. Zhang, A. S. Prasad, J. A. Glasscock, C. Chatzichristodoulou, S. Ramousse, A. Kaiser, *Acta Mater.* **2013**, *61*, 6290; b) J. Chen, M. Ouyang, P. Boldrin, A. Atkinson, N. P. Brandon, *ACS Appl. Mater. Interfaces* **2020**, *12*, 47564.

© 2023 The Authors. Small Methods published by Wiley-VCH GmbH

23669608, 0, Downloaded from https://onlinelibrary.wiley.com/doi/10.1002/smtd.202201713 by Danish Technical Knowledge, Wiley Online Library on [01/06/2023]. See the Terms and Conditions (https://onlinelibrary.wiley.com/terms-and-conditions) on Wiley Online Library for rules of use; OA articles are governed by the applicable Creative Commons License

[14] a) B. Goris, S. Turner, S. Bals, G. Van Tendeloo, *ACS Nano* **2014**, *8*, 10878; b) S.-G. Frederik, *Master thesis*, DTU Energy, DTU, Kgs. Lyngby, **2020**; c) R. Sinclair, S. C. Lee, Y. Shi, W. C. Chueh, *Ultramicroscopy* **2017**, *176*, 200.
[15] a) X. Guo, R. Waser, *Prog. Mater. Sci.* **2006**, *51*, 151; b) Y. Lin, S. Fang, D. Su, K. S. Brinkman, F. Chen, *Nat. Commun.* **2015**, *6*, 6824.
[16] P. Marmet, L. Holzer, J. G. Grolig, H. Bausinger, A. Mai, J. M. Brader, T. Hocker, *Phys. Chem. Chem. Phys.* **2021**, *23*, 23042.
[17] a) W. Lai, S. M. Haile, *J. Am. Ceram. Soc.* **2005**, *88*, 2979; b) X. Guo, W. Sigle, J. Maier, *J. Am. Ceram. Soc.* **2003**, *86*, 77.
[18] D. Pérez-Coll, E. Céspedes, A. J. Dos santos-García, G. C. Mather, C. Prieto, *J. Mater. Chem. A* **2014**, *2*, 7410.
[19] W. C. Chueh, S. M. Haile, *Phys. Chem. Chem. Phys.* **2009**, *11*, 8144.
[20] a) G. B. Balazs, R. S. Glass, *Solid State Ionics* **1995**, *76*, 155; b) T. Kudo, H. Obayashi, *J. Electrochem. Soc.* **1975**, *122*, 142.
[21] C. Chatzichristodoulou, P. V. Hendriksen, *Phys. Chem. Chem. Phys.* **2011**, *13*, 21558.
[22] N. Mazzanti, *in submission* **2022**.
[23] a) S. Wang, T. Kobayashi, M. Dokiya, T. Hashimoto, *J. Electrochem. Soc.* **2000**, *147*, 3606; b) M. Mogensen, N. M. Sammes, G. A. Tompsett, *Solid State Ionics* **2000**, *129*, 63.
[24] J. Jamnik, J. Maier, *J. Electrochem. Soc.* **1999**, *146*, 4183.
[25] N. Mazzanti, *Ph.D. thesis* , DTU Energy, DTU, Kgs. Lyngby, **2021**.
[26] a) Z. A. Feng, F. El Gabaly, X. Ye, Z.-X. Shen, W. C. Chueh, *Nat. Commun.* **2014**, *5*, 4374; b) T. Wu, Q. Deng, H. A. Hansen, T. Vegge, *J. Phys. Chem. C* **2019**, *123*, 5507.
[27] Y. Choi, S. K. Cha, H. Ha, S. Lee, H. K. Seo, J. Y. Lee, H. Y. Kim, S. O. Kim, W. Jung, *Nat. Nanotechnol.* **2019**, *14*, 245.
[28] G. J. Brug, A. L. G. van den Eeden, M. Sluyters-Rehbach, J. H. Sluyters, *J. Electroanal. Chem. Interfacial Electrochem.* **1984**, *176*, 275.
[29] Y.-W. Lan, W.-H. Chang, Y.-C. Chang, C.-S. Chang, C.-D. Chen, *Nanotechnology* **2015**, *26*, 055705.
[30] T. W. Hansen, J. B. Wagner, J. R. Jinschek, R. E. Dunin-Borkowski, *Microsc. Microanal.* **2009**, *15*, 714.
[31] L.-j. Liu, J.-j. Wang, presented at *2001 6th Int. Conf. on Solid-State Integrated Circuit Technol. Proc. (Cat. No.01EX443)*, Shanghai, China, October **2001**.

 © 2023 The Authors. Small Methods published by Wiley-VCH GmbH

23669608, 0, Downloaded from https://onlinelibrary.wiley.com/doi/10.1002/smtd.202201713 by Danish Technical Knowledge, Wiley Online Library on [01/06/2023]. See the Terms and Conditions (https://onlinelibrary.wiley.com/terms-and-conditions) on Wiley Online Library for rules of use; OA articles are governed by the applicable Creative Commons License

Appendix 2: *Manuscript of "Ion-beam deposited platinum as electrical contacting material in operando electron microscopy experiments at elevated temperatures"*

Ion-beam deposited platinum as electrical contacting material in *operando* electron microscopy experiments at elevated temperatures

Søren Bredmose Simonsen[a*], Zhongtao Ma[a], Elisabeth Mariegaard[a], Salvatore De Angelis[a], Waynah Lou Dacayan[a], Kristian Speranza Mølhave[b], Christodoulos Chatzichristodoulou[a]

[a]DTU Energy, Fysikvej, Kgs. Lyngby. Denmark,
[b]DTU Nanolab, Ørsteds Plads, Kgs. Lyngby. Denmark.
*sobrs@dtu.dk

Abstract

Establishing a stable and well conducting contacting material is critical for *operando* electron microscopy experiments of electrical and electrochemical devices at elevated temperatures. In this contribution, the nanostructure and electrical conductivity of ion beam deposited Pt are investigated both in vacuum and in oxygen as a function of temperature. Its microstructure is relatively stable up to a temperature of approx. 800 °C and up to an applied current density of approx. 100 kA/cm^2. Its conductivity increases with temperature, attributed to densification, with changes in the hydrocarbon matrix being less important. Recommendations are provided with respect to the Pt deposition parameters in terms of maximizing stability and minimizing electrical resistance.

Keywords: ion-beam deposited Pt, conductivity, resistance, *operando* electron microscopy, electrical measurements

1. Introduction

In electron microcopy, *in-situ* and *operando* methods are becoming increasingly more important. In particular, in transmission electron microscopy (TEM), the introduction of Micro Electronic Mechanical System (MEMS) chip-based holders has led to the rapid development of methodologies allowing to directly relate structure and composition with material functionality [1–10]. MEMS chips are also employed in conjunction with scanning electron microscopy (SEM) for *in-situ* and *operando* experiments [11,12].

One important class of *in-situ/operando* experiments involves electrical measurements, yielding the electrical or electrochemical response of materials/devices with nanoscale dimensions [9,10,13,14]. Such experiments have given insight into e.g. solid state battery dynamics [15–19]. With the use of combined heating-biasing holders, such measurements can be performed as a function of temperature [11]. In a recent study, we showed that by combining the heating-biasing chips with an environmental TEM (ETEM) it is possible to perform reliable electrochemical impedance spectroscopy (EIS) measurements of solid oxide cell components in the TEM [20].

For electrical measurements, it is crucial to ensure sufficient electrical contact between the sample and the current collecting pads of the MEMS chip. To realize this, lithography methods are sometimes used to deposit a conducting material connecting the sample with the MEMS chip [21,22]. Another method is ion-beam (IB) or electron-beam (EB) deposition using a focused ion beam SEM (FIB-SEM) [23]. An advantage of this approach is that the sample can be mounted precisely on the MEMS chip with a micro-manipulator while using the IB to deposit the conducting and connecting material, as well as for further thinning and adjusting the sample and contact geometry.

Materials that are commonly available for IB deposition in a FIB are Pt [24,25], C [26], and W [27,28]. Other metals such as Au [29,30], Pd [31], Al [32], Cu [33], Fe [34], Ta [27], as well as insulators, e.g. SiO_2 [35], and tetraethoxysilane (TEOS) [36] are also used. For electrical measurements in vacuum and at RT, all metals can be used for contacting. For experiments at elevated temperature, a thermally stable material must be employed. Here, C, W, Ta, Pt and Pd are the best candidates. If the *in-situ* experiment is performed in a gas phase (e.g., in an ETEM), an inert contacting material is required. For high temperature experiments performed in an oxidizing gas, materials that easily oxidize cannot be used, which excludes C, W, Ta, Al, Cu, Fe, and to some extent Pd. Accordingly, Pt stands out as the most versatile contacting material and seems to be the best candidate for *in-situ/operando* experiments in oxidizing gasses at elevated temperatures. For these reasons, this work focuses on Pt as electrical contacting material.

IB- and EB-deposited Pt has a complex nanostructure with a mixture of Pt nanoparticles and partly decomposed Pt-containing hydrocarbon species from the precursor [23,24]. The Pt-to-hydrocarbon ratio depends on the deposition conditions, with increasing Pt content upon increasing IB current [24]. For EB deposition, the Pt content is typically lower [37]. For IB deposition, the material will also contain ions from the FIB source (e.g. Ga, Ar, Xe, etc.).

The deposition method and conditions impact the conductivity of the deposited material. Tao et al. reported that the resistivity of IB deposited Pt increases 10^3 times (from approx. 70 µΩ cm to 70 mΩ cm) when decreasing the beam current by a factor of 10 (from 222 to 22 pA) [24]. The resistivity of EB-deposited Pt is generally even higher, with reported values varying within a factor of 10^3 from approx. 4 mΩ cm [37] to approx. 1 Ω cm [23]. Both IB- and EB-deposited Pt have much higher resistivity compared to bulk Pt (approx. 0.1 µΩ cm), making it challenging to carry out resistivity measurements of highly conductive materials. Since IB-deposited Pt has higher conductivity compared to EB-deposited Pt, this is usually the best choice as a contacting material. Only in cases that require minimal overspray of the deposited Pt, it can be necessary to use EB deposition [15].

In the present study, we investigate the conductivity of IB-deposited Pt as a function of temperature, up to 900 °C where instability of the contacting material was observed. The experiments are carried out both in vacuum and in 2 mbar of O_2 in an ETEM, to study the possible influence of an oxidizing gas environment. In addition, the relation between the applied current and internal Joule heating of the Pt is described. Finally, we investigate the effect of a thermal oxidation pre-treatment to remove the hydrocarbon precursor from the IB-deposited Pt to form a pure metallic Pt contacting material.

2. Methods

2.1 Ion-deposition

Pt was IB-deposited on commercial MEMS heating-biasing chips (DENS solutions). The conditions for the various depositions are presented in Table 1. In all cases, the precursor $C_5H_4CH_3Pt(CH_3)_3$ (purchased from Zeiss) was used.

Table 1: Ion beam deposition conditions, deposition thickness and conditions for the in situ experiment.

Acronym	Ion	Voltage (kV)	Current (pA)	Thickness (nm)	***In-situ*** **condition**
GaPt	Ga	30	20	80	2 mbar O_2
ArPt	Ar	30	200	200	vacuum
XePt	Xe	30	300	200	vacuum

2.2 Microscopy and Electrical measurements

Imaging and electrical measurements were conducted in a Crossbeam 1540XB SEM with a field-emission gun (ZEISS), a TM3000 SEM (ZEISS) with an Quantax EDS detector (Brucker), and a Titan 80-300 ETEM [38]. TEM images were recorded at 300 kV using a OneView Camera (Gatan). SEM images were recorded with the Crossbeam at 10 kV using an Everhart Thornley Detector and with the TM3000 at 15 kV using a backscatter detector.

For experiments in vacuum, the heating and electrical polarization were performed using a Keithley Model 2450 and the Impulse software (DENS solutions). The MEMS chips were connected to the Keithley via a Lightning heating-biasing TEM holder or an *in-situ* FIB stub in the FIB-SEM (both DENS solutions). Four probe measurements were conducted by applying a constant current in steps up to 2 mA while measuring the voltage from which the resistance was calculated.

For the ETEM experiment, a Gamry FAS2 Femtostat was connected to the TEM holder. Two-point electrochemical impedance spectroscopy (EIS) was conducted within the frequency range 0.1-10^5 Hz and amplitude of 20 mV. The method of combining EIS with ETEM for nanoscale samples in gasses and elevated temperatures has recently been described in detail [20]. The resistance was obtained from the analysis of Nyquist plots. For comparison, linear sweep voltammetry (LSV) in the range 0-5 mV was also conducted and the resistance was extracted from the slope. The measured resistances from EIS and LSV were almost identical and only the values from EIS are presented in the following analysis. The ETEM experiments were performed in 2 mbar O_2.

For all experiments, the temperature was ramped stepwise. Imaging and electrical measurements were performed while keeping the temperature constant. For the TEM analysis, the temperature ramping rate was 100 °C/min while for SEM it was 3 °C/min. To minimize the influence of the electron beam, the sample was only exposed when images were recorded, blanking the beam otherwise.

The resistivity and conductivity are calculated from the resistance by using the sample geometries. Here, the inner distance between the chip electrodes is used as the sample length. The width is measured from the SEM or TEM images. For the ETEM experiment, the Pt was deposited on the approx. 20 nm thick electron transparent SiN window. An approximately 80 nm thick Pt film was deposited in the center enforced by thicker layers (approx. 130 nm) on the sides. The thicknesses were measured using electron energy loss spectroscopy (EELS). For SEM experiments, the Pt was deposited on the 400 nm thick SiN support membrane. In this case, EELS measurement was not possible, due to the large total thickness, and the indicated Pt film thicknesses (Table 1) are the expected values according to the chosen deposition parameters.

3. Results and discussions

3.1. Conductivity at room temperature

Figure 1 presents SEM images of the deposited Pt films connecting the electrodes on commercial MEMS chips for *in-situ/operando* microscopy (deposition parameters described in Table 1). In this work, the Ar IB deposited Pt is not perfectly uniform and cavities or holes are observed (Figure 1a). On the contrary, the Xe and Ga ions give a more uniform deposition (Figure 1b-c). The inhomogenity will result in a larger uncertainty when calculating the resistivity from the measured resistance because the Pt film geometry is less well-defined.

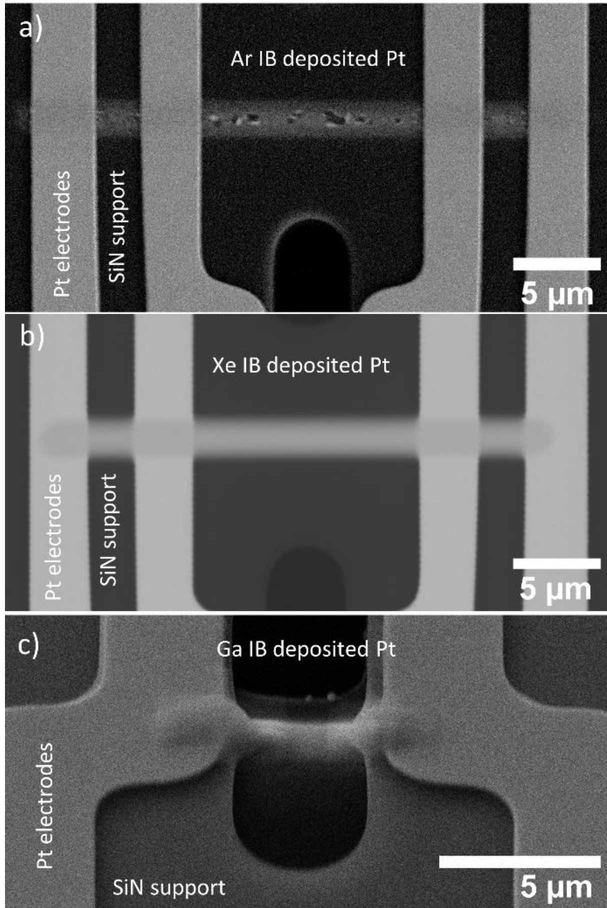

Figure 1: SEM images of MEMS chips with (a) Ar, (b) Xe and (c) Ga IB deposited Pt films.

Figure 2 presents the resistivity and conductivity as a function of ion current for the IB deposited Pt (deposition parameters described in Table 1). Generally, the conductivity increases as a function of the ion current, and this trend is consistent with a previous report from Tao et al. [24].

The resistivities of the IB deposited Pt films are 10^3-10^5 times higher than that of metallic Pt. According to Bruggeman's model the conductivity for a porous material, σ_{por} depends on the conductivity of the bulk material, σ_{bulk}, the volume fraction of the conducting phase, ε and the tortuosity, τ in the following way [39]:

$$\sigma_{por} = \sigma_{bulk}\frac{\varepsilon}{\tau}$$

The equation shows that the conductivity of the porous material is controlled by structural factors. Increasing porosity or tortuosity will decrease the conductivity. The relatively low conductivity for the IB deposited Pt according to Figure 2 is partly due to its porous nature with tortuosity values greater than 1. The deposited Pt may even, to some degree, consist of poorly connected Pt islands on the basis of previously reported nanostructures for EB deposited Pt [23].

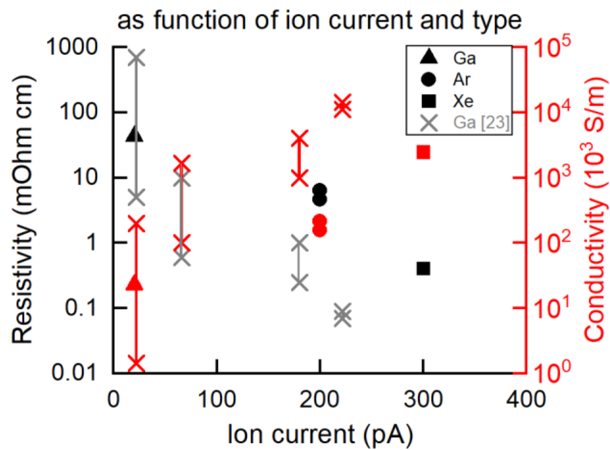

Figure 2: Resistivity (black and grey) and conductivity (red) as a function of ion current for IB deposited Pt. Data for Ga ions (triangles), Ar ions (circles) and Xe ions (squares) are compared to reference data [24] for Ga ions (X's). For the reference data the total ion dose was varied and the X's indicate the maximum and minimum values for each ion current.

3.2. Conductivity as a function of temperature

The temperature of IB deposited Pt (Figure 1a, ArPt in Table 1) was elevated in the high vacuum of an SEM (< 10^{-5} mbar).

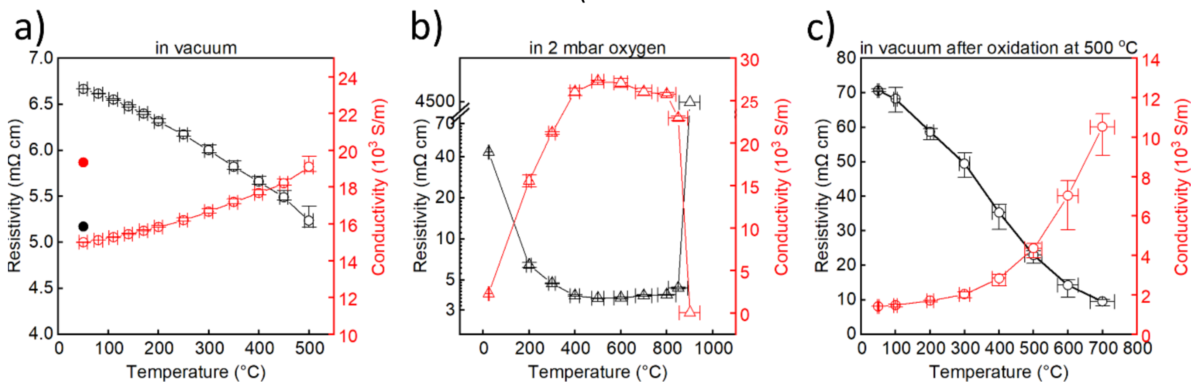

Figure 3a (open symbols) shows that the resistivity decreases (and conductivity increases) as a function of temperature up to 500 °C. The filled symbols present the resistivity and conductivity after ramping the temperature down and shows that the changes are irreversible. Zhong et al. observed a similar but much more pronounced trend for EB deposited Pt with approximately 10^3 times larger decrease in resistivity within the same temperature range [23]. They explained the temperature dependence by Pt crystallization and grain growth [23], leading to lower tortuosity and possibly lower porosity.

Below 500 °C, supported Pt nanoparticles are known to be relatively stable and the particle growth is not likely due to Ostwald ripening or particle migration [40–44]. The Pt particle growth could instead be due to the coalescence of Pt nanoparticles already in physical contact [45,46], and perhaps due to further decomposition of deposited Pt precursor.

When using deposited Pt as electrical contacting material, it is important that the resistivity is stable within the measuring conditions. According to Figure 3a, the resistivity stays within approx. 1 mΩ cm over a temperature range of approx. 500 °C. Larger changes in the measured resistivity of a sample connected to the electrodes with IB deposited Pt can therefore be attributed to the actual sample and not to changes in the contacting material.

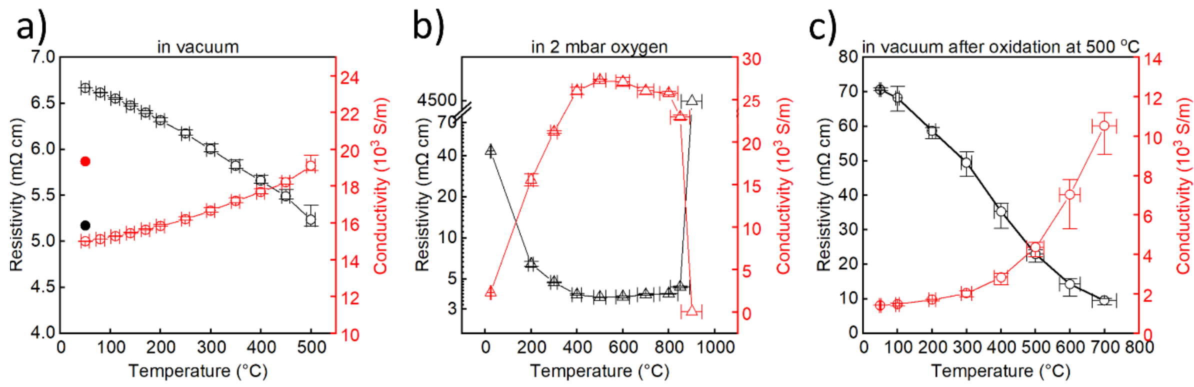

Figure 3: Resistivity (black) and conductivity (red) as function of a temperature for IB deposited Pt (a) Ar-IB, in vacuum, (b) Ga-IB, in 2 mbar O_2 in an ETEM and (c) Ar-IB, in vacuum after being heated to 500 °C in ambient air. The filled circles in (a) presents the measured values after ramping the temperature down.

3.3. Low oxygen pressure

In some cases, *operando* microscopy experiments are conducted in reactive gasses [20]. In an oxidizing environment, it can be expected that the hydrocarbon matrix and the surface of Pt will oxidize [47]. The conductivity of IB deposited Pt (GaPt in Table 1) was investigated in an ETEM in 2 mbar O_2.

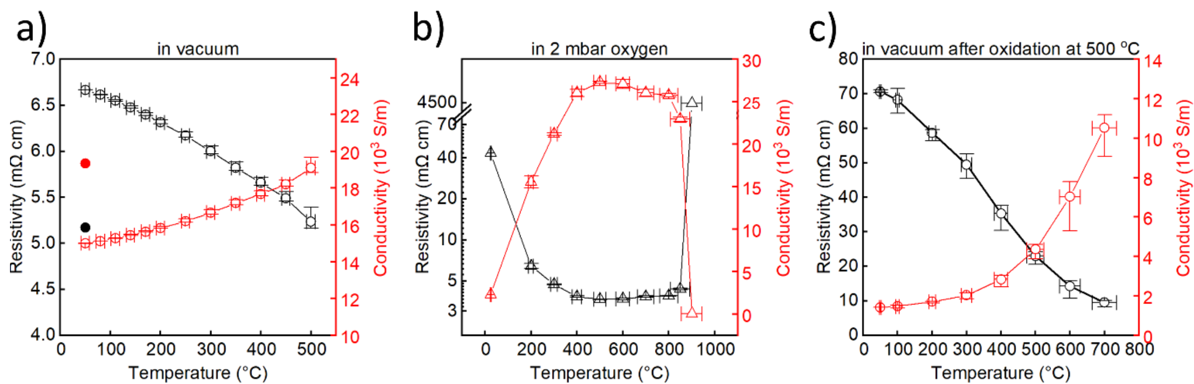

Figure 3b shows that the decrease in resistivity (and increase in conductivity) in 2 mbar O_2 up to 500 °C is approximately 10 times larger than that in vacuum. At the temperatures above 500 °C, the resistivity is relatively stable, until 900 °C where it increases by a factor of about 10^3.

Figure 4 presents EELS spectra in the energy range of the carbon edge (284 eV) recorded during the same experiment as presented by Figure 3b. The spectra show the presence of carbon in the sample at 300 °C and 400 °C, while the carbon has been fully removed at 500 °C. The sample was kept at 500 °C for 25 min before the EELS spectrum was recorded. This shows that the hydrocarbon matrix is removed by thermal oxidation, and that metallic Pt remains as the contacting material.

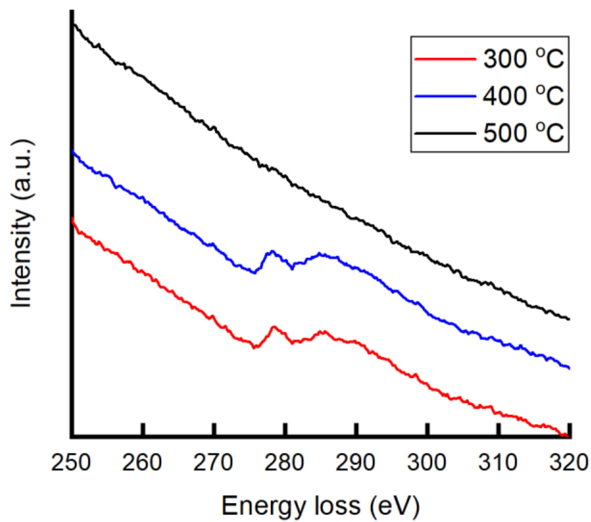

Figure 4: (a) EELS spectra of Ga IB deposited Pt recorded at 300 – 500 °C in 2 mbar O_2. The spectra energy range is chosen to show the C K-edge. The spectra are shifted relative to each other on the y-axis to avoid overlap.

The drastic increase in resistivity at 900 °C (

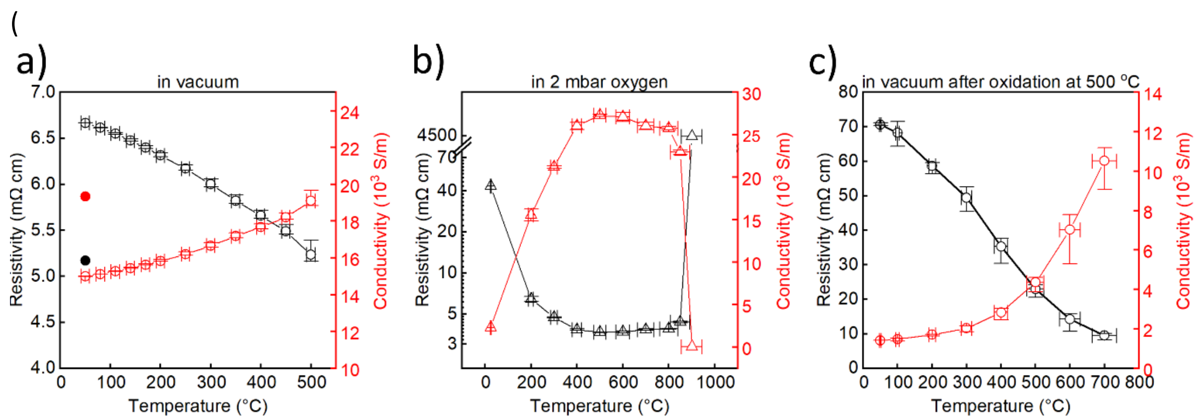

Figure 3b) is therefore not related to changes in the hydrocarbon matrix but must be associated with changes in the Pt nanostructure. This is supported by the ETEM images recorded in the same experiment (Figure 5). Up to 800 °C, the nanostructure of the deposited Pt appears to be relatively stable, despite the removal of the hydrocarbon matrix at 500 °C. At 850 °C, and more pronounced at 900 °C, Pt coarsening is observed as larger structures appear and larger contrast differences indicate regions with varying density of Pt. Since no Pt is added to the sample during the experiment, the Pt added to the denser regions must have migrated from other areas which leads to increased tortuosity.

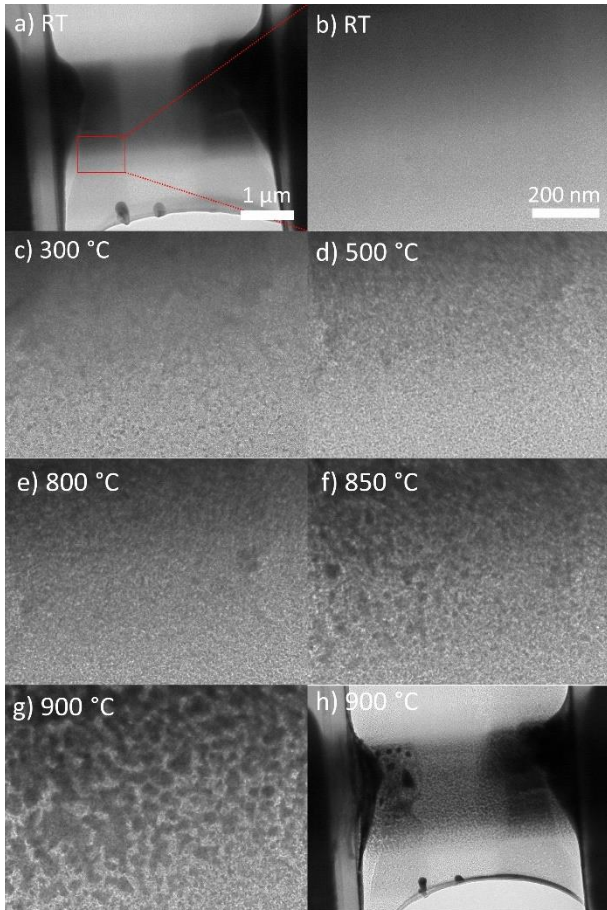

Figure 5: (a) presents a TEM image of Ga IB deposited Pt. (b-g) presents TEM images of the sample region marked by a red box in (a) as a function of temperature in 2 mbar O_2. The images are recorded approx. 5 min after reaching the indicated temperatures. (h) presents a TEM image recorded at 900 °C and at the same magnification as (a).

The results in

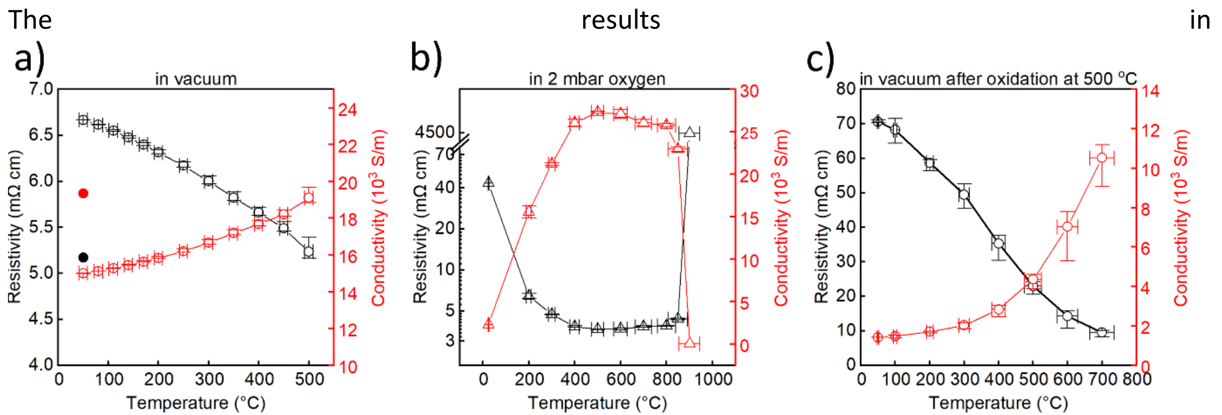

Figure 3 and Figure 5 show that IB-deposited Pt is relatively stable in O_2 at temperatures up to 800 °C both in terms of structure and conductivity. This means that IB-deposited Pt can be used as electrical contacting material for *operando* microscopy experiments in oxidizing gasses and up to approx. 800-850 °C. Above this temperature, the IB deposited Pt is not stable in O_2 and the electrical measurements are likely to be influenced by the drastic resistance increase in the contacting material.

3.4. High oxygen pressure

Although Pt is a noble metal, it is known that nanostructured Pt can surface oxidize [47]. In our case, where the electrical contacting material consists of connected Pt nanodomains, such surface oxidation may influence the overall conductivity. The ETEM experiment presented in the previous section was conducted in a relatively low oxygen pressure of 2 mbar. In this section, we present how the Pt conductivity is influenced when the oxygen pressure is increased by a factor of 100.

To investigate this, the *in-situ* SEM experiment presented in

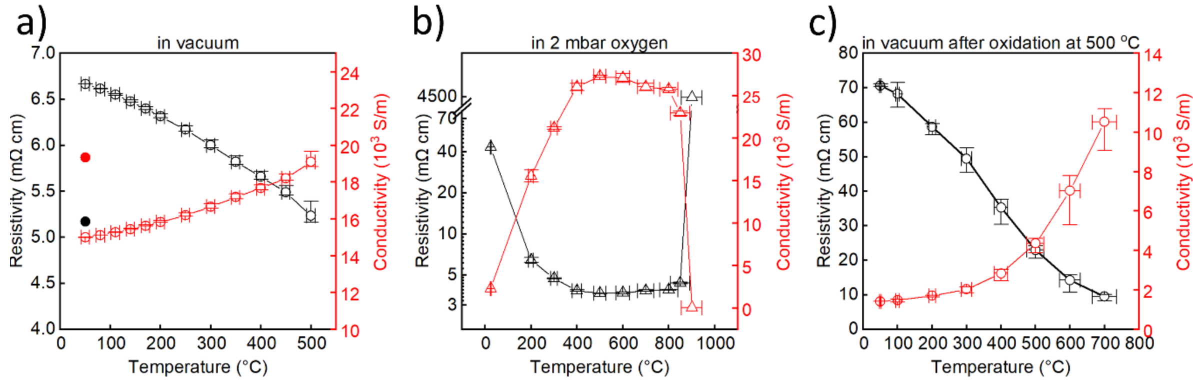

Figure 3a was stopped after reaching 500 °C, the *in-situ* stage was removed from the SEM, the temperature was raised to 500 °C and kept for about 20 min in ambient air.

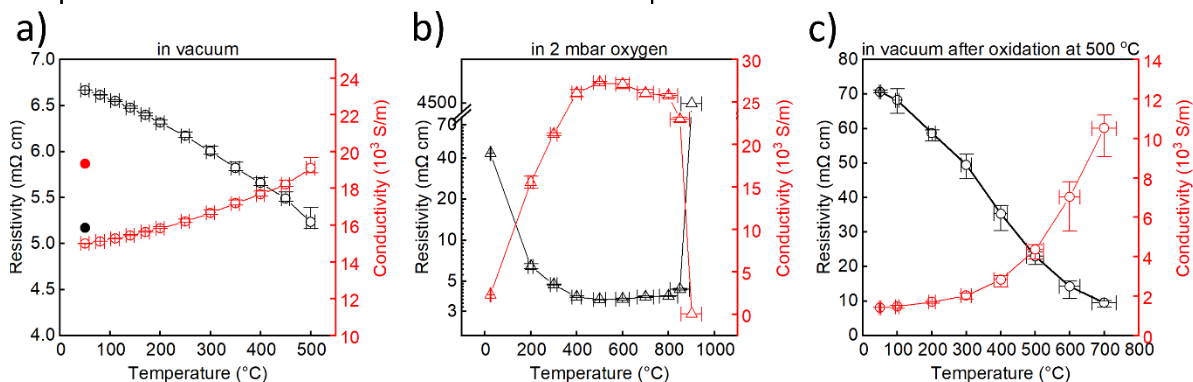

Figure 3c shows the temperature dependence of the resistivity (and conductivity) in the vacuum of the SEM after this treatment.

Interestingly, the oxidation in the higher oxygen concentration led to an increase in the resistivity by a factor of 10 (comparing Figure 3a and 3c). Complete removal of the hydrocarbon component is anticipated to occur with the treatment in air (Figure 4). The observed change must therefore be related to the Pt component and/or the film micro- and nanostructure. A treatment in 210 mbar O_2 will not lead to bulk oxidation of Pt, but it is known that surface-oxidation will take place [47]. It is likely that the higher O_2 concentration when heating in ambient air, leads to Pt surface oxidation to an extent that it worsens the electrical connections between metallic Pt nano-domains.

In conclusion,

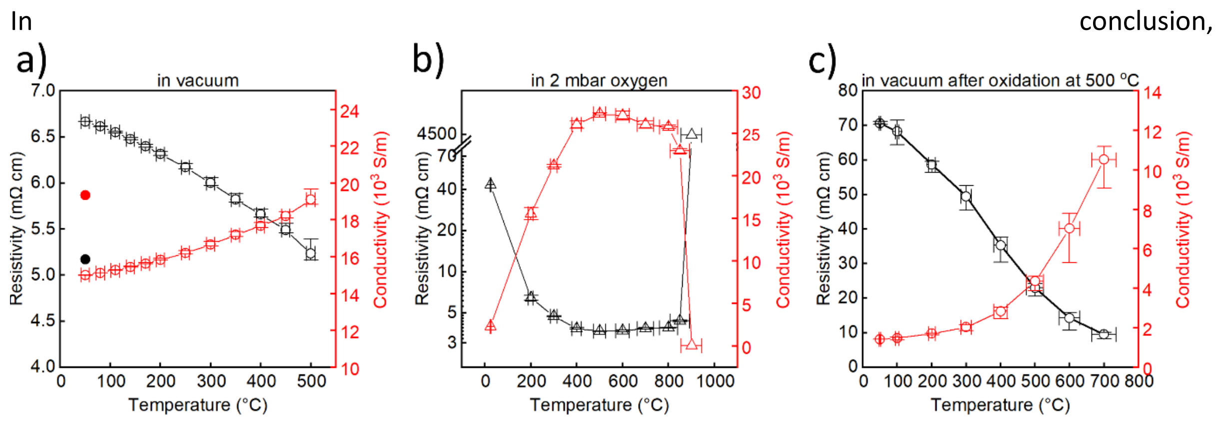

Figure 3 shows that in vacuum a pretreatment at 500 °C can stabilize the conductivity of IB deposited Pt. A similar pretreatment in ambient air will not stabilize the conductivity of IB deposited Pt, if the following *operando* experiment is to be carried out in vacuum.

3.5. Influence on conductivity from Joule heating

In the previous section, we found that the IB-deposited Pt is relatively stable as electronic contacting material at temperatures up to approx. 800-850 °C. This is, however, only when Joule heating from the electrical current in the Pt is not considered. In this section, we study the effect of electric current on the stability of the film.

In the vacuum of the SEM, films of deposited Pt (ArPt in Table 1) were exposed to a stepwise increase in the applied electrical current until a sudden decrease in electrical conductivity was observed. This was done for two different films: one kept at room temperature and one at 800 °C, just below the temperature where the IB-deposited Pt becomes unstable in 2 mbar O_2 according to Figure 3b.

Figure 6 presents the measured resistivity (and conductivity) as a function of current density at RT and at 800 °C. At RT, the resistivity is relatively stable for current densities up to approx. 100 kA/cm^2. At higher current densities, the resistivity decreases until a sudden increase at approx. 320 kA/cm^2. On the basis of the temperature dependence of the resistivity (Figure 3), this behavior can be attributed to the influence of Joule heating.

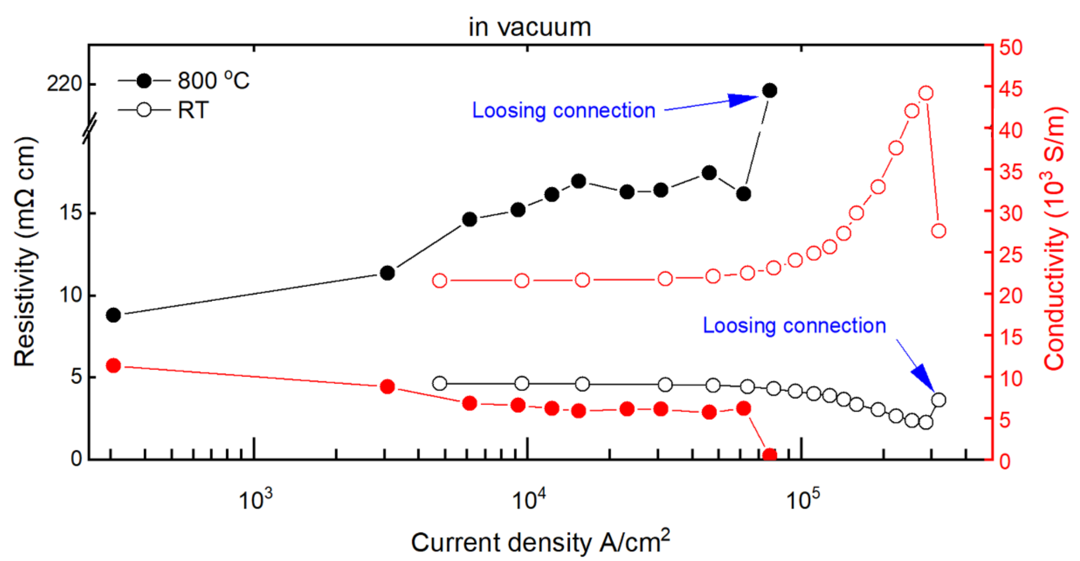

Figure 6: Resistivity (black) and conductivity (red) as function of applied current density through IB deposited Pt films measured in the vacuum of an SEM at RT (open symbols) and at 800 °C (filled symbols).

An SEM image was recorded for each step in applied current, showing no structural changes until reaching 320 kA/cm^2. Figure 7 shows that the structure changed significantly when going from 290 to 320 kA/cm^2. Inhomogeneities and holes were also observed in the Pt chip electrodes when applying a current density of 320 kA/cm^2. Mele at al. performed a similar experiment using Ga IB deposited Pt and observed loss of electrical contact at approx. 500 kA/cm^2 [1], which is in the same order of magnitude to the value observed in the present study. EDS analysis (Figure 7c) shows that the bright pattern that appears around the film during exposure to a current density of 320 kA/cm^2 (Figure 7b) consists of Pt, apparently mobile in the heated region between the microelectrode contacts that act as heat sink.

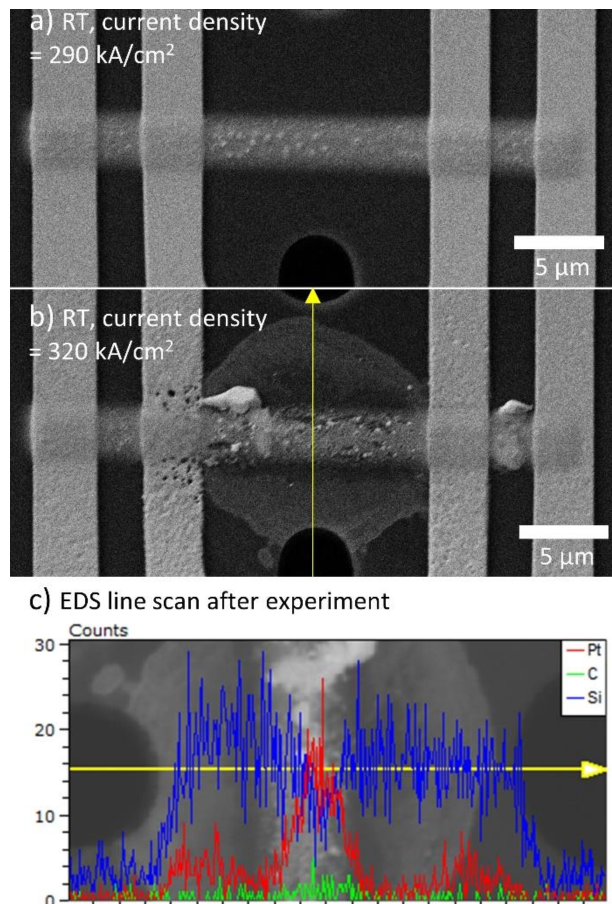

Figure 7: (a-b) SEM images of a MEMS chip with Ar IB deposited Pt recorded at RT when applying a current density of (a) 290 kA/cm^2 and (b) 320 kA/cm^2. (c) EDS line scan overlayed with an SEM image. The yellow lines in (b) and (c) indicate where the line scan was recorded.

When raising the temperature via the heating element of the chip and Joule heating via an electric current through the deposited Pt, it can be expected that loss in the electrical connection will be observed at lower currents compared to RT. Indeed, as shown in Figure 6, the resistivity at 800 °C is relatively stable only up to approx. 60 kA/cm^2, while it increases abruptly above this value.

From these results, we conclude that when using IB deposited Pt as electrical contacting material, the applied current densities should be kept below a few hundred kA/cm^2 to operate in a stable regime. However, when the temperature is raised by a heating element on the chip, the maximum current density limit needs to be lowered. The higher the temperature, the lower the limit.

3.6. Time and electron beam

Two limitations should be mentioned regarding the present results. The effect of time and of the electron beam has not been investigated in this study. Even though the IB deposited Pt was relatively stable at 800 °C below approx. 60 kA/cm^2 or at RT below approx. 300 kA/cm^2, instability may have been observed if the experiments were performed over a longer time span as electromigration over time can cause disconnection [48].

Also, it has been well-documented that Pt nanostructures are sensitive to effects of the electron beam and can easily be mistaken for thermal instabilities [41]. In this study, the beam dose was minimized in the electron microscopes by only exposing the sample to the electron beam when images were recorded, and the beam was otherwise blanked. The images showed no signs of structural changes by the beam. However, it cannot be fully excluded that the electron beam had an effect which was not observed in the images, but nevertheless influenced the electrical measurements.

4. Conclusion

IB deposited Pt is a good option as electrical contacting material when performing *in-situ* or *operando* electron microscopy in vacuum or in oxygen, and at temperatures of 20-800 °C. The structure of the IB deposited Pt is relatively stable up to a temperature of approx. 800 °C and up to an applied current density of approx. 100 kA/cm^2. The conductivity is observed to irreversibly increase as a function of temperature. This is mainly explained by thermally activated coarsening and densification of the nanostructured Pt. On the contrary, high temperature treatment in ambient conditions can deteriorate conductivity, likely by Pt surface oxidation.

The resistivity of IB deposited Pt films is generally high compared to good electronic conductors. For example, 10^3-10^5 times higher than that of bulk metallic Pt. This can make it challenging to conduct accurate measurements on highly conducting materials. The routes to lowering the resistance of the contacting material is a) depositing thicker layers and b) reducing the resistivity. The resistivity of the contacting material can be reduced by increasing the applied ion current during deposition and by thermal annealing at a temperature of 500 °C in a few mbar of oxygen.

Acknowledgments

This project has received funding from the European Research Council (ERC) under the European Union’s Horizon 2020 research and innovation programme (grant agreement No 850850)”

References

[1] L. Mele, S. Konings, P. Dona, F. Evertz, C. Mitterbauer, P. Faber, R. Schampers, J.R. Jinschek, A MEMS-based heating holder for the direct imaging of simultaneous *in-situ* heating and biasing experiments in scanning/transmission electron microscopes, Microsc. Res. Tech. 79 (2016) 239–250. https://doi.org/10.1002/jemt.22623.

[2] F. Niekiel, S.M. Kraschewski, J. Müller, B. Butz, E. Spiecker, Local temperature measurement in TEM by parallel beam electron diffraction, Ultramicroscopy. 176 (2017) 161–169. https://doi.org/10.1016/j.ultramic.2016.11.028.

[3] T. Yokosawa, T. Alan, G. Pandraud, B. Dam, H. Zandbergen, In-situ TEM on (de)hydrogenation of Pd at 0.5-4.5bar hydrogen pressure and 20-400°C, Ultramicroscopy. 112 (2012) 47–52. https://doi.org/10.1016/j.ultramic.2011.10.010.

[4] A. Zintler, U. Kunz, Y. Pivak, S.U. Sharath, S. Vogel, E. Hildebrandt, H.J. Kleebe, L. Alff, L.

Molina-Luna, FIB based fabrication of an operative Pt/HfO_2/TiN device for resistive switching inside a transmission electron microscope, Ultramicroscopy. 181 (2017) 144–149. https://doi.org/10.1016/j.ultramic.2017.04.008.

[5] S. Vijayan, M. Aindow, Temperature calibration of TEM specimen heating holders by isothermal sublimation of silver nanocubes, Ultramicroscopy. 196 (2019) 142–153. https://doi.org/10.1016/j.ultramic.2018.10.011.

[6] J.F. Creemer, S. Helveg, P.J. Kooyman, A.M. Molenbroek, H.W. Zandbergen, P.M. Sarro, A MEMS reactor for atomic-scale microscopy of nanomaterials under industrially relevant conditions, J. Microelectromechanical Syst. 19 (2010) 254–264. https://doi.org/10.1109/JMEMS.2010.2041190.

[7] L.F. Allard, W.C. Bigelow, M. Jose-Yacaman, D.P. Nackashi, J. Damiano, S.E. Mick, A new MEMS-based system for ultra-high-resolution imaging at elevated temperatures, Microsc. Res. Tech. 72 (2009) 208–215. https://doi.org/10.1002/jemt.20673.

[8] F. Gaulandris, S.B. Simonsen, J.B. Wagner, K. Mølhave, S. Muto, L.T. Kuhn, Methods for Calibration of Specimen Temperature during in Situ Transmission Electron Microscopy Experiments, Microsc. Microanal. 26 (2020) 3-17. https://doi.org/10.1017/S1431927619015344.

[9] S.B. Alam, C.R. Andersen, F. Panciera, A.A.S. Nilausen, O. Hansen, F.M. Ross, K. Mølhave, In situ TEM modification of individual silicon nanowires and their charge transport mechanisms, Nanotechnology. 31 (2020) 494002. https://doi.org/10.1088/1361-6528/ababc8.

[10] H. Zheng, X. Lu, K. He, In situ transmission electron microscopy and artificial intelligence enabled data analytics for energy materials, J. Energy Chem. 68 (2022) 454–493. https://doi.org/10.1016/j.jechem.2021.12.001.

[11] D. Schwarzbach, J. Gonzalez-Julian, O. Guillon, V. Roddatis, C.A. Volkert, Towards In-Situ Electron Microscopy Studies of Flash Sintering, Ceramics 2 (2019) 472-487. https://doi.org/10.3390/ceramics2030036.

[12] K. Mølhave, D.N. Madsen, S. Dohn, P. Bøggild, Constructing, connecting and soldering nanostructures by environmental electron beam deposition, Nanotechnology. 15 (2004) 1047–1053. https://doi.org/10.1088/0957-4484/15/8/033.

[13] R.J. Kamaladasa, A.A. Sharma, Y.-T. Lai, W. Chen, P.A. Salvador, J.A. Bain, M. Skowronski, Y.N. Picard, *In Situ* TEM Imaging of Defect Dynamics under Electrical Bias in Resistive Switching Rutile-TiO_2, Microsc. Microanal. 21 (2015) 140–153. https://doi.org/10.1017/S1431927614013555.

[14] B. Haas, J.L. Rouvière, V. Boureau, R. Berthier, D. Cooper, Direct comparison of off-axis holography and differential phase contrast for the mapping of electric fields in semiconductors by transmission electron microscopy., Ultramicroscopy. 198 (2019) 58–72. https://doi.org/10.1016/J.ULTRAMIC.2018.12.003.

[15] M. Hammad Fawey, V.S.K. Chakravadhanula, M.A. Reddy, C. Rongeat, T. Scherer, H. Hahn, M. Fichtner, C. Kübel, In situ TEM studies of micron-sized all-solid-state fluoride ion batteries: Preparation, prospects, and challenges, Microsc. Res. Tech. 79 (2016) 615–624. https://doi.org/10.1002/jemt.22675.

[16] Z. Yang, Z. Zhu, J. Ma, D. Xiao, X. Kui, Y. Yao, R. Yu, X. Wei, L. Gu, Y.-S. Hu, H. Li, X. Zhang, Z. Yang, J. Ma, D. Xiao, Y. Yao, R. Yu, L. Gu, Y. Hu, H. Li, Z. Zhu, X. Zhang, X. Kui, X. Wei, Phase Separation of Li_2S/S at Nanoscale during Electrochemical Lithiation of the Solid-State Lithium-

Sulfur Battery Using In Situ TEM, Adv. Energy Mater. 6 (2016) 1600806. https://doi.org/10.1002/aenm.201600806.

[17] Z. Wang, Y. Tang, L. Zhang, M. Li, Z. Shan, J. Huang, In Situ TEM Observations of Discharging/Charging of Solid-State Lithium-Sulfur Batteries at High Temperatures, Small 16 (2020) 2001899. https://doi.org/10.1002/smll.202001899.

[18] Z. Zhang, Z. Wang, L. Zhang, D. Liu, C. Yu, X. Yan, J. Xie, J. Huang, Unraveling the Conversion Evolution on Solid-State Na–SeS_2 Battery via In Situ TEM, Adv. Sci. 9 (2022) 2200744. https://doi.org/https://doi.org/10.1002/advs.202200744.

[19] S. Basak, K. Dzieciol, Y.E. Durmus, H. Tempel, H. Kungl, C. George, J. Mayer, R.-A. Eichel, Characterizing battery materials and electrodes via in situ/operando transmission electron microscopy, Chem. Phys. Rev. 3 (2022) 31303. https://doi.org/10.1063/5.0075430.

[20] Z. Ma, W. Lou Dacayan, C. Chatzichristodoulou, K.S. Mølhave, F.M. Chiabrera, W.A. Zhang, S.B. Simonsen, Electrochemical Impedance Spectroscopy integrated with Environmental Transmission Electron Microscopy, Small Methods. accepted (2023).

[21] A. Seeger, S. Paulson, M. Falvo, A. Helser, R.M.T. Ii, R. Superfine, S. Washburn, Hands-on tools for nanotechnology, Cit. J. Vac. Sci. Technol. B Microelectron. Nanom. Struct. Process. 19 (2001) 2717. https://doi.org/10.1116/1.1412890.

[22] S.A. Evans, J.L. Bartelt, B.J. Sloan, G.L. Varnell, Fabrication of Integrated Injection Logic Using E-Beam Lithography., J Vac Sci Technol. 15 (1978) 969–972. https://doi.org/10.1116/1.569687.

[23] C. Zhong, R. Qi, Y. Zheng, Y. Cheng, W. Song, R. Huang, The relationships of microscopic evolution to resistivity variation of a FIB-deposited platinum interconnector, Micromachines. 11 (2020). 588. https://doi.org/10.3390/MI11060588.

[24] T. Tao, J. Ro, J. Melngailis, Z. Xue, H.D. Kaesz, Focused ion beam induced deposition of platinum, J. Vac. Sci. Technol. B Microelectron. Nanom. Struct. 8 (1990) 1826. https://doi.org/10.1116/1.585167.

[25] J. Puretz, L.W. Swanson, Focused ion beam deposition of Pt containing films, J. Vac. Sci. Technol. B Microelectron. Nanom. Struct. 10 (1992) 2695. https://doi.org/10.1116/1.586028.

[26] B. Van Leer, Y.-C. Wang, L.A. Ciannuzzi, Protective Carbon Deposition for Superior FIB Prepared (S)TEM Specimens, in: Microsc. Microanal., 2009: pp. 336–337. https://doi.org/10.1017/S1431927609093428.

[27] K. Gamo, D. Takehara, Y. Hamamura, M. Tomita, S. Namba, Maskless ion beam assisted deposition of W and Ta films, Microelectron. Eng. 5 (1986) 163–170. https://doi.org/10.1016/0167-9317(86)90043-2.

[28] Z. Xu, T. Kosugi, K. Gamo, S. Namba, An x-ray photoelectron spectroscopy study on ion beam induced deposition of tungsten using WF_6, J. Vac. Sci. Technol. B Microelectron. Nanom. Struct. 7 (1989) 1959. https://doi.org/10.1116/1.584656.

[29] J.S. Ro, A.D. Dubner, C.V. Thompson, J. Melngailis, Microstructure of Gold Films Grown by Ion Induced Deposition, MRS Proc. 101 (1987) 255. https://doi.org/10.1557/PROC-101-255.

[30] P.G. Blauner, S. Ro, Y. Butt, J. Melngailis, Focused ion beam fabrication of submicron gold structures, J. Vac. Sci. Technol. B Microelectron. Nanom. Struct. 7 (1989) 609. https://doi.org/10.1116/1.584803.

[31] M.E. Gross, W.L. Brown, J. Linnros, L.R. Harriott, K.D. Cummings, H.O. Funsten, Photon and

Ion Beam-Induced Chemistry of Palladium Acetate Films, MRS Online Proc. Libr. 75 (1986) 91–97. https://doi.org/10.1557/PROC-75-91.

[32] K. Gamo, N. Takakura, D. Takehara, S. Namba, Characteristics of Selective Deposition of Metal Organic Films Using Focused Ion Beams., Conf. Solid State Devices Mater. (1984) 31–34. https://doi.org/10.7567/ssdm.1984.a-2-5.

[33] A.D. Della Ratta, J. Melngailis, C. V. Thompson, Focused-ion beam induced deposition of copper, J. Vac. Sci. Technol. B Microelectron. Nanom. Struct. 11 (1993) 2195. https://doi.org/10.1116/1.586455.

[34] K. Furuya, Nanofabrication by advanced electron microscopy using intense and focused beam, Sci. Technol. Adv. Mater. 9 (2008) 14110. https://doi.org/10.1088/1468-6996/9/1/014110.

[35] H. Komano, Y. Ogawa, T. Takigawa, Silicon oxide film formation by focused ion beam (FIB)-assisted deposition, Jpn. J. Appl. Phys. 28 (1989) 2372–2375. https://doi.org/10.1143/JJAP.28.2372.

[36] R.J. Young, J. Puretz, Focused ion beam insulator deposition, J. Vac. Sci. Technol. B Microelectron. Nanom. Struct. 13 (1995) 2576. https://doi.org/10.1116/1.588026.

[37] Protochips, Sample Prep Fib Sample Preparation, (2017). http://www.protochips.com/wp-content/uploads/2017/10/prep-fib-samples.pdf.

[38] T. Hansen, J. Wagner, J. Jinschek, R. Dunin-Borkowski, The Titan Environmental Transmission Electron Microscope: Specifications, Considerations and First Results, Microsc. Microanal. 15 (2009) 714–715. https://doi.org/10.1017/S1431927609097396.

[39] B. Tjaden, S.J. Cooper, D.J. Brett, D. Kramer, P.R. Shearing, On the origin and application of the Bruggeman correlation for analysing transport phenomena in electrochemical systems, Curr. Opin. Chem. Eng. 12 (2016) 44–51. https://doi.org/10.1016/j.coche.2016.02.006.

[40] P. Lööf, B. Stenbom, H. Nordén, B. Kasemo, Rapid Sintering in NO of Nanometre-Sized Pt Particles on gamma-Al_2O_3 Oberved by CO Temperature-Programmed Desorption and Transmission Electron Microscopy, J. Catal. 144 (1993) 60–76. https://doi.org/10.1006/jcat.1993.1314.

[41] S.B. Simonsen, I. Chorkendorff, S. Dahl, M. Skoglundh, J. Sehested, S. Helveg, Direct observations of oxygen-induced platinum nanoparticle ripening studied by in situ TEM, J. Am. Chem. Soc. 132 (2010) 7968–7975. https://doi.org/10.1021/ja910094r.

[42] S.B. Simonsen, I. Chorkendorff, S. Dahl, M. Skoglundh, J. Sehested, S. Helveg, Ostwald ripening in a Pt/SiO_2 model catalyst studied by in situ TEM, J. Catal. 281 (2011) 147–155. https://doi.org/10.1016/j.jcat.2011.04.011.

[43] S.B. Simonsen, I. Chorkendorff, S. Dahl, M. Skoglundh, K. Meinander, T.N. Jensen, J. V. Lauritsen, S. Helveg, Effect of particle morphology on the ripening of supported Pt nanoparticles, J. Phys. Chem. C. 116 (2012) 5646–5653. https://doi.org/10.1021/jp2098262.

[44] S.B. Simonsen, Y. Wang, J.O. Jensen, W. Zhang, Coarsening of carbon black supported Pt nanoparticles in hydrogen, Nanotechnology. 28 (2017) 475710. https://doi.org/10.1088/1361-6528/aa91a8.

[45] P. Wynblatt, N.A. Gjostein, Supported Metal Crystallites, Prog. Solid State Chem. 9 (1976) 21–58. https://doi.org/10.1016/0079-6786(75)90013-8.

[46] M.A. Asoro, D. Kovar, Y. Shao-Horn, L.F. Allard, P.J. Ferreira, Coalescence and sintering of Pt

nanoparticles: *in situ* observation by aberration-corrected HAADF STEM, Nanotechnology. 21 (2010) 025701. https://doi.org/10.1088/0957-4484/21/2/025701.

[47] M.A. Van Spronsen, J.W.M. Frenken, I.M.N. Groot, Observing the oxidation of platinum, Nat. Commun. 8 (2017) 429. https://doi.org/10.1038/s41467-017-00643-z.

[48] G.L. Baldini, I. De Munari, A. Scorzoni, F. Fantini, Electromigration in thin-films for microelectronics, Microelectron. Reliab. 33 (1993) 1779–1805. https://doi.org/10.1016/0026-2714(93)90086-E.

Research Highlights

It is feasible to use ion beam deposited Pt as electrical contacting material in *operando* electron microscopy. The deposited Pt is relatively stable up to 800 °C and approx. 100 kA/cm^2. The resistivity can be reduced by increasing the applied ion current during deposition and by thermal annealing at a temperature of 500 °C in a few mbar of oxygen.

Graphical Abstract

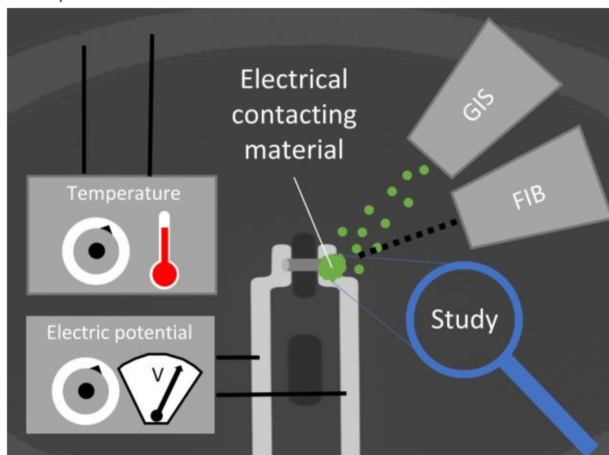

Ion beam deposited Pt is found to be a stable and well conducting contacting material for *operando* electron microscopy experiments at temperatures below 800 °C.

Appendix 3: *Licenses of 1) using the manuscript of Chapter 5 and 2) Figure 2 in Chapter 2*

ELSEVIER LICENSE
TERMS AND CONDITIONS

May 10, 2023

This Agreement between Mr. Zhongtao Ma ("You") and Elsevier ("Elsevier") consists of your license details and the terms and conditions provided by Elsevier and Copyright Clearance Center.

License Number	5545310834452
License date	May 10, 2023
Licensed Content Publisher	Elsevier
Licensed Content Publication	Micron
Licensed Content Title	Exploring the environmental transmission electron microscope
Licensed Content Author	Jakob B. Wagner,Filippo Cavalca,Christian D. Damsgaard,Linus D.L. Duchstein,Thomas W. Hansen
Licensed Content Date	Nov 1, 2012
Licensed Content Volume	43
Licensed Content Issue	11
Licensed Content Pages	7
Start Page	1169
End Page	1175
Type of Use	reuse in a thesis/dissertation

Portion	figures/tables/illustrations
Number of figures/tables/illustrations	1
Format	both print and electronic
Are you the author of this Elsevier article?	No
Will you be translating?	No
Title	Electrochemical TEM experiments on solid oxide cells
Institution name	DTU Energy
Expected presentation date	Sep 2023
Order reference number	666999555
Portions	Figure 1 Schematic diagram of a differentially pumped TEM column
Requestor Location	Mr. Zhongtao Ma DTU building 310, Lyngby, 2800, Denmark Kongens Lyngby, 2800 Denmark Attn: Mr. Zhongtao Ma
Publisher Tax ID	GB 494 6272 12
Total	0.00 EUR

Terms and Conditions

INTRODUCTION

1. The publisher for this copyrighted material is Elsevier. By clicking "accept" in connection with completing this licensing transaction, you agree that the following terms and conditions apply to this transaction (along with the Billing and Payment terms and conditions

established by Copyright Clearance Center, Inc. ("CCC"), at the time that you opened your Rightslink account and that are available at any time at http://myaccount.copyright.com).

GENERAL TERMS

2. Elsevier hereby grants you permission to reproduce the aforementioned material subject to the terms and conditions indicated.

3. Acknowledgement: If any part of the material to be used (for example, figures) has appeared in our publication with credit or acknowledgement to another source, permission must also be sought from that source. If such permission is not obtained then that material may not be included in your publication/copies. Suitable acknowledgement to the source must be made, either as a footnote or in a reference list at the end of your publication, as follows:

"Reprinted from Publication title, Vol /edition number, Author(s), Title of article / title of chapter, Pages No., Copyright (Year), with permission from Elsevier [OR APPLICABLE SOCIETY COPYRIGHT OWNER]." Also Lancet special credit - "Reprinted from The Lancet, Vol. number, Author(s), Title of article, Pages No., Copyright (Year), with permission from Elsevier."

4. Reproduction of this material is confined to the purpose and/or media for which permission is hereby given.

5. Altering/Modifying Material: Not Permitted. However figures and illustrations may be altered/adapted minimally to serve your work. Any other abbreviations, additions, deletions and/or any other alterations shall be made only with prior written authorization of Elsevier Ltd. (Please contact Elsevier's permissions helpdesk here). No modifications can be made to any Lancet figures/tables and they must be reproduced in full.

6. If the permission fee for the requested use of our material is waived in this instance, please be advised that your future requests for Elsevier materials may attract a fee.

7. Reservation of Rights: Publisher reserves all rights not specifically granted in the combination of (i) the license details provided by you and accepted in the course of this licensing transaction, (ii) these terms and conditions and (iii) CCC's Billing and Payment terms and conditions.

8. License Contingent Upon Payment: While you may exercise the rights licensed immediately upon issuance of the license at the end of the licensing process for the transaction, provided that you have disclosed complete and accurate details of your proposed use, no license is finally effective unless and until full payment is received from you (either by publisher or by CCC) as provided in CCC's Billing and Payment terms and conditions. If full payment is not received on a timely basis, then any license preliminarily granted shall be deemed automatically revoked and shall be void as if never granted. Further, in the event that you breach any of these terms and conditions or any of CCC's Billing and Payment terms and conditions, the license is automatically revoked and shall be void as if never granted. Use of materials as described in a revoked license, as well as any use of the materials beyond the scope of an unrevoked license, may constitute copyright infringement and publisher reserves the right to take any and all action to protect its copyright in the materials.

9. Warranties: Publisher makes no representations or warranties with respect to the licensed material.

10. Indemnity: You hereby indemnify and agree to hold harmless publisher and CCC, and their respective officers, directors, employees and agents, from and against any and all claims arising out of your use of the licensed material other than as specifically authorized pursuant to this license.

11. No Transfer of License: This license is personal to you and may not be sublicensed, assigned, or transferred by you to any other person without publisher's written permission.

12. No Amendment Except in Writing: This license may not be amended except in a writing signed by both parties (or, in the case of publisher, by CCC on publisher's behalf).

13. Objection to Contrary Terms: Publisher hereby objects to any terms contained in any purchase order, acknowledgment, check endorsement or other writing prepared by you, which terms are inconsistent with these terms and conditions or CCC's Billing and Payment terms and conditions. These terms and conditions, together with CCC's Billing and Payment terms and conditions (which are incorporated herein), comprise the entire agreement between you and publisher (and CCC) concerning this licensing transaction. In the event of any conflict between your obligations established by these terms and conditions and those established by CCC's Billing and Payment terms and conditions, these terms and conditions shall control.

14. Revocation: Elsevier or Copyright Clearance Center may deny the permissions described in this License at their sole discretion, for any reason or no reason, with a full refund payable to you. Notice of such denial will be made using the contact information provided by you. Failure to receive such notice will not alter or invalidate the denial. In no event will Elsevier or Copyright Clearance Center be responsible or liable for any costs, expenses or damage incurred by you as a result of a denial of your permission request, other than a refund of the amount(s) paid by you to Elsevier and/or Copyright Clearance Center for denied permissions.

LIMITED LICENSE

The following terms and conditions apply only to specific license types:

15. **Translation**: This permission is granted for non-exclusive world **English** rights only unless your license was granted for translation rights. If you licensed translation rights you may only translate this content into the languages you requested. A professional translator must perform all translations and reproduce the content word for word preserving the integrity of the article.

16. **Posting licensed content on any Website**: The following terms and conditions apply as follows: Licensing material from an Elsevier journal: All content posted to the web site must maintain the copyright information line on the bottom of each image; A hyper-text must be included to the Homepage of the journal from which you are licensing at http://www.sciencedirect.com/science/journal/xxxxx or the Elsevier homepage for books at http://www.elsevier.com; Central Storage: This license does not include permission for a scanned version of the material to be stored in a central repository such as that provided by Heron/XanEdu.

Licensing material from an Elsevier book: A hyper-text link must be included to the Elsevier homepage at http://www.elsevier.com . All content posted to the web site must maintain the copyright information line on the bottom of each image.

Posting licensed content on Electronic reserve: In addition to the above the following clauses are applicable: The web site must be password-protected and made available only to bona fide students registered on a relevant course. This permission is granted for 1 year only. You may obtain a new license for future website posting.

17. **For journal authors:** the following clauses are applicable in addition to the above:

Preprints:

A preprint is an author's own write-up of research results and analysis, it has not been peer-reviewed, nor has it had any other value added to it by a publisher (such as formatting, copyright, technical enhancement etc.).

Authors can share their preprints anywhere at any time. Preprints should not be added to or enhanced in any way in order to appear more like, or to substitute for, the final versions of articles however authors can update their preprints on arXiv or RePEc with their Accepted Author Manuscript (see below).

If accepted for publication, we encourage authors to link from the preprint to their formal publication via its DOI. Millions of researchers have access to the formal publications on ScienceDirect, and so links will help users to find, access, cite and use the best available version. Please note that Cell Press, The Lancet and some society-owned have different preprint policies. Information on these policies is available on the journal homepage.

Accepted Author Manuscripts: An accepted author manuscript is the manuscript of an article that has been accepted for publication and which typically includes author-incorporated changes suggested during submission, peer review and editor-author communications.

Authors can share their accepted author manuscript:

- immediately
  - via their non-commercial person homepage or blog
  - by updating a preprint in arXiv or RePEc with the accepted manuscript
  - via their research institute or institutional repository for internal institutional uses or as part of an invitation-only research collaboration work-group
  - directly by providing copies to their students or to research collaborators for their personal use
  - for private scholarly sharing as part of an invitation-only work group on commercial sites with which Elsevier has an agreement
- After the embargo period
  - via non-commercial hosting platforms such as their institutional repository
  - via commercial sites with which Elsevier has an agreement

In all cases accepted manuscripts should:

- link to the formal publication via its DOI
- bear a CC-BY-NC-ND license - this is easy to do
- if aggregated with other manuscripts, for example in a repository or other site, be shared in alignment with our hosting policy not be added to or enhanced in any way to appear more like, or to substitute for, the published journal article.

Published journal article (JPA): A published journal article (PJA) is the definitive final record of published research that appears or will appear in the journal and embodies all value-adding publishing activities including peer review co-ordination, copy-editing, formatting, (if relevant) pagination and online enrichment.

Policies for sharing publishing journal articles differ for subscription and gold open access articles:

<u>Subscription Articles:</u> If you are an author, please share a link to your article rather than the full-text. Millions of researchers have access to the formal publications on ScienceDirect, and so links will help your users to find, access, cite, and use the best available version.

Theses and dissertations which contain embedded PJAs as part of the formal submission can be posted publicly by the awarding institution with DOI links back to the formal publications on ScienceDirect.

If you are affiliated with a library that subscribes to ScienceDirect you have additional private sharing rights for others' research accessed under that agreement. This includes use for classroom teaching and internal training at the institution (including use in course packs and courseware programs), and inclusion of the article for grant funding purposes.

Gold Open Access Articles: May be shared according to the author-selected end-user license and should contain a CrossMark logo, the end user license, and a DOI link to the formal publication on ScienceDirect.

Please refer to Elsevier's posting policy for further information.

18. **For book authors** the following clauses are applicable in addition to the above: Authors are permitted to place a brief summary of their work online only. You are not allowed to download and post the published electronic version of your chapter, nor may you scan the printed edition to create an electronic version. **Posting to a repository:** Authors are permitted to post a summary of their chapter only in their institution's repository.

19. **Thesis/Dissertation**: If your license is for use in a thesis/dissertation your thesis may be submitted to your institution in either print or electronic form. Should your thesis be published commercially, please reapply for permission. These requirements include permission for the Library and Archives of Canada to supply single copies, on demand, of the complete thesis and include permission for Proquest/UMI to supply single copies, on demand, of the complete thesis. Should your thesis be published commercially, please reapply for permission. Theses and dissertations which contain embedded PJAs as part of the formal submission can be posted publicly by the awarding institution with DOI links back to the formal publications on ScienceDirect.

Elsevier Open Access Terms and Conditions

You can publish open access with Elsevier in hundreds of open access journals or in nearly 2000 established subscription journals that support open access publishing. Permitted third party re-use of these open access articles is defined by the author's choice of Creative Commons user license. See our open access license policy for more information.

Terms & Conditions applicable to all Open Access articles published with Elsevier:

Any reuse of the article must not represent the author as endorsing the adaptation of the article nor should the article be modified in such a way as to damage the author's honour or reputation. If any changes have been made, such changes must be clearly indicated.

The author(s) must be appropriately credited and we ask that you include the end user license and a DOI link to the formal publication on ScienceDirect.

If any part of the material to be used (for example, figures) has appeared in our publication with credit or acknowledgement to another source it is the responsibility of the user to ensure their reuse complies with the terms and conditions determined by the rights holder.

Additional Terms & Conditions applicable to each Creative Commons user license:

CC BY: The CC-BY license allows users to copy, to create extracts, abstracts and new works from the Article, to alter and revise the Article and to make commercial use of the Article (including reuse and/or resale of the Article by commercial entities), provided the user gives appropriate credit (with a link to the formal publication through the relevant DOI), provides a link to the license, indicates if changes were made and the licensor is not represented as endorsing the use made of the work. The full details of the license are available at http://creativecommons.org/licenses/by/4.0.

CC BY NC SA: The CC BY-NC-SA license allows users to copy, to create extracts, abstracts and new works from the Article, to alter and revise the Article, provided this is not done for commercial purposes, and that the user gives appropriate credit (with a link to the formal publication through the relevant DOI), provides a link to the license, indicates if changes were made and the licensor is not represented as endorsing the use made of the work. Further, any new works must be made available on the same conditions. The full details of the license are available at http://creativecommons.org/licenses/by-nc-sa/4.0.

CC BY NC ND: The CC BY-NC-ND license allows users to copy and distribute the Article, provided this is not done for commercial purposes and further does not permit distribution of the Article if it is changed or edited in any way, and provided the user gives appropriate credit (with a link to the formal publication through the relevant DOI), provides a link to the license, and that the licensor is not represented as endorsing the use made of the work. The full details of the license are available at http://creativecommons.org/licenses/by-nc-nd/4.0. Any commercial reuse of Open Access articles published with a CC BY NC SA or CC BY NC ND license requires permission from Elsevier and will be subject to a fee.

Commercial reuse includes:

- Associating advertising with the full text of the Article
- Charging fees for document delivery or access
- Article aggregation
- Systematic distribution via e-mail lists or share buttons

Posting or linking by commercial companies for use by customers of those companies.

20. **Other Conditions**:

v1.10

Questions? customercare@copyright.com.

JOHN WILEY AND SONS LICENSE
TERMS AND CONDITIONS

May 10, 2023

This Agreement between Mr. Zhongtao Ma ("You") and John Wiley and Sons ("John Wiley and Sons") consists of your license details and the terms and conditions provided by John Wiley and Sons and Copyright Clearance Center.

License Number	5545320793375
License date	May 10, 2023
Licensed Content Publisher	John Wiley and Sons
Licensed Content Publication	Small Methods
Licensed Content Title	Electrochemical Impedance Spectroscopy Integrated with Environmental Transmission Electron Microscopy
Licensed Content Author	Zhongtao Ma, Waynah Lou Dacayan, Christodoulos Chatzichristodoulou, et al
Licensed Content Date	Apr 10, 2023
Licensed Content Volume	0
Licensed Content Issue	0
Licensed Content Pages	10
Type of use	Dissertation/Thesis
Requestor type	Author of this Wiley article
Format	Print and electronic

Portion	Full article
Will you be translating?	No
Title	Electrochemical TEM experiments on solid oxide cells
Institution name	DTU Energy
Expected presentation date	Sep 2023
Order reference number	666999551
Requestor Location	Mr. Zhongtao Ma DTU building 310, Lyngby, 2800, Denmark Kongens Lyngby, 2800 Denmark Attn: Mr. Zhongtao Ma
Publisher Tax ID	EU826007151
Total	0.00 EUR

Terms and Conditions

TERMS AND CONDITIONS

This copyrighted material is owned by or exclusively licensed to John Wiley & Sons, Inc. or one of its group companies (each a"Wiley Company") or handled on behalf of a society with which a Wiley Company has exclusive publishing rights in relation to a particular work (collectively "WILEY"). By clicking "accept" in connection with completing this licensing transaction, you agree that the following terms and conditions apply to this transaction (along with the billing and payment terms and conditions established by the Copyright Clearance Center Inc., ("CCC's Billing and Payment terms and conditions"), at the time that you opened your RightsLink account (these are available at any time at http://myaccount.copyright.com).

Terms and Conditions

- The materials you have requested permission to reproduce or reuse (the "Wiley Materials") are protected by copyright.
- You are hereby granted a personal, non-exclusive, non-sub licensable (on a stand-alone basis), non-transferable, worldwide, limited license to reproduce the Wiley

Materials for the purpose specified in the licensing process. This license, **and any CONTENT (PDF or image file) purchased as part of your order,** is for a one-time use only and limited to any maximum distribution number specified in the license. The first instance of republication or reuse granted by this license must be completed within two years of the date of the grant of this license (although copies prepared before the end date may be distributed thereafter). The Wiley Materials shall not be used in any other manner or for any other purpose, beyond what is granted in the license. Permission is granted subject to an appropriate acknowledgement given to the author, title of the material/book/journal and the publisher. You shall also duplicate the copyright notice that appears in the Wiley publication in your use of the Wiley Material. Permission is also granted on the understanding that nowhere in the text is a previously published source acknowledged for all or part of this Wiley Material. Any third party content is expressly excluded from this permission.

- With respect to the Wiley Materials, all rights are reserved. Except as expressly granted by the terms of the license, no part of the Wiley Materials may be copied, modified, adapted (except for minor reformatting required by the new Publication), translated, reproduced, transferred or distributed, in any form or by any means, and no derivative works may be made based on the Wiley Materials without the prior permission of the respective copyright owner.**For STM Signatory Publishers clearing permission under the terms of the STM Permissions Guidelines only, the terms of the license are extended to include subsequent editions and for editions in other languages, provided such editions are for the work as a whole in situ and does not involve the separate exploitation of the permitted figures or extracts,** You may not alter, remove or suppress in any manner any copyright, trademark or other notices displayed by the Wiley Materials. You may not license, rent, sell, loan, lease, pledge, offer as security, transfer or assign the Wiley Materials on a stand-alone basis, or any of the rights granted to you hereunder to any other person.

- The Wiley Materials and all of the intellectual property rights therein shall at all times remain the exclusive property of John Wiley & Sons Inc, the Wiley Companies, or their respective licensors, and your interest therein is only that of having possession of and the right to reproduce the Wiley Materials pursuant to Section 2 herein during the continuance of this Agreement. You agree that you own no right, title or interest in or to the Wiley Materials or any of the intellectual property rights therein. You shall have no rights hereunder other than the license as provided for above in Section 2. No right, license or interest to any trademark, trade name, service mark or other branding ("Marks") of WILEY or its licensors is granted hereunder, and you agree that you shall not assert any such right, license or interest with respect thereto

- NEITHER WILEY NOR ITS LICENSORS MAKES ANY WARRANTY OR REPRESENTATION OF ANY KIND TO YOU OR ANY THIRD PARTY, EXPRESS, IMPLIED OR STATUTORY, WITH RESPECT TO THE MATERIALS OR THE ACCURACY OF ANY INFORMATION CONTAINED IN THE MATERIALS, INCLUDING, WITHOUT LIMITATION, ANY IMPLIED WARRANTY OF MERCHANTABILITY, ACCURACY, SATISFACTORY QUALITY, FITNESS FOR A PARTICULAR PURPOSE, USABILITY, INTEGRATION OR NON-INFRINGEMENT AND ALL SUCH WARRANTIES ARE HEREBY EXCLUDED BY WILEY AND ITS LICENSORS AND WAIVED BY YOU.

- WILEY shall have the right to terminate this Agreement immediately upon breach of this Agreement by you.

- You shall indemnify, defend and hold harmless WILEY, its Licensors and their respective directors, officers, agents and employees, from and against any actual or threatened claims, demands, causes of action or proceedings arising from any breach of this Agreement by you.

- IN NO EVENT SHALL WILEY OR ITS LICENSORS BE LIABLE TO YOU OR ANY OTHER PARTY OR ANY OTHER PERSON OR ENTITY FOR ANY SPECIAL, CONSEQUENTIAL, INCIDENTAL, INDIRECT, EXEMPLARY OR PUNITIVE DAMAGES, HOWEVER CAUSED, ARISING OUT OF OR IN CONNECTION WITH THE DOWNLOADING, PROVISIONING, VIEWING OR USE OF THE MATERIALS REGARDLESS OF THE FORM OF ACTION, WHETHER FOR BREACH OF CONTRACT, BREACH OF WARRANTY, TORT, NEGLIGENCE, INFRINGEMENT OR OTHERWISE (INCLUDING, WITHOUT LIMITATION, DAMAGES BASED ON LOSS OF PROFITS, DATA, FILES, USE, BUSINESS OPPORTUNITY OR CLAIMS OF THIRD PARTIES), AND WHETHER OR NOT THE PARTY HAS BEEN ADVISED OF THE POSSIBILITY OF SUCH DAMAGES. THIS LIMITATION SHALL APPLY NOTWITHSTANDING ANY FAILURE OF ESSENTIAL PURPOSE OF ANY LIMITED REMEDY PROVIDED HEREIN.

- Should any provision of this Agreement be held by a court of competent jurisdiction to be illegal, invalid, or unenforceable, that provision shall be deemed amended to achieve as nearly as possible the same economic effect as the original provision, and the legality, validity and enforceability of the remaining provisions of this Agreement shall not be affected or impaired thereby.

- The failure of either party to enforce any term or condition of this Agreement shall not constitute a waiver of either party's right to enforce each and every term and condition of this Agreement. No breach under this agreement shall be deemed waived or excused by either party unless such waiver or consent is in writing signed by the party granting such waiver or consent. The waiver by or consent of a party to a breach of any provision of this Agreement shall not operate or be construed as a waiver of or consent to any other or subsequent breach by such other party.

- This Agreement may not be assigned (including by operation of law or otherwise) by you without WILEY's prior written consent.

- Any fee required for this permission shall be non-refundable after thirty (30) days from receipt by the CCC.

- These terms and conditions together with CCC's Billing and Payment terms and conditions (which are incorporated herein) form the entire agreement between you and WILEY concerning this licensing transaction and (in the absence of fraud) supersedes all prior agreements and representations of the parties, oral or written. This Agreement may not be amended except in writing signed by both parties. This Agreement shall be binding upon and inure to the benefit of the parties' successors, legal representatives, and authorized assigns.

- In the event of any conflict between your obligations established by these terms and conditions and those established by CCC's Billing and Payment terms and conditions, these terms and conditions shall prevail.

- WILEY expressly reserves all rights not specifically granted in the combination of (i) the license details provided by you and accepted in the course of this licensing transaction, (ii) these terms and conditions and (iii) CCC's Billing and Payment terms and conditions.

- This Agreement will be void if the Type of Use, Format, Circulation, or Requestor Type was misrepresented during the licensing process.

- This Agreement shall be governed by and construed in accordance with the laws of the State of New York, USA, without regards to such state's conflict of law rules. Any legal action, suit or proceeding arising out of or relating to these Terms and Conditions

or the breach thereof shall be instituted in a court of competent jurisdiction in New York County in the State of New York in the United States of America and each party hereby consents and submits to the personal jurisdiction of such court, waives any objection to venue in such court and consents to service of process by registered or certified mail, return receipt requested, at the last known address of such party.

WILEY OPEN ACCESS TERMS AND CONDITIONS

Wiley Publishes Open Access Articles in fully Open Access Journals and in Subscription journals offering Online Open. Although most of the fully Open Access journals publish open access articles under the terms of the Creative Commons Attribution (CC BY) License only, the subscription journals and a few of the Open Access Journals offer a choice of Creative Commons Licenses. The license type is clearly identified on the article.

The Creative Commons Attribution License

The Creative Commons Attribution License (CC-BY) allows users to copy, distribute and transmit an article, adapt the article and make commercial use of the article. The CC-BY license permits commercial and non-

Creative Commons Attribution Non-Commercial License

The Creative Commons Attribution Non-Commercial (CC-BY-NC)License permits use, distribution and reproduction in any medium, provided the original work is properly cited and is not used for commercial purposes.(see below)

Creative Commons Attribution-Non-Commercial-NoDerivs License

The Creative Commons Attribution Non-Commercial-NoDerivs License (CC-BY-NC-ND) permits use, distribution and reproduction in any medium, provided the original work is properly cited, is not used for commercial purposes and no modifications or adaptations are made. (see below)

Use by commercial "for-profit" organizations

Use of Wiley Open Access articles for commercial, promotional, or marketing purposes requires further explicit permission from Wiley and will be subject to a fee.

Further details can be found on Wiley Online Library
http://olabout.wiley.com/WileyCDA/Section/id-410895.html

Other Terms and Conditions:

v1.10 Last updated September 2015

Questions? customercare@copyright.com.